

THESIS / THÈSE

DOCTOR OF SCIENCES

Catalyst nanomaterials for applications in hydrogen fuel cells

a new approach for the synthesis and surface functionalization by low-pressure plasmas

Da Silva Pires, Mathieu

Award date:
2020

Awarding institution:
University of Namur

[Link to publication](#)

General rights

Copyright and moral rights for the publications made accessible in the public portal are retained by the authors and/or other copyright owners and it is a condition of accessing publications that users recognise and abide by the legal requirements associated with these rights.

- Users may download and print one copy of any publication from the public portal for the purpose of private study or research.
- You may not further distribute the material or use it for any profit-making activity or commercial gain
- You may freely distribute the URL identifying the publication in the public portal ?

Take down policy

If you believe that this document breaches copyright please contact us providing details, and we will remove access to the work immediately and investigate your claim.



UNIVERSITÉ DE NAMUR
Faculté des sciences
Département de Physique



Catalyst nanomaterials for applications in hydrogen fuel cells: a new approach for the synthesis and surface functionalization by low-pressure plasmas

Dissertation présentée en vue de l'obtention du grade de
Docteur en Sciences
par
Mathieu da Silva Pires

Membres du jury:

Dr.	Yan Busby	Institut franco-allemand de recherches de Saint-Louis
Prof.	Amaël Caillard	CNRS/Université d'Orléans
Prof.	Nathalie Job	Université de Liège
Dr.	Jean-François Colomer	FNRS/Université de Namur (Président)
Prof.	Laurent Houssiau	Université de Namur (Promoteur)

Namur, le 20 Août 2020

*For You.
Forever.*

Remerciements

"We must find time to stop and thank the people who make a difference in our lives." – John F. Kennedy

Après quasiment six années d'assistantat consacrées aux services de l'enseignement et de la recherche, le temps est venu de faire le bilan. Cette période d'une vie que l'on ne peut oublier car elle constitue une étape de transformation importante pour le doctorant. Cette vie qui réserve des surprises à chaque instant. Je ne pourrais pas mentionner toutes les personnes ayant marqués ces six années mais toutes mes pensées vont d'ores et déjà vers elles.

Je commencerai par cette anecdote qui a tout changé. Je me rappelle encore de ce jour où mon ami Louis m'a contacté pour m'avertir de l'ouverture d'un poste à l'UNamur. Cela faisait un an que j'avais terminé mon Master et souhaitais continuer à faire de la physique. Malgré le fait que mes connaissances en sciences des matériaux étaient limitées, cette envie d'apprendre et comprendre des phénomènes physiques me poussait à postuler car, pour moi, la curiosité et la motivation sont deux des caractéristiques principales qu'un physicien se doit de développer et/ou entretenir. Je remercie déjà Louis Dellieu, avec qui j'ai passé quelques années sur les bancs de la fac, car je ne serais pas là où j'en suis sans lui.

Mes remerciements vont ensuite à mon promoteur, Laurent Houssiau, qui m'a fait confiance et permis de réaliser une thèse au sein de l'unité de recherche LISE alors que mon parcours atypique n'était pas gage d'une réussite assurée. Ensuite, un tout grand merci à Yan de m'avoir entraîné dans le domaine des nanoparticules ainsi que pour sa disponibilité, son enthousiasme, son écoute,... Et je ne cite là qu'une petite partie de ce qu'il a pu m'apporter tant sur le plan scientifique qu'humain. Je n'oublie pas ce bon vieux Fred qui, malgré ses multiples péripéties, a toujours répondu à mes appels et avec qui j'ai beaucoup eu l'occasion de faire du "diagnostic" vis-à-vis de problématiques diverses et variées ;-). Je tiens aussi à remercier chaleureusement toutes les personnes impliquées dans ma thèse, d'avoir pris de leur temps afin de m'aider que ce soit pour les expériences, les articles scientifiques ou pour la rédaction de mon manuscrit. Merci pour vos commentaires pertinents et constructifs ainsi que votre relecture très attentive.

Je n'oublie pas mes collègues avec lesquels nous avons passé beaucoup de bons moments : Céline, Pauline, Julie, Nicolas, Mathilde, Matthieu et j'en passes ! Que de franches rigolades ou discussions animées à propos de l'organisation des cours, des examens et bien d'autres choses. Je pense que pour certains Proximus restera gravé dans les mémoires :-p. Je souhaite bonne continuation à mes collègues assistants avec qui j'ai eu l'occasion de partager quelques années. J'ai aussi eu la chance de rencontrer des personnes incroyables qui m'ont permis de découvrir pleins de choses. Je pense à Pascale, Gabriel, Linda, Charles-Eric et bien d'autres de l'ULaval lors de mon voyage à Québec.

Même si ce n'est pas toujours évident de se voir, je pense aussi très fort à mes meilleures amies Morgane et Caro. Nos chemins se sont croisés un beau jour et quelles aventures nous avons pu vivre depuis :-p Vous m'avez, à votre manière, soutenu durant toutes ces années. Merci à vous d'être là.

Que dire sur le soutien de ma famille... Ils m'ont encouragés depuis bien longtemps et, même s'ils n'ont pas toujours très bien compris ce que je faisais exactement, ils ont toujours été fier de mon parcours. Je crois qu'ils savent à quel point il ne m'est pas facile d'exprimer ce que je ressens mais je suis persuadé qu'ils savent à quel point je leur suis reconnaissant. Enfin, un pensée spéciale dans ces remerciements : Aan mijn vriend Bram die me al jaren steunt, bedankt dat je er bent in deze periode van mijn leven. Het is niet altijd even gemakkelijk geweest, maar we zijn erin geslaagd vele stappen te nemen en ik hoop dat we er in de toekomst nog veel meer zullen doorlopen.

Finalement, comme l'a si bien dit mon prédécesseur, Xavier : qu'est-ce que ça fait du bien quand la thèse ça s'arrête...

Milles mercis à tous d'avoir été là !

Contents

Remerciements	i
Symbols and abbreviations	vii
List of Figures	ix
List of Figures	ix
List of Tables	xvii
List of Tables	xvii
List of Publications	xix
Introduction	1
1 Polymer electrolyte membrane fuel cells	7
1.1 Fuel cells history	7
1.2 PEM fuel cell's working principle	8
1.3 Chemical reaction mechanisms and catalysts developments for PEM fuel cells	11
1.3.1 Mechanisms in HOR and the role of the catalyst	11
1.3.2 Pt-free or synergistic catalysts for the hydrogen oxidation reaction	13
1.3.3 Mechanisms in oxygen reduction reaction and the role of the catalyst	13
1.3.4 Pt alloys and non-precious metal catalysts for the oxygen reduction reaction	17
1.4 Influence of the carbon support on the catalytic activity	19
1.5 Nitrogen-doping of the carbon support	22
2 Low-pressure plasma	25
2.1 Concepts in plasma physics	26
2.1.1 Plasma criteria	26
2.1.2 Debye shielding length	26

2.1.3	Ionization degree and quasi-neutrality	27
2.1.4	Langmuir frequency	27
2.1.5	Plasma sheaths	28
2.2	Low-pressure non-local thermal equilibrium plasma	28
2.3	Gas discharge plasmas	31
2.3.1	Direct current or glow discharge plasmas	31
2.3.2	Radio-frequency plasmas	32
2.3.3	Radio-frequency inductively coupled plasmas	33
2.3.4	E-to-H transition	34
3	Synthesis of nanoparticles and carbon functionalization : from chemical to physical methodologies	37
3.1	Methodologies developed to synthesize nanoparticles	37
3.1.1	Wet chemical processes	37
3.1.2	Physico-chemical techniques	38
3.2	Experimental setup	40
3.2.1	The plasma reactor	40
3.2.2	The RF-ICP source	40
3.2.3	Gas injection and pumping system	41
3.2.4	Pressure gauges	42
3.3	Nanoparticle synthesis procedure	42
4	Characterization techniques	45
4.1	X-Ray Photoelectron Spectroscopy	45
4.1.1	Operating principle of an XPS	46
4.1.2	Information extracted from the collected photoelectrons	49
4.2	Powder X-ray diffraction	51
4.3	Transmission electron microscopy	53
4.3.1	Scanning transmission electron microscopy	54
4.3.2	Energy dispersive X-ray analysis	55
4.4	Optical emission spectroscopy	55
4.5	Electrochemical methods	56
4.5.1	Oxygen Reduction Reaction	57
4.5.2	CO stripping voltammetry	58
4.6	Nitrogen adsorption-desorption method	58
5	Advances in the fabrication of Pt nanoparticles supported on carbon substrates	63
5.1	Introduction	63
5.2	Synthesis of Pt/xerogel nanoparticles by using different metal pre- cursors	64
5.2.1	Decomposition of the metal precursors by one-step plasma treatments	66

5.2.2	On the agglomeration of the nanoparticles through a morphology study	68
5.2.3	Chemical analysis of the fabricated Pt/xerogel nanoparticles	71
5.2.4	Evaluation of the energy consumption related to the fabrication of a Pt/xerogel catalyst	74
5.2.5	Conclusions	75
5.3	Study of the Pt/C nanomaterials fabricated on graphene sheets .	76
5.3.1	Structural and morphological analyses of the Pt/graphene particles	77
5.3.2	Chemical environment and oxidation state characteristics of the Pt/graphene particles	77
5.3.3	Influence of the pretreatment on the nanoparticles synthesis	79
5.4	Conclusions	83
6	Influence of the plasma chemistry on the synthesis of Ni/C composites	85
6.1	Introduction	85
6.2	Organometallic precursor decomposition dependence with the plasma chemistry	87
6.3	Morphology of the synthesized nanoparticles	94
6.4	Analysis of the Ni/C nanocatalysts chemical composition and state	95
6.5	Functionalization of the carbon support	98
6.6	Conclusions and perspectives	102
7	Defective Pt-Ni/graphene composites fabricated by low-pressure oxygen plasma treatment	105
7.1	Introduction	105
7.2	Experimental section	107
7.2.1	Experimental section	107
7.2.2	Reducing effect of the oxygen plasma	108
7.3	Decomposition of the precursors and nanoparticle formation . . .	109
7.3.1	Morphology of the Pt-Ni/graphene nanocomposites	110
7.4	Chemical analysis of the Pt-Ni/graphene composites	114
7.5	Catalytic activity of the Pt-Ni/graphene composites	117
7.5.1	Procedure setup for the electrochemical characterizations .	117
7.5.2	Electrochemical characterizations of the Pt-Ni/C composites	118
7.6	Conclusions and perspectives	120
8	Nitrogen-doping of carbon xerogels by low-pressure plasma discharges	123
8.1	Introduction	123
8.2	E-to-H transition for NH ₃ and N ₂ plasma discharges	124
8.3	Elemental and chemical analysis of NH ₃ treated carbon xerogels .	127
8.4	Elemental and chemical analysis of a N ₂ treated carbon xerogel .	131

8.5	Impact of the plasma treatment on the pore texture	133
8.6	Conclusions and perspectives	134
	General conclusion and perspectives	137
A	Bright field TEM images of the Pt/CXG nanomaterials	141
B	High-resolution C 1s and O 1s XPS spectra of Pt/CXG nanomaterials	143
C	Asymmetrical shape fitting in XPS	145
D	XRD diffractogram of Pt/GNP nanomaterials	147
E	High-resolution Ni 2p XPS spectra of metal nickel and oxides	149
F	Ni-Pt phase diagram	151
G	XPS survey spectra of Pt-Ni/graphene nanomaterials	153
H	Electrochemical characterizations : sample preparation	155
	Bibliography	157

Symbols and abbreviations

ARFPT: Atmospheric radio-frequency plasma torch

at. %: Atomic percentage

BET: Brunauer-Emmett-Teller

BE: Binding energy

BF: Bright field

BJH: Barrett-Joyner-Halenda

CB: Carbon black

CCP: Capacitively coupled plasma

CL: Catalyst layer

CNT: Carbon nanotube

CXG: Carbon xerogel

EDX: Energy dispersive X-ray

FC: Fuel cell

GC: Glassy carbon

GDL: Gas diffusion layer

GNP: Graphene nanoplatelets

HAADF: High-angle annular dark field

HOR: Hydrogen Oxidation Reaction

HR-XPS: High-resolution X-ray photoelectron spectroscopy

ICP: Inductively coupled plasma

KE: Kinetic energy

LTE: Local thermal equilibrium

MA: Mass activity

NLTE: Non-local thermal equilibrium

NP: Nanoparticle

OES: Optical emission spectroscopy

OM: Organometallic

ORR: Oxygen Reduction Reaction

PEM: Polymer electrolyte membrane or Proton exchange membrane

PGM: Platinum group metal

RF: Radio-frequency

RHE: Reference hydrogen electrode

rpm: rotation per minute

SA: Specific activity

sccm: Standard cubic centimeters per minute

SSA: Specific surface area

STEM: Scanning transmission electron microscopy

TEM: Transmission electron microscopy

TSA: Total surface area

UHV: Ultra high vacuum

wt. %: Weight percentage

XPS: X-ray photoelectron spectroscopy

XRD: X-ray diffraction

List of Figures

1	Evolution of the energy production by fuel between 1986 and 2018.	1
2	Evolution of the mass of CO ₂ released in the atmosphere by fuel combustion and cement production.	2
1.1	The first historic fuel cell created by William R. Grove in 1839. . .	8
1.2	Working principle diagram of a PEMFC.	9
1.3	Picture and sketch of a bipolar plate with a multiple serpentine flow channel design.	10
1.4	Schematic view of a) the Tafel-Volmer route and b) the Heyrovsky-Volmer route on Pt extended surface.	12
1.5	Typical "volcano curve" of the exchange current density in function of the binding energy of hydrogen for several metals.	12
1.6	Complete ORR mechanisms in the case of noble catalysts. The main way is the formation of water through a 4-electron process. Parasite reactions may occur and lead to the formation of hydrogen peroxide.	14
1.7	Map of the ORR activity for some metals as a function of the O and OH binding energies	16
1.8	Repartition of the PGM reserves by country in 2018.	16
1.9	Hybridization of the metal <i>d</i> -band when interacting with an adsorbate. The <i>d</i> -band center location, with respect to the Fermi level, can be measured to evaluate the strength of a bond.	17
1.10	Volcano plot of some Pt alloys. Measured kinetic current density are reported relatively to Pt.	18
1.11	Scanning electron microscopy images of a) carbon black, b) graphene nanoplatelets, c) carbon nanotubes and d) carbon xerogel.	21
1.12	Global overview of the main techniques employed to produce N-doped carbon materials.	23
2.1	Schematic representation of a confined plasma with the creation of a space charge sheath close to the surface. The quasi-neutrality is only verified within the plasma bulk and deviate in the sheath. . .	29
2.2	Illustration of the different plasma classes versus the electron temperature and density.	30
2.3	Global overview of a glow discharge tube.	32

2.4	Illustration of a) inner planar and b) outer planar electrodes geometries for the CCPs, c) planar and d) cylindrical coil geometries in the case of ICPs.	34
2.5	Representation of (a) the skin depth δ in a cylindrical volume which limits the field penetration and (b) the transformer model of the source-plasma coupling.	35
3.1	Sketch of the proposed mechanism for the NP nucleation by a low temperature radio-frequency plasma.	40
3.2	Schematic picture of the plasma reactor. The most energetic area of the plasma is located at the center of the quartz tube wrapped with the coil.	41
3.3	Sketch of the methodology set up for the nanoparticles synthesis.	43
4.1	Illustration of the electron population in core levels and the emission principle of photoelectrons induced by X-rays.	46
4.2	Schematic drawing of the working principle of an X-ray Photoelectron Spectrometer.	47
4.3	Schematic diagram of one channel electron multiplier.	48
4.4	Sketch of the XPS analysis together with the parameters influencing the peaks intensities.	50
4.5	a) Illustration of the Bragg diffraction. b) Schematic drawing of the operating principle of an X-ray powder diffraction instrument.	52
4.6	Schematic drawing of the operating principle of a transmission electron microscope (Taken from JEOL 2000FX Handbook).	54
4.7	Sketch of the rotating disk electrode method, with the streamlines generated by the rotation, employed for the ORR activity measurements.	57
4.8	Size effect in a CO stripping voltammogram. Positions of current peaks provide information on the size distribution of the catalysts.	59
4.9	Sketch of the BET methodology employed to measure the specific area and the porosity of various materials.	60
4.10	Illustration of the different isotherm curves obtained after a gas adsorption-desorption experiment. Mesoporous carbon are usually characterized by Type IV isotherms.	61
4.11	Schematic drawing of a cylindrical pore usually considered in the BJH theory to calculate the pore characteristics.	62
5.1	Molecular structure of a) Pt(II) acetylacetonate, b) (1,5)-cyclo-octadiene dimethylplatinum(II) and c) hydrogen hexahydroxyplatinatate(IV).	64

5.2	XRD diffractograms of the pristine powder and after the different plasma treatments for a) the Pt(II) acetylacetonate (OM1) and b) (1,5-Cyclooctadiene) dimethylplatinum(II) (OM2) and the hydrogen hexahydroxyplatinate (IV) (AM) precursors.	67
5.3	TEM images of the O ₂ plasma treated samples (OM1-1 (a), OM2-1 (c) and AM1 (e)) or "mixed" Ar/O ₂ plasma treatments (OM1-3 (b), OM2-4 (d) and AM2 (f)).	69
5.4	High-resolution Pt 4f XPS spectra of the plasma treated sample using the three metallic precursor (a,c,e) with their corresponding oxidation states relative percentages (b,d,f).	72
5.5	High-resolution XPS Pt 4f core level spectra of the organometallic (Pt(acac) ₂ and Pt(cod)(Me) ₂) and the inorganic precursors (platinic acid), respectively.	73
5.6	TEM images of selected samples fabricated following the plasma conditions given in Table 5.3. The NP synthesis for GNP-01 and GNP-02 were performed in low-energy "one-pot" plasma treatments while GNP-03 and GNP-04 were produced following a 2-step approach (low- and high-energy treatments).	78
5.7	High-resolution a) C 1s, b) O 1s and c) Pt 4f XPS core level spectra of the Pt/GNP nanocatalysts synthesized by O ₂ plasma discharges following the conditions given in Table 5.3. d) Relative percentages of the Pt oxidation states.	79
5.8	Bright field TEM images of the GNP ^N -01 (a,b) and GNP ^N -02 (c,d) plasma treated samples. Preferential nucleation of the NPs at the edges of the sheets is drastically decreased which is probably due to the presence of structural defects induced by the pretreatment.	81
5.9	High-resolution a) C 1s, b) N 1s (with four components attributed to pyridinic-N (1), pyrrolic-N (2), -NO (3) and -NO ₂ (4) functional groups), c) O 1s and d) Pt 4f XPS core level spectra of the Pt/GNP catalysts synthesized on pretreated graphene sheets in a N ₂ plasma discharge.	82
6.1	Molecular structure of the nickel(II) acetylacetonate employed as precursor for the fabrication of Ni/C nanocatalyst.	86
6.2	In-situ OES spectra taken at the beginning of the ammonia, nitrogen and oxygen plasmas at a power of 140 W. The OH A-X, N ₂ C-B, CN and Ar I lines are identified and the evolution over time of some of them are monitored to follow the OM decomposition.	88
6.3	Evolution of the OH-related (309.2 nm) and CN (388.2 nm) lines for Ar:O ₂ , Ar:N ₂ and Ar:NH ₃ plasmas. The plasma power was fixed at 140 W in each case.	89

6.4	Diffractograms of a) the untreated powder of the OM precursor together with the most energetic plasma discharges for both Ar:O ₂ and Ar:N ₂ , and b) the Ar:NH ₃ treatments at several transmitted powers. The evaluation of the average size distribution, thanks to the Debye-Scherrer formula, is shown for the Ni nanocrystals in the inset.	90
6.5	a) Corrected OES intensity of the CN emission line (388.2 nm) for a 140 W Ar:N ₂ plasma treatment. Integrals in the determination of the OM molecular fraction are represented by the two surface areas (orange diagonal lines and gray-filled). b) Evolution of OM molecular fraction as a function of the treatment time obtained following Equation 6.7.	91
6.6	Curve of a) the OES intensity natural logarithm for an Ar:N ₂ plasma discharge with a power of 120 W, b) the reaction order n , c) the kinetic constant k and d) the analogy with an Arrhenius plot for the determination of an "activation power" through the calculation of the linear fit slope.	92
6.7	High-angle annular dark field (HAADF) STEM micrographs of the Ni/xerogel NPs, seen as bright spots in the different images. Images of the a) Ar:O ₂ and b) Ar:N ₂ plasma treatments at 200 W are shown while the Ar:NH ₃ plasma treatments at c) 90 W and d) 200 W are presented. The focus in image d) highlights a brighter shell (where contrast was exacerbated on purpose for a better visualization) specific to the ammonia plasma treatments.	95
6.8	Atomic percentage quantification derived from the analysis of HR-XPS spectra for a) oxygen, b) nitrogen and c) nickel as a function of the transmitted power.	96
6.9	a) HR-XPS Ni 2p _{3/2} spectra at 90 and 200 W for the three plasma chemistries. b) Peak fitting of the HR-XPS Ni 2p _{3/2} spectrum for an Ar:NH ₃ treatment at 200 W allowing the quantification of the chemical oxidation state of the Ni NPs.	98
6.10	High-resolution C 1s spectrum of a) the untreated powder mixture, b) the modified surface after an Ar:O ₂ plasma, c) the modified surface after an Ar:NH ₃ plasma and d) the modified surface after an Ar:N ₂ plasma.	99
6.11	HR-XPS N 1s spectra of a 200 W plasma treatment for an a) Ar:NH ₃ and b) an Ar:N ₂ gas mixture.	101
6.12	a) Global chemical composition of the treated samples (200 W) for the different plasma chemistries. b) Relative percentage of the nitrogen-groups derived from the analysis of the N 1s spectra for the two explored N-containing gas mixtures explored (200 W). . .	101

7.1	Sketch of the simultaneous (T_1) and sequential (T_{2A} and T_{2B}) treatments employed for the fabrication of the Pt-Ni/GNP nanocomposites.	107
7.2	HR-XPS Pt 4f spectra resulting of an O_2 , Ar and N_2 plasma treatments respectively following the conditions presented for T_2 . The reducing effect in the case of an O_2 discharge is clearly evidenced.	109
7.3	Diffraction patterns of the metallic precursors (blue and green lines), the sequential treatment (T_{2A} and T_{2B} , purple lines) and the simultaneous treatment (T_1 , rust-colored line). The graphene and platinum peaks are clearly indicated with the corresponding Miller indexes as well as the precursor traces.	110
7.4	(a) High-resolution TEM image of the Pt-Ni/GNP composites obtained after the simultaneous plasma treatment (T_1). (b) STEM image together with the EDX maps acquired on a specific region (shown on the STEM image) highlighting the Pt and Ni species distribution on the surface.	111
7.5	Size distribution for the simultaneous (T_1 , rust-colored line) and sequential (T_2 , purple line) plasma treatments derived from the TEM/STEM images.	112
7.6	Bright field TEM images of (a) the pristine GNPs employed as a support for the NPs and (b) sub-nanometer Ni seeds formed on the carbon support surface after the T_{2A} plasma treatment of the GNP mixed the Ni precursor.	112
7.7	(a) Low magnification and (b) high magnification bright field STEM images of the Pt-Ni/GNP composites obtained after the sequential plasma treatment (T_2). Well-separated 1-3 nm Pt-Ni nanocomposites are clearly homogeneously dispersed at the surface of the graphene sheets.	113
7.8	High angle annular dark field STEM image of the synthesized Pt-Ni/GNP nanocomposites after (a) the one-step (T_1) plasma treatment and (b) the two-step (T_2) plasma treatment of the two OM precursors. The bright spots correspond to elements with a high element number and is expected to be Pt. The brighter spots correspond to elements with a high element number and are due to the metal atoms, while the darker areas correspond to carbon.	114
7.9	HR-XPS core level spectra of the a) C 1s, b) O 1s, c) Pt 4f and d) Ni 2p elements after the simultaneous (T_1 , rust-colored line) and the sequential (T_2 , purple line) treatments.	116
7.10	Electrochemical characterizations of the simultaneous (T_1) and sequential (T_2) Pt-Ni/GNP catalysts and the reference Pt/C catalyst. a) CO stripping voltammograms, b) ORR voltammograms and c) the derived Tafel plot.	119

7.11	Sketch of the proposed NP nucleation and growth mechanism for the sequential (T_2) plasma treatment.	121
8.1	OES spectra at pressures of 7.10^{-3} (a,c) and 133.10^{-3} (b,d) mbar for the NH_3 and N_2 plasma discharges, respectively.	125
8.2	Evolution of the OES intensities for the NH_3 and N_2 plasma discharges as a function of the transmitted power. The evolution of the emission lines at 356.3 (b,d) and 668.3 (a,c) nm, respectively, are shown for both plasma chemistries.	126
8.3	a) Survey and HR-XPS b) C 1s, c) N 1s and d) O 1s spectra of the untreated carbon xerogel.	129
8.4	HR-XPS C 1s, N 1s and O 1s core level spectra at 7.10^{-3} (a,c,e) and 133.10^{-3} (b,d,f) mbar for the NH_3 plasma discharge at 90 W transmitted power.	130
8.5	Evolution of the N 1s content for the NH_3 discharges (20, 90 and 200 W) as a function of the treatment time at a) 7.10^{-3} and b) 133.10^{-3} mbar.	131
8.6	a) Survey spectrum and HR-XPS b) C 1s, c) N 1s and d) O 1s core level spectra at 7.10^{-3} mbar for the N_2 plasma discharge at 90 W transmitted power.	132
A.1	Bright field TEM images of the a) OM1-1, b) OM1-2, c) OM2-4 and d) AM2 samples. The non-uniform distributions of the nanoparticles at the surface is clearly visible in most cases as well as agglomeration.	141
B.1	High-resolution XPS spectra of the C 1s and O 1s elements for the organometallic $Pt(acac)_2$ (OM1, (a,b)) and $Pt(cod)(Me)_2$ (OM2, (c,d)) precursors. The different chemical environments were fitted for all spectra and are shown for the O_2 plasma treatments.	143
B.2	High-resolution XPS spectra of the C 1s and O 1s elements for the inorganic platinumic acid precursor (AM, (a,b)). The different chemical environments were fitted for all spectra and are shown for the O_2 plasma treatments.	144
D.1	XRD diffractogram of the GNP-06 sample. The analysis of the peaks positions indicate the presence of cubic face centered Pt crystallites with an average size derived from the Debye-Scherrer formula (Equation 4.5) of 9.7 ± 1.4 nm. No precursor trace was visible after the plasma conditions explored in the present case.	147
E.1	High-resolution Ni 2p XPS spectra of a) metallic Ni, b) NiO, c) γ -NiOOH and d) Ni(OH) $_2$	149
F.1	Ni-Pt phase diagram	151

G.1	XPS survey spectra of the simultaneous (T_1) treatment.	153
G.2	XPS survey spectra of the sequential (T_2) treatment.	154

List of Tables

2.1	Several examples of energy transfer and collision processes involved in cold plasmas.	31
3.1	Main characteristics of the organometallic precursors used to form nanoparticles : Pt(II) acetylacetonate ($\text{Pt}(\text{acac})_2$), (1,5)-cyclooctadiene dimethylplatinum(II) ($\text{Pt}(\text{cod})(\text{Me})_2$), hydrogen hexahydroxyplatinate(IV) (platinic acid) and Ni(II) acetylacetonate ($\text{Ni}(\text{acac})_2$).	44
5.1	Plasma conditions explored for the decomposition of the different metallic precursor and the formation of Pt particles supported on carbon xerogel from a reactant mixture with a metal loading of 20 wt.%. In some cases, two lines are indicated and give the plasma discharge conditions of two successive treatments applied without bringing back the plasma reactor to the atmosphere.	66
5.2	Electric consumption required during the fabrication of 2.5 g of a Pt/CXG catalyst by using the low-pressure plasma methodology.	75
5.3	Plasma conditions explored for the synthesis of Pt particles supported on graphene from a mixture with a metal loading of 20 wt.%. For GNP-03 and -04, the plasma treatments were following a 2-step approach in which a low-energy plasma was applied and directly followed by higher energy conditions.	76
5.4	Plasma conditions explored for the synthesis of Pt particles supported on graphene. A pretreatment of the graphene sheets was performed to investigate the role of structural defects for the NPs synthesis (GNP^N).	80
8.1	Textural parameters derived from the N_2 adsorption/desorption analysis of the untreated and plasma treated samples.	133

List of Publications

Published articles

(1) M. da Silva Pires, E. Haye, A. Zubiaur, N. Job, J.-J. Pireaux, L. Houssiau, & Y. Busby, Defective Pt-Ni/graphene nanomaterials by simultaneous or sequential treatments of organometallic precursors by low-pressure oxygen plasma, *Plasma Processes and Polymers*, 16(5):1800203, 2019.

(2) E. Haye, Y. Busby, M. da Silva Pires, F. Bocchese, N. Job, L. Houssiau, & J.-J. Pireaux, Low-Pressure Plasma Synthesis of Ni/C Nanocatalysts from Solid Precursors: Influence of the Plasma Chemistry on the Morphology and Chemical State, *ACS Applied Nano Materials*, 1(1), 265-273, 2018.

Article not directly related to the present thesis

G. Morand, P. Chevalier, L. Bonilla-Gameros, S. Sturgeon, M. Cloutier, M. da Silva Pires, M. Tatoulian, L. Houssiau, D. Montovani. A single carbide interface enhances the adhesion of diamond-like carbon coatings on 316L stainless steel surfaces by low-pressure plasma process, submitted to *Biointerphases*, under review.

Proceedings

Y. Busby, E. Haye, M. da Silva Pires, V. Stergiopoulos, N. Job, & J.-J. Pireaux, Versatile Catalyst Materials Fabrication by Low-Pressure Plasma Treatments, Proceeding of EFC 2017.

Posters

(a) M. da Silva Pires, Y. Busby, E. Haye, N. Job, J.-J. Pireaux, & L. Houssiau, Dry plasma treatment of organometallic precursor for the synthesis of fuel cells catalyst material, 4th International Conference on Advanced Complex Inorganic Nanomaterials (ACIN), Namur (Belgium), 2018.

(b) M. da Silva Pires, Y. Busby, E. Haye, V. Stergiopoulos, N. Job, & L. Houssiau, New bimetallic Pt-Ni catalysts for proton exchange membrane fuel cells: a plasma approach, 7th World Hydrogen Technology Convention (WHTC), Prague (Czech Republic), 2017.

(c) E. Haye, Y. Busby, M. da Silva Pires, J.-J. Pireaux, & L. Houssiau, Growth of nanoparticles for fuel cells catalysts application by low pressure plasma treatment of a solid precursor, 7th World Hydrogen Technology Convention (WHTC), Prague (Czech Republic), 2017.

(d) Y. Busby, V. Stergiopoulos, N. Job, M. da Silva Pires, E. Haye, J.-J. Pireaux, & L. Houssiau, Low-pressure Plasma Deposition of Pt/C and bimetallic catalysts for efficient PEM Fuel Cells, 17th European Conference on Applications of Surface and Interface Analysis (ECASIA), Montpellier (France), 2017.

(e) M. da Silva Pires, Y. Busby, J.-J. Pireaux, & L. Houssiau, Catalyseurs bimétalliques Pt-Ni/C pour piles à combustible : synthèse par plasma et caractérisations, 7^{ime} conférence francophone sur les spectroscopies délectrons, Paris (France), 2016

Introduction

Nowadays, the production or use of energy based on non-renewable sources is ordinary, from power plants to transportation systems. Efforts have been made to find alternative solutions like photovoltaic panels, wind turbines, geothermal energy, etc. Unfortunately, non-renewable sources of energy are still predominant and alternatives only represent few percentages of the total, as seen in Figure 1, even if renewable sources of energy have seen their share grow from 3 to 9% in ten years. Yet, coal and natural gas represent more than 60% of the current global energy production.

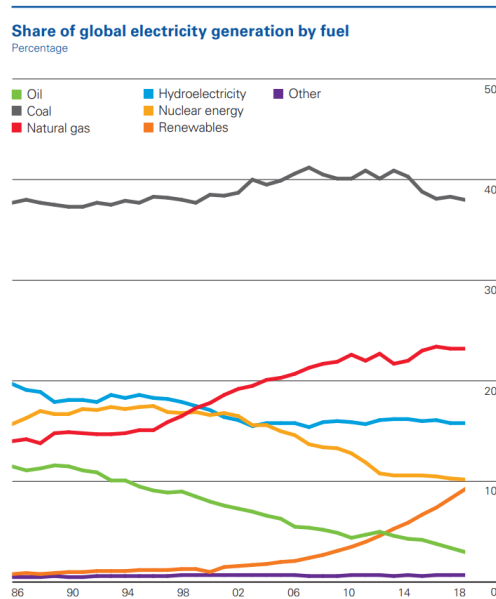


Figure 1: Evolution of the energy production by fuel between 1986 and 2018 (Taken from BP Statistical Review of World Energy 2019).

Moreover, in 2017, the world's carbon dioxide emissions have increased by 1.6%; in term of mass, it represents an emission of 36.2 Gt of CO₂ released in the atmosphere which is not compensated by the decarbonization [1]. The direct impacts of the production of greenhouse effect gases (CO₂, NO_x, SO_x) are climate change leading to a global warming, health problems developed by the release of harmful particles which can penetrate in the lungs. The consequences

are intensification of hazards like natural disasters that affect humans [2]. The main causes on the emission of greenhouse effect gases are combustion of fossil fuel (coal, petroleum, natural gas, etc.) and production of cement which release over 90% of the CO₂ produced by human activities [1]. Figure 2 illustrates the critical evolution of the world emissions of CO₂ until 2017. Furthermore, with the rarefaction of non-renewable sources, it is urgent to face this problem by proposing alternative sources of energy with a lower environmental impact. Conventional renewables can not offer a continuous source of energy since the production depends on the environment. For example, wind turbines and solar panels are constrained by weather conditions or their geographical position.

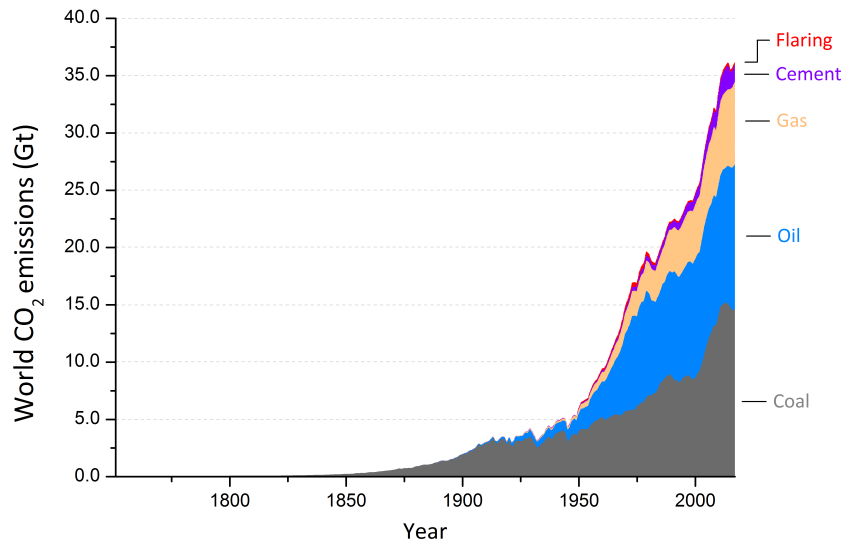


Figure 2: Evolution of the mass of CO₂ released in the atmosphere by fuel combustion and cement production.

Transportation systems (cars, buses, etc.) are at the heart of the problematic and new ways of energy production without the limitations of the conventional renewable must be developed. One of the most promising way to reach a sustainable development in the future is to stock energy and give it back thanks to electrochemical reactions [3,4]. This is typically done in fuel cells (FC) which convert chemical energy into an electrical one. Especially, polymer electrolyte fuel cells (also named Proton Exchange Membrane Fuel Cells, PEMFC) seem to be a key technology for a net reduction of the greenhouse gas emissions [5]. Indeed, only heat and water are produced as residuals of the chemical reaction. Moreover, PEMFCs seem to be a highly promising way to provide electricity for applications requiring mobile, portable and small stationary systems [6].

Chapter 1 presents a brief history on the developments of such a technology, from its invention by Sir William Grove to the research performed to improve its efficiency, durability and lower the impact on the environment. The working principle and parts constituting a PEMFC are also detailed, this to provide the basics needed to understand the different issues that led to the numerous research and the work presented in this thesis. A special attention is then given on the developments made on the catalysts layers which are related to the chemical reactions involved in the PEMFCs. Thus, the hydrogen oxidation and the oxygen reduction reactions are explained in details together with the state-of-the-art on the materials employed as catalysts, from the mainly employed Pt catalyst to new Pt-free alternatives, and their efficiency in both chemical reactions. The influence of the carbon support towards the catalytic activity is discussed as well as the effect of nitrogen-doping of the matrix.

A general introduction on the low-pressure plasmas is then given in chapter 2. The criteria which define a plasma are discussed from the Debye shielding length to the plasma sheaths, and includes the ionization degree definition, the quasi-neutrality concept and the Langmuir frequency definition. The low-pressure non-local thermal equilibrium plasmas are then presented and two examples given : the glow discharges and the radio-frequency inductively coupled (RF-ICP) plasmas. The latter was employed for the synthesis of the nanoparticles (NPs) which is at the heart of this work. Finally, the transition between capacitive and inductive modes in RF-ICP is debated in the last section.

Afterwards, the methodologies developed to synthesize NPs are discussed in chapter 3; a brief overview of some wet chemical and physico-chemical processes is given. Especially, a research using the low-pressure plasma method, which is the one employed in this work, is detailed. The experimental setup used is then presented including the plasma reactor, the RF-ICP source, the gas injection and pumping systems, and the pressure gauges. The last section concerns the procedure setup to synthesize the NPs. In this thesis, organometallic precursors were mixed with a carbon matrix and all the reactants treated in a plasma discharge. The decomposition of the precursor then leads to the formation of anchored NPs at the surface of the carbon support.

Several characterization techniques were used to get new insights on the NPs fabrication mechanisms taking place during the plasma treatments, and the influence of the plasma conditions on the synthesis and the carbon functionalization. A general overview of these techniques are presented in chapter 4. The main technique used was the X-ray photoelectron spectroscopy (XPS) which allows to determine the overall composition and chemical environment of the elements present at the surface of the samples; its working principle is explained as well as the specifications of the device used in this work. A systematic structural anal-

ysis was checked thanks to an X-ray diffractometer (XRD) following the powder method; basics of the principle and measurements is provided. Images of the samples produced were acquired by transmission electron microscopy (TEM) and, in some cases, chemical information on the NPs was derived from an energy dispersive X-ray (EDX) analysis. The catalytic activity of the supported NPs could also be measured thanks to electrochemical methodologies which include CO stripping and oxygen reduction reaction measurements in a three-electrode cell.

In chapter 5, an in-depth study was performed on Pt/C materials fabricated from various metallic precursors and treated under different plasma conditions (transmitted power, treatment time, gas mixture, etc.). The influence of two carbon supports (carbon xerogel or graphene nanoplatelets) on the NP nucleation and growth was also explored. Results and discussions on the new insights obtained about the nucleation mechanisms, growth and agglomeration of NPs are presented. More specifically, the so-called "one-pot" strategy is compared to the newly developed "2-step" method in which a low-energy plasma treatment (pulsed and/or lower transmitted power plasma) was applied and followed by a high-energy one (continuous and/or higher transmitted power plasma). The last part of this chapter concerns a study on the effect of a pretreatment of the carbon matrix.

Afterwards, a work on Ni/C nanocatalysts is discussed in chapter 6; the decomposition mechanisms and kinetics were investigated together with the NPs morphology and chemical composition. Three plasma chemistries were studied : an oxygen and two nitrogen-based gas mixtures. Considering an analogy with an Arrhenius law, an "activation power" was calculated for each plasma condition and compared to each other.

In chapter 7, the synthesis of bimetallic Pt-Ni/graphene by simultaneous or sequential plasma treatments is then presented. The systematic XPS, XRD and TEM analyses were used to characterize the produced materials and proposed mechanisms are given to explain the nucleation processes in both strategies. Moreover, electrochemical measurements were performed in order to determine the catalytic activity of the Pt-Ni/graphene nanocomposites and compared with the activity of a commercial Pt/C catalyst.

Chapter 8 deals with the incorporation of N atoms in a carbon xerogel by using NH_3 or N_2 plasmas. The first part of this chapter is dedicated to the determination of the E-to-H transition, *i.e.* threshold power between the capacitive E and inductive H mode in RF-ICP discharges. Previous works shown that the coupling mode affects the reactive species present in the plasma region. Therefore, it was believed that different N-functionalizations could result of the plasma treatment conditions. This could be useful for applications that require specific functional

groups grafted at the surface of the carbon support. Two pressures and transmitted plasma powers between 20 and 200 W were investigated with a NH_3 gas mixture. Chemical analyses of the treated carbon xerogels under these plasma conditions are discussed. The last part of this thesis concerns the analysis of a N_2 treated carbon xerogel under the best plasma conditions regarding the results found for the NH_3 treatment.

Finally, this manuscript ends with a sum up of the main achievements obtained and few perspectives which could be explored in the future to improve the plasma-assisted methodology for both NP synthesis and N-doping of carbon matrices.

Chapter 1

Polymer electrolyte membrane fuel cells

This chapter aims to introduce a brief history on fuel cells, among them polymer electrolyte fuel cells, and their recent developments. A description of the working principle of polymer electrolyte membrane fuel cell is then given, this kind of device being a promising key technology to replace conventional ways of producing energy. More specifically, the chemical reactions and mechanisms involved in such fuel cells are explained and are related to catalyst materials employed. The present thesis being focused on the synthesis of nanoparticles for various applications, among which catalysis; it is necessary to introduce the developments performed in the past few years to improve their efficiency while lowering the amount of critical raw materials used in their fabrication. For both chemical reactions in those fuel cells, the influence of the catalyst material is discussed. Afterwards, discussions on the catalyst support and nitrogen doping of the latter is given.

1.1 Fuel cells history

Back in 1839, Sir William Grove invented a way to produce energy from the reverse process of water electrolysis, *i.e.* separation of hydrogen and oxygen atoms in water. He demonstrated that a chemical reaction can occur between hydrogen and oxygen with the help of a catalyst leading to the generation of electricity [7]. His apparatus is shown in Figure 1.1. Unfortunately, his discovery did not get any improvement for almost a century. It is only in 1937 that Francis T. Bacon redeveloped the idea of Grove and created a 40-cell stack in 1950 [8].

Several attempts have been made by the NASA to use fuel cells in Gemini spacecrafts, from 1962 to 1965, but each of them suffered from malfunctions or from the lack of performance [9]. The technology was thus replaced by alkaline fuel cells in the Apollo program [9]. The development of the technology was stalled

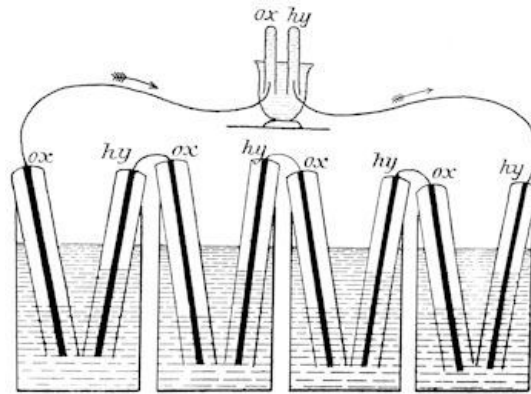


Figure 1.1: The first historic fuel cell created by William R. Grove in 1839 (Reprinted from [7]).

for the second time in History. The real breakthrough arrived in the late 1980s with research performed by Ballard Power Systems. Their main goal was and still is to develop PEMFCs for a sustainable planet with a wide range of applications, mostly in the automotive industry. However, the expensive cost and the use of critical raw materials, *i.e.* referring to elements in the platinum group (PGM - Pd, Rh, Os, Ir and Ru), in such devices limit the widespread commercialization among population.

Currently, scientists try to find new ways to produce PEMFCs at a reduced cost and free of hardly recyclable parts like noble metal-based catalysts. A recent study showed that only 17% of the noble metals processed worldwide is recycled while the global demand is high compared to the amount of resources available [10,11]. Moreover, studies have been done to show the negative impact of the PGM elements released in the environment due to mining or to their use in general : soil pollution, food contamination, hazardous effects on health, etc. [12–16]. New technologies have to be found to surpass those issues and make catalysts in PEMFC more eco-friendly. This will be discussed in sections 1.3.2 and 1.3.4.

1.2 PEM fuel cell's working principle

Among the different kinds of fuel cells, there is one which gained rapidly in popularity, the so-called PEMFC, as mentioned previously. Advantages of PEMFC, in comparison with the others FC, are numerous. Those systems can operate at low temperature, are relatively compact, able to supply high power and use a quasi-solid electrolyte [17]. The central part of the FC is the membrane electrode assembly (MEA). It is made of a polymer electrolyte membrane, two catalytic layers (CLs), two gas diffusion layers (GDLs) and two bipolar plates, as seen in Figure 1.2.

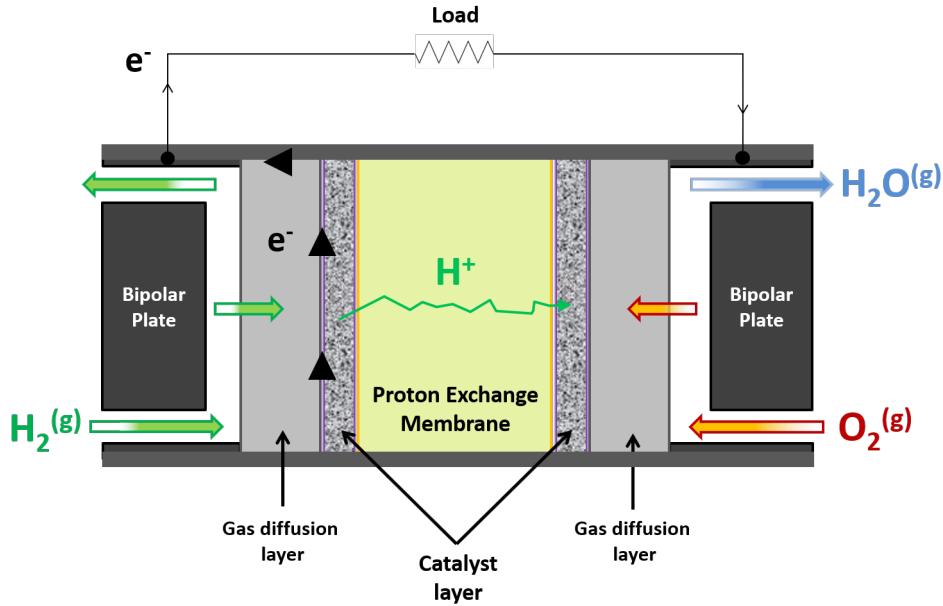


Figure 1.2: Working principle diagram of a PEMFC.

Basically, a PEMFC transforms hydrogen and oxygen into water owing to the reverse chemical reaction of water electrolysis and with the use of a catalyst :



In more detail, hydrogen molecules are supplied by a bipolar plate flow to the anode side of the FC, then pass through a gas diffusion layer and encounter the catalytic layer on which hydrogen will react to produce electrons and protons. The chemical reaction is called the hydrogen oxidation reaction (HOR) :



The polymer electrolyte membrane is placed next to the region where HOR occurs. It plays a major role in the principle of PEMFC; it must conduct protons produced by the HOR (*i.e.* ionic conductor), while it is impermeable to electrons (*i.e.* electronic insulator) and all gases so they cannot pass to the other side of the cell but rather through an electrical circuit. Electrons pass through the GDLs and the bipolar plates in order to reach the circuit.

On the cathode side of the MEA, an oxygen or air stream is sent which has to pass through a GDL as well before arriving on the catalytic layer. The second chemical reaction involved in the process is the oxygen reduction reaction (ORR) in which electrons, protons and oxygen react all together to form water :



On both sides of the PEM, catalyst layers allow the chemical reactions to occur at a faster rate. Since their recent development, catalysts employed are mainly made of platinum due to its high activity for both HOR and ORR [17–20]. As mentioned previously, alternatives have been studied and are discussed in sections 1.3.2 and 1.3.4.

The purpose of the GDLs is essential in PEMFCs. They are made of porous materials to let reactants easily flow towards the carbon-supported catalysts [17]. GDLs also have to be electrically conductive to permit electrons produced on the catalytic layer to reach the bipolar plates. Thus, they ensure a good electrical connection between those two parts. In addition, water molecules produced near the electrode/electrolyte interface in PEMFCs have to be removed and transported into the gas flow channels by passing through the GDLs [21]. For this reason, GDLs are made of a porous material to ensure the water evacuation; it has been shown that the removal of water in vapor phase occurs due to thermal and vapor concentration gradients across the GDLs at typical fuel cells' operating conditions [22].

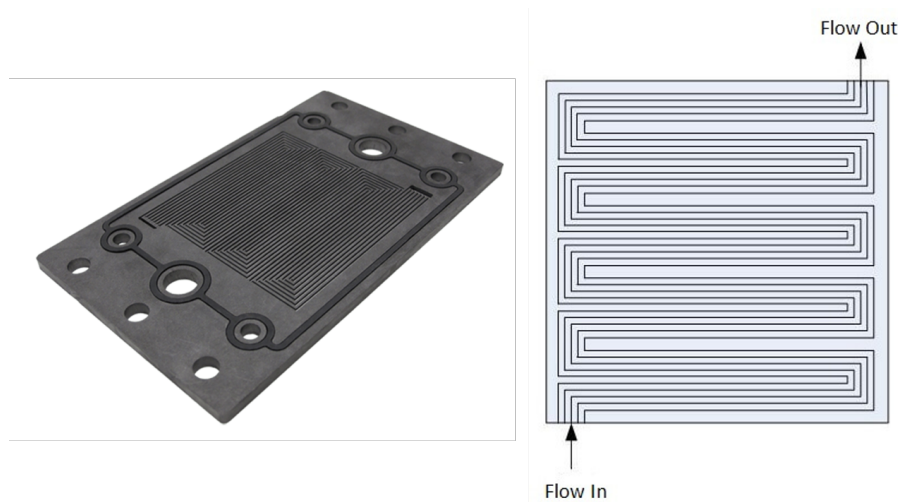


Figure 1.3: Picture and sketch of a bipolar plate with a multiple serpentine flow channel design (Taken from [23, 24]).

Finally, the last part of a PEMFC is the bipolar plates. The versatility of this component makes it one of the most problematic and expensive part of the FC [25]. Like GDLs, they must be conductive to provide a good electrical connection while they also have to remove water produced by the FC through flow channels designed on their surface (Figure 1.3). They should be as much as possible impermeable to all the gases. They also have to be chemically stable and resistant to corrosion due to operation in a relatively acidic environment.

1.3 Chemical reaction mechanisms and catalysts developments for PEM fuel cells

A lot of efforts are devoted to improve every part of the PEMFC technology as issues appear for each of them. Lowering the cost of such device while increasing the durability is at the heart of numerous projects and research [26–28]. Mechanisms involved in HOR and ORR are discussed in order to understand how catalysts affect those reactions. Since the present study is focused on the catalytic layer of the fuel cell, general assumptions on Pt-based catalysts and the recent developments made are also presented in this section.

1.3.1 Mechanisms in HOR and the role of the catalyst

Equation 1.2 is too simple to describe the real process which takes place in the electrooxidation of hydrogen. In fact, three sequential steps could be involved in HOR [17] :

1. The hydrogen stream arrives at the GDL and molecules are diffused towards the surface of the catalytic layer. Hydrogen molecules are then adsorbed onto the surface of the catalyst.
2. Two different mechanisms may happen in the hydration/ionization step of adsorbed hydrogen. The first one is called the Tafel-Volmer (TV) route :



Firstly, hydrogen is dissociated and adsorbed on the surface of the catalyst (Equation 1.4). After that, each hydrogen molecule goes through an oxidation process leading to the formation of protons and electrons (Equation 1.5). Figure 1.4(a) illustrates the mechanism of the TV way.

Another possibility is the Heyrovsky-Volmer (HV) route in which Equation 1.5 is also involved after the following one :

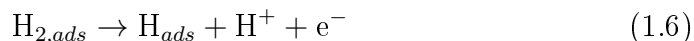


Figure 1.4(b) shows the HV route. In this case, hydrogen molecules are dissociated and one hydrogen atom is chemisorbed onto the surface of the catalyst. The second atom is in an ionized form and transported to the cathode.

3. The last step consists of the desorption of the product generated by the different reactions. H^+ ions are transported through the PEM and electrons pass through the electric circuit resulting in an exchange current density. Ions and electrons then react with oxygen molecules on the other side.

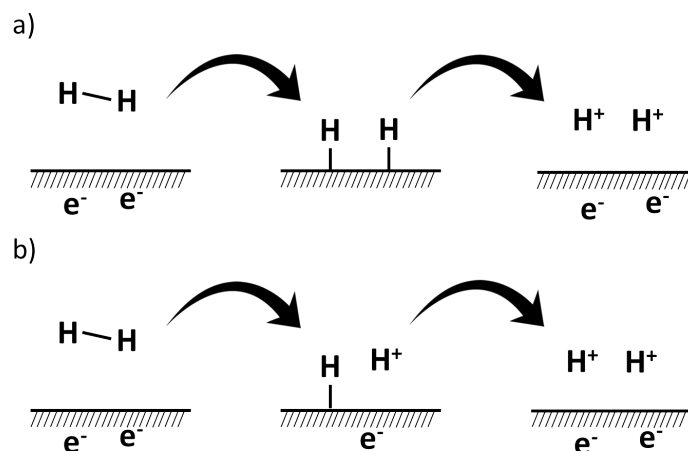


Figure 1.4: Schematic view of a) the Tafel-Volmer route and b) the Heyrovsky-Volmer route on Pt extended surface.

At this point, it is important to note that adsorption of hydrogen at the surface of a catalyst will intrinsically modify its activity. The nature of the element employed is therefore a critical parameter. A "volcano plot" is often drawn for HOR to show the correlation between the hydrogen binding energy and the exchange current density, as seen in Figure 1.5. Elements of the PGM exhibit the highest current density with an intermediate metal-hydrogen (M-H) binding energy. At lower M-H bonds, adsorption becomes less strong which limits the kinetics of the reaction while, at higher M-H bonds, hydrogen desorption is more difficult [17].

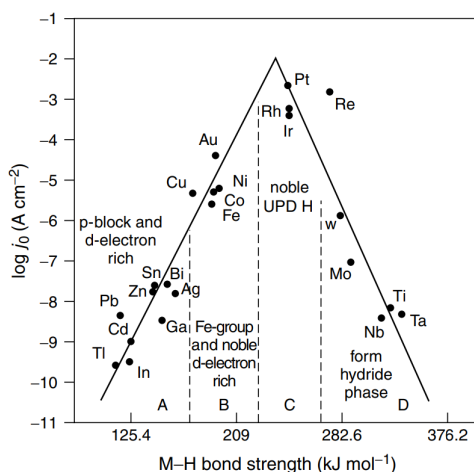


Figure 1.5: Typical "volcano curve" of the exchange current density in function of the binding energy of hydrogen for several metals (Reprinted from [29]).

There are a few studies only on HOR kinetics but one of them, performed by Antoine *et al.* [30], showed the particle size of Pt catalyst has an effect on the specific activity, *i.e.* "the activity per unit surface area of the active component" as defined in [31]. Typically, decreasing the size of the nanoparticles from 10 to 2.8 nm will increase the specific activity by a factor 10 approximately.

1.3.2 Pt-free or synergistic catalysts for the hydrogen oxidation reaction

Alternatives or synergies with Pt have been already investigated several years ago already. Few studies focused on Pd-based materials as catalysts in PEMFCs due to its high CO tolerance (the effect of CO is discussed in section 4.5.2) [32,33]. Pronkin *et al.* [34] worked on the HOR kinetics of Pd/C and showed that the activity is lower than the one of Pt as previously reported in the literature [35]. However, Kwon *et al.* [36] demonstrated an enhancement of the activity of Pd alloys with the use of tungsten oxide as co-catalyst.

Levy *et al.* [37] worked on tungsten carbide (WC) and demonstrated the platinum-like behavior of such materials as catalyst. Moreover, studies showed that WC has an improved resistance to CO poisoning and a better stability in acid solutions considering the anodic potentials [38,39]. Weigert *et al.* [39] even worked on WC covered by a Pt submonolayer which could significantly enhance the stability without affecting much the activity. Advantages of the submonolayer would be a reduction of the Pt loading, *i.e.* all the atoms are at the surface and participate to the catalytic reaction, and less Pt agglomerates (preventing a decrease of the activity) due to strong interaction between WC and Pt.

Li *et al.* [40] synthesized Ir-V/C nanoclusters; those exhibit a very high activity, higher than the one of commercial Pt/C catalyst. On the other hand, their Ir-V/C materials seem to have a very promising longevity according to tests of 100h performed which showed no significant degradation of the FC performance.

1.3.3 Mechanisms in oxygen reduction reaction and the role of the catalyst

Oxygen is involved in lots of chemical reactions and one of the most important is the ORR, with applications going from life science to energy production in fuel cells. Equation (1.3) presented previously is too simple to explain the full process of such chemical reaction in PEMFCs. In fact, ORR is difficult to explain and depends on the nature of the catalyst, the electrolyte, etc. The mechanisms involved in ORR are not yet well understood. However, it seems that few pathways exist, the 4-electron one transforming O_2 into H_2O , as seen in Figure 1.6, has a great interest since it is the reaction taking place in PEMFCs.

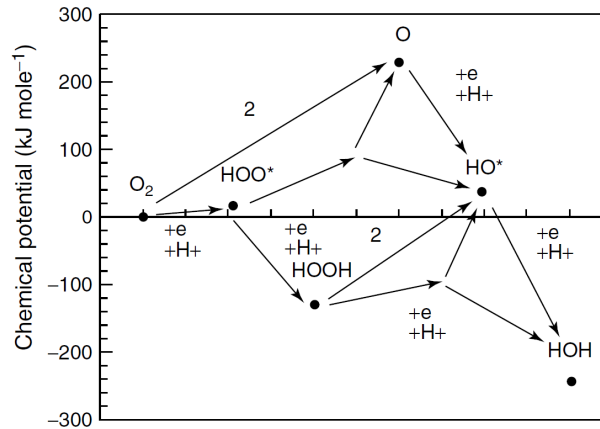


Figure 1.6: Complete ORR mechanisms in the case of noble catalysts. The main way is the formation of water through a 4-electron process. Parasite reactions may occur and lead to the formation of hydrogen peroxide (Taken from [41]).

The choice of an efficient catalyst is even more important in this case due to a very slow kinetics compared to HOR. Higher ORR kinetics is needed and intensively investigated in PEMFCs research [42, 43].

Recent theoretical studies have been performed for a better understanding of ORR. A dissociative route and an associative one have been proposed in the case of ORR on a Pt(111) surface and based on thermodynamics of the reactions [44]. The first possibility is the dissociative way in which oxygen molecules are diffused through the GDL and are adsorbed on the metal surface creating bonds with the metal. Afterwards, a 1-electron transfer activates the O_2 chemisorb leading to the cleavage of the latter into O_{ads} (Equation (1.7)). The formation of adsorb hydroxide (OH_{ads}) is then realized by protonation and electron reduction (Equation (1.8)). A second protonation/reduction process occurs to transform OH_{ads} into H_2O (Equation (1.9)). The final step is the desorption of water from the surface of the catalyst.



The second route consists of an associative mechanism. Oxygen molecules only bind "vertically" to the metal with one O atom. Thus, O_2 molecules are not cleaved but rather transformed into OOH_{ads} thanks to a reduction and protonation processes (Equation (1.10)). Another protonation and reduction occurs which leads to the formation of adsorbed water and oxygen (Equation (1.11)). H_2O_{ads} is

then removed from the catalyst while the O_{ads} follows the steps of the dissociative route (Equations (1.8) and (1.9)).



In Figure 1.6, another path is represented with hydrogen peroxide as intermediate before its possible transformation into water. This reaction has a negative effect on the PEM, free radicals generated at the cathode (and the anode as well by oxygen permeation) cause the degradation of the latter by inducing the creation of pinholes and membrane thinning [45, 46]. A study performed by Antoine *et al.* [47] showed that under typical working potential conditions in ORR, the production rate of hydrogen peroxide is quite small.

Metal related ORR kinetics

It is now important to focus on the ORR kinetics with respect to the nature of the metal employed as catalyst. Norskov *et al.* [44] indicated that ORR activity depends on both O and OH bonds. Moreover, it seems there is a linear correlation between those two binding energies and the nature of the catalyst, as seen in Figure 1.7. Transition metals, *i.e.* iron, copper and nickel, are not suitable for the ORR due to their higher oxygen affinity [48]. Gold presents too low binding energies which do not lead to a good activity [49–51]. The principle exposed in section 1.3 is applicable in this case as well. Too strong or weak bonds do not permit faster kinetics.

Among all metals present in Figure 1.7, platinum has intermediate binding energies for both O (ΔE_O) and OH (ΔE_{OH}) which makes it the best for ORR. However, several effects impact the ability of Pt to perform ORR such as the size of the nanoparticles and surface oxidation [17, 31, 52]. Other limitations to the extensive use of Pt as commercialized catalyst in industry are its cost (~ 950 \$ per ounce), rarity and heterogeneous repartition on Earth. Figure 1.8 shows countries in which the PGM reserves were distributed in 2018. Since chemical reactions in PEMFCs are "surface-sensitive", *i.e.* the size of NPs affects the specific electrocatalytic activity [31], only the top surface of the nanoparticles participate in the process and atoms in the bulk are "useless". By reducing the size of the NPs, the cost of the catalyst layers could be decreased. For example, a 1 nanometer-sized nanoparticle would see around 90% of its constituting atoms exposed to the reactants. This allows to significantly lower the production cost. However, too small NPs lead to some issues as well, like too strong oxygenated species adsorption affecting the stability and activity of the NPs [31, 53]. Shao *et al.* [52] and Perez-Alonso *et al.* [54] showed the size dependence of supported Pt NPs on the specific ORR and mass activities. In both studies, optimum activities

are given for NPs with an average size of ~ 3 nm. Those results are in agreement with previous theoretical calculations [55]. Water formation rate on the edges of the NPs is decreased due to strongly bonded O and OH radicals while this is not the case on planar terraces. Thus, for particles smaller than 3 nm, there is not enough planar terraces which results in a less important activity.

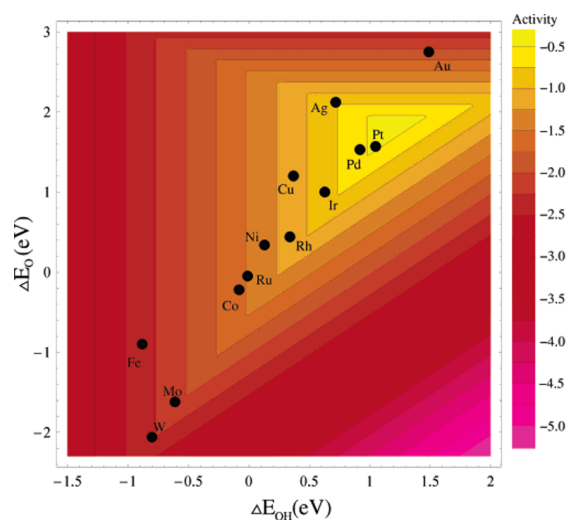


Figure 1.7: Map of the ORR activity for some metals as a function of the O and OH binding energies (Reprinted from [44]).

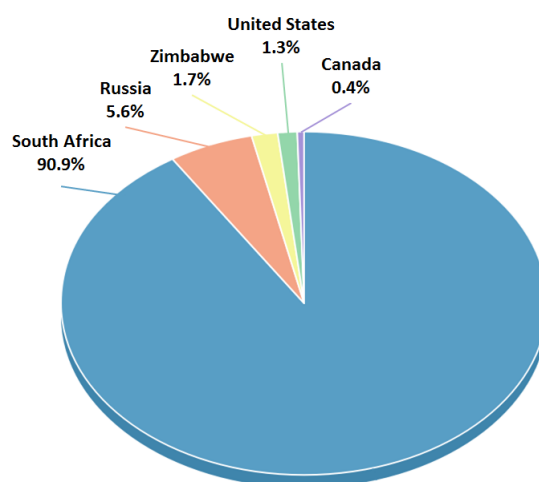


Figure 1.8: Repartition of the PGM reserves by country in 2018 (Data taken from USGS - Mineral Commodity Summaries 2019).

1.3.4 Pt alloys and non-precious metal catalysts for the oxygen reduction reaction

Besides Pt, its alloys are well-known for being excellent catalysts in the case of the electroreduction reaction of oxygen molecules [56–59]. More specifically, bimetallic Pt-M (M=Ni, Co, Fe, Mn, etc.) have been investigated in the past decades [60–63]. The explanation of such better ORR activity for Pt alloys lies in an electronic structure modification (Pt d -band vacancy) as well as geometric effects (interatomic distance between Pt atoms). It has been demonstrated that the d -band vacancy strongly influences the binding energy of adsorbates at the surface of a metal [64,65]. More precisely, interaction of the adsorbate's binding state with the Pt d -band has a keen interest. An hybridization of the metal d -band occurs with the adsorbate's binding (σ) orbital, as seen in Figure 1.9. This leads to the formation of two new states : bonded ($d-\sigma$) and anti-bonded ($d-\sigma$)*. In the case of Pt, only the anti-bonded state is not fully occupied. The most interesting part is the dependence of the filling extent of that state on the density of state, *i.e.* the electronic structure at the metal surface. When the anti-bonded ($d-\sigma$)* state is more filled, the binding with the adsorbate is weaker due to a decrease of the metal-adsorbate interaction. The so-called d -band center allows to measure the extent of filling of the anti-bonded ($d-\sigma$)* state by determining its location with respect to the Fermi level.

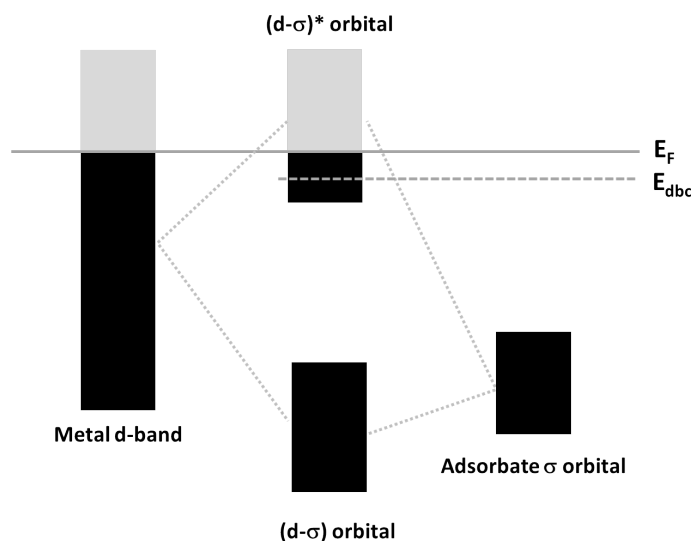


Figure 1.9: Hybridization of the metal d -band when interacting with an adsorbate. The d -band center location, with respect to the Fermi level, can be measured to evaluate the strength of a bond (Adapted from [66]).

In comparison with Pt, the anti-bonded ($d-\sigma$)* states of its alloys are more filled. Therefore, their d -band center is lower than the Pt one which leads to less strongly bound species. Figure 1.10 shows the ORR volcano plot for some Pt alloys. Stamenkovic *et al.* [61] demonstrated that Pt₃Ni has an ORR activity 10 times higher than Pt(111) and 90 times compared to commercial Pt/C catalysts. However, the main drawback of Pt alloys is the dissolution of transition metals at typical operational voltages in PEMFCs.

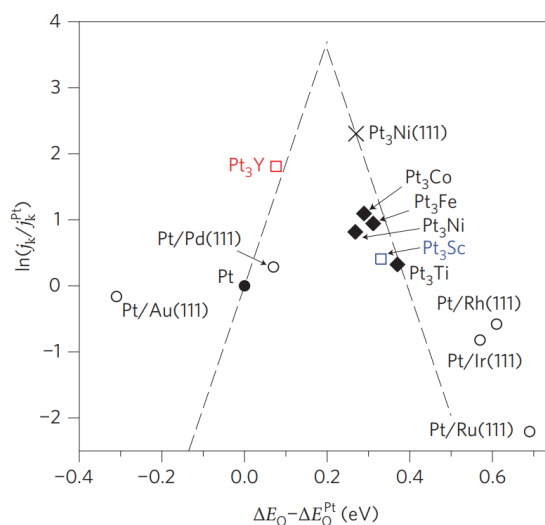


Figure 1.10: Volcano plot of some Pt alloys. Measured kinetic current density are reported relatively to Pt (Reprinted from [55]).

Recently, Dubau *et al.* [67] and Asset *et al.* [68] worked on hollow Pt-Ni/C NPs and showed that the ORR kinetics was enhanced in the presence of structural defects, *i.e.* grain boundaries and bulk defects due to multiple domain orientations, small aggregates, etc. [59, 67, 69]. A previous research performed by Kuzume *et al.* [70] showed that the presence or not of steps at the surface of the catalyst strongly affects the ORR catalytic activity. Cherstiouk *et al.* [71] and Maillard *et al.* [72] demonstrated that Pt/C aggregates lead to an enhancement of the CO electrooxidation. This phenomenon, attributed to defects at the surface of the catalyst or its support, is largely reported in the literature and no further development will be given in the present work.

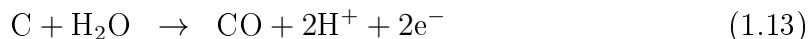
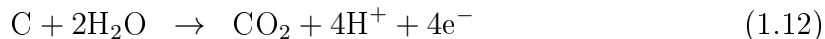
Among the different research performed to improve the catalytic activity and durability of PEMFC, PGM-free materials are promising to replace Pt-based catalysts, especially transition metals like cobalt and iron have been extensively studied in the past few years [73–77]. In 2011, Proietti *et al.* [78] developed an iron-based electrocatalyst for the PEMFC's cathode with the highest non-platinum

activity reported in the literature. Going further, a special attention has been paid to transition metal/nitrogen (M-N_x/C) materials (M = Co, Fe, Ni, Mn, etc.) [76]. Indeed, material precursors leading to their formation are abundant and inexpensive. Moreover, as mentioned above, they present a promising catalytic activity for the ORR. In order to increase the stability of such catalysts as well as the number of active sites for ORR, they have been heated at relatively high temperature (400–1000 C) during the synthesis process which modifies the carbon support [76]. The role played by the nitrogen functionalization of the carbon support is discussed later in the chapter.

1.4 Influence of the carbon support on the catalytic activity

The choice for a material with excellent performance, *i.e.* high catalytic activity for both HOR and ORR at a low cost, is essential in PEMFCs for widely commercialized applications. However, catalysts without any support, even if their use has been reported in the literature [79–81], are not stable over time and nanoparticles coalescence occurs after few cycles of use. The global effect of this is a decay of the activity due to a loss of the catalyst active surface. Pt/C catalysts are also affected by a loss of their surface area per unit mass. The main cause is the so-called Ostwald ripening, NPs are dissolved and atoms re-deposited at non-desired locations. Coalescence of NPs or aggregation has also been noticed and is due to the migration of crystallites at the surface. Therefore, it is critical to resolve the catalysts' stability issue and supports are thus needed.

The carbon support controls the transport of gases in, and water out, of the fuel cell through a porous structure. Corrosion of the latter also has a negative impact on the fuel cell's performance. Maillard *et al.* [82] reviewed the carbon corrosion (or oxidation) process and its effects in PEMFCs. The possible chemical reactions occurring at typical operating conditions in PEMFCs are given by Equation (1.12)–(1.14) [82] :



Kangasniemi *et al.* [83] reported such a simultaneous formation of oxygen-containing carbon surface groups (C_xO_yH_z) and evolution of carbon dioxide under usual operating conditions in PEMFCs. This could be accompanied by a less accentuated hydrophobicity which directly affects water transport and causes the electrode pore structure to collapse [84]. Moreover, carbon corrosion results in

detachment of the nanoparticles from the catalyst layers, increasing the deterioration of the fuel cell's efficiency. Efforts have to be done to improve the corrosion stability as well. A proposed solution is the carbon graphitization in order to increase the carbon support crystallinity, *i.e.* reduced surface heterogeneity, and then increase the resistance to corrosion [85, 86]. In addition, a higher degree of graphitization would lead to a better metal resistance to sintering [87], an increased thermal and electrochemical stability because of less defective sites [88, 89].

In order to be used in FC applications, carbon supports must fulfill some criteria. The requirements can be found in [90] and are summarized as follows :

- A high dispersion of the NPs at the surface of the support material is needed to avoid agglomeration.
- Impurities should not be involved in the electrochemical reactions because of a chemically inert and pure support material.
- The carbon support should be highly conductive to provide an efficient electron transport.
- Porosity of the carbon support should be adapted for an efficient mass transport of the different reactants from the bipolar plates to the catalyst layers and inversely for the products generated by the reactions. Therefore, water is easily evacuated towards the bipolar plate.
- The carbon support has to be compatible with the PEM to ensure the transport of protons through the catalyst layers.
- The carbon support should exhibit a relatively high resistance to corrosion.

The most common carbon supports for catalysts are carbon blacks (CBs), *i.e.* aggregates of round shape carbon particles with a wide range of size (~ 10 – 400 nm), porosity, morphology and surface chemistry, produced by pyrolysis or incomplete combustion of compounds containing carbon [91]. Carbon particles are bound together by van der Waals interactions to form loosely bond superstructures of 1 to $100 \mu\text{m}$. Nevertheless, their porosity is highly difficult to control, depends on their way of production and can hardly be functionalized. In addition, it has been shown that the durability of CB under PEMFCs operating conditions needs further improvement [87].

Even if microporous supports like CBs, and especially Vulcan XC-72, are suitable for catalysis in PEMFCs, ordered mesoporous carbon-based materials with better characteristics have been investigated to replace the latter. A report of some possible alternative propositions is given here. The production of graphene,

i.e. single-atom-thick hexagonal carbon crystallite, led to some of those new carbon supports for catalysis. Graphene nanoplatelets (GNPs) constitute one of the promising candidates and are made of one or few-stacked graphene layers. Moreover, GNPs are highly ordered graphitic materials which allow an excellent stability at a reduced cost [92]. Another kind of support is the carbon nanotubes (CNT) consisting in one or more graphene sheets rolled-up (single- or multi-walled CNTs). Finally, carbon xerogels are almost spherical shaped amorphous carbon materials with tunable pore size and are notably produced by the polycondensation of resorcinol and formaldehyde in a solvent and then followed by a drying process and pyrolysis [93–95]. Those carbon supports are in a good agreement with the criteria presented above as they present excellent electron conductivities and relatively high surface areas [92, 96–99]. Figure 1.11 shows SEM images of the carbon supports cited above.

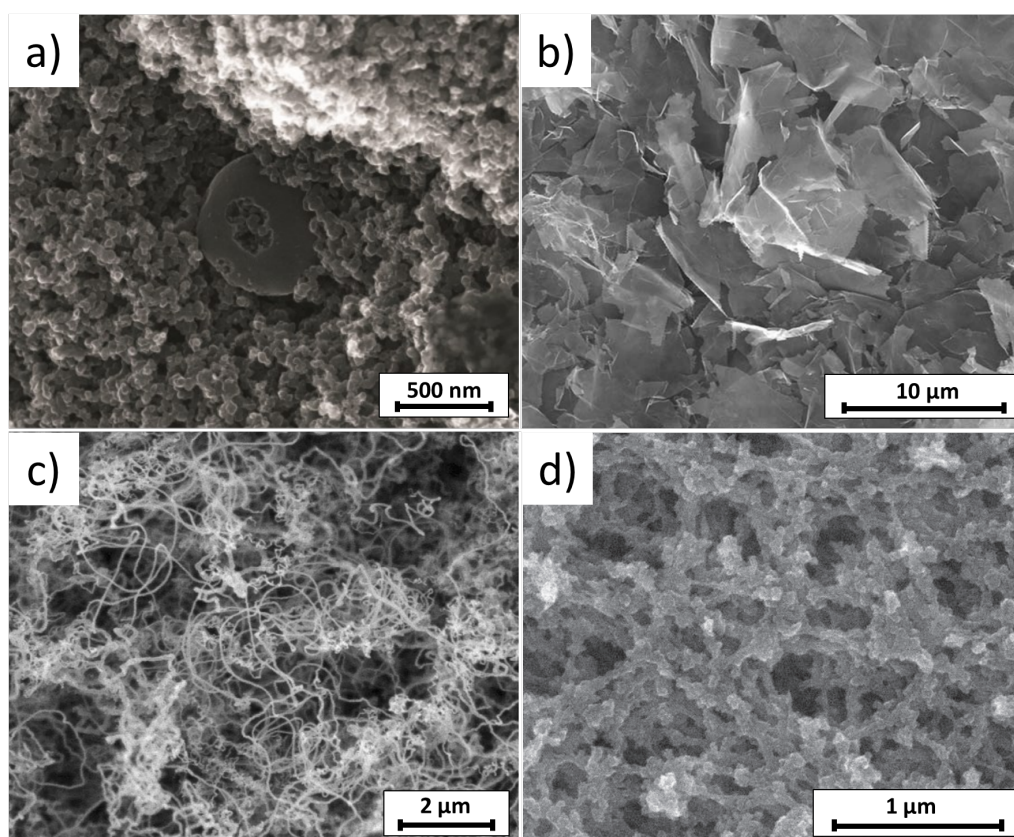


Figure 1.11: Scanning electron microscopy images of a) carbon black, b) graphene nanoplatelets, c) carbon nanotubes and d) carbon xerogel (Reprinted from [100–103]).

1.5 Nitrogen-doping of the carbon support

Studies showed that doping the carbon support with nitrogen could have positive effects on catalysis due to modification of the properties of both support and catalyst [87, 104, 105]. However, effects of the nitrogen incorporation is complex and not yet well understood. Nevertheless, enhancement of the ORR catalytic activity was performed by using nitrogen-doped carbon material supporting or not metallic catalysts [105–108]. Such results could be attributed to the behavior of nitrogen atoms who act as an electron donor (doping carbon with nitrogen is similar to a n type in the semiconductors field), which leads to a stronger π -bonding with the NPs [88, 109–111]. This is expected to have a positive impact on the durability of the catalyst.

It is also well-known that the properties of the carbon support affect the stability of the supported NPs and the grow mechanism of Pt NPs [112]. More specifically, the NPs' mobility at the surface depends on the Lewis basicity (according to the Lewis definitions, basis are electron-pair donors) of the support. Coloma *et al.* [88] demonstrated that the basicity of carbon depends on both N-doping and graphitization; stronger anchoring sites of Pt at the surface of the support are created in the case of an increased Lewis basicity. Moreover, the presence of structural defects at the surface of the support, *i.e.* replacement of a carbon atom by another element or atom removal from the surface, leads to an enhancement of the nanoparticle nucleation [113]. Several studies tend to state that defective regions or step edges could be preferential nucleation sites [105, 114, 115]. In the case of Pt NPs, the anchoring site seems to be not directly located at the N-defect but rather at the next-nearest neighbor location [105]. Holme *et al.* [116] showed from theoretical calculation that Pt NPs attach preferentially on the carbon atom situated next to the defect. In addition, a more homogeneous distribution of the NPs at the surface is observed [105].

Methods to incorporate N atoms into the NPs support are various; Figure 1.12 illustrates the major techniques employed to achieve N-doping. Most of the time, those methodologies involve toxic solvents or are performed in a liquid phase, and are time-consuming. Re-aggregation of the carbon support, such as the stacking of graphene platelets often occurs during a liquid-phase process [117]. The idea consists in carbonizing nitrogen containing compounds or treat them under a nitrogen atmosphere at high temperatures to produce highly reactive radicals after the decomposition of the materials. Tao *et al.* [118] carried out experiments on graphene oxide in ammonia solution and were able to perform N-doping with the help of ultra-sonication. They achieved an incorporation of nitrogen up to ~ 3.5 at%. However, the main disadvantages of such processes are the extent use of solvent, relatively long treatment time and limited nitrogen incorporation [119].

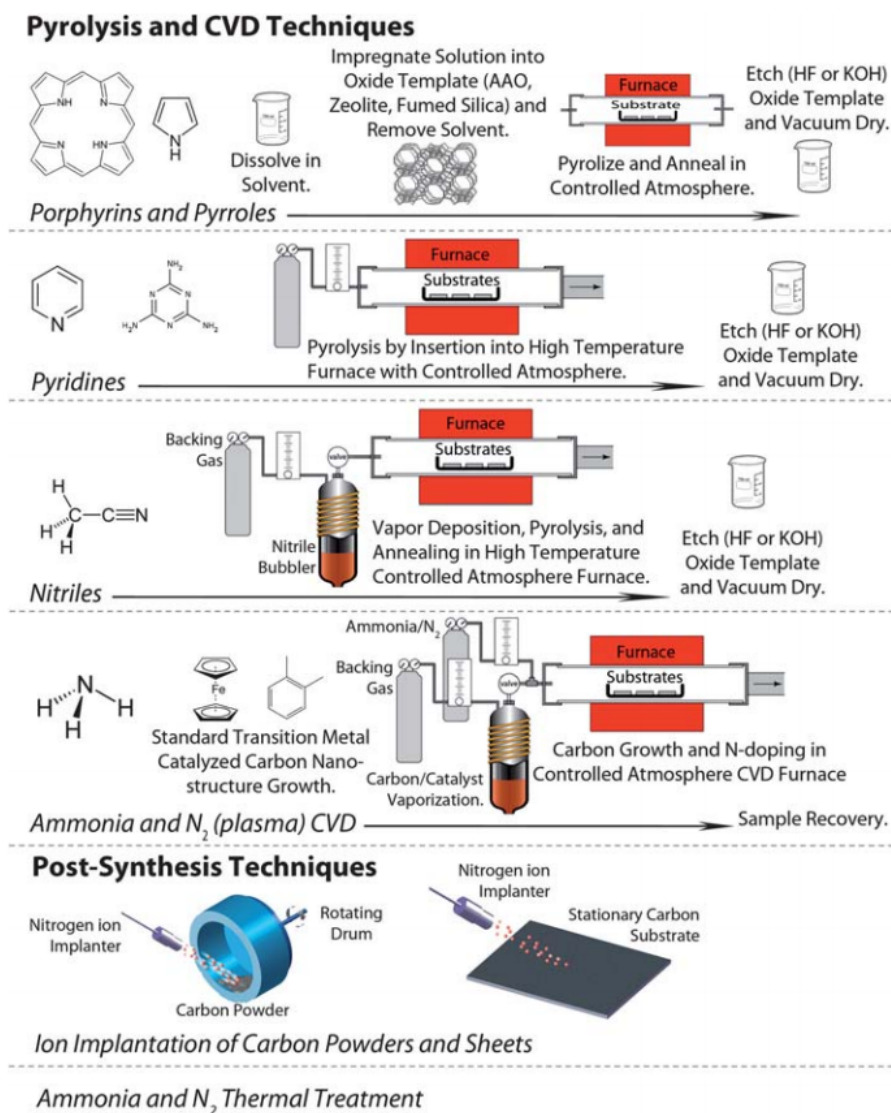


Figure 1.12: Global overview of the main techniques employed to produce N-doped carbon materials (Taken from [105]).

In the past few years, a growing attention has been paid to dry plasma-related treatments to add N functions to carbon, with the advantages of being a versatile tool more respectful of the environment because of solvent-free, fast, simple and cost saving processes [119, 120]. Furthermore, re-aggregation of the carbon support which often occurs during a liquid-phase process, like GNPs, is minimized after a low temperature plasma treatment [117]. In 2007, low-pressure radio-frequency (RF) plasma discharge had already been used for preliminary treatment of multi-walled CNTs followed by a thermal evaporation of a metal in order to decorate the latter [121]. In the present thesis, the N-doping of the carbon support was

achieved following this procedure : a nitrogen containing gas (N_2 or NH_3) at a fixed flux was injected in the vacuum chamber and a low-pressure RF inductively coupled plasma ignited to treat the carbon matrix. Moreover, incorporation of nitrogen was also achieved directly during the synthesis of the nanoparticles and is discussed in chapter 6. The specific study on the N-doping of carbon xerogel is presented in chapter 8.

Chapter 2

Low-pressure plasma

Our universe is made up of several constituents, from the expected dark energy and dark matter to the well-known antimatter, radiations, neutrinos and regular matter. The last one is subdivided into the four states of matter : solid, liquid, gas and plasma. An interesting point is that the plasma state represents more than 99% of the global amount of matter in the universe but is the less well-known among population. We are surrounded in our everyday life by plasmas : fluorescent lamps, flames, the solar core, the solar wind, auroras, etc. Since the present work is based on the use of low-pressure plasmas, it is more than necessary to introduce the so-called fourth state of matter.

Basically, a plasma is defined as an ionized gas in which free electrons, ions and neutral species are moving randomly [122]. Henceforth, it can conduct electricity but is usually considered electrically quasi-neutral, the negatively charged density almost completely compensates the positive one. Plasmas sometimes emit a diffuse light with a color characteristic of the ionized gas. Irving Langmuir introduced the term *plasma* in 1928 due to the same aspect of the gas discharge as blood plasma [123, 124].

A common classification used by the scientific community to describe the different sorts of plasmas is based on the electron density and temperature. The so-called thermal plasmas, like those produced in stellar cores, are characterized by very high densities and temperatures. The gas is completely ionized and the energy distributed to every species, *i.e.* electrons, ions and neutral species. Thus, a thermal equilibrium means that the temperature is equal for the electrons, ions and neutrals. For non-thermal plasmas, the ionized gas is colder and less dense. There is no thermal equilibrium in that case which means that the temperature is not the same for the different species. However, species in specific zones of the plasma can locally have the same temperature and then the term "local thermal equilibrium", or LTE, is employed. Both local and non-local thermal equilibrium (NLTE) can be produced in the laboratories and used to develop applications

in various domains such as in medicine, surface treatment and functionalization, nanomaterials fabrication, etc.

2.1 Concepts in plasma physics

In this section, several definitions will be given for a further understanding of plasma physics. The first point concerns the criteria defining exactly what a plasma is. Afterwards, plasma characteristics will be introduced : Debye shielding length, ionization degree and quasi-neutrality concept, Langmuir (or plasma) frequency, plasma sheaths. These notions will be applied for gas discharge plasma as discussed in the next section.

2.1.1 Plasma criteria

An ionized gas does not define, strictly speaking, a plasma. At least three other criteria have to be fulfilled [125,126] : (i) Particles out of the Debye sphere (with a radius equal to the Debye length, defined below) centered on a charged particle are not influenced electrostatically by the latter. The number of charge carriers inside the Debye sphere is sufficiently high to shield the electrostatic influence, this is the plasma approximation. (ii) The concept of quasi-neutrality must be respected and will be described in section 2.1.3. Interactions at the edges of the plasma are less important than the ones in the bulk. (iii) The Langmuir frequency has to be higher than the electron-neutral frequency. When that condition is satisfied, gas kinetic processes are dominated by electrostatic interactions. Thus, the quasi-neutrality is guaranteed, the electrons' reactivity time is lower than the time needed between two collisions.

2.1.2 Debye shielding length

One of the most important parameters in plasma physics is the Debye length which describes the shielding effect of an internal or external electric field over a characteristic plasma size scale. Said differently, the plasma is considered quasi-neutral above the Debye length but, below it, negative and positive densities can be different. The following equation gives the mathematical expression of the Debye length [127] :

$$\lambda_D = \sqrt{\frac{\epsilon_0 k_B T_e}{e^2 n_e}} \quad (2.1)$$

with ϵ_0 the permittivity of free space, k_B the Boltzman constant, T_e the electron temperature and e the charge of an electron. In laboratory plasmas, an average value of the Debye length is approximately equal to 100 μm for typical values of the electron density and temperature ($n_e \sim 10^{10} \text{ cm}^{-3}$ and $T_e \sim 3 \text{ eV}$).

2.1.3 Ionization degree and quasi-neutrality

The atmosphere all around us is generally considered as a very good electrical insulator. No electricity can be conducted or, at least, this is true when the air is especially dry. However, it is not completely neutral. A small fraction of charged particles are created, free to move and then recombine. The constant creation of charged species originates in the continuous flow of cosmic rays coming from the outer space, passing through the Earth, a few of them interacting with molecules leading to ionization of the air. Natural radioactivity is also partially responsible for the ionization.

The degree of ionization is a useful tool to estimate the content of charged particles in comparison to global particle concentrations in a given volume. Considering only electrons, ions and neutrals, the degree of ionization χ is defined by [127] :

$$\chi = \frac{n_e}{n_e + n_n} \quad (2.2)$$

with n_e the electron density and n_n the neutral density.

For plasmas, χ is comprised in a wide range starting at 10^{-8} , for weakly ionized plasmas, up to 1, for strongly ionized ones. In the case of non-thermal plasmas, the degree of ionization can vary from 10^{-6} to 10^{-4} [127].

The quasi-neutrality concept is directly linked to the charged particle densities. It means that the negative density is almost equal to the positive one. If multiply charged ions are present, the quasi-neutrality can be written as follows [128] :

$$n_e \approx \sum_z z \cdot n_z \quad (2.3)$$

with z the charge number of a positive ion and n_z the density of z -times charged ions.

Going a little bit further, quasi-neutrality of a plasma is only valid at a macroscopic scale. It means that the space occupied by the plasma has to be large compared to the Debye length. Looking at the microscopic scale, deviation of the quasi-neutrality can be observed and is mainly due to the electrons.

2.1.4 Langmuir frequency

The Langmuir frequency, also named the electron plasma frequency ω_{pe} , describes the time scale over which the electrons oscillate around their equilibrium

position and conducting to a deviation from the quasi-neutrality. A relative displacement of the electrons out of their equilibrium, in comparison with the ions, will create an electric field. In reaction, an opposite movement of the electrons is thus initiated and results in an oscillation of the negative distribution at the Langmuir frequency.

It can be shown, by assuming the plasma as a continuum, that the electron plasma frequency is given by [127] :

$$\omega_{pe} = \sqrt{\frac{e^2 \cdot n_e}{m_e \cdot \epsilon_0}} \quad (2.4)$$

where m_e is the mass of an electron. A typical value of ω_{pe} in the case of a low-pressure plasma is around 5 GHz (considering an electron density as mentioned in the definition of the Debye length). This means that below 5 GHz, electrons are able to follow the alternative electric field.

2.1.5 Plasma sheaths

An infinite plasma, or at least without boundary, is described by elementary processes like collisions and some electrodynamic quantities. However, in industry and laboratories, plasmas are confined in vacuum chambers. A boundary layer appears near the walls, the so-called plasma sheath, which consists of positively charged space between the walls and the plasma region [129]. The formation mechanism of sheaths can be explained by considering that electrons are able to move faster than ions in the plasma and first reach the walls or any surfaces. A negative potential is therefore created, this is the negative self-bias. Since negative charges left the plasma within a region close to the boundary, a positively charged layer is formed with a thickness of few Debye length [130]. The quasi-neutrality is not anymore respected in the sheath, as seen in figure 2.1. A difference of potential appears between the walls and the plasma bulk which is named the plasma sheath. An equilibrium is found when the flux of ions reaching the surface is equal to the flux of electrons. Thus, there is no net current through the sheath.

2.2 Low-pressure non-local thermal equilibrium plasma

As mentioned in the introduction, plasmas can be sorted depending on the electron density and temperature. Figure 2.2 illustrates the classification for several natural and man-made plasmas. Most specifically, low-pressure NLTE plasmas, which are commonly used in industry and laboratories, are characterized by an

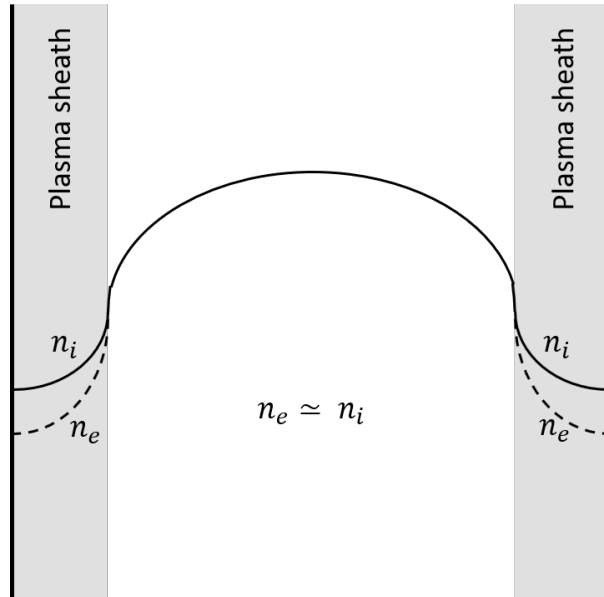


Figure 2.1: Schematic representation of a confined plasma with the creation of a space charge sheath close to the surface. The quasi-neutrality is only verified within the plasma bulk and deviate in the sheath (Adapted from [122]).

electron density range between 10^9 and 10^{12} electrons per cm^3 , an electron temperature lying between 10^4 to 10^6 K and a pressure range between 10^{-3} and 10 mbar. Those characteristics lead to a weak ionization degree varying from 10^{-6} up to 10^{-4} [127]. However, species (electrons, ions and neutrals) in the generated plasma include radicals which are reactive molecular fragments and reactive or in excited state atoms. Such radicals allow chemical reactions in the plasma and then are useful for surface cleaning and modifications, material functionalizations, etc. Low-pressure NLTE plasmas can be considered as a versatile tool characterized by a low-energy consumption process and allowing to reduce the environmental impact in the fabrication of nanoparticles when compared to some conventional chemical processes, as discussed in section 3.1.

The last important point about that kind of plasma concerns some additional precisions about the thermodynamic equilibrium. In the case of most plasmas produced in laboratories, photons are emitted and this induces a net loss of energy for the plasma due to the fact that the re-absorption of light does not compensate the emission. If nothing is done, the ionization degree will decrease and no plasma can be sustained. Such a process does not fulfill the micro-reversibility concept in which all the processes involved and their reverse statistically compensate. Only thermal plasmas verify the micro-reversibility concept, like in stellar cores. No external source of energy is needed to sustain the plasma.

For non-thermal plasmas, also named "cold" plasmas because heavier particles have a lower temperature compared to the electrons, an external source of energy is required to produce enough charged species and to be able to balance recombination and ionization. Because electrons do not interact enough with ions and neutral species, it results in a weak distribution of their energy due to the low number of inelastic collisions between electrons and atoms. This leads to different temperatures for all the species in presence but each of them still can be described by statistical distributions like the Maxwell-Boltzmann distribution for the velocities. The plasma is described by an average energy rather than a concept of temperature.

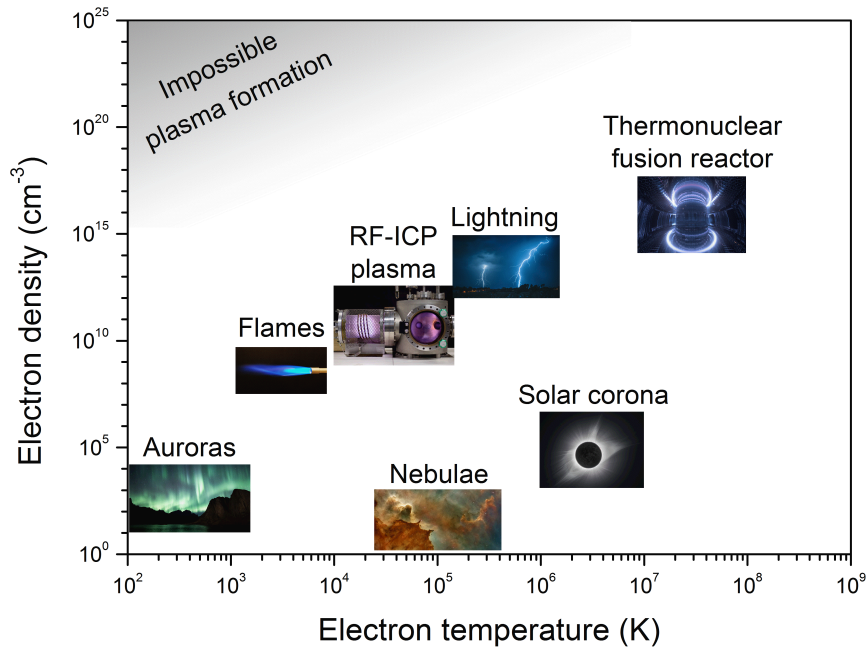


Figure 2.2: Illustration of the different plasma classes versus the electron temperature and density.

The acceleration of charged species in a gas by applying an external electromagnetic field results in collisions between electrons and the other species as previously mentioned. An energy exchange process thus occurs which allows to create new charged particles through ionization, excitation or fragmentation of the species present in the gas. Several processes are involved in cold plasmas and some of them are presented in Table 2.1.

$A_2 + e^- \rightarrow A_2 + e^-$	Transfer of kinetic energy
$A_2 + e^- \rightarrow A_2^* + e^-$	Excitation
$A_2 + e^- \rightarrow A^- + A^+ + e^-$	Dissociative attachment
$A_2 + e^- \rightarrow A_2^*$	Associative attachment
$A_2 + e^- \rightarrow 2A + e^-$	Dissociation
$A_2 + e^- \rightarrow A_2^+ + 2e^-$	Ionization
$A_2 + e^- \rightarrow A^+ + A + e^-$	Dissociative ionization
$A_2 + M^* \rightarrow 2A + M$	Penning dissociation
$A_2 + M^* \rightarrow A_2^+ + M + e^-$	Penning ionization

Table 2.1: Several examples of energy transfer and collision processes involved in cold plasmas (Adapted from [131].)

2.3 Gas discharge plasmas

It is now clear that laboratory plasmas must be produced with the help of an external source of energy that permits the creation of ions and neutrals, this to counterbalance the recombinations as well as the loss of energy with the surrounding environment such as energy absorption by the walls and emission of radiations. For example, gas discharge plasmas have been more and more employed in the past few years for a wide range of applications by taking advantages of the non-thermal aspects. Practically, an electric field is applied to the gas. The natural ionization, induced by the interaction of cosmic rays with nearby particles or by natural radioactivity, reacts to that field, especially the electrons since they are much lighter than the ions. The free charges will be accelerated and gain energy. When the charges have acquired a sufficient amount of energy, collisions occur with neutral molecules and can therefore ionize the latter by energy transfer. The new charges then produced will also increase their energy when interacting with the electric field. A collision cascade is thus created which results in an increase of the ionization degree. The plasma state is obtained and maintained stable only if the global production rate of charged particles is exactly the same as the recombination one.

2.3.1 Direct current or glow discharge plasmas

Literature covers a wide variety of gas discharge plasmas with their applications. Historically, the first NLTE plasmas studied were produced by the application of a constant and sufficiently high voltage between two electrodes in an electrical discharge tube filled with gas, the so-called DC discharges. The electric field generated accelerates the electrons emitted near the cathode by cosmic rays and a collision cascade allows the formation of a plasma, some of them characterized by the emission of radiation which gives the name of *glow discharge* to the process. A general overview of a glow discharge tube is shown in Figure 2.3. Important features can be outlined from the schematic drawing. Three glow areas

are created with dark spaces in between. The cathode glow situated just after the Aston dark space is a relatively thin bright area. Then, the negative glow, which is the brightest part in the tube, sees its luminosity decreasing towards the Faraday dark space. The positive column has a less important light intensity compared to the negative glow but has a more uniform emission. Finally, the last bright area is the thin anode glow. Each bright zone has its own light intensity. Thus, plasmas created in this type of discharge tube are non-uniform.

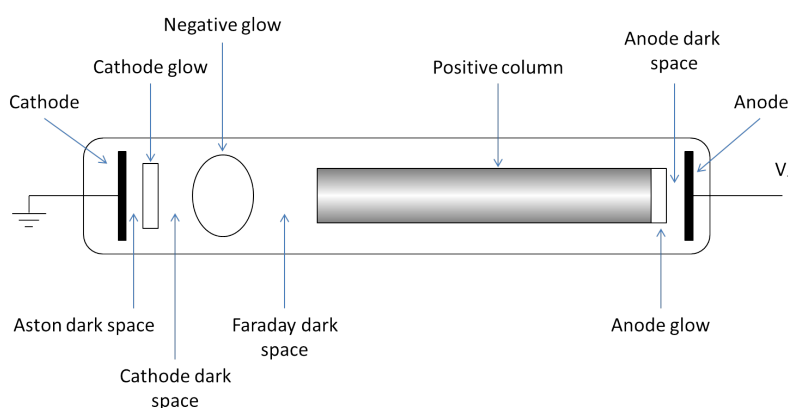


Figure 2.3: Global overview of a glow discharge tube (Adapted from [132]).

For example, glow discharges have been used for analytical spectrochemistry; the ability of the plasma to create ions and fast atoms which bombard the electrode surface allow the phenomenon of sputtering. Atoms released by the electrode are then collected by a mass spectrometer for further analysis [133].

One of the drawbacks of this sort of plasma is the impossibility to deposit dielectric materials in glow discharge plasmas since the deposition will lead to the formation of a non-conductive layer between the electrodes. However, it is needed to sustain the plasma by a continuous charge compensation at the cathode and the anode, which could not be possible with a dielectric between them. Indeed, negatively charged particles could not be collected at the cathode and positive particles at the anode. This is why alternative plasma systems have been developed.

2.3.2 Radio-frequency plasmas

Radio-frequency (RF) plasmas are operated at frequencies lying between 1 kHz and 100 MHz with most systems operating at 13.56 and 27.12 MHz. The limitation in frequency is due to the fact that most of the RF spectrum is reserved for telecommunications and then interferences are avoided. The use of RF plasmas has a great interest in industry or laboratories since they present multiple

advantages compared to DC discharges [133, 134]. Firstly, electrons always instantaneously follow the electromagnetic field generated at lower RF, the electron plasma frequency typically varies from $9 \cdot 10^8$ to $3 \cdot 10^{10}$ Hz which is obviously higher than 13.56 MHz, and can gain energy over a RF period. This leads to a more efficient ionization process. Secondly, massive ions in the plasma are also able to immediately respond to the electromagnetic field generated at the same frequency, except the heavier ones that only see a time-averaged electric field because the ion plasma frequency is inversely proportional to the mass. Therefore, they do not have enough time to reach the electrodes and their loss is reduced. Moreover, RF plasmas can be sustained at lower pressures, this is related to the decrease of the discharge impedance when the frequency increases. They also are globally more spatially uniform. Finally, they are suitable for depositing dielectric materials. Precisely, charges gathered during one half-period will be partially neutralized by the opposite charges gathered during the next half-period since every electrode will alternatively act as the anode and the cathode.

The RF plasmas are classified in two types depending on how the coupling power is achieved : (i) the capacitively coupled plasma (CCP) in which an alternative current is applied between two electrodes (planar, cylindrical, ...) resulting in the generation of an electric field responsible of the gas ionization, and (ii) the inductively coupled plasma (ICP) consisting in the application of an alternative current at both ends of a coil which leads to the generation of an electromagnetic field allowing the gas ionization. Figure 2.4 shows some of the common geometries employed in both cases.

2.3.3 Radio-frequency inductively coupled plasmas

Different types of plasma source geometries exist and can provide the electric field required, as mentioned in section 2.3.2. The ICP, in which the electromagnetic field generation is performed by using alternative currents in coils, was discovered by Hittorf in 1884 [135]. This type of plasma was employed in the present work. The principle of ICP is based on the Maxwell-Faraday equation :

$$\nabla \times \vec{E} = \frac{\partial \vec{B}}{\partial t} \quad (2.5)$$

A RF magnetic flux is produced when a RF current runs in the coil and penetrates the plasma region. A solenoidal RF electric field is therefore induced by the time-varying magnetic flux density which accelerates the free electrons and sustains the discharge.

Inductive sources present the same or even better advantages in comparison with other kinds of RF sources like in capacitively coupled plasmas; the concept is relatively simple, plasmas provided are highly uniform, stable and reproducible,

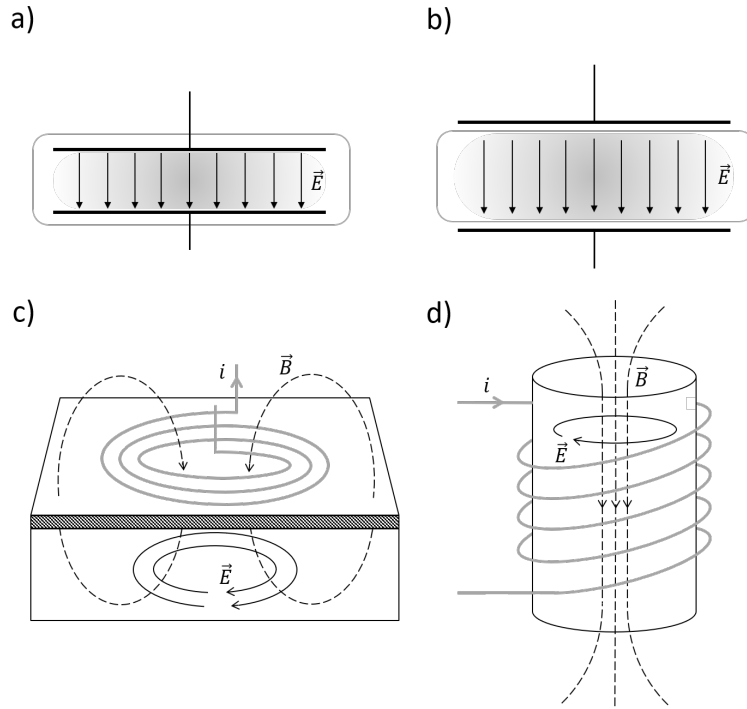


Figure 2.4: Illustration of a) inner planar and b) outer planar electrodes geometries for the CCPs, c) planar and d) cylindrical coil geometries in the case of ICPs (Adapted from [132]).

no DC magnetic field is required, and they have high electron densities (typically 10^{11} - 10^{12} cm^{-3} in efficient low-pressure ICP discharge, which is over 10 times higher than capacitively-coupled plasmas) [133, 134, 136].

2.3.4 E-to-H transition

Three operating modes exist in ICP discharges : the capacitive E mode, the inductive H mode and the helicon W mode. They are characterized by different electron densities and mechanisms responsible of the power transmission from the source to the plasma. In the present work, low (20 W) to intermediate powers (200 W) were employed which signifies that the discharges were only driven in the E and H modes. Therefore, the helicon W mode will not be discussed further in this chapter.

In order to understand the capacitive E mode, inductive H mode and the transition principle, a cylindrical coil will be considered. The conductive plasma is thus contained in a cylinder with the coil wrapped around it. When applying an alternative current passing through the coil, an electromagnetic field is created which goes into the plasma. This is the primary source field. However, a shielding ef-

fect occurs due to induced currents in the conductive plasma (also called "plasma currents") that opposed the source current. The primary field decreases exponentially within the plasma and the depth penetration is limited to a restrained value, the so-called skin depth δ . Figure 2.5(a) shows a schematic diagram of cylindrical ICP with the skin depth. Electrons located within the skin depth thickness interact with the time-varying inductive magnetic field which allows the energy transfer by ohmic dissipation and collisionless heating process, it is the inductive H mode which leads to a bright light emission and is valid at sufficiently high electron densities.

Another way to describe such a mode is by considering a transformer model, as seen in figure 2.5(b). The primary coil is characterized by an inductance L_S and a resistance R_S . The plasma discharge is considered as a one-turn coil with a geometrical L_G and an electron inertia L_e inductance, and a resistance R_P . A voltage V_S is applied to the primary coil in order to generate a current I_S . A magnetic field is produced and will interact with the secondary coil by induction. The power transmitted to the plasma is given by [137] :

$$P_{transmitted} = \rho I_S^2 \quad (2.6)$$

with ρ the change in plasma resistance.

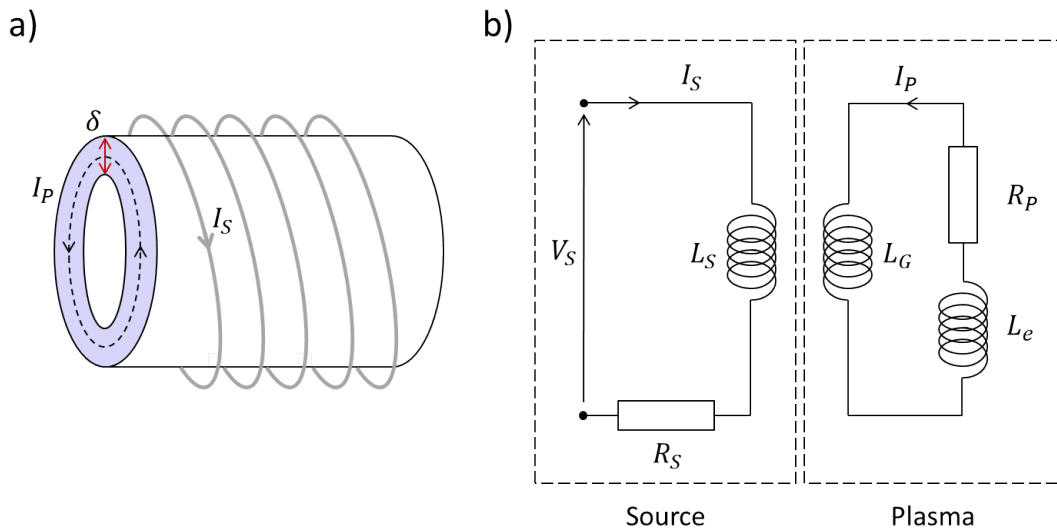


Figure 2.5: Representation of (a) the skin depth δ in a cylindrical volume which limits the field penetration and (b) the transformer model of the source-plasma coupling.

If the electron density is not high enough, power transmission can not be performed by induced currents because of their too low intensities. The primary

source is not anymore the magnetic field but rather an electrostatic one. In this case, the electromagnetic field is able to penetrate far in the plasma since the skin depth is much larger (for low-pressure discharges, skin depth is approximately inversely proportional to the square-root of the electron density). Put simply, the so-called capacitive E mode, characterized by a faint light emission, takes place when an electrostatic field between segments of current coil generates a low plasma density. Referring to figure 2.5(b), a high-voltage V_G (generally more than 1000 V) is applied to the primary coil. Since the skin depth is large, the potential created goes deep into the plasma volume and the resulting electric field is able to transfer energy to the electrons. This situation is similar to charged electrodes which gives the name of capacitive discharge to the process.

An abrupt transition between the E mode and H mode exists, leading to an important increase of the electron density and light emission. However, the explanation is quite complex and few theoretical researches have been performed to bring an answer to the jump in density and light intensity. A proposed mechanism responsible for the transition based on the non-linearity of power absorption and dissipation was presented by Turner *et al.* [138] and El-Fayoumi *et al.* [139]. The electron power balance is affected by these non-linearities; the power dissipated in the plasma, the power dissipated by the electrons or both do not present a linear behavior anymore. Considering an electron density n_e at a fixed applied source power near the transition, a slight increase of n_e will result in a reinforcement of the power coupling. The ionization becomes more important since the absorbed power increases. Therefore, the electron density rises and leads to a positive feedback loop which deviates from a linear dependency due to the emergence of a skin effect [140].

In chapter 8, the E-to-H transition of ammonia- and nitrogen-based plasma has been studied and related to the carbon matrix functionalization. Vesel *et al.* [141] showed the difference between the E and H modes; the capacitive mode presenting a less destructive effect on their substrate and allowing to functionalize the material at relatively low plasma power while the inductive mode, which is a more powerful plasma, exhibits a different functionalization. In the present work, the effect of the transmitted power in the two modes (from 20 W to 200 W) and of the plasma chemistry (NH_3 and N_2) on the carbon functionalization was studied.

Chapter 3

Synthesis of nanoparticles and carbon functionalization : from chemical to physical methodologies

In this chapter, a general overview of the methodologies employed to synthesize nanoparticles supported or not on a carbon matrix is presented. The methodology used in this work is then discussed and, afterwards, the experimental setup for the nanomaterial fabrication and the surface functionalization is detailed. Firstly, a description of the plasma reactor, the RF-ICP source, the gas injection system and pressure controllers are depicted in section 3.2, while the procedure setup for the synthesis of nanoparticles is then detailed in section 3.3.

3.1 Methodologies developed to synthesize nanoparticles

In chapter 1, special attention was given to the material employed as catalyst and the role of the carbon support. It is now important to provide an overview of the different methods used to synthesize NPs. Especially, the low-pressure plasma discharge methodology used in the present thesis is described in more details. Even though a large number of conventional techniques to fabricate the NPs are based on wet chemical processes, only few of them are briefly presented in this thesis.

3.1.1 Wet chemical processes

As mentioned above, a large number of wet chemical processes exist. Among them, the low-temperature chemical precipitation is one of the most well-known techniques; the procedure consists in adding a reducing agent to a metal-salt solution, this to ideally reach the metallic state by reducing the salt, and then let the formation of the catalysts occur by precipitation [17]. In order to produce

supported NPs, carbon can be added prior to the reduction process. Such a technique is suitable for single or bimetallic catalysts synthesis.

Another way to obtain NPs is the colloidal technique as described by Bashir *et al.* [142]; a mixture is realized with at least two substances : a metal source and a reducing agent. The procedure is similar to the precipitation method but allows a control over the NP size and prevents agglomeration thanks to the use of a third substance in the mixture, *i.e.* a capping agent. Particles are suspended in the solution followed by their reduction. Larger NPs are created through the aggregation of the suspended particles by van der Waals forces. Furthermore, a carbon support can be added before or after the NP synthesis which leads to the production of supported catalysts [143]. Bimetallic particles have also been successfully synthesized by the colloidal method [144].

The last chemical process mentioned here is the so-called impregnation methodology, one of the most simple to implement; a mesoporous material is mixed with a catalyst precursor in an aqueous solution and then the solvent is evaporated to form particles bound to the support. However, Gélin *et al.* [145] reported a poisoning effect due to the commonly employed salts during the impregnation; it resulted in a decay of the catalytic activity. This negative effect could be avoided by using other kind of salts like metal carbonyl complexes [146]. Moreover, particles agglomeration has been reported in the literature which decreases the surface area [147,148]. Finally, collapse of the support can easily occur due to high surface tension of the solution [149].

3.1.2 Physico-chemical techniques

The main disadvantages of the wet chemical methodologies, and not only for those described above, are the extensive use of toxic solvents, the need of a relatively high reaction temperature in some cases and often slow synthesis reaction rate. On the other hand, physico-chemical methods can be used without the help of any solvent, be fast and flexible.

The term physical vapor deposition (PVD) regroups two categories of techniques; mechanical (such as cathodic sputtering) and thermal (*i.e.* evaporation) methods. For example, experiments using magnetron sputtering in vacuum conditions successfully produced nanocatalysts on various supports, thus confirming the convenience of the technique for NP growth [150–153]. The principle of magnetron sputtering is based on the generation of a plasma, *i.e.* ionized gas (see chapter 2 for more details), between a substrate and a target made of the desired material to deposit; atoms from the target are ejected and accelerated towards the substrate. However, it is difficult to produce materials suitable for catalysis due to the quick formation of a thin film at the surface of the substrate [151].

Post-treatments or improved magnetron sputtering techniques, like the gas aggregation source methodology, are then required [151, 153]. In addition, this method requires quite an expensive vacuum equipment and is hardly scalable to industrial production. However, efforts have been made and studies tend to demonstrate the possibility to reach a large-scale production [154, 155].

Besides magnetron sputtering, other plasma-assisted methodologies to synthesize NPs emerged. Both high- and low-pressure plasmas have been investigated to produce single or bimetallic particles. The interest of plasma treatments is their ability to generate anchoring sites for metallic NPs at the surface of a carbon support [156]. Several studies showed that better interactions between NPs and the support materials were obtained thanks to plasma treatments [156, 157]; thus catalyst stability is gained. Recently, Merche *et al.* [158] employed an atmospheric RF plasma torch (ARFPT) with argon as vector gas to decompose an organometallic precursor mixed with a carbon support and form NPs. Two circular electrodes were used with one perforated to let the argon gas flow between them. The plasma is ignited by applying an alternative high voltage of 13.56 MHz. In comparison with usual methods presented in the literature, ARFPT is an easy, robust and fast technique which operates at near ambient temperature but a major drawback is the lack of control on the size distribution [158].

Among all the low-pressure plasma processes for the synthesis of FC electrocatalysts reported in the literature [159–162], a novel method developed by Pireaux *et al.* [163] is promising for growing NPs on various substrates. Going further, in 2014, Laurent-Brocq *et al.* [164] reported on the successful deposition of Pt/C particles by the same method; a Pt organometallic precursor was mixed with a carbon support and placed in a vacuum chamber followed by a short plasma treatment. Typically, homogeneously dispersed NPs with an average size of 3 ± 0.8 nm were obtained after an oxygen plasma with stirring conditions for a reactant mixture containing a metal loading up to 40 wt.%; as discussed in section 1.3.3, such a size distribution is optimum for an efficient specific ORR activity. Moreover, Pt/C NPs synthesized are mainly metallic resulting in a reducing effect of the oxygen plasma [165]. This is probably due to the formation of reducing, such as O^+ and O_2^+ , or reactive species in the plasma. However, the reducing effect of oxygen-based plasmas is not well understood yet and further investigations should be performed.

A mechanism allowing the nucleation of Pt NPs was also proposed by Laurent-Brocq *et al.* [164] : (i) decomposition of the precursor under a plasma discharge is performed, thermal and chemical effects are assumed as the main causes of such a process, (ii) at the same time, species formed in the plasma interact with the carbon and induce both structural and chemical defects (oxygen functions are added at the surface), (iii) defects just created act as anchoring sites for the NPs

nucleation. A sketch of the mechanism is shown in Figure 3.1. This so-called "one-pot" process is therefore relatively easy to handle, time- and energy-saving (see section 5.2.4 for more details).

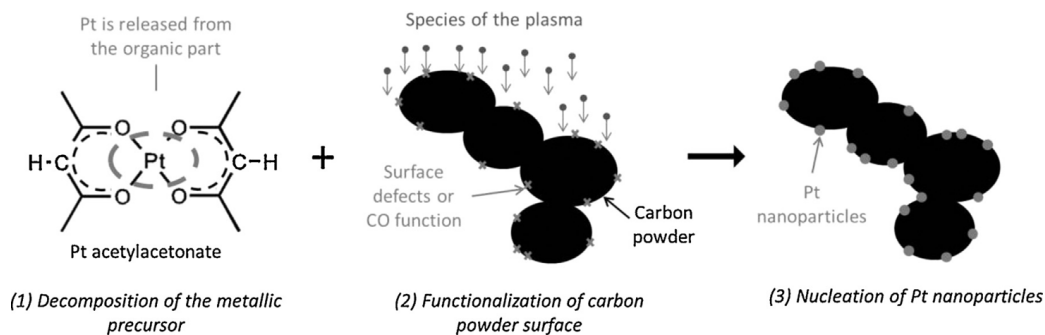


Figure 3.1: Sketch of the proposed mechanism for the NPs nucleation by a low temperature radio-frequency plasma (Taken from [164]).

The procedure and experimental setup used in this work is the same as presented in [164]. Section 3.2 describes the home-made vacuum chamber developed at the LISE research unit and employed for the synthesis of NPs or N-doping of the carbon support. The NP synthesis is discussed in detail in section 3.3.

3.2 Experimental setup

3.2.1 The plasma reactor

A low-pressure RF plasma reactor was used to synthesize the nanomaterials and to functionalize the carbon support. Figure 3.2 shows the experimental setup. It consists of a vacuum chamber made of stainless steel with a cylindrical quartz tube extension in which the samples are positioned. The plasma source is composed of a RF generator, a matching network and a coil surrounding the quartz tube. A gas injection system is placed next to the cylinder and controlled by flowmeters. The vacuum is ensured by a pumping system. Finally, pressure gauges are installed to monitor the working pressure while a plasma treatment is performed.

3.2.2 The RF-ICP source

The RF-ICP source consists in a helical coil made of four spires wrapped around a quartz tube and connected to a matching network. The variable power at a frequency of 13.56 MHz sent to the coils is coming from a Dressler Cesar

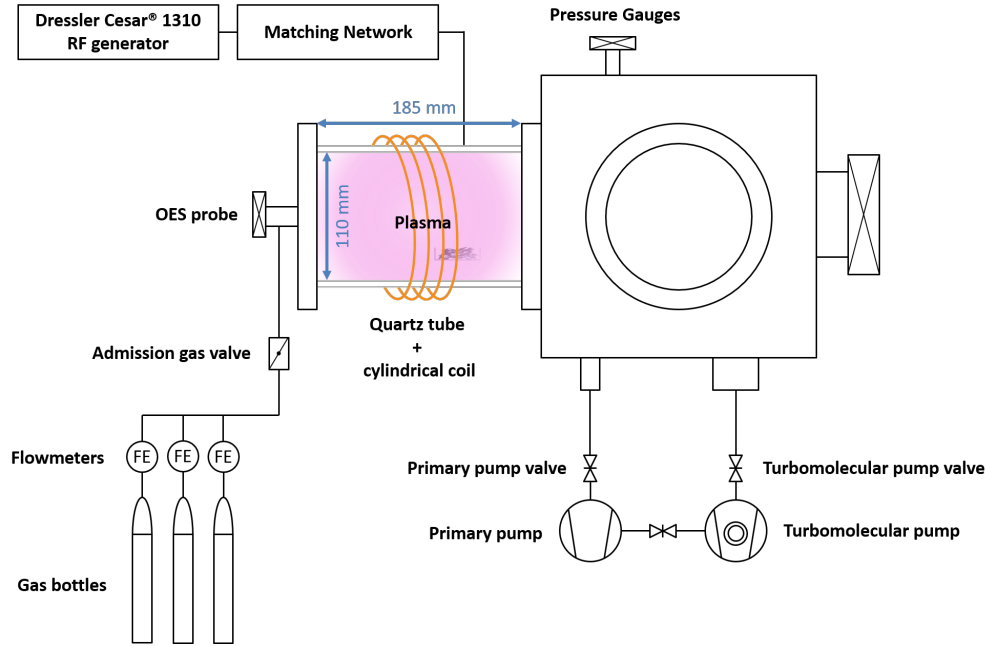


Figure 3.2: Schematic picture of the plasma reactor. The most energetic area of the plasma is located at the center of the quartz tube wrapped with the coil.

1310 generator (Advanced Energy, Germany). The matching unit allows an optimal transmission of the power to the source-plasma couple by varying the circuit impedance. Thus, the 50Ω impedance of the generator matches with the source-plasma one by varying capacitance integrated in the source. Indeed, the impedance is varying with the plasma conditions and time. Moreover, it is difficult to modify the inductance. The matching was manually driven to lower the reflected power which was usually below 1% of the desired transmitted power.

3.2.3 Gas injection and pumping system

Gas bottles (Ar, O₂, N₂, NH₃, H₂) are linked to flowmeters (MKS mass flow MFC and MF-1) which allows a monitoring of the flux injected via a vacuum controller (MKS 946 vacuum system controller). Gases directly flow in the plasma discharge area. The pressure can then be adjusted when the flux set-point is reached by closing pumping valves.

As mentioned in the previous chapter, plasmas ignited at the laboratory are low-pressure RF-ICP. A pumping system is therefore used to reach the desired pressure. The system is composed of a rotary vane pump (Pfeiffer DUO 10 MC, $10 \text{ m}^3/\text{h}$), protected upstream by a zeolite trap, and a turbo-molecular pump (Pfeiffer TMU 261, 210 l/s). Both pumps are connected to the chamber and can be isolated by using different valves. The primary pump is also connected to the

turbo-molecular pump but separated by a valve, such protection takes place to avoid a return to the air when pumping back the chamber.

The zeolite trap placed at the entry of the primary pump helps to remove most of the hydrocarbons released during a plasma treatment as well as gases injected in the vacuum chamber. It avoids the frequent replacement of the oil pump, increases its lifetime without degrading the pressure condition in the plasma reactor over several experiments.

3.2.4 Pressure gauges

Three different kinds of gauges were used to measure the pressure in the plasma reactor, each having their own range of measurement. The first measuring instrument is a Pirani gauge (Agilent ConvecTorr P-type) based on the heat transfer by convection to the surrounding gas. A sensing filament produces heat when a current is passing through it. At a few mbar, the mean free path of the gas has the same order of magnitude as the filament radius and the heat transferred is dependent on the pressure. The variation of the pressure is related to the variation of the thermal conductivity. Typically, Pirani gauges can measure pressure from 1000 to 10^{-4} mbar. However, it has been shown that ConvecTorr gauges are gas dependent [166].

A capacitance manometer (Baratron MKS gauge) has also been used to avoid the gas dependency. The principle relies on the fact that a thin diaphragm is translated when the pressure is modified, pushing or releasing the membrane which induces an electrical signal proportional to the pressure. The range of measurement varies from ~ 1 down to 10^{-4} mbar.

Finally, a penning gauge (Agilent IMG 100) was installed on the vacuum chamber. When the turbo-molecular pump takes over the primary pump to reach high vacuum, the pressure drops below the minimum value displayable by the two other manometers and is monitored by the penning gauge. A high voltage is applied to a cathode and an anode to accelerate the electrons between the electrodes in order to ionize the surrounding gas. A magnet is placed around the cathode/anode system to make electrons move spirally and increase the interacting time with the gas. Ions generated will be collected by the electrodes creating an ion current and then converted into a pressure measurement. Such a device typically works with pressure lying between 10^{-2} to 10^{-9} mbar.

3.3 Nanoparticle synthesis procedure

In this work, NPs supported on a carbon support were synthesized through the decomposition of one or several precursors (organometallic or inorganic) in a low-

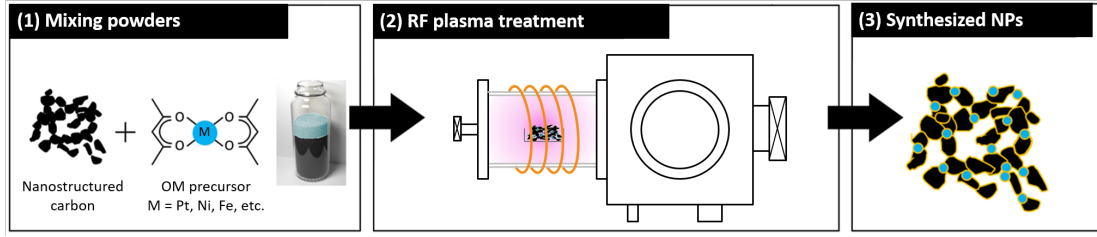


Figure 3.3: Sketch of the methodology set up for the nanoparticles synthesis (Adapted from [167]).

pressure plasma discharge, as described by Laurent-Brocq *et al.* [164]. A sketch of the procedure followed for the particle fabrication is shown in Figure 3.3. It starts with mixing a fixed mass of one or two organometallic (OM) precursors with a fixed amount of carbon support. The different masses were precisely measured to match a desired metal loading in the samples at the end of the plasma treatment and are calculated following this general equation :

$$W_{met.load.} = \frac{m_{metal}}{m_{OM} + m_{CS}} \quad (3.1)$$

with $W_{met.load.}$ the total metal loading in the sample, m_{metal} the mass of metal used to form nanoparticles, m_{OM} the mass of the OM precursor, and m_{CS} the mass of carbon support. In other words, this equation gives the metal fraction compared to the total amount of powder constituting the sample.

A more convenient formula can be considered by introducing the maximum metal loading possible χ_{metal} assuming that the OM precursor is completely decomposed and the organic part pumped down by the vacuum system :

$$\chi_{metal} = \frac{m_{metal}}{m_{OM}} = \frac{M_{metal}}{M_{OM}} \quad (3.2)$$

where M_{metal} and M_{OM} are the molar mass of the metal and the OM precursor, respectively. The last equality is true only if the number of moles is the same for both the metal and OM which is the case for all the precursors used in the present work. Therefore, the equation (3.1) can be rewritten taking into account equation (3.2) :

$$W_{met.load.} = \frac{\chi_{metal}}{1 + \delta} \quad (3.3)$$

$$\delta = \frac{m_{CS}}{m_{OM}} \quad (3.4)$$

	Linear Formula	Molecular Weigth (uma)	Melting point (°C)	χ_{metal} (wt.%)
Pt(acac) ₂	Pt(C ₅ H ₇ O ₂) ₂	393.29	~250 [168]	49.6
Pt(cod)(Me) ₂	Pt(C ₈ H ₁₂)(CH ₃) ₂	333.33	~105 [169]	58.5
Platinic acid	H ₂ Pt(OH) ₆	299.14	-	65.2
Ni(acac) ₂	Ni(C ₅ H ₇ O ₂) ₂	256.91	~230 [170]	22.8

Table 3.1: Main characteristics of the organometallic precursors used to form nanoparticles : Pt(II) acetylacetonate (Pt(acac)₂), (1,5)-cyclooctadiene dimethylplatinum(II) (Pt(cod)(Me)₂), hydrogen hexahydroxyplatinate(IV) (platinic acid) and Ni(II) acetylacetonate (Ni(acac)₂).

Four different precursors were used and some of their characteristics are reported in Table 3.1. The maximum wt.% is indicated in the last column for each of them. Among the four compounds, only the platinic acid is inorganic and no available melting point value could be found in the literature.

When the mixing of all the powders is done, the next step of the procedure consists in uniformly dispersing the powder mixture in a glass Petri box and insert it in the plasma reactor to be treated. The valve connected to the primary pump and the vacuum chamber is then slowly opened. This precaution is taken to avoid the pumping of the powder. Different parameters can be set up for the plasma treatment and affect the synthesis of NPs such as the power of the plasma, the plasma chemistry, the pressure in reactor, or the treatment time. Next chapters in the present thesis are dedicated to the experiments performed to synthesize Pt-, Ni-, Pt-Ni- and Fe-based NPs, and include detailed discussions on the effect of the plasma parameters on the formation of those nanoparticles. The last step consists in the characterization of the fabricated materials thanks to several techniques, each of them described in chapter 4.

Chapter 4

Characterization techniques

This chapter is dedicated to the presentation of the different techniques employed to characterize the treated samples. An overview of an X-ray Photoelectron Spectrometer (XPS), an X-Ray Diffractometer (XRD) and a Transmission Electron Microscope (TEM) are reported. The Optical Emission Spectroscopy (OES) method is also briefly introduced. Afterwards, the electrochemical and nitrogen adsorption-desorption methods used to determine the catalytic activities, the specific surface areas and pore texture of the samples are described.

4.1 X-Ray Photoelectron Spectroscopy

X-Ray Photoelectron spectroscopy (XPS) is an old technique developed at the very beginning of the 20th century thanks to the discovery of the photoelectric effect by Heinrich Hertz in 1887 but understood and explained by Albert Einstein in 1905. In the 1950's and the 1960's, Professor Kai Siegbahn brought a major development to the technique demonstrating the wide range of materials possibly analyzable and encouraging scientists to use it [171].

The photoelectric effect

Based on the Max Plank's idea that energy can be quantified, Einstein proposed that light can act sometimes as energy particles, the photons, and another time as a wave. This is the wave-particle duality. Going further, when monochromatic photons with a sufficiently high energy encounter matter, electrons may absorb them and then may be ejected from the atom if their energy exceed the work function of the material. The historic explanation made by Einstein were involving electrons in the conductive band of metals and UV light was enough to eject electrons.

In the 1960's, Siegbahn showed that by using X-rays instead of UV light, it was possible to extract electrons from core levels of any material; the first XPS

was born. Basically, an X-ray beam is sent on the surface to be analyzed and induces the ejection of core level atom's electrons, the so-called photoelectrons, as seen in Figure 4.1. Each element has a characteristic signature depending on the core levels' energy which is exploited in the XPS through the determination of the binding energy (BE) of the photoelectrons ejected by measuring their kinetic energy (KE).

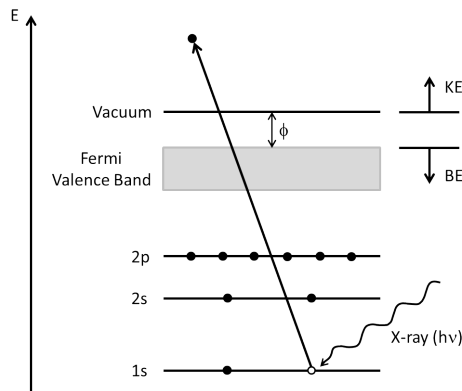


Figure 4.1: Illustration of the electron population in core levels and the emission principle of photoelectrons induced by X-rays.

4.1.1 Operating principle of an XPS

Since 2013, the laboratory is equipped with a K-Alpha and an ESCALAB™ 250 XI from ThermoScientific, both having the same operating principle and only differ by their photoelectron detector. Figure 4.2 illustrates the principle of an XPS and will be described in details. A pumping system is installed on the machines to reach an ultra high vacuum (UHV) in the analysis chamber down to 10^{-10} mbar. The need of UHV is based on the following considerations :

- An accurate XPS analysis is performed if the information of the transmitted photoelectrons is not modified. Therefore, it is needed to decrease as much as possible the interactions between the extracted photoelectrons and the residual gas molecules in the analysis chamber. Moreover, the photoelectrons mean-free path is increased under UHV which allows them to reach the detector area.
- The surface contamination of the material due to gas residuals is minimized during the analysis. The adsorption of a gas residual monolayer takes only few seconds at a pressure of 10^{-6} mbar [172].
- The design of the spectrometer requires to work under UHV. Several components are then preserved like the filaments and the surface condition of the device.

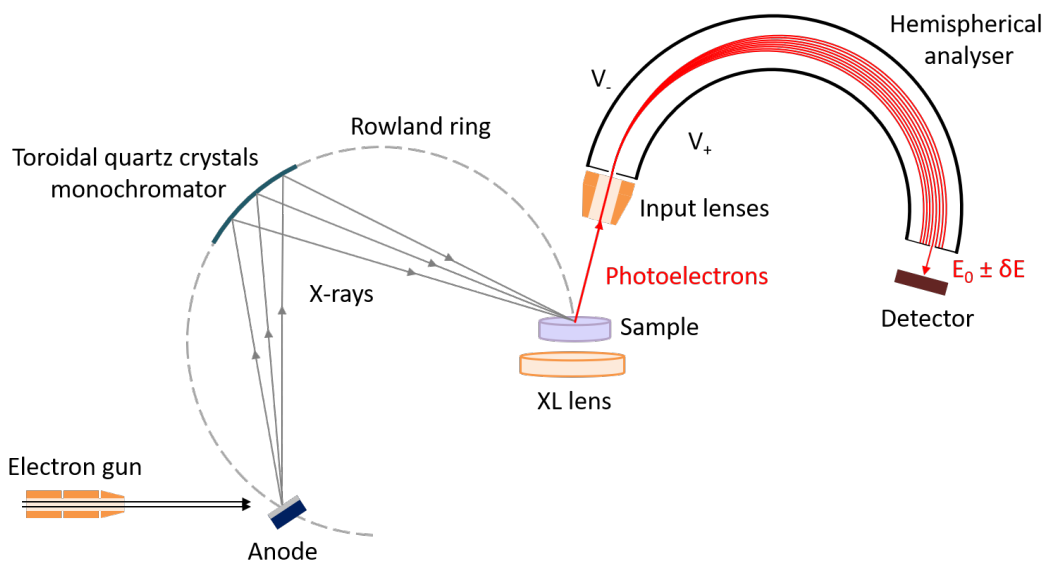


Figure 4.2: Schematic drawing of the working principle of an X-ray Photoelectron Spectrometer.

The production of X-rays is performed by bombarding an anode with highly energetic electrons generated and focused in an electron gun. The anode is made of aluminum or magnesium in order to limit the energy width of the X-rays emitted which is smaller than other metals. For the ESCALAB™ 250 XI, an aluminum anode is used and the $K_{\alpha 1,2}$ emission line at 1486.6 eV is selected by a twin-crystal monochromator placed on a 0.5 m Rowland circle.

The sample receives the focused X-ray beam, with a typical spot size of about 300 μm , leading to a photoelectric effect at its surface. Photoelectrons are emitted towards a set of electrostatic lenses, the so-called "input lenses", focusing them before their entry in the hemispherical analyzer. The "input lenses" are employed to increase of the number of electrons collected which are then transmitted to the hemispherical analyzer with limited losses. Moreover, an electromagnetic lens (XL lens), which is placed beneath the sample, can be used to first focus the photoelectrons sent to the "input lenses". The combination of those two lens systems is the so-called "magnetic mode".

The hemispherical analyzer is then employed to select the KE of the photoelectrons that will be sent to the detector. It consists of two concentric hemispherical electrodes set to opposite potentials. The inner electrode has a positive potential while the outer one is negative, a radial electric field is created between them. Electrons passing in the field region will be deflected along a circular trajectory by the electric force and those with the desired KE are transmitted to the detector

by the exit slit. However, the resolution in energy ΔE of the analyzer depends on the KE of the photoelectrons according to the following equation [173] :

$$\frac{\Delta E}{E_0} = \frac{\alpha^2}{2} + \frac{\Delta S}{2R_0} \quad (4.1)$$

with E_0 the pass energy (energy of the electrons which pass through the slit in the middle of the analyzer) of the transmitted electrons, α the angle of the entry beam, ΔS the width of the exit slit and R_0 the mean radius of the hemispheres. In order to acquire spectra with a constant resolution, it is needed to keep the pass energy E_0 constant too. This is realized by slowing down the photoelectrons just before entering the analyzer. Based on the full-width at half-maximum (FWHM) of Ag $3d_{5/2}$ peaks, the resolution of the ESCALAB™ system is 0.6 eV at a pass energy of 20 eV.

The last part of the XPS is the detecting area constituted of a 6-channel electron multiplier, also called the "channeltron detector". Figure 4.3 shows a schematic representation of one channel electron multiplier. Each channeltron is able to detect photoelectrons in a given energy range. It has a large dynamic range and is used to rapidly acquire spectra. A channeltron is made of two parts; an input cone collects the photoelectrons which are transmitted to a spiral ceramic tube. The latter is coated with a high resistance material; transmitted photoelectrons hit the coating which results in a secondary electron effect consisting in the production of more electrons at lower energies. These electrons are then accelerated towards another channeltron placed beneath the first one and the same secondary electron effect occurs leading in a electron cascade production. The signal is sent to pre-amplifiers and data are finally collected by the Avantage™ data system manager electronics.

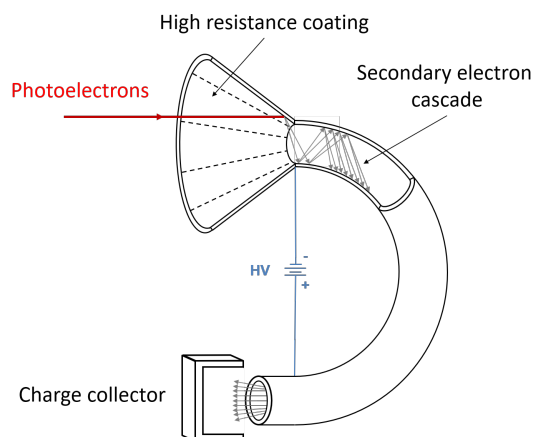


Figure 4.3: Schematic diagram of one channel electron multiplier.

4.1.2 Information extracted from the collected photoelectrons

Considering the conservation of energy, the BE of the extracted electrons can be deduced using the following equation :

$$BE = h\nu - KE - \phi \quad (4.2)$$

with $h\nu$ the X-ray photon energy, KE the kinetic energy of the extracted electrons and ϕ the work function of the spectrometer. The latter is simply a correction factor and adjustable by the instrument.

As mentioned above, XPS can be used to analyze the surface of different materials. One of the main characteristic making XPS advantageous is the quantitative aspect of the spectroscopy. The signal intensity is proportional to the global amount of element present in the sample. Taking into account the Scofield factor, *i.e.* the probability to ionize an element, the inelastic mean free path and the detection efficiency of the analyzer, the relative amount of two elements can be calculated through their signal. In the case of homogeneous surfaces, the XPS intensity for a given element I_j can be written as follows :

$$I_j(\theta) = \Phi \cdot N_j \cdot \sigma_j \cdot A_0 \cdot \Omega_0 \cdot T \cdot D \int e^{-\frac{z}{\lambda \cdot BE \cdot \cos \theta}} dz \quad (4.3)$$

where θ is angle of photoelectron emission compared to the normal of the surface, Φ is the X-ray flux, N_j is the number of emitting atoms, σ_j is the cross-section of the photoelectron production, A_0 is the aperture size of the analyzer, Ω_0 is the solid angle, T is the spectrometer transmission factor, D is a detector performance factor, z is the analysis depth length of the material and λ is the electron mean free path. Figure 4.4 illustrates the different parameters which are influencing the XPS intensity.

The atomic concentrations derived from the relative XPS peak intensities deviate from the true concentrations at the surface for heterogeneous samples like the formation of NPs on a carbon substrate. The latter effect is well known in the literature [174, 175]. Fulghum *et al.* [175] reported the difficulties to perform quantification on non-homogeneous surfaces and the effect of these on the XPS signal.

The mean free path of the electrons is an important parameter and provides information on the depth analysis. From Equation 4.3, attenuation of the signal is given by the exponential decay function in the integral term and depends of the electron mean free path λ . Seah and Dench [176] proposed theoretical models to calculate the electron mean free paths in various cases. Put simply, this parameter

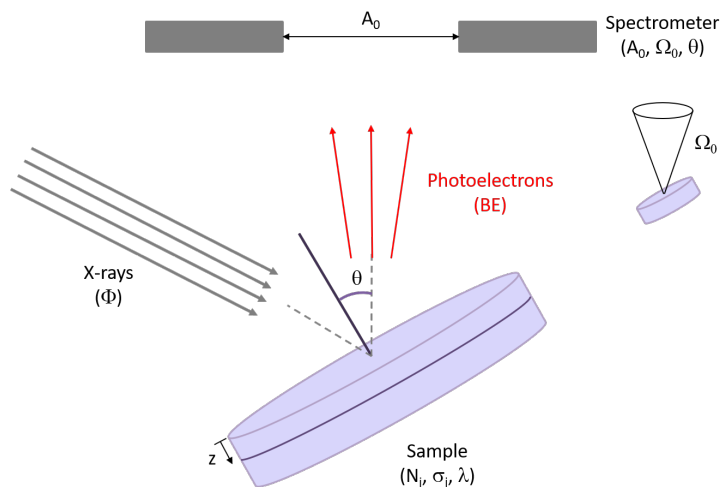


Figure 4.4: Sketch of the XPS analysis together with the parameters influencing the peaks intensities.

depends on the atom size, the monolayer thickness and the KE of the photoelectrons emitted. Regarding the depth analysis, it is generally accepted that around 95% of the XPS signal comes from three times the electron mean free path which represents a depth analysis comprised between ~ 3 and 10 nm (considering that $\cos \theta = 1$).

A second aspect is the determination of the chemical environment at the top surface of samples by measuring the change in BE for a same atom, the so-called "chemical shifts". This phenomenon is due to a modification of the electron core binding energies by removing or adding electronic charges. The charge potential model has been extensively used to provide the physical basis of such a phenomenon [177]. Put simply, considering an hollow conductive spherical atom surrounded by other atoms, the electron energy level depends on the vacuum level, the self-energy of the considered atom with a charge q_i and the energy induced by the charge distribution of the surrounding atoms. When the atom is chemically bounded, the charge on the sphere is modified due to transfer of electrons which leads to a change of potential. Therefore, it results in a shift of the inner electrons BE. This effect will be studied in the present work by analyzing to chemical shifts in the different XPS spectra and by identifying their corresponding chemical environments. This is particularly important for the determination of the oxidation states of the metal-containing particles synthesized by low-pressure RF ICP discharges or the carbon functionalization. XPS is thus considered as a chemical spectroscopy allowing to characterize the surface of materials.

Finally, it is possible to get chemical information about insulators by taking some precautions. Indeed, for such materials, the removal of surface electrons will conduct to a sample with a net charge which will prevent the emission of photoelectrons. A charge compensation is thus needed to avoid this phenomenon. The ESCALAB™ 250 XI is mounted with a flood gun that spreads low-energy electrons, combined with the diffusion of argon ions, on the surface to neutralize the net charge.

The Synthesis, Irradiation, and Analysis of Materials (SIAM) platform of the University of Namur is acknowledged for the XPS measurements presented in the present thesis.

4.2 Powder X-ray diffraction

A second method based on X-rays was used in this study, the X-ray diffraction on powders. In 1912, a paper from W. Friedrich, P. Knipping and M. Laue showed experimentally that X-rays passing through crystalline substances lead to interferences [178]. Therefore, crystals can be considered as 3D diffraction gratings. A year later, W. H. Bragg and W. L. Bragg explained why X-rays sent on crystals appear to be reflected at certain angles [179].

For scientists, the word *crystal* has a meaning different than from its daily life use. In solid-state physics, crystal structures are ordered and periodic arrangement of atoms depending on their nature. Therefore, a crystal can be defined by a Bravais lattice and a basis. Since the atoms are regularly repeated in space, it is possible to find planes parallel to each other and passing through all of the atoms, this is the so-called "reticular planes". Those planes are characterized by integer numbers h , k and l , the Miller indices. Taken together, these three numbers refer to a family of planes and are involved in the calculation of the X-ray diffraction peaks. When a X-ray beam encounters the crystal, diffraction can occur if the Bragg's relation is fulfilled :

$$2d_{hkl} \sin \theta = n\lambda \quad (4.4)$$

where d_{hkl} is the distance between two reticular planes depending on the Miller indices, θ is the reflected angle of X-rays, n is the diffraction order and λ is the wavelength of the X-ray beam. Constructive interferences occur if the optical path difference is equal to the integer number of times the wavelength. Figure 4.5(a) illustrates the diffraction of X-rays in the case of a 2D lattice.

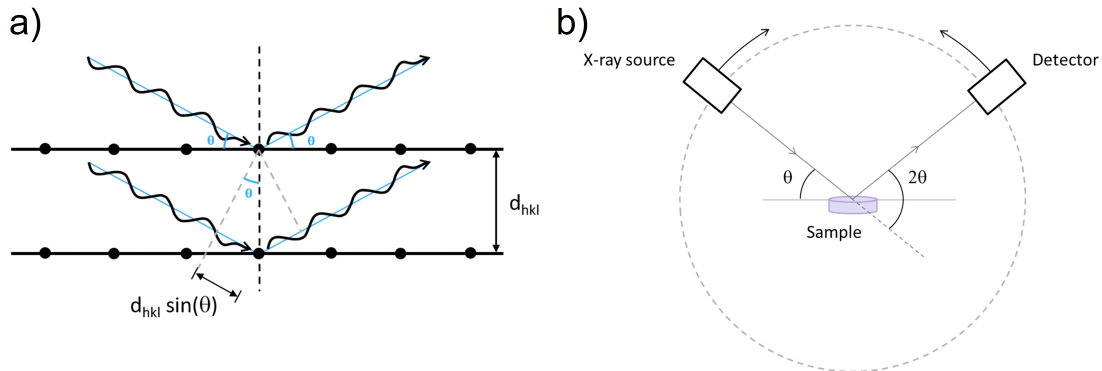


Figure 4.5: a) Illustration of the Bragg diffraction. b) Schematic drawing of the operating principle of an X-ray powder diffraction instrument.

XRD is useful to identify if a material has a crystalline structure or not and can provide an approximation on the size distribution of the nanoparticles in a sample thanks to the Scherrer equation [180] :

$$\tau = \frac{K\lambda}{\beta \cos \theta} \quad (4.5)$$

where τ is the mean size of the crystalline domains, K is a shape factor, β is the FWHM of the considered Bragg angle, and θ is the Bragg angle.

The Physico-Chemical Characterization (PC²) platform is acknowledged for the XRD measurements presented in this thesis. The device used (XPert PRO PANalytical) is based on the powder method and is made of three basic elements : an X-ray source, the sample holder and an X-ray detector.

The principle of X-ray production is similar to the production described for the XPS. An electron beam bombards an anode which results in the emission of highly energetic photons. A copper anode is employed in our case and the Cu K_{α} radiation is selected ($\lambda_{Cu K_{\alpha}} = 0.154$ nm). X-rays are then collimated, sent to the sample and diffracted towards a detector as shown Figure 4.5(b). The X-ray source and the detector are mounted on a mobile arm and both rotate around the sample holder with an angle 2θ . This geometry was employed to analyze powders in which crystalline structures were randomly oriented. By varying the angle 2θ , it is then possible to access all the orientation leading to constructive interferences. A diffractogram is then recorded showing the intensity variation of the diffracted radiation as a function of the diffraction angle 2θ .

4.3 Transmission electron microscopy

The limitation of optical microscopy in terms of image resolution is due to the wavelength of visible light. In other words, an optical microscope can resolve the distance between two points separated by 200 nm which is the same order of the visible light wavelength. As a point of comparison, the smallest distance between two points that a human eye is able to resolve is "only" about 0.1 mm. Alternatives were essential to improve the resolution and this is why transmission electron microscopes (TEM) have been developed. Historically, in 1925, Louis de Broglie showed that electrons can have a wave-like behavior with a wavelength smaller than visible light [181]. Two years later, experiments on the electron diffraction were carried out by two groups of scientists without any consultation [182,183]. Finally, Knoll and Ruska were the first to propose the idea of an electron microscope in 1932 [184].

The wavelength of electrons can be calculated thanks to the de Broglie equation with a correction taking into account relativistic effects since electrons can move at velocities close to the light's velocity [185] :

$$\lambda_e = \frac{h}{\sqrt{2m_0E(1 + \frac{E}{2m_0c^2})}} \quad (4.6)$$

with h the Planck's constant, m_0 the rest mass of an electron, E the energy of the accelerated electron and c the speed of light. A common value for λ_e is $3.7 \cdot 10^{-3}$ nm when they are accelerated with a potential difference of 100 kV [186]. Under this accelerating potential condition, the TEM resolution is about 0.1 nm which is 1000 times better than conventional optical microscopes.

A schematic picture of a TEM is shown in Figure 4.6. However, there remains always the question about how possible it is to obtain images of samples with electrons. A global explanation of the operating principle of the TEM will thus be presented to answer to that question.

The first part of the microscope is the electron gun providing a stable and bright source. A filament in tungsten is heated by applying a high voltage (up to 100–200 kV), a thermionic emission current density is then produced. Electrons emitted are accelerated towards the anode (generally grounded) and transmitted to an electromagnetic condenser lens to be focused parallel for illuminating the sample. The electron beam passes through the specimen (thin enough to let the electron reach the other side of the microscope, usually less than 100 nm thick), some of them interact with materials constituting the sample and other are transmitted to a second lens system. Finally, an image can be visualized on a fluorescent screen or even with a camera allowing data processing via a computer.

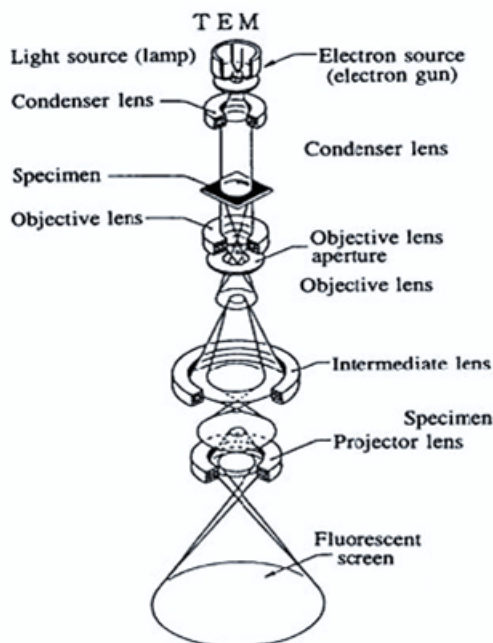


Figure 4.6: Schematic drawing of the operating principle of a transmission Electron Microscope (Taken from the JEOL 2000FX handbook).

A vacuum system is installed on the microscope to increase the electron mean free path like in XPS, as mentioned in section 4.1. A rotary vane pump operates in the introduction lock to transfer samples in and out of the device. Operations in the microscope are realized at a high vacuum level which is reached by a turbo-molecular pump.

In the present study, two electron microscopes were used (FEI Tecnai 10 and Tecnai Osiris) for imaging the NP formation on the carbon substrates. The Tecnai Osiris is equipped with an EDX (Energy Dispersive X-ray, allowing a chemical analysis) and can provide TEM images as well as STEM (Scanning Transmission Electron Microscope, see below for further information) images. The Morphology and Imaging (MORPH-IM) platform, and SERMA Technologies are acknowledged for the TEM/STEM images acquisition and EDX measurements presented in this work.

4.3.1 Scanning transmission electron microscopy

As mentioned above, a STEM was also employed to acquire images of the samples. The principle of the technique is similar to the one presented for the conventional TEM, an electron beam passes through the sample and interact with it. However, in the case of a STEM analysis, the electron beam does not

illuminate the whole specimen analyzed but is focused in a fine spot with a typical size comprised between 0.05 to 0.2 nm [187]. The electron beam then scans the surface of the sample and scattered electrons are collected. The image formation is performed taking into account the direction of the incoming scattered electrons hitting the detector as a function of the probe position [188]. Going further, it was shown that the STEM technique is highly sensitive to the atomic Z number of the elements present in the sample [188]. This is particularly visible when using the dark field mode in which brighter spots correspond to higher atomic Z number elements. Therefore, STEM analyses allow to highlight areas with heavier elements. This will be shown in the present thesis in chapters 6 and 7.

4.3.2 Energy dispersive X-ray analysis

Electrons are not the only information that could be gathered during a STEM analysis. The interaction between the electron beam and the surface atoms of the sample could also result in the ejection of inner shell electrons. Therefore, X-rays can be emitted with wavelengths characteristic of the atomic structure of the excited elements [189]. Analysis of the X-ray energies can be performed by using an energy dispersive detector. This is to the so-called "Energy dispersive X-ray" (EDX) analysis which allows to derive an elemental compositions of the sample. In this work, the EDX spectroscopy was employed to characterized the chemical environment of bimetallic Pt-Ni/C nanocomposites (see chapter 7).

4.4 Optical emission spectroscopy

One of the most convenient and useful method to bring diagnostics on low-pressure plasmas is the optical emission spectroscopy (OES) since it does not require any physical contact with the plasma [190–193]. Moreover, OES only needs an optical fiber to transport the light information, a spectrometer covering wavelengths from the UV to near-IR regions ($\sim 200\text{--}900$ nm) to collect it and a dedicated program to visualize spectra.

When atoms or molecules are excited by collisions with electrons in the plasma, they can release their excess in energy by emitting light resulting in electronic transitions between two energy levels. The spectral lines produced are characteristic of the atoms or molecules involved in the process. By analyzing these spectral lines and their evolution, elements present in the plasma can be determined, the decomposition of organometallic precursors followed [167], or the E-H transition highlighted [136]. In chapter 6, the decomposition of the nickel precursor is discussed; and in chapter 8, the E-H transition is shown in the case of nitrogen- and ammonia-based plasmas for nitrogen functionalization of carbon supports. In the present thesis, the OES spectra were recorded by using an Ocean Optics USB4000-XR spectrometer. The numerical aperture of the single-strand optical

fiber carrying the signal is about 0.22. The processing of the different spectra was then performed with the SpectraSuite software.

ICP-OES operating principle

The last point to note is the use of the ICP-OES method to quantify the metal loading in the samples treated by low-pressure plasma discharge. This is particularly important for the calibration of the catalytic activity curves (see section 7.5).

The sample preparation was realized at the LISE research unit of the University of Namur. The complete methodology employed to produce a solution with a fixed metal concentration was performed as follows :

- A solution of aqua regia, *i.e.* an acidic solution made of nitric (HNO_3) and hydrochloric (HCl) acids in a molar ratio of 1:3, were prepared to dissolve the nanoparticles. The ultrapure nitric and hydrochloric acids having concentrations of 65 wt.% and 37 wt.% respectively, it was needed to dilute the solutions with ultrapure Milli-Q water to reach a maximum concentration of 5 wt.% to avoid the degradation of the device during the ICP-OES measurements.
- A fixed amount of the sample is taken and mixed with a calculated volume of aqua regia to obtain a final solution with a fixed metal concentration.
- The solution is then put under stirring conditions and heated to 50 C for at least three days to ensure a complete dissolution of the metallic NPs.
- Afterwards, the sample is centrifuged during 20 minutes at 4000 rpm to separate the carbon support from the concentrated solution.

Finally, the solution is injected in an Ar plasma, vaporized and ionized. The injection is performed by a nebulizer in order to obtain a fine aerosol. Light emitted due to the deexcitation of atoms to their fundamental energy state is analyzed by a spectrometer as explained above. The intensity of spectral lines is compared to standard samples and leads to the quantification of the metal loading. Standards were prepared by diluting stock solutions with ultrapure Milli-Q water.

4.5 Electrochemical methods

The electrochemical measurements have been performed within the Department of Chemical Engineering - Nanomaterials, Catalysis, Electrochemistry (NCE) at the University of Liège. A three-electrode cell has been used allowing measurements of the activity for the Oxygen Reduction Reaction (ORR) and the CO stripping voltammetry [194]. A brief overview of the measurement principles is debated in this section.

4.5.1 Oxygen Reduction Reaction

As explained in section 1.3.3, ORR occurs with very slow kinetics. Catalysts are required to faster the chemical reaction, higher ORR kinetics are needed in fuel cells and are intensively investigated in PEMFC researches [42,43]. It is therefore critical to measure the activity of that reaction in order to evaluate the usefulness of the NPs fabricated by low-pressure plasma discharges.

The rotating disk electrode methodology has been used for measuring the ORR activity. A catalyst layer is placed on a glassy carbon disk and immersed in an O_2 -saturated electrolyte solution. The working electrode is rotated at a fixed speed while its potential is decreased linearly and the oxygen reduction current is monitored. The rotation of the disk allows to create a stable and laminar flow of reactant towards the rotating disk on which the catalyst layer is placed (Figure 4.7); the rotation speed directly influence the study of the reaction kinetics. ORR voltammograms are then recorded at different rotation speeds and corrected by the mass-transport limitations.

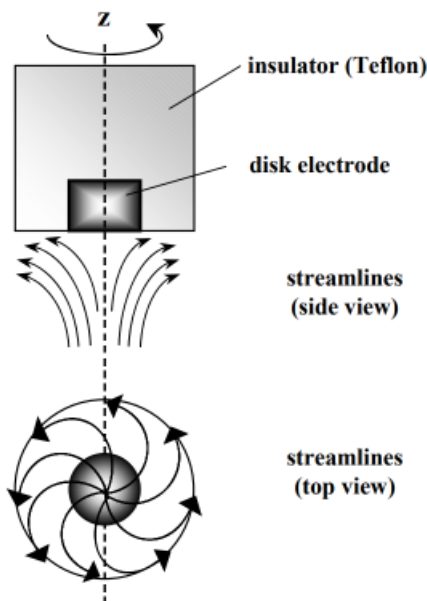


Figure 4.7: Sketch of the rotating disk electrode method, with the streamlines generated by the rotation, employed for the ORR activity measurements (Taken from [195]).

The ORR activity is finally determined by calculating the kinetic current and the so-called Tafel plot is drawn, *i.e.* potential as a function of the kinetic current.

The best catalyst exhibits a higher kinetic current in comparison to others at a fixed potential. However, information are often related to the slope of the curve which indicates if the reaction rate is strongly affected or not by changes of the applied potential.

4.5.2 CO stripping voltammetry

The CO stripping voltammetry was used to highlight the effect of a non-reversible reaction on the catalysts, the CO electro-oxidation. Carbon monoxide has a "poisoning" effect in fuel cells, they attach on the catalyst surface which decrease the number of sites available for the hydrogen reaction [196, 197]. Numerous researches have been realized to increase the CO-tolerance and are still ongoing [198, 199]. Since the NPs fabricated by plasma discharges could be potential catalysts in PEMFCs, it is mandatory to control their CO-tolerance.

The principle of the measurement consists in immersing the catalyst layer in the electrolyte solution of a three-electrode cell. Carbon monoxide is then bubbled on the surface of the sample while the working electrode is kept at a fixed potential until the surface of the catalyst has been completely covered by CO molecules. Afterwards, the excess of CO is dissolved by bubbling Ar in the solution.

The potential of the working electrode is then increased linearly leading to the electro-oxidation of the adsorbed CO molecules. This step produces electrons passing through an electric circuit which induces an electric current. The latter is recorded as a function of the working electrode potential, this is the so-called CO stripping voltammogram. Several voltammograms are recorded by sweeping the working electrode potential between two values.

When the potential is high enough, CO electro-oxidation occurs at the surface of the catalyst and a peak in current appears in the voltammogram. The main information can be extracted from the area under the current peak which is proportional to the electroactive surface area of the catalyst NP.

Recently, it was shown that the catalytic activity measured by CO stripping voltammetry depends on the size of the nanoparticles as well on the presence of agglomerates and grain boundaries [72, 200, 201]. Figure 4.8 illustrates such a dependency in a CO stripping voltammogram.

4.6 Nitrogen adsorption-desorption method

In 1918, Irving Langmuir developed a theory to calculate the coverage of the surface of a solid substrate through the adsorption of a gas molecule monolayer,

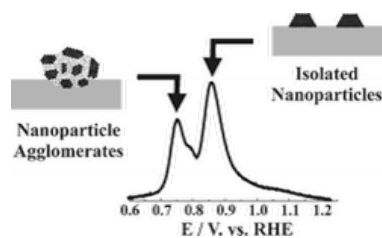


Figure 4.8: Size effect in a CO stripping voltammogram. Positions of current peaks provide information on the size distribution of the catalysts (Taken from [200]).

also called adsorbate, depending on the gas pressure at a given temperature [123] :

$$\Theta = \frac{\alpha P}{1 + \alpha P} \quad (4.7)$$

with Θ the fractional cover of the surface, P the gas pressure and α a constant.

Several assumptions were made to lead to Equation 4.7. Usually, nitrogen or argon is used as an adsorbate and the adsorption energy is considered equal for all the sites at the surface. Those sites are defined as the areas where the molecules are able to be adsorbed and only one molecule can occupy each site. Finally, the adsorption process at one site is completely independent of the one occurring at neighboring sites. Nevertheless, the Langmuir theory is too simple and flaws have been pointed out. In 1939, the Brunauer-Emmett-Teller (BET) theory was developed to extend the latter to multilayer adsorption [202]. In this case, gas molecules are able to be adsorbed and form a non-finite number of layers which are assumed to not interact with each others.

The principle of the adsorption-desorption measurement is based on the amount of molecules adsorbed on the surface of the material exposed to the gas. The most common gas employed is nitrogen due to an easily achieved high purity and relatively strong interaction with various materials. The sample is kept at a constant temperature, typically at the nitrogen boiling temperature (77 K), under vacuum. A gas valve is opened to let the molecules interact with the sample and begin to be physisorbed at its surface; such a process is described in Figure 4.9. The surface coverage increases as the pressure in the sample holder is increased leading first to a monolayer. Adsorption of gas molecules continues with higher pressure to reach a multilayer adsorbate onto the surface of the material. At a certain point, no adsorption can occur due to saturation; the sample pores are completely filled with gas molecules. The next step of the method consists in removing the sample from the N_2 atmosphere, placing it in a heated environment

to desorb the nitrogen from the surface and quantify the released molecules. It results in an isotherm on which the amount of gas adsorbed is plotted as a function of the relative pressure applied during the experiment by using the BET theory (Figure 4.10).

Multilayer formation

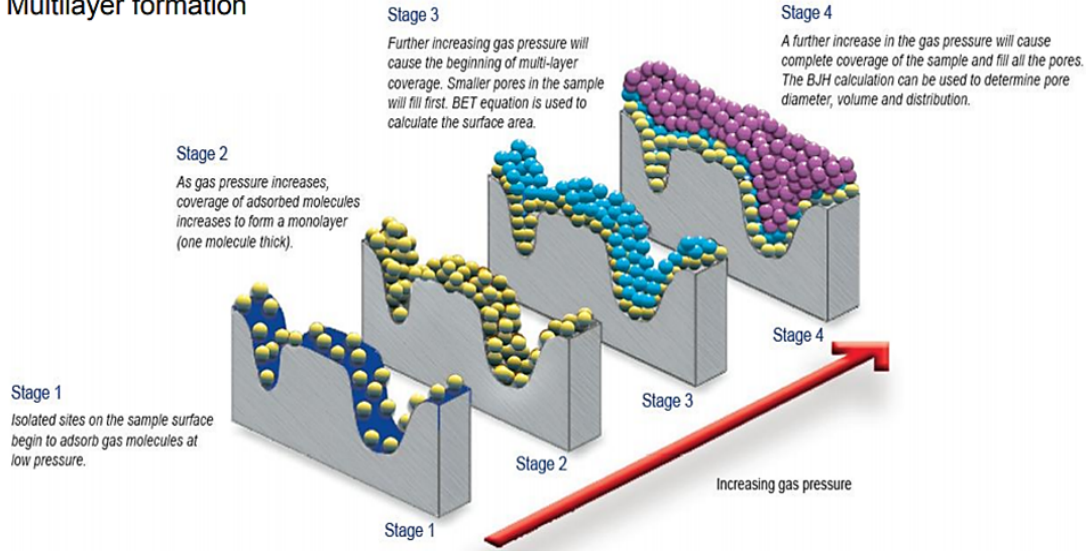


Figure 4.9: Sketch of the BET methodology employed to measure the specific area and the porosity of various materials (Taken from [203]).

Calculation of the specific surface area and the porosity are based on the BET equation [202] :

$$\frac{P}{V_a(P_0 - P)} = \frac{1}{V_m C} + \frac{(C - 1) P}{V_m C P_0} \quad (4.8)$$

where P is the equilibrium pressure, P_0 is the saturation pressure, V_a is the weight of gas adsorbed, V_m is the weight of an adsorbate monolayer and C is the BET constant. Equation 4.8 is linear within a range of relative pressure and allows the measurement of V_m by determining the intercept and slope of the latter. Therefore, the total surface area (TSA) can be deduced from the following equation :

$$\text{TSA} = \frac{V_m N}{M} A_{acs} \quad (4.9)$$

where N is the Avogadro number, M is the molecular weight of adsorbate and A_{acs} is the adsorbate cross sectional area (*i.e.* effective size area of the adsorbate molecule).

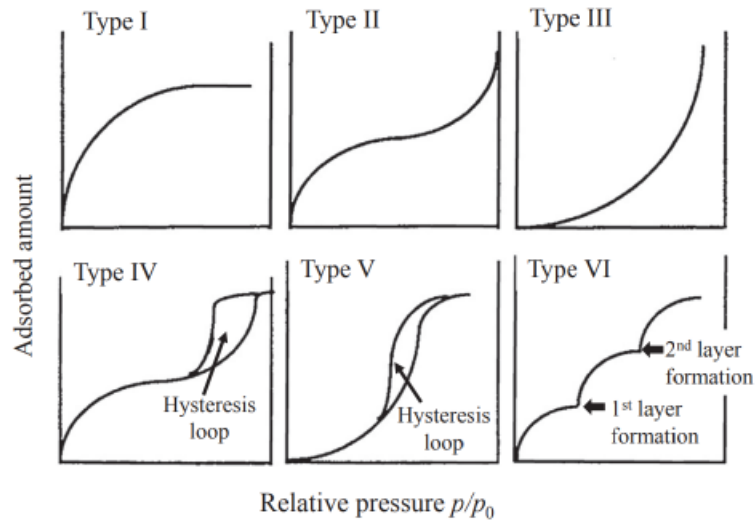


Figure 4.10: Illustration of the different isotherm curves obtained after a gas adsorption-desorption experiment. Mesoporous carbon are usually characterized by Type IV isotherms (Taken from [204]).

Finally, the specific surface area (SSA) is derived from Equation 4.9 :

$$\text{SSA} = \frac{\text{SA}}{w} \quad (4.10)$$

with w the sample weight.

The pore texture (pore volume, pore size distribution, etc.) of the materials can also be derived from the adsorption or desorption of adsorbates at the surface; if the material is mesoporous, an hysteresis in the isotherm plot appears which can be exploited to get information on the pores (Figure 4.10). The determination of the pore size distribution is performed thanks to the Barrett, Joyner and Halenda (BJH) theory which uses the Kelvin model of pore filling [205]. Put simply, geometrical properties of the porous material are related to the thermodynamical data obtained for the nitrogen adsorption-desorption measurements. The total pore volume is determined by using the Kelvin equation :

$$r_k = \frac{2V_m \sigma \cos \theta}{RT \ln (P/P_0)} \quad (4.11)$$

with r_k the radius of curvature of the condensed adsorbates in the pore, V_m the molar gas volume of an ideal gas, σ the surface tension, θ the contact angle, P the equilibrium pressure and P_0 the saturation pressure.

The BJH theory assumes that the pores have a cylindrical shape and a correction to the radius is applied taking into account the thickness of the adsorbed film t_a which is evaluated considering a given theory; this correction is due to condensation that occurs after the formation of an adsorbed layer at the surface of the pore walls. The cylindrical pore radius is thus given thanks to the following equation :

$$r_p = r_k + t_a \quad (4.12)$$

Figure 4.11 illustrates the model employed to calculate the pore radius r_p . This model is useful to derive the pore size distribution and pore volume for a given pore geometry. However, the pore shape is often more complex.

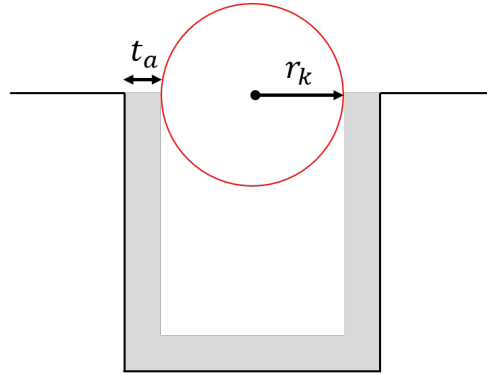


Figure 4.11: Schematic drawing of a cylindrical pore usually considered in the BJH theory to calculate the pore characteristics.

The minimum size that could be measured through the BJH theory is related to the size of the adsorbate which is about 0.4 nm for nitrogen while the maximum size measurable is about 300 nm due to difficulty in the determination of the total amount of gas that has been adsorbed at high pressure [206].

Chapter 5

Advances in the fabrication of Pt nanoparticles supported on carbon substrates

5.1 Introduction

A few years ago, Laurent-Brocq *et al.* [164] demonstrated the fabrication of Pt NPs supported on CB by low-pressure RF-ICP treatments. It was shown that the novel approach employed was efficient to synthesize NPs on a carbon support which could be used in applications such as PEMFCs. The methodology is fast, easy, solvent-free and no high temperature treatment is required. However, as discussed in section 1.4, other mesoporous carbon supports with better characteristics (high surface areas, stability, resistance to corrosion, etc.) have been investigated. Thus, in the present chapter, further studies were performed to create Pt NPs on CXGs and GNPs. The impact of the metal precursor on the NP synthesis was also studied; two OM and one inorganic precursors were used. The main purpose in using two OM precursors relies on the important difference in their melting point. Therefore, an additional parameter can be taken into account and is particularly interesting for the synthesis of metallic NPs. Moreover, the chemical and thermal actions taking place during a dry plasma treatment are better understood, especially the strong interaction between them. Indeed, the decomposition of the metal precursors is mainly due to thermal effects, while the chemical actions impact the NP oxidation state and carbon functionalization [164]. The fundamental mechanisms involved in the synthesis of particles and their understanding are thus at the heart of this study. Controlling the way precursors are decomposed, the formation of NPs and their agglomeration is essential to synthesize sustainable materials used in various applications among which catalysis. Some plasma parameters are also investigated by varying the treatment time, plasma chemistry and power. Section 5.2 is dedicated to the impact of the metal precursor on the synthesis of Pt NPs supported on CXGs, while the formation of

Pt nanocatalysts on GNPs is discussed in section 5.3. Finally, a pretreatment of GNPs was performed by using a nitrogen-based plasma and its effect is debated in section 5.3.3. Especially, a study on the effect of the defects induced by the plasma on the graphene sheets was investigated.

Thus, this work aims to have a better understanding and control over the nucleation, growth and agglomeration of metallic NPs to reach a high coverage and uniformly dispersed materials with a desired size distribution and morphology at the surface of the carbon substrate. The author of this thesis contributed to (1) the sample production of Pt/C nanocatalysts on CXGs and GNPs, and (2) the acquisition and interpretation of several XPS spectra, TEM images and XRD diffractograms.

5.2 Synthesis of Pt/xerogel nanoparticles by using different metal precursors

The first point developed in the present chapter is the impact of the metal precursor with different characteristics, namely their melting point and the chemical functions attached to the metallic part in the molecules, on the synthesis of Pt/C NPs. Three different precursors were employed; two OM precursors, *i.e.* Pt(II) acetylacetonate ($\text{Pt}(\text{acac})_2$, $\text{C}_{10}\text{H}_{14}\text{O}_4\text{Pt}$, 99.99%; Strem Chemicals) and (1,5)-cyclooctadiene dimethylplatinum(II) ($\text{Pt}(\text{cod})(\text{Me})_2$, $\text{C}_{10}\text{H}_{18}\text{Pt}$, 97%; Sigma Aldrich), and an inorganic precursor, *i.e.* hydrogen hexahydroxyplatinate(IV) (Platinic acid, $\text{H}_2\text{Pt}(\text{OH})_6$, 99.9%, Sigma Aldrich). Their molecular structures are represented in Figure 5.1. The main characteristics of these metallic precursors are presented in Table 3.1.

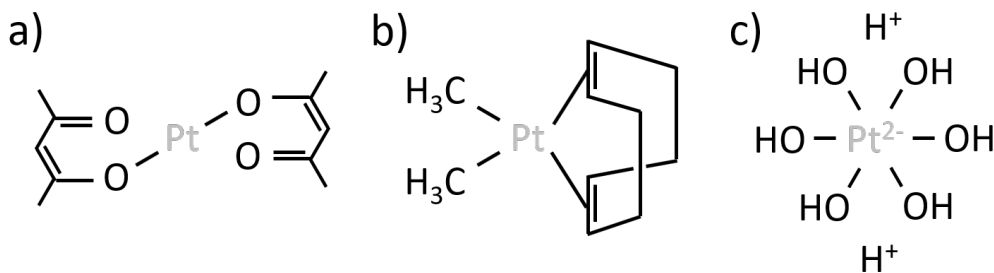


Figure 5.1: Molecular structure of a) Pt(II) acetylacetonate, b) (1,5)-cyclooctadiene dimethylplatinum(II) and c) hydrogen hexahydroxyplatinate(IV).

A CXG was used as a support for the fabricated NPs, and is characterized by an average pore size of 60–70 nm and a BET surface area determined by N_2 adsorption

of $660 \text{ m}^2 \text{ g}^{-1}$. The carbon matrix was produced following the method described in ref. [95] by the Department of Chemical Engineering - Nanomaterials, Catalysis, Electrochemistry (NCE) at the University of Liège. The methodology employed for the preparation and fabrication of Pt/xerogel nanocatalysts is described in section 3.3. It starts by mixing a fixed amount of metallic precursor with the CXG in order to reach a metal loading of 20 wt.%. Afterwards, the reactants are placed in a vacuum chamber which is pumped down by using a rotary valve pump allowing to reach a pressure down to $\sim 10^{-3}$ mbar. Oxygen or argon is then injected with a fixed flux in the plasma reactor. Afterwards, the reactants are treated under stirring conditions by applying a plasma discharge to synthesize the Pt/xerogel particles.

The plasma conditions have been adapted and optimized for each precursor in order to decompose the metal-containing molecule and then form NPs. For the rest of this chapter, the Pt(II) acetylacetonate and the (1,5)-cyclooctadiene dimethylplatinum(II) precursors are denoted as "OM1" and "OM2", respectively, while the amorphous hydrogen hexahydroxyplatinate(IV) is denoted as "AM". The different employed parameters are reported in Table 5.1. The effect of the plasma chemistry has been investigated with an O_2 or "mixed" O_2/Ar treatments at a transmitted power of 100 W (continuous) or 150 W (pulsed with a duty cycle of 50% at a frequency of 10 Hz). At this point, it is important to note that pulsed plasmas were not sufficiently efficient to properly decompose the OM1 precursor. Thus, in that case, the study was focused on the use of continuous plasma only in order to decompose the metal precursor.

Systematic XRD analyses were performed to monitor the OM precursors decomposition; both are in a crystalline form and present characteristic peaks in the diffractograms which disappear after an optimized plasma treatment. The formation of crystalline domains was also controlled through the analysis of the diffractograms. The amorphous precursor does not exhibit peaks in the diffractogram, thus its decomposition after the plasma treatment is more difficult to evaluate. However, the production of crystalline NPs in this case still can be checked by analyzing the data acquired from the XRD experiments. Complementary bright-field TEM images acquisitions have been performed to determine the morphology of the fabricated NPs and their dispersion on the carbon support. Moreover, evaluation of the NP agglomeration was realized in each case. Finally, the chemical composition of the fabricated NPs and the carbon functionalization were inspected by XPS.

	Plasma	Type	Flux (sccm)	Time (min.)
Pt(acac)₂				
OM1-1	O ₂ , 100 W	continuous	5	10
OM1-2	O ₂ , 100 W	continuous	5	5
	Ar, 100 W	continuous	5	10
OM1-3	Ar, 100 W	continuous	5	5
	O ₂ , 100 W	continuous	5	10
Pt(cod)(Me)₂				
OM2-1	O ₂ , 100 W	continuous	5	20
OM2-2	O ₂ , 150 W	pulsed	5	10
OM2-3	Ar, 100 W	continuous	5	10
	O ₂ , 100 W	continuous	5	10
OM2-4	Ar, 100 W	continuous	5	15
	O ₂ , 100 W	continuous	5	10
Platinic acid				
AM-1	O ₂ , 150 W	pulsed	5	20
AM-2	Ar, 100 W	continuous	5	10
	O ₂ , 150 W	pulsed	5	15

Table 5.1: Plasma conditions explored for the decomposition of the different metallic precursor and the formation of Pt particles supported on carbon xerogel from a reactant mixture with a metal loading of 20 wt.%. In some cases, two lines are indicated and give the plasma discharge conditions of two successive treatments applied without bringing back the plasma reactor to the atmosphere.

5.2.1 Decomposition of the metal precursors by one-step plasma treatments

The decomposition of the OM1 and OM2 crystalline precursors was checked by XRD and their diffractograms are shown in Figure 5.2. Three peaks located at 39.8, 46.3 and 67.5° are present and attributed to (111), (200) and (220) face-centered cubic Pt crystalline NPs, respectively [207]. Moreover, the signal from the precursor is still visible on the diffractograms for OM1 (Figure 5.2(a)). This indicates an incomplete decomposition of the precursor under the explored plasma conditions. A fit of the peaks induced by crystalline Pt NPs has been performed by using a Pearson VII profile in order to determine their full width at half maximum (FWHM); the Debye-Scherrer formula (Equation (4.5)) allows then to calculate

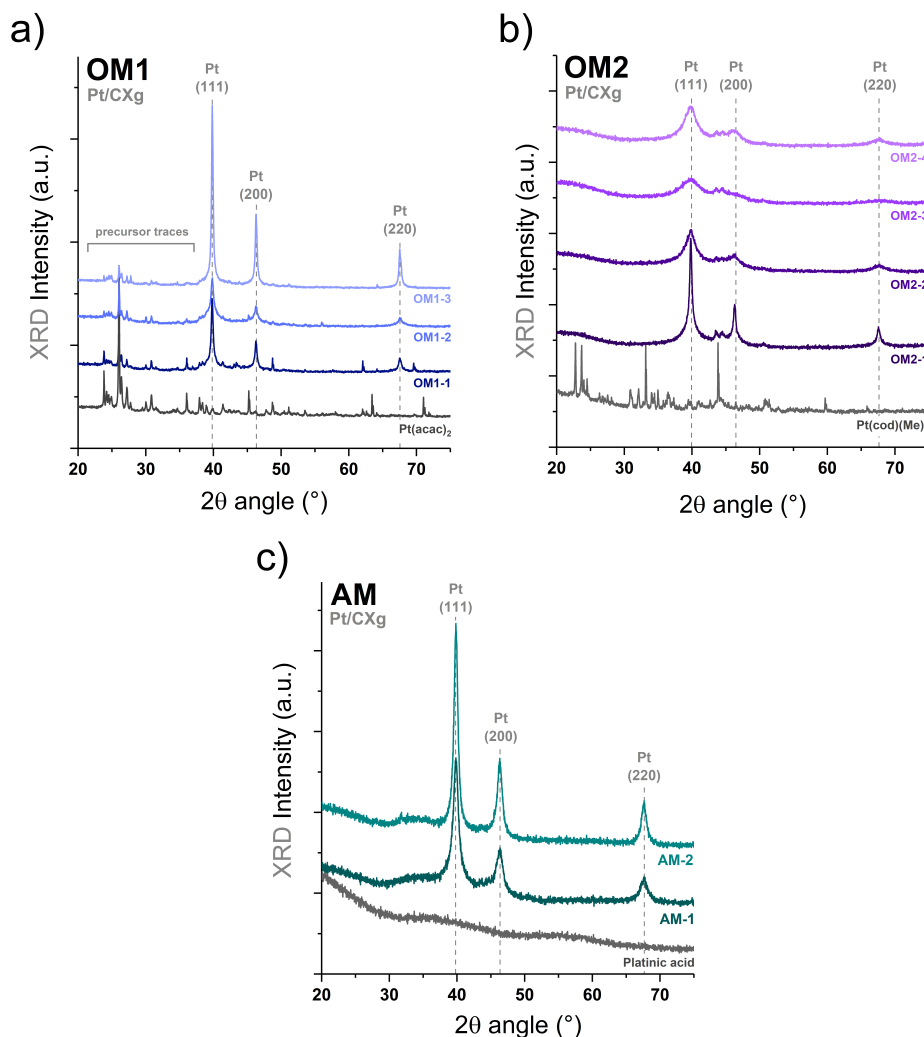


Figure 5.2: XRD diffractograms of the pristine powder and after the different plasma treatments for a) the Pt(II) acetylacetonate (OM1) and b) (1,5-Cyclooctadiene) dimethylplatinum(II) (OM2) and the hydrogen hexahydroxyplatinate (IV) (AM) precursors.

the average size of the Pt NPs. Interestingly, for the OM1 precursor, the mean sizes of the particles are 22.9 ± 2.8 , 11.5 ± 1.6 and 29.2 ± 3.9 nm for OM1-1, OM1-2 and OM1-3, respectively. Those particularly large crystalline domains sizes could indicate an important aggregation of the Pt particles at the surface of the xerogel. The analysis of TEM images could corroborate this result. For the plasma treatments of the OM2 precursor, analysis of the diffractograms in Figure 5.2(b) indicates that the mean sizes distribution are lower than the OM1 results. Typically, the average domains sizes are 13.7 ± 1.5 , 4.9 ± 0.4 , 2.2 ± 0.4 and 5.3 ± 0.3 nm for OM2-1, OM2-2, OM2-3 and OM2-4, respectively. Therefore, it seems that

relatively long oxygen-based plasma treatments at 100 W lead to Pt agglomeration while this phenomenon can be avoided or reduced with pulsed O₂ or "mixed" Ar/O₂ plasma discharges. At this point, the hypothesis proposed is the decrease of the maximal temperature reached during the "mixed" plasma treatments which limits the mobility of the Pt atoms. Thus, coalescence of the NPs is decreased. However, it is not easy to measure the temperature during the treatments. As discussed in section 2.2, electrons have a higher temperature in comparison with ions and neutral species. Therefore, the concept of temperature is not unique in cold plasmas and an average energy should be used instead. Several attempts were done to measure this parameter with a thermocouple sensor but without any success. Nevertheless, the glass Petri box seemed to be less warm when removing it from the vacuum chamber directly after the "mixed" Ar/O₂ plasma treatment in comparison with the O₂ one. Further experiments should be conducted to measure the temperature reached during the treatments and confirm this hypothesis mentioned above.

For the inorganic AM precursor, the diffractograms unambiguously show peaks attributed to crystalline Pt particles (Figure 5.2(c)) and, from the two explored plasma conditions, the mean particle size vary from 8.5 ± 1.5 to 12 ± 1.5 nm for AM-1 and AM-2, respectively. As mentioned above, the AM precursor is not crystalline and does not exhibit peaks in the diffractogram. Therefore, it is difficult to state on the complete degradation of the precursor after the different plasma treatments. However, from the analysis performed by XRD and the derived average NP sizes, it seems most likely that agglomeration of particles occurred, which has to be confirmed by the TEM images.

5.2.2 On the agglomeration of the nanoparticles through a morphology study

The XRD analysis were completed by a study on the morphology of the fabricated Pt/CXG NPs. TEM image acquisitions were performed to corroborate the results discussed in section 5.2.1. Prior to TEM analyses, the samples were prepared as follows : (i) a fixed amount of powder was mixed with a volume of isopropanol and sonicated during at least 10 minutes to obtain homogeneously dispersed Pt/C catalysts in the solution, (ii) a droplet of the latter was then taken and deposited on a TEM grid. Afterwards, the sample was placed in the microscope and images were acquired by using an acceleration potential of 80 kV. The average NP sizes have been derived from the analysis of the TEM images by using the ImageJ processing software. The TEM images confirm the formation of NPs on the surface of the carbon matrix after the plasma treatment of the different precursors employed in this study, as seen in Figure 5.3. Complementary TEM images of the samples are presented in appendix A.

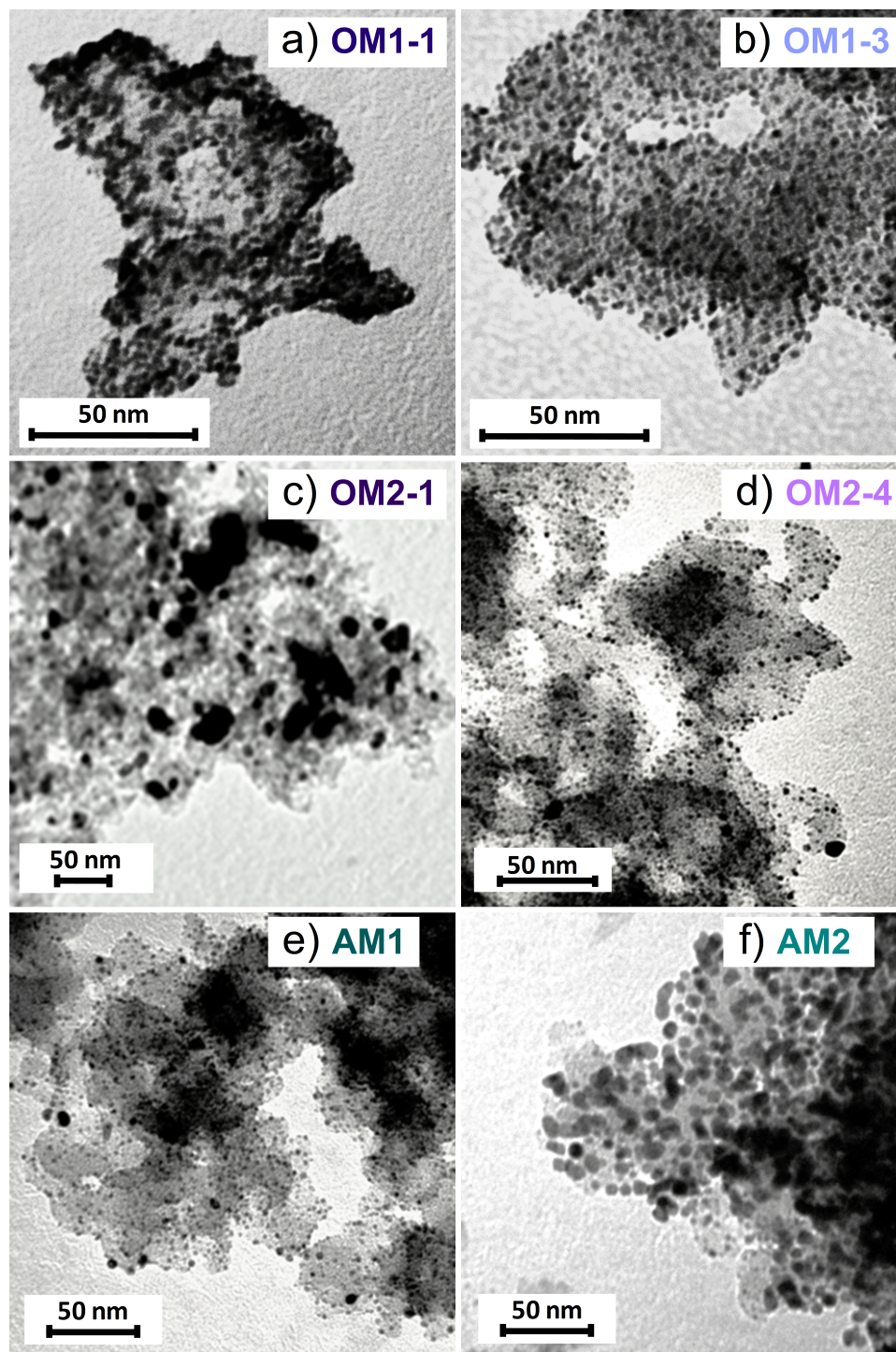


Figure 5.3: TEM images of the O₂ plasma treated samples (OM1-1 (a), OM2-1 (c) and AM1 (e)) or "mixed" Ar/O₂ plasma treatments (OM1-3 (b), OM2-4 (d) and AM2 (f)).

The NP formation after the treatment of the OM1 precursor for the O₂ and "mixed" Ar/O₂ plasma discharges at a transmitted power of 100 W are shown in Figure 5.3(a) and (b), respectively. Both treatments clearly show agglomeration of particles which could support the results found with the XRD analysis. Moreover, the coverage of NPs at the surface is not uniform (Figure 5.3(a)). Therefore, it was not easily possible to derive an average size due to the presence of too many interconnected domains. This could be due to the high-energy (continuous) treatment conditions which are not optimized to completely decompose the precursor and prevent the growth of particles. This is in agreement with the hypothesis of a higher mobility of the Pt atoms which results in the coalescence of the NPs. In order to complete the decomposition, longer treatments or an increased plasma power should be applied. However, these highly energetic conditions tend to damage the carbon support which modifies its physico-chemical properties [208]. For that reason, the plasma conditions were limited to low power to avoid as much as possible such a negative impact on the support. For the "mixed" Ar/O₂ plasma treatment, the coverage seems to be more uniform (Figure 5.3(b)). Besides that, excluding the large domains, average sizes of the NPs are similar regarding the different explored conditions (3.9 ± 0.5 , 3.6 ± 0.5 and 3.8 ± 0.3 nm for OM1-1, OM1-2 and OM1-3).

For the OM2 treatments, TEM images of the OM2-1 and OM2-4 are shown in Figure 5.3(c) and (d), respectively. In both cases, NPs are non-homogeneously dispersed on the carbon support. Moreover, a few agglomeration of particles is clearly visible with the presence of grain boundaries or larger domains which are believed to correspond to melted Pt (Figure 5.3(c,d)). Interestingly, the average NP sizes derived from the TEM images between the two plasma conditions are similar with average sizes of 4.3 ± 0.6 and 3.2 ± 0.3 nm for OM2-1 and OM2-4. In comparison with the XRD analysis, the average NP size of the OM2-1 sample deviates significantly. Nevertheless, the TEM image analyses confirm the presence of large domains which are believed to be in a crystalline form and contribute to the narrowing of the XRD peaks.

Finally, for the AM precursor treatments, the morphology analysis indicates the formation of non-homogeneously dispersed NPs at the surface of the carbon support as well as some agglomeration or interconnected domains which are more visible for the AM-2 plasma treated sample (Figure 5.3(e,f)). The average sizes derived from the TEM images are 2.3 ± 0.6 and 4.7 ± 0.6 nm (AM-1 and AM-2, respectively). From the XRD pattern (Figure 5.2), the same conclusions as presented for the OM1 are found; the XRD average size are systematically overestimated and are believed to be due to large crystalline domains.

5.2.3 Chemical analysis of the fabricated Pt/xerogel nanoparticles

The chemical composition of the nanocatalysts formed during the plasma treatments were investigated by XPS measurements. For each explored plasma conditions, the spot size was fixed at 300 μm , including survey and high-resolution spectra acquired with a pass energy of 200 and 30 eV, respectively. The global composition is given in Appendix B and will not be discussed here. Indeed, the carbon and oxygen functionalizations do not change significantly with the different plasma conditions. Thus, this work is focused on the analysis of the Pt 4f spectra. In the present section, the oxidation states of the Pt NPs formed from the plasma treatment of the three precursors are presented, as seen in Figure 5.4. The high-resolution Pt 4f spectra were fitted using four spin-orbit coupling doublets (Pt 4f_{7/2} and Pt 4f_{5/2}). The intensity ratio between the two peaks in a doublet was kept constant at 0.77, which is close to the theoretical ratio of 0.75 [177]. The BE difference between the four components was constrained following the values reported in the literature; the peaks were centered at 71.2 \pm 0.3, 72.4 \pm 0.3, 74.0 \pm 0.3 and 74.9 \pm 0.3 eV BEs (Pt 4f_{7/2}), and were attributed to metallic Pt, Pt(OH)₂, PtO and PtO₂, respectively [209, 210]. For the metallic component, an asymmetrical shape was fitted in agreement with the literature [211]; the fitting parameters were determined thanks to an XPS analysis of a reference Pt electrode : the tail mix, tail height and tail exponent were fixed at 16.14%, 0.0% and 0.1157, respectively (see Appendix C for more details). The quantification of the Pt amount, which were derived from the peak area analysis of the high-resolution C 1s, O 1s and Pt 4f spectra, was performed for all treatment conditions.

For the OM1 precursor, NPs fabricated by O₂ and O₂/Ar plasma discharges at 100 W are strongly oxidized with a relative percentage of metallic Pt which does not exceed 50% while the Ar/O₂ treatment allows to form more metallic particles (up to 60% of the Pt content, Figure 5.4(c,d)). According to the reference OM1 XPS Pt 4f spectra (Figure 5.5), it is believed that the signals at 72.4, 74.0 and 74.9 eV BEs are due to both residual fragments and oxides. Surprisingly, the "mixed" Ar/O₂ treatment allows a better Pt reduction in comparison with the two other treatments. It is expected that the Ar plasma could not lead to the reduction of the metal and only allows to partially degrade the precursor and form small NPs which act as germination sites. Afterwards, the NPs are able to grow and are reduced during the O₂ plasma. In the case of the OM1-1 and OM1-2 samples, O₂ plasmas only are not able to efficiently decompose the precursor, which is visible on the diffractograms (Figure 5.2(a)), and the Ar plasma not suitable for the NP growth probably due to the lack of chemical interactions.

Regarding the plasma treatments of OM2, the same four components were fitted on the HR-XPS Pt 4f spectra, as seen in Figure 5.4(c). Even if the signal

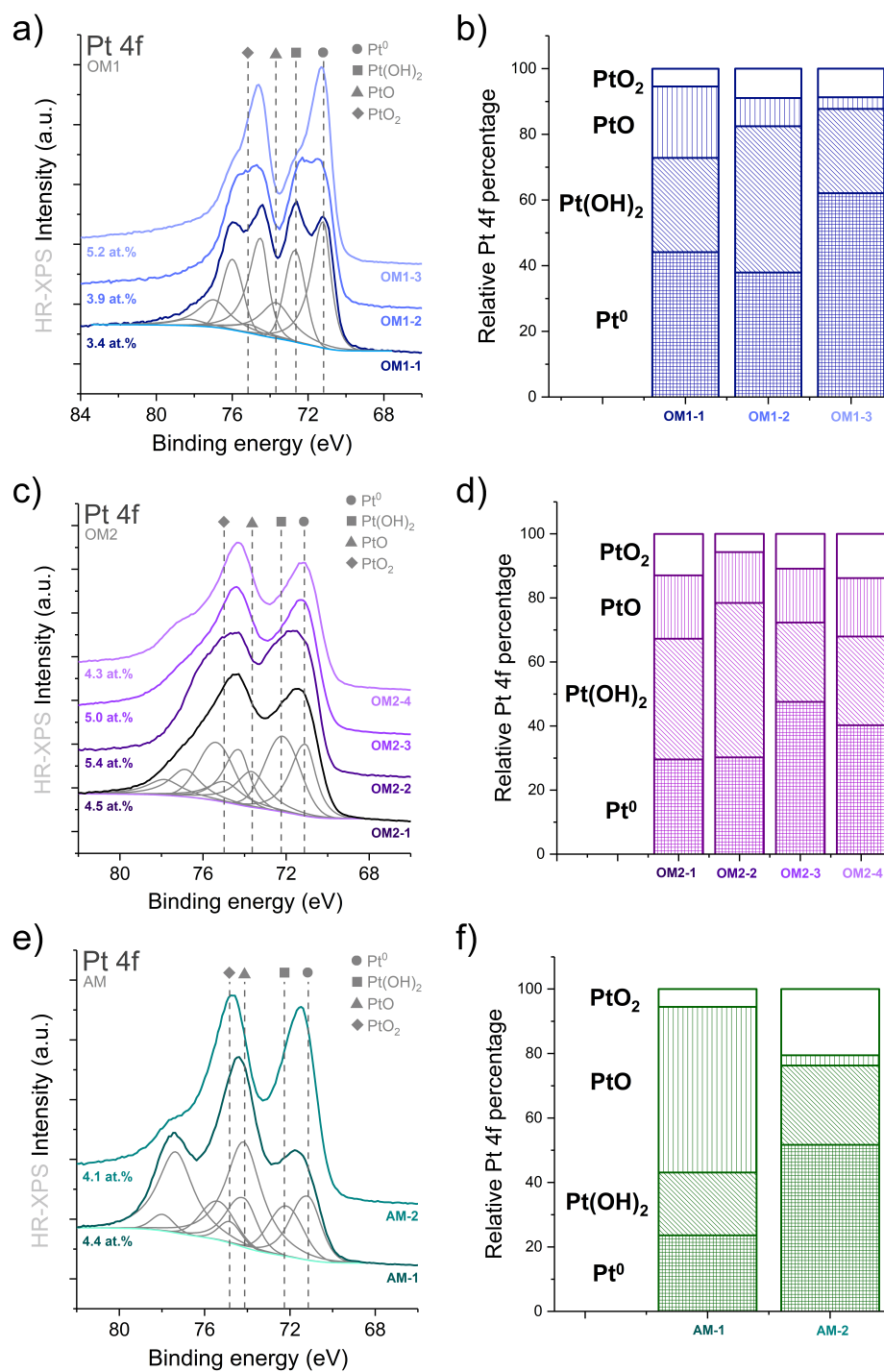


Figure 5.4: High-resolution Pt 4f XPS spectra of the plasma treated sample using the three metallic precursor (a,c,e) with their corresponding oxidation states relative percentages (b,d,f).

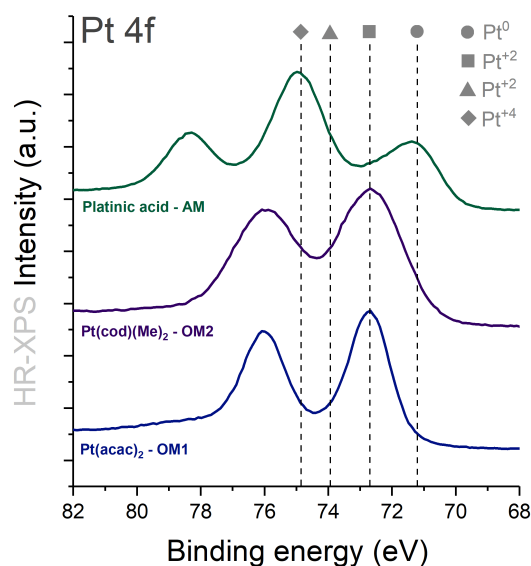


Figure 5.5: High-resolution XPS Pt 4f core level spectra of the organometallic ($\text{Pt}(\text{acac})_2$ and $\text{Pt}(\text{cod})(\text{Me})_2$) and the inorganic precursors (platinic acid), respectively.

characteristic of the crystalline precursor fully disappeared in the diffractograms after a low-energy O_2 plasma (pulsed at 100 W, Figure 5.2(b)), the Pt content in the samples stays relatively low (from 4.5 up to 5.4 at.%). Moreover, the relative percentage of Pt^0 does not exceed 50% (Figure 5.4(d)); this suggests a complete decomposition of the precursor but not completely used for the nucleation of metallic Pt NPs. It is important to note that the precursor does not contain oxygen groups and only show a major component at 72.4 eV which corresponds to a Pt^{+2} state (Figure 5.5). Therefore, if the decomposition of the molecule occurs, oxygen most probably binds to the Pt atoms to form mainly $\text{Pt}(\text{OH})_2$. It is also possible that the decomposition is partial and leads to non-crystalline fragments (resulting in no signal in the XRD diffractogram).

Finally, the inorganic AM precursor treatments lead to similar observations with a highly oxidized Pt for the O_2 plasma treatment at 150 W while the "mixed" Ar/ O_2 plasma discharge allows to limit the formation of Pt oxides (Figure 5.4(e)). Interestingly, as seen in Figure 5.4(f), the AM1 sample presents the highest content in PtO bonds ($\sim 50\%$ of the total Pt 4f peak area) and, the AM2 sample is mainly in a metallic form ($\sim 50\%$ of the total Pt 4f peak area as well); this also suggests a partial decomposition of the precursor while the formed Pt particles are already agglomerated. Indeed, as seen on the AM Pt 4f reference spectrum in Figure 5.5, peaks centered at 72.7, 74.0 and 74.9 eV BEs are also visible. As hypothesized

for the OM precursor, residues of the AM precursor and Pt oxides are believed to be still present after the plasma treatments. Moreover, the global content in Pt is weak with a maximum of ~ 4.5 at.%.

5.2.4 Evaluation of the energy consumption related to the fabrication of a Pt/xerogel catalyst

In this section, the energy consumption employed during the fabrication of a Pt/CXG loaded at 20 wt.% (following the OM1-3 strategy, see Table 5.1) is discussed. This study was performed to evaluate the environmental impact of the plasma-based methodology and compared to a conventional wet chemical process (*i.e.* colloidal method). In order to obtain the evaluation of the energy consumption, it is required to detail the production procedure described in section 3.3. The fabrication of a Pt/CXG catalyst by low-pressure plasma methodology can be divided in five steps :

- (1) Introduction of the glass petri box, containing the reactant and a magnetic agitator, in the plasma reactor
- (2) Pumping of the vacuum chamber by using the primary and secondary pump systems
- (3) Injection of a fixed gas flux (Ar or O₂)
- (4) Plasma generation and treatment of the reactant under stirring conditions
- (5) The pumping is stopped, the plasma reactor pressurized and the catalyst removed

Only steps (2) to (4) include energy consumption processes for the catalyst fabrication. For each of them, the energetic consumption was measured by using a Chacon[™] 54355 energy meter. Results are summarized in Table 5.2 and clearly show that the primary pumping is the most important source of energy consumption. However, in comparison with other methods, the low-pressure plasma approach seems to be to most energy-saving. Indeed, the production of 0.3 g of a Pt/CXG catalyst loaded at 21 wt.% by using the colloidal methodology was performed at the Department of Chemical Engineering - Nanomaterials, Catalysis, Electrochemistry (NCE) at the University of Liège. In that case, the use of a magnetic stirring during 48h and a drying process at 60 °C overnight are responsible of an energy consumption of about 39.6 and 16.0 kWh. These two factors represent more than 100 times higher energy consumption compared to the whole plasma-based process.

Step	Process	E (kWh)
(2)	Primary pumping	0.35
(2)	Secondary pumping	0.03
(4)	Plasma generation and stirring conditions	0.05
(2)–(4)	Pressure gauges and gas injection controllers	0.05

Table 5.2: Electric consumption required during the fabrication of 2.5 g of a Pt/CXG catalyst by using the low-pressure plasma methodology.

5.2.5 Conclusions

In the present section, the synthesis of Pt/CXG nanocatalysts following the methodology previously described in [164] was successfully performed through the thermal decomposition of Pt precursors. This study was focused on the use of three different precursors with their own characteristics. The decomposition of the OM1 organometallic precursor, monitored by XRD analysis, was not completely achieved while aggregation already occurred as seen on TEM images. For the OM2 precursor, this effect was only noticed for the energetic O₂ plasma treatment and, for the AM precursor, all explored plasma conditions lead to the same result. Thus, too energetic oxygen plasma treatments result in a frequent agglomeration of the NPs while this effect could be avoided with "mixed" Ar/O₂ treatments in which the maximal temperature reached was believed to be appreciably reduced (see section 5.2.1). This allows to prevent NP coalescence during the plasma discharge. Moreover, the explored conditions do not allow to form highly metallic Pt NPs as shown by the XPS analysis. The maximum metallic Pt content was found for the "mixed" Ar/O₂ treatments of the OM1 precursor.

However, the present study is in agreement with the nucleation mechanisms proposed by Laurent-Brocq *et al.* [164] : (i) the thermal decomposition of the metallic precursor occurs first and allows to release the Pt atoms, (ii) oxygen groups are grafted on the surface of the carbon support or structural defects are created during the plasma treatment of the reactants, and (iii) the nucleation of Pt nanocatalysts takes place in the defects, those acting as germination sites. Nevertheless, the combination of Ar and O₂ plasma discharges seems to play a key role in a better growth control of the Pt NPs. It is believed that a first Ar treatment is suitable for the formation of small NPs anchored on the carbon matrix and then grown during the O₂ treatment; the agglomeration of NPs is thus limited.

5.3 Study of the Pt/C nanomaterials fabricated on graphene sheets

The second carbon topology investigated as a support for the synthesis of NPs was GNPs which are characterized by a lateral size of $\sim 5 \mu\text{m}$, a thickness of $\sim 6 \text{ nm}$ and a surface area of $\sim 150 \text{ m}^2\text{g}^{-1}$. As mentioned in section 1.4, this carbon support, as well as CXGs, presents high surface/mass ratios and high chemical stability. Therefore, they are promising for electrochemical applications. The Pt(II) acetylacetonate (OM1) precursor was used to fabricate the nanocatalysts following the procedure described in section 3.3. The choice of metal precursor for the NP synthesis was based on the cost of the OM materials, which are ~ 70 and $\sim 350 \text{ €}$ per g for OM1 and OM2, respectively. The metal loading was also fixed at 20 wt.% to allow comparison between the two supports employed in the present chapter. The plasma conditions are reported in Table 5.3; plasma treatments have been realized by injecting oxygen with a fixed flux of 5 sccm. The original approach developed in this section is based on a "2-step" methodology. It was shown in section 5.2 that "one-pot" plasma discharges do not allow to avoid a frequent agglomeration of the NPs. Thus, a combination of low- (pulsed plasmas with duty cycle of 50% at a frequency of 10 Hz) and high-energy (continuous plasmas) treatments was performed. The first step of this method should allow to create seeds anchored on the support that act as germination sites for the particles growth during the second step at a higher energy condition.

	Plasma	Type	Time (min.)
GNP-01	O ₂ , 80 W	pulsed	15
GNP-02	O ₂ , 80 W	pulsed	65
GNP-03	O ₂ , 80 W	pulsed	65
	O ₂ , 100 W	continuous	5
GNP-04	O ₂ , 80 W	pulsed	65
	O ₂ , 100 W	continuous	5
	O ₂ , 150 W	continuous	5

Table 5.3: Plasma conditions explored for the synthesis of Pt particles supported on graphene from a mixture with a metal loading of 20 wt.%. For GNP-03 and -04, the plasma treatments were following a 2-step approach in which a low-energy plasma was applied and directly followed by higher energy conditions.

5.3.1 Structural and morphological analyses of the Pt/graphene particles

The decomposition was checked by XRD analysis but will not be discussed here; a complete degradation of the molecule was only found for GNP-04 (see Appendix D) with an average size distribution of the Pt crystallites calculated as 9.7 ± 1.4 nm with the Debye-Scherrer formula (Equation 4.5). Nevertheless, the acquisition of TEM images was performed to show the presence of NPs synthesized by the plasma treatments and their morphologies (Figure 5.6). The TEM images of the low-energy treatments GNP-01 and GNP-02 show that the NP nucleation occurs preferentially at the edges of the graphene sheets. The nucleation at the center of the sheets appears after 65 minutes of treatment (GNP-02) and are homogeneously dispersed on the surface of the support. The proposed nucleation mechanism at low energy consists first in the formation of particles preferentially at the structural defects while a longer plasma discharge is required to produce these defects at the surface of the carbon matrix. During the second step of the treatment, at a higher plasma power and in a continuous mode, the decomposition of the precursor occurs relatively faster; two consecutive treatments of only 5 minutes at 100 and 150 W are sufficient to completely degrade the OM precursor. Moreover, the NP density and size increase as seen in Figure 5.6 for GNP-03 and GNP-04.

5.3.2 Chemical environment and oxidation state characteristics of the Pt/graphene particles

The chemical compositions and quantification of the different plasma treated samples were derived from the high-resolution C 1s, O 1s and Pt 4f (Figure 5.7). The fit of the C 1s core level XPS spectra indicates the presence of five components at 284.8, 285.9, 288.1, 289.9 and 292.0 eV BEs which are attributed to C-C/C-H, C-O, C=O, COOH and π - π^* satellite, respectively [166]. The carbon functionalization does not vary significantly between the different plasma treatments (Figure 5.7(a)). Furthermore, the fitting of the O 1s core level spectra have been also performed (Figure 5.7(b)); three components located at 530.9, 531.8 and 533.1 eV BEs were attributed to metal oxides, O=C and O-C/O-H functional groups, respectively. Interestingly, the same observations as for the carbon functionalization are valid; the chemical environment of oxygen shows a low dependence on the plasma conditions.

Regarding the Pt 4f core level spectra (Figure 5.7(c)), it is clear that the "2-step" methodology greatly influence the oxidation state of Pt. The four components mentioned in section 5.2.3 were fitted for all spectra. The low-energy treatments do not allow to form metallic Pt which was expected due to the lack of precursor decomposition, *i.e.* Pt atoms are still bond to oxygen ; the temperature reached

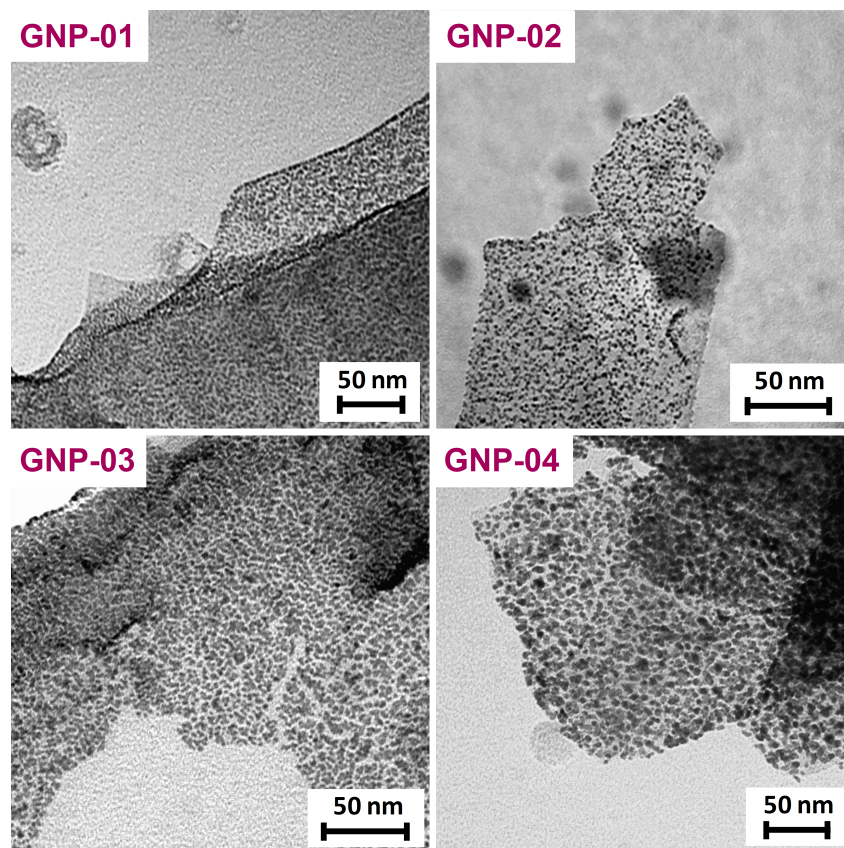


Figure 5.6: TEM images of selected samples fabricated following the plasma conditions given in Table 5.3. The NP synthesis for GNP-01 and GNP-02 were performed in a low-energy "one-pot" plasma treatments while GNP-03 and GNP-04 were produced following the "2-step" approach (low- and high-energy treatments).

during the first treatment phase is not high enough. Moreover, the quantification is similar between the 15 and 65 minutes of treatment with a maximum of ~ 5.2 at.% for GNP-02; the relative Pt 4f percentage shows that Pt is mainly in an oxidized form with only $\sim 10\%$ of metallic content (Figure 5.7(d)). Afterwards, the second phase allows to decompose the OM precursor and reduce the Pt content; the relative percentage of Pt^0 reaches up to 80% for GNP-04. Surprisingly, the amount of Pt increases up to ~ 32 at.% which is equivalent to ~ 90 wt.% at the top surface (between 2-5 nm in depth analysis). Thus, the "2-step" methodology seems promising to fabricate highly metallic particles anchored to the surface of the carbon matrix.

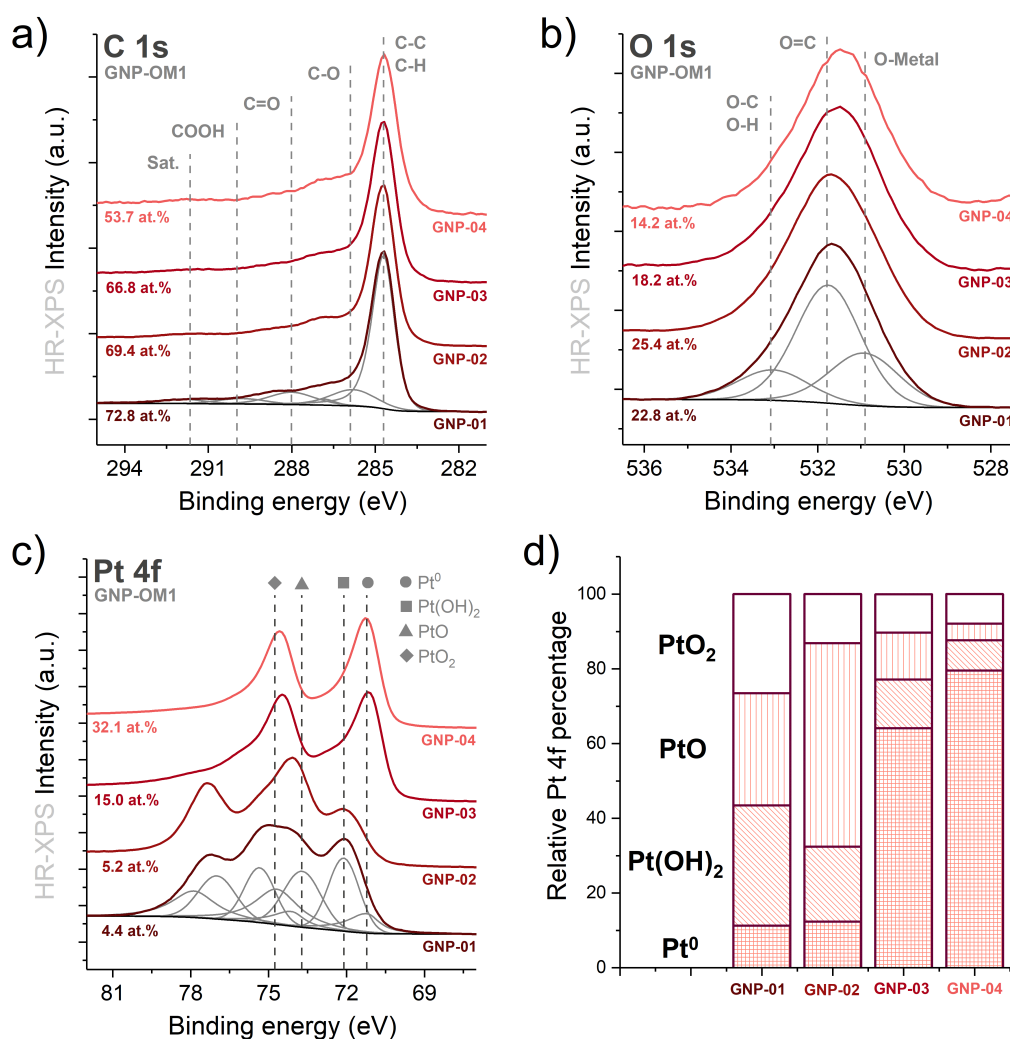


Figure 5.7: High-resolution a) C 1s, b) O 1s and c) Pt 4f XPS core level spectra of the Pt/GNP nanocatalysts synthesized by O₂ plasma discharges following the conditions given in Table 5.3. d) Relative percentages of the Pt oxidation states.

5.3.3 Influence of the pretreatment on the nanoparticles synthesis

A pretreatment of the graphene sheets was performed by using a nitrogen-based plasma treatment, this to induce structural defects on the surface of the support before mixing the OM precursor and then treating the reactants in an oxygen-based plasma discharge to synthesize the Pt/GNP NPs. As mentioned in section 1.5, incorporation of nitrogen in the sheets could have a beneficial effect on the electrochemical characteristics of the support itself and on the stability of the NPs anchored on the surface. The same metal loading as the Pt/CXG

catalysts was chosen (20 wt.%) and the nitrogen flux was fixed at 5 sccm. The pretreatment and NP synthesis conditions are reported in Table 5.4; the graphene sheets were first treated by a continuous N₂ plasmas at 150 and 50 W (GNP^N), while the NP fabrication was done by a pulsed O₂ plasmas at 80 W (GNP^N-01 and -02). The physico-chemical properties of the carbon matrix being sensitive to the presence of too many defects. The treatment time and the transmitted power were limited to avoid the negative impact of the plasma for applications such as in catalysis [212].

	Plasma	Type	Time (min.)
GNP ^N	N ₂ , 150 W	continuous	5
	N ₂ , 50 W	continuous	20
GNP ^N -01	O ₂ , 80 W	pulsed	15
GNP ^N -02	O ₂ , 80 W	pulsed	65

Table 5.4: Plasma conditions explored for the synthesis of Pt particles supported on graphene. A pretreatment of the graphene sheets was performed to investigate the role of structural defects for the NPs synthesis (GNP^N).

Results from the TEM images analysis indicate that the preferential nucleation of the NPs at the edges of the carbon support is decreased and that NPs are now formed on the whole surface of the sheet already after 15 minutes of treatment (Figure 5.8(a,b)). This observation is clearly visible for the GNP^N-02 sample, with homogeneously dispersed particles on the surface of the graphene (Figure 5.8(c,d)). The analysis of the HR-XPS C 1s core level spectra shows a functionalization of the carbon with the different oxygen-containing groups (C-O, C=O, COOH; Figure 5.9(a)). Interestingly, an additional component was fitted at 286.5 eV, which was not seen previously, and represents ~5% and ~10% of the total C 1s peak area for GNP^N-1 and GNP^N-2, respectively; this was attributed to C-O-CO groups [166]. It is important to note that C-N bonds are located at the same BE as C-O groups. Therefore, it is not possible to provide an accurate elemental quantification for the C 1s spectra. However, quantification of nitrogen incorporated to the carbon support was derived from the N 1s spectra (Figure 5.9(b); the amount of nitrogen does not exceed 1.2 at.% (GNP^N-1) and 2.2 at.% (GNP^N-2) but is believed to play a key role for the anchoring of the Pt/GNP nanocatalysts, as discussed in section 1.5. Thus, the impact of C-N bounds in the carbon functionalization should be limited. Two components were fitted, for GNP^N-1, at 398.2 and 399.8 eV BEs corresponding to pyridinic- and pyrrolic-N groups, respectively [213]. Surprisingly, two additional components must be fitted at 403.7 and 406.3 eV BE for the GNP^N-2 sample; these are most probably

attributed to -NO and -NO₂ functional groups [214]. These components could result from a relatively long interaction time – *i.e.* 65 minutes for GNP^N-2, which is 4 times longer than GNP^N-1 – between incorporated nitrogen and oxygen atoms from the plasma discharge. The analysis of the HR-XPS O 1s core level spectra shows that a longer plasma treatment results in the highest amount of oxygen, which was expected (Figure 5.9(c)).

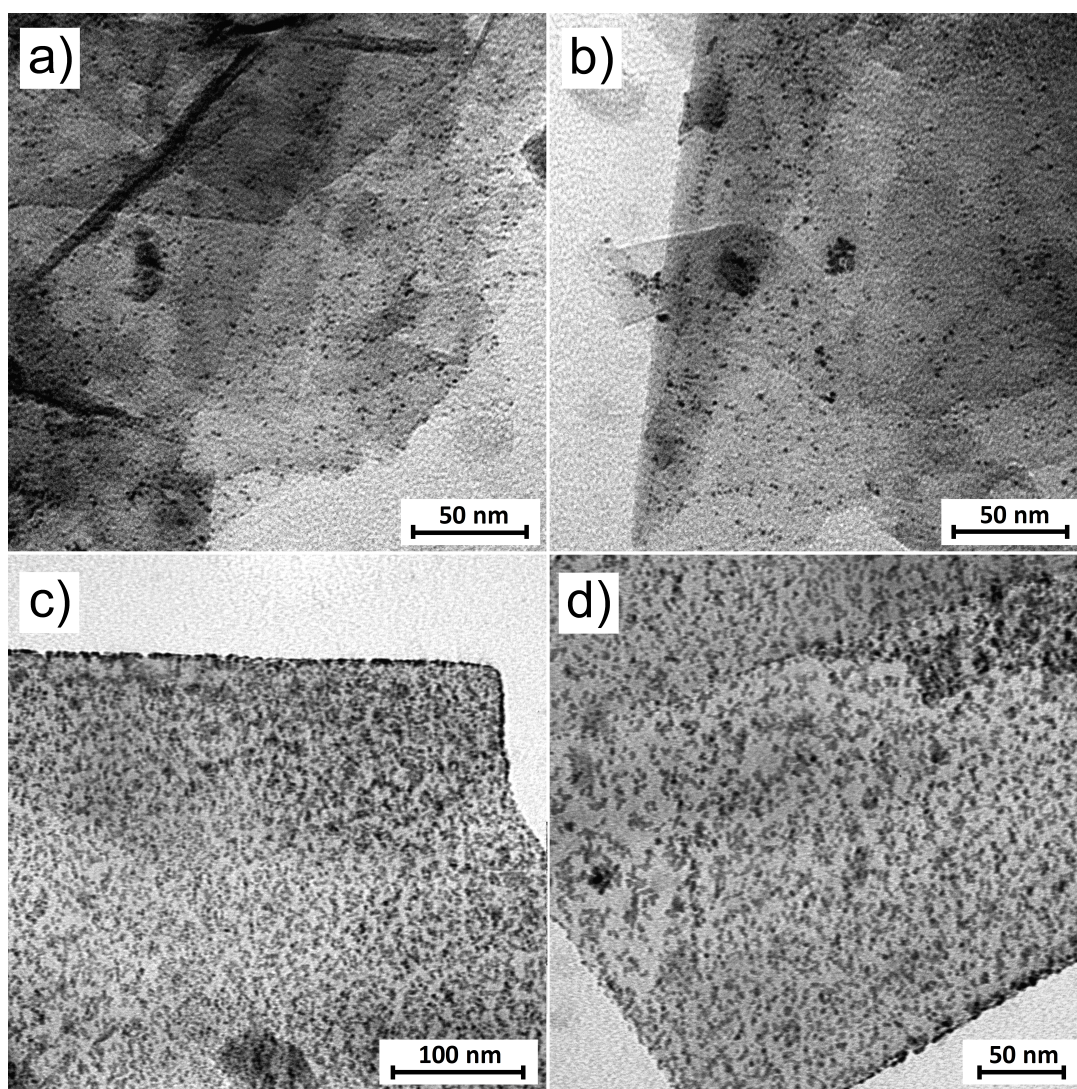


Figure 5.8: Bright field TEM images of the GNP^N-01 (a,b) and GNP^N-02 (c,d) plasma treated samples. Preferential nucleation of the NPs at the edges of the sheets is drastically decreased which is probably due to the presence of structural defects induced by the pretreatment.

The HR-XPS Pt 4f spectra analysis unambiguously shows a better decomposition of the OM precursor (Figure 5.9(d)) in comparison with the samples produced without any pretreatment (GNP-01 and -02, Figure 5.7(c)). The Pt content in the samples GNP-02 and GNP^N-02, which were both treated in a low-energy O₂ plasma discharge during 65 minutes but without pretreatment in the first case, increases from 5.2 to 16.9 at.%. However, the Pt content is highly oxidized (metallic Pt represents $\sim 30\%$ of the total peak area for GNP^N-02) which was previously observed with low-energy plasma discharges, as seen Figure 5.7(a).

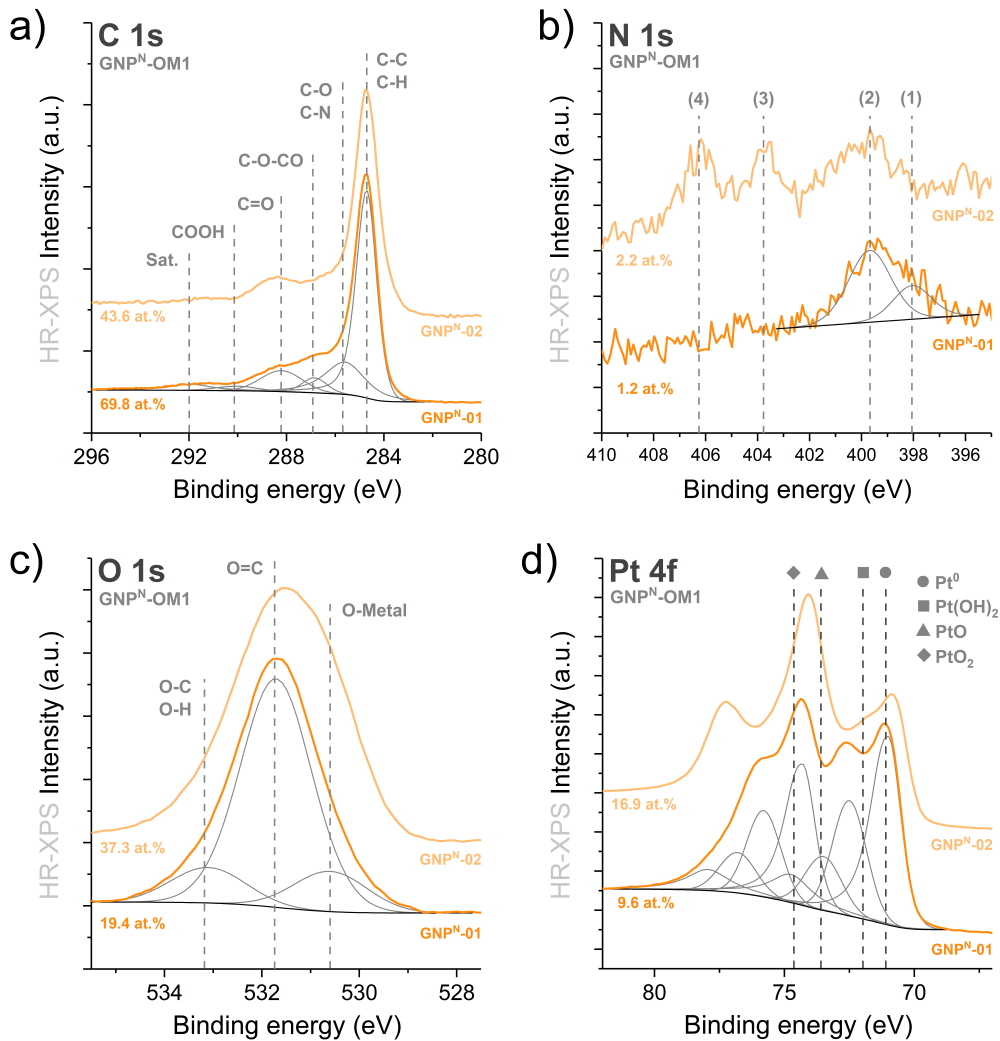


Figure 5.9: High-resolution a) C 1s, b) N 1s (with four components attributed to pyridinic-N (1), pyrrolic-N (2), -NO (3) and -NO₂ (4) functional groups), c) O 1s and d) Pt 4f XPS core level spectra of the Pt/GNP catalysts synthesized on pretreated graphene sheets in a N₂ plasma discharge.

The analysis of the Pt/GNP nanocatalysts synthesized on pretreated graphene sheets tends to confirm the effect of structural defects at the surface of the carbon support. These defects allow to limit the diffusivity of the metallic NPs at the surface of the sheets by creating anchoring sites in which the particles are able to grow with a reduced amount of agglomeration. Plasma treatment at higher transmitted power and/or in a continuous mode can be then applied to decompose the precursor and form metallic particles.

5.4 Conclusions

In summary, for both methodologies investigated in this chapter, the nucleation mechanisms described in the work of Laurent-Brocq et al. [164] are consistent with the presented results. However, the carbon topography highly influences the plasma conditions required to synthesize the NPs. In the case of the "one-pot" treatment leading to the formation of Pt/CXG catalysts, it was shown that the employed metallic precursor directly impacts the way to produce NPs as well as the agglomeration phenomenon. Interestingly, the best conditions to produce mainly metallic Pt NPs were found for the Pt(acac)₂ precursor, while coalescence of NPs could hardly be avoided except for the Pt(cod)(Me)₂ precursor. The inorganic platinumic acid precursor seems to be less attractive for the NP nucleation due to the difficulty to monitor the precursor decomposition (no XRD peaks visible in the diffractograms) and the observed frequent agglomerations. Besides the issues in producing NPs homogeneously dispersed on the CXG, the "mixed" Ar/O₂ discharge exhibits the most promising results. A proposed explanation would be a less important maximal temperature reached during the treatment which limits the particles diffusion. This hypothesis should be confirmed by measuring the temperature. Unfortunately, this parameter is one of the most complex to derive in plasma discharges and could not be measured during the treatments. Finally, the Ar plasma is believed to decrease the coalescence phenomenon by inducing structural defects at the surface of the CXG; these defects playing the role of germination sites on which the NPs first nucleate and then grow during the oxygen plasma.

Going further, a novel approach was developed to better control the formation of NPs and their agglomeration. The "2-step" methodology consists in two plasma treatments : (i) a low-energy plasma discharge is applied to the reactants in order to produce defects at the surface of the support and form small (sub-nanometer to ~1 nm) particles which act as seeds for the nucleation of larger particles and then (ii) growth of the NPs preferentially on the defects. Thus, low-energy treatments provide a beneficial effect for the synthesis. In the highly energetic conditions (continuous plasmas with transmitted power greater than or equal to 100 W and/or with relatively long treatment time), the maximal reached temperature is important enough to cause diffusion and coalescence of the fabricated NPs as seen with

Pt/CXG catalysts. A pretreatment of the support confirmed the key role of the presence of structural defects to limit the particle coalescence.

The comparison between the so-called "one-pot" treatments and the new "2-step" approach highlighted the negative impact of too energetic plasma discharges as well as the beneficial effect of the pretreatment of the carbon support that allows to form NPs homogeneously dispersed on the graphene sheets. The "one-pot" and "2-step" approaches were employed to synthesized bimetallic Pt-Ni/GNP nanocomposites, this will be discussed in details in chapter 7.

Chapter 6

Influence of the plasma chemistry on the synthesis of Ni/C composites

This chapter describes the results that have been the object of the following publication [167] :

E. Haye, Y. Busby, M. da Silva Pires, F. Bocchese, N. Job, L. Houssiau, & J.-J. Pireaux, Low-Pressure Plasma Synthesis of Ni/C Nanocatalysts from Solid Precursors: Influence of the Plasma Chemistry on the Morphology and Chemical State, *ACS Applied Nano Materials*, 1(1), 265-273, 2018.

6.1 Introduction

The motivation for the synthesis of non-noble metal particles relies on the broad possibilities to reduce the use of critical raw materials found in various applications, among which catalysis. The strategy developed in this work is similar to the one presented for the synthesis of Pt/C composites in the previous chapter. Insights into the nucleation process and growth mechanism of Ni NPs supported on carbon xerogel are highlighted; it is expected that the different plasma chemistries, the OM precursor and carbon support employed in this chapter influence the NP nucleation and growth as it was shown for Pt/C NPs in the work of Laurent-Brocq *et al.* [164] and in chapter 5. The effect of three gases was investigated, namely N₂, O₂ and NH₃ plasmas were employed to decompose the Ni precursor. More specifically, the decomposition of the OM precursor and its kinetics as a function of the gas mixture is discussed as well as the functionalization of the carbon matrix. At the same time as the Ni OM is degraded, the adjunction of functional groups, like oxygen- (C-O, C=O) and nitrogen-based (C-N) functions, to the carbon matrix was expected to occur in the plasma discharges and are also discussed. A carrier gas (Ar) was added during the plasma treatments which is responsible of (i) a higher plasma stability, (ii) a better effect on the decomposition of the OM precursor and (iii) a higher ionization degree. It is believed that ionized

(Ar⁺) or metastable (Ar^{*}) argon atoms transfer their energy to oxygen species which leads to an increase of the reactive species in the plasma. It was shown that several reactions involving argon and molecular or atomic oxygen could occur within the plasma region in an Ar:O₂ mixture [215] :



The methodology employed for the preparation and fabrication of Ni/C nanocatalysts is described in section 3.3. Nickel(II) acetylacetonate (Ni(acac)₂, > 95%, Strem Chemicals) powder was mixed with a carbon xerogel characterized by a pore size of ~100 nm. The melting point of the Ni OM is 240 °C and a molecular representation is given in Figure 6.1. The carbon support was provided by the group of Prof. N. Job and was made following the method described in ref. [95]. As mentioned in chapter 5, the two reasons leading to the choice of carbon xerogel as support for the fabricated NPs are (i) being a high-purity carbon and (ii) the relative ease of control over the pore texture, which plays a major role in limiting the material transfer and provides a large number of anchoring sites for the NPs [94, 216]. The OM precursor and the carbon matrix were mixed together, with the mass ratio required to reach a metal loading of 20 wt.%.

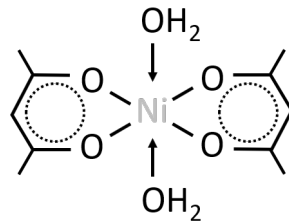


Figure 6.1: Molecular structure of the nickel(II) acetylacetonate employed as precursor for the fabrication of Ni/C nanocatalyst.

Optical emission spectroscopy (OES) was used to monitor the OM decomposition by following the change in intensity of several emission lines characteristic of the species in the plasma in comparison with a reference line constant over time. The OES results were further confirmed by XRD measurements : the OM precursor being crystalline, peaks attributed to its signature in the diffractograms disappear as results of the decomposition. Moreover, XRD measurements allowed

to monitor the crystal structure of the Ni particles. The chemical composition of the samples, *i.e.* the global composition, the oxidation state of the Ni NPs and the carbon functionalization, were studied by XPS. Finally, the morphology of the synthesized NPs was investigated by TEM/STEM, including bright field (BF) and high-angle annular dark field (HAADF), with an acceleration potential of 200 kV.

In this work, the author of the present thesis contributed to (1) the synthesis of several Ni composites by low-pressure plasma discharges, (2) the acquisition and analysis of some XPS spectra, (3) XRD diffractogram acquisitions and analysis, and (4) the preparation of the manuscript for its publication. The Physico-Chemical Characterization (PC²) and the Synthesis, Irradiation and Analysis of Materials (SIAM) platforms of the University of Namur are acknowledged for the XRD and XPS measurements, respectively; while SERMA Technologies is acknowledged for TEM/STEM images acquisition.

6.2 Organometallic precursor decomposition dependence with the plasma chemistry

As mentioned previously, three plasma chemistries were investigated to bring a better understanding of the decomposition of the Ni precursor and the formation of NPs anchored on a high surface area carbon matrix : (i) a less reactive Ar:N₂, (ii) a reducing Ar:NH₃ and (iii) an oxidizing Ar:O₂ mixture. For all of them, the Ar flow rate was fixed to 5 sccm while it was set at 2 sccm for both N₂ and O₂. In order to have the same amount of nitrogen atoms in the plasma discharge, a 4 sccm NH₃ flow rate was set with respect to N₂. The plasma power was varied from 90 to 200 W and applied until the OM precursor was fully degraded according to the OES measurements (see below for a detailed discussion); typically, the treatment time was varying from 45 up to 60 minutes and depended on the power as well as on the gas mixture. Pressures in the vacuum chamber were measured between 3 and 7 mTorr (~ 0.4 to 1 Pa) for the different experiments and do not significantly affect the emission line intensities monitored by OES.

The optical spectrometer calibration in wavelength was checked by using a standard Hg lamp with a known spectrum. During the plasma treatment, several emission line intensities were recorded to diagnose on the OM decomposition. In particular, argon lines (Ar I) are mainly located in two regions of the spectra (395–435 nm and 680–895 nm, [193]) and do not vary in intensity while degrading the Ni precursor. Therefore, these are suitable for the normalization of the OES signals and the 811.5 nm line was chosen due to its relatively high intensity. For the oxidizing Ar:O₂ plasma, emission lines at 306.7, 309.2 and 313.6 nm, the so-called A-X lines, could be followed and are attributed to OH groups [217], while

for the Ar:N₂ and Ar:NH₃ plasmas, N₂ C-B lines appear in the range 310–390 nm as well as the CN violet system at 386.7 and 388.2 nm, respectively [218, 219]. The formation of CN lines is expected to occur in gas phase and comes from the interaction of carbon atoms from the sample and nitrogen atoms from the dissociation of N₂ or NH₃ molecules. Moreover, C₂ Swan bands were observed in the spectra within the 505–518 nm region [220]. For the NH₃ gas mixture, H_α and H_β are visible at 656.3 and 486.7 nm, respectively [221, 222]. Figure 6.2 shows the typical spectra obtained at the beginning of 140 W plasma treatments.

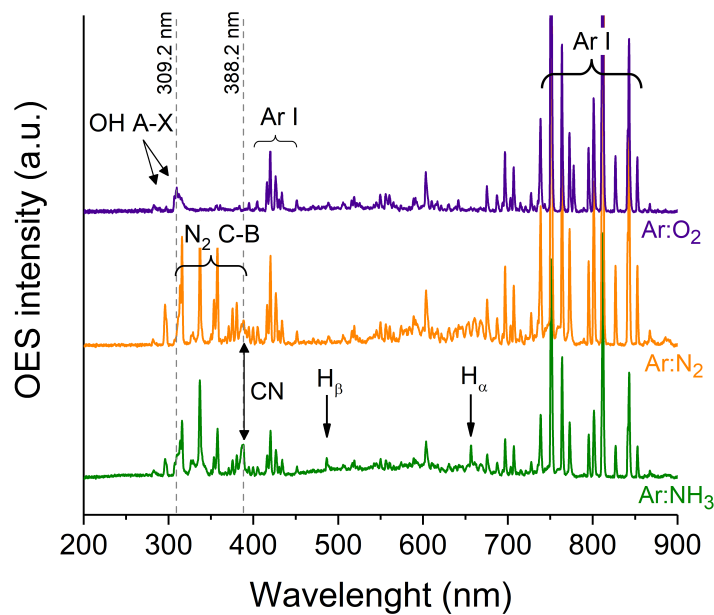


Figure 6.2: In-situ OES spectra taken at the beginning of the ammonia, nitrogen and oxygen plasmas at a power of 140 W. The OH A-X, N₂ C-B, CN and Ar I lines are identified and the evolution over time of some of them are monitored to follow the OM decomposition.

The most intense lines were chosen for further analysis, namely the OH-related line at 309.2 nm for the Ar:O₂ plasma and the CN line at 388.2 nm for both Ar:N₂ and Ar:NH₃ gas mixtures. An example of this systematic study is shown in Figure 6.3, the OES intensity is measured over time and plotted after correction of the intensity normalized to the Ar line mentioned above. The OM precursor is completely decomposed when no more variation of the OES signal is recorded. This is confirmed by a complementary study performed by XRD measurements. Indeed, the precursor is in a crystalline form and exhibits characteristic peaks in the diffractogram. These peaks disappear when the complete decomposition is achieved; if the grown NPs tend to form nanocrystals, peaks related to their structural arrangement are visible. Diffractograms shown in Figure 6.4 were ac-

quired considering the longest treatment time based on the OES signal, *i.e.* the fall in intensity was reached. In Figure 6.4(a), the fingerprint of the Ni(acac)₂ powder is shown together with the last power treatment employed for Ar:O₂ and Ar:N₂ plasmas; only a relatively weak NiO phase can be seen which means that Ni NPs should be most likely in an amorphous and oxidized state. On the other hand, Figure 6.4(b) shows the diffractograms between 90 and 200 W for Ar:NH₃ discharges; crystallinity is observed directly for the lowest transmitted power, the peak positions of the three main contributions to the diffractogram and their corresponding Miller indexes are also mentioned (namely (110), (002) and (111)). According to the literature, nickel nitride (Ni₃N) phase crystalline domains have been formed during the treatment [223] with an average size distribution, calculated following the Debye-Scherrer formula (Equation 4.5), increasing linearly with the transmitted power (inset present in Figure 6.4(b)).

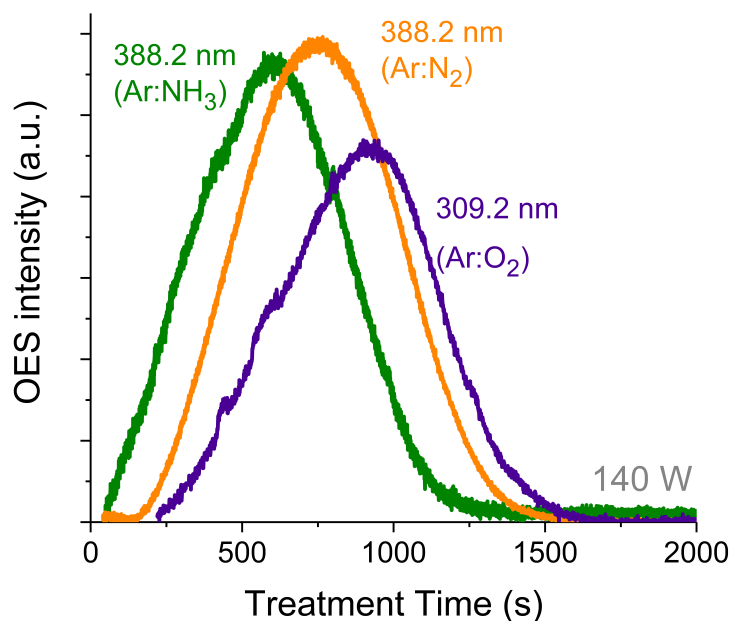


Figure 6.3: Evolution of the OH-related (309.2 nm) and CN (388.2 nm) lines for Ar:O₂, Ar:N₂ and Ar:NH₃ plasmas. The plasma power was fixed at 140 W in each case.

The OM decomposition kinetics and its efficiency for each plasma treatment is evaluated by considering the reaction presented in Equation 6.5 [167] :



where k is the kinetic constant, F_1^* is the organic volatile fragment in an excited state produced by the degradation of the OM and assumed to be pumped down,

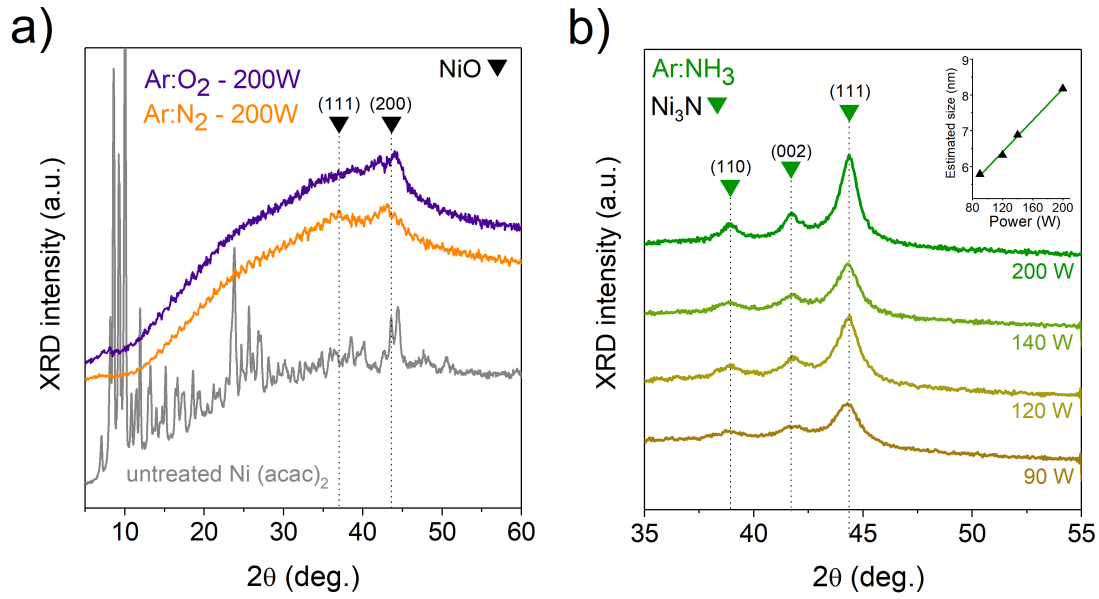


Figure 6.4: Diffractograms of a) the untreated powder of the OM precursor together with the most energetic plasma discharges for both Ar:O₂ and Ar:N₂, and b) the Ar:NH₃ treatments at several transmitted powers. The evaluation of the average size distribution, thanks to the Debye-Scherrer formula, is shown for the Ni nanocrystals in the inset.

while F_2 is the nickel-containing intermediate molecule. The generation of OH or CN emission lines recorded by the OES measurements is believed to come from the relatively fast relaxation process occurring for the F_1^* product, going from an excited to the ground state.

Once the relaxation of the F_1^* products is achieved, the resulting F_1 fragments are assumed to be pumped down from the vacuum chamber and the formation of Ni NPs occurs gradually thanks to the decomposition of the F_2 molecules. The rate of consumption r is then defined as follows :

$$r = -\frac{d[OM]}{dt} = k.[OM]^n \quad (6.6)$$

with $[OM]$ the molecular fraction of precursor depending on the time t and n the reaction order. Basically, the reaction order indicates how the kinetic constant k depends on the OM molecular fraction. The fraction of F_1^* fragments is reasonably expected to be proportional to the OES intensity, named as I_{raw} in the next developments, of a characteristic OH or CN emission line. From that hypothesis, the OM molecular fraction can then be deduced considering Equation 6.5, the evaluation of the latter at time t is performed thanks to the following equation :

$$[OM] = 1 - \frac{\int_0^t I_{raw} dt}{\int_0^\infty I_{raw} dt} \quad (6.7)$$

The upper integral term in Equation 6.7 is simply the surface area under the curve of the OES intensity as a function of time between 0 and t , while the lower term allows the normalization of the OES intensity and is constant for a given plasma treatment, as seen in Figure 6.5(a). From Equation 6.7, it is hypothesized that the OM molecular fraction is proportional to I_{raw} and varies from 1 at the beginning of the treatment to 0 at the end, as seen in Figure 6.5(b).

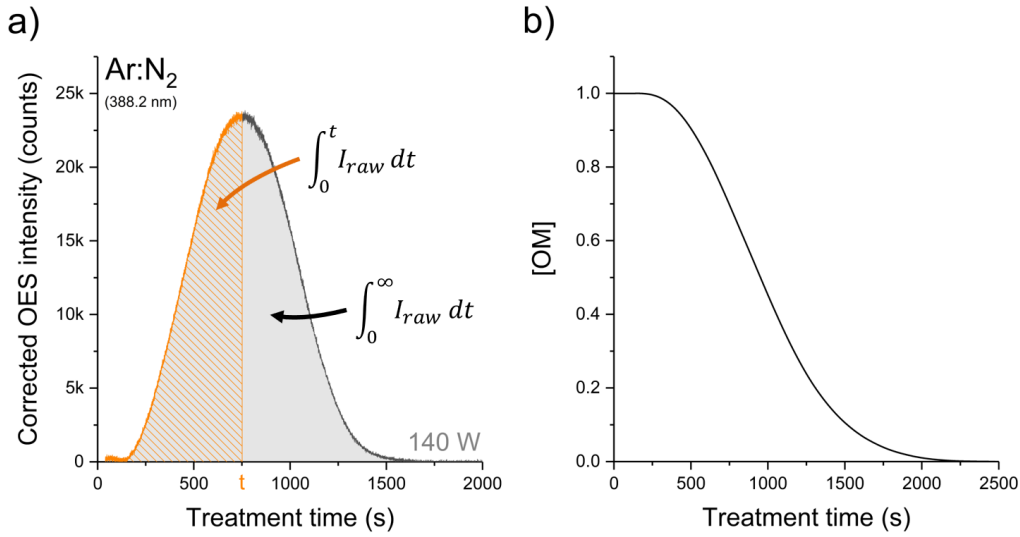


Figure 6.5: a) Corrected OES intensity of the CN emission line (388.2 nm) for a 140 W Ar:N₂ plasma treatment. Integrals in the determination of the OM molecular fraction are represented by the two surface areas (orange diagonal lines and gray-filled). b) Evolution of OM molecular fraction as a function of the treatment time obtained following Equation 6.7.

Equation 6.6 can be modified taking into account the previous development (Equation 6.7) and by using the natural logarithm :

$$\ln(I_{raw}) = \ln \int_0^\infty I_{raw} dt + \ln k + n \cdot \ln \left(1 - \frac{\int_0^t I_{raw} dt}{\int_0^\infty I_{raw} dt} \right) \quad (6.8)$$

The determination of the reaction order and the kinetic constant is easily performed by plotting the OES intensity I_{raw} as a function of the last term appearing in Equation 6.8, and then calculating the slope (reaction order) and y-axis

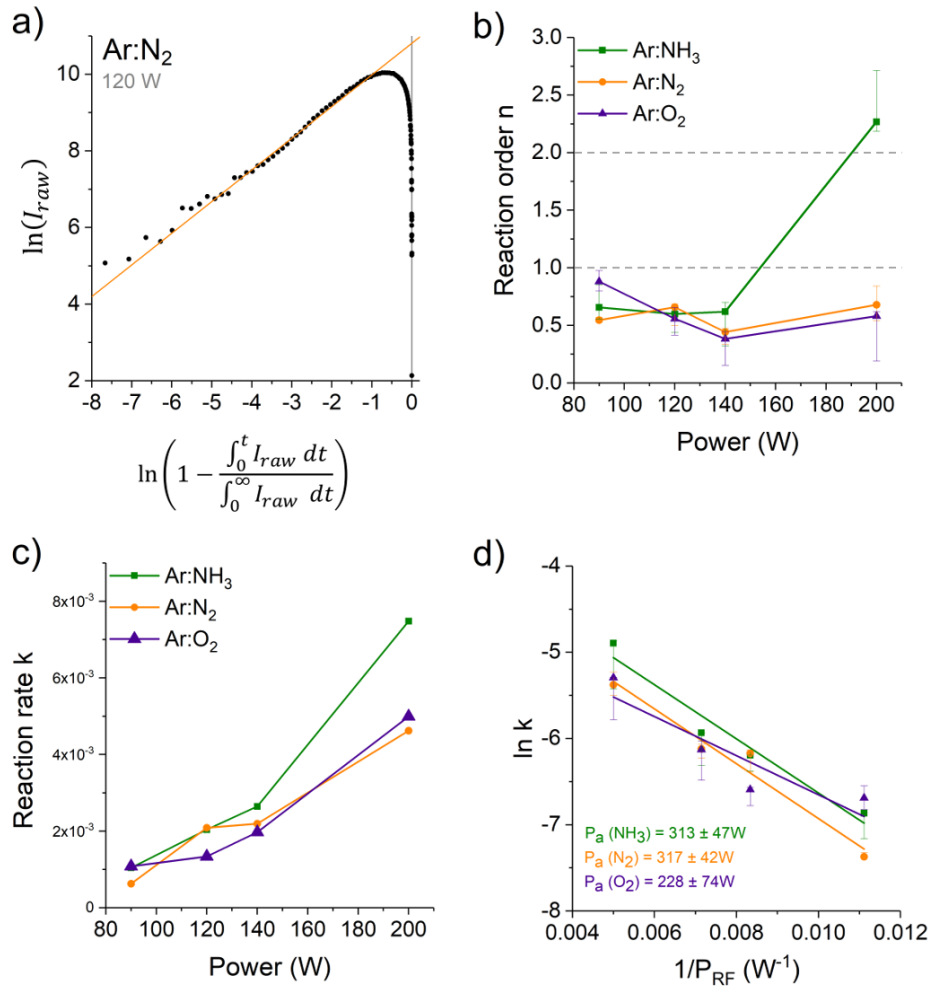


Figure 6.6: Curve of a) the OES intensity natural logarithm for an Ar:N₂ plasma discharge with a power of 120 W, b) the reaction order n , c) the kinetic constant k and d) the analogy with an Arrhenius plot for the determination of an "activation power" through the calculation of the linear fit slope.

intercept (related to the kinetic constant). Figure 6.6(a) shows the graph of the natural logarithm of the OES intensity and the plotted linear function which allow the calculation of n and k . Results obtained for both parameters in the case of the three plasma chemistries at different transmitted power are shown in Figure 6.6(b) and (c); uncertainties were determined by considering the upper and lower values of each parameter. Besides the treatment at 200 W with an Ar:NH₃ gas mixture, the reaction order does not vary significantly, with a value ~ 0.5 (Figure 6.6(b)). Therefore, the relatively weak dependence on the plasma power could indicate that processes involved in the degradation of the OM precursor are roughly the same for the different treatments except for the most energetic

ammonia plasma. Moreover, interpretation of the values found for the reaction order is the proportionality between the consumption rate and the OM molecular fraction (Equation 6.6). However, the value of 0.5 for the reaction order indicates rather complex decomposition mechanisms. It would be necessary to perform further experiments (analysis of the fragments released during the decomposition by using mass spectrometry, for example) in the future to derive a model of the decomposition pathways which is able to give such a reaction order. Regarding the kinetic constant k , it is clear that there is a dependence on the energy furnished during the treatment, the kinetic constant being higher at higher transmitted power (Figure 6.6(c)). Between 90 and 140 W, there is no significant differentiation with the plasma chemistry; nevertheless, the kinetic constant for the 200 W Ar:NH₃ treatment increased notably in comparison with the two other gas mixtures. A proposed explanation for such an effect is the increased amount of reducing species released during the treatment by ammonia. More specifically, hydrogen is assumed to be released by the splitting of NH₃ molecules and should be the main agent responsible for the reducing effect. The decomposition of the OM precursor is then believed to take a new route in comparison with the other plasma conditions due to those new species in the discharge. Further experiments should be performed to confirm these observations.

The final approach employed to characterize the OM decomposition is based on an analogy with an Arrhenius plot in which the energy required to activate the reaction is estimated at a given temperature. Thus, a so-called "activation energy" is derived from the measurement of the kinetic constant and by using the following equation :

$$k = A. \exp\left(-\frac{E_a}{RT}\right) \quad (6.9)$$

where A is a pre-exponential factor, E_a is the activation energy, R is the gas constant and T is the temperature at which the reaction occurs. The main issue with low-pressure plasma-assisted degradation of molecules is the impossibility to derive only one temperature for the species in the discharge. As discussed in chapter 2, NLTE plasmas present different temperatures for electrons, ions and neutrals; in a cold plasma, electrons have a higher temperature compared to ions and neutrals. For that reason, a modified Arrhenius equation is proposed by introducing an "activation power" (P_a) instead since the plasma power is a more accessible parameter and is directly linked to the energy transmitted :

$$k = A. \exp\left(-\frac{P_a}{P_{RF}}\right) \quad (6.10)$$

with P_{RF} the RF discharge power applied during the treatment. This "activation power" is then defined as the power required to activate the decomposition reaction of the OM. A linear fit can thus be obtained by plotting the natural

logarithm of the kinetic constant ($\ln(k)$) as a function of the inverse value of P_{RF} . The apparent linear behavior for plasma powers between 90 and 200 W shown in Figure 6.6(d) is believed to be in agreement with the previous point exposed to justify, a posteriori, the use of the Arrhenius plot analogy. The "activation powers" deduced for the nitrogen-containing discharges ($P_a = 313 \pm 47$ W for Ar:NH₃ and $P_a = 317 \pm 42$ W for Ar:N₂) are roughly the same, while for the oxygen-based plasma the trend seems to indicate a lower value ($P_a = 228 \pm 74$ W). However, several points need to be highlighted in order to understand these three parameters. First, the mechanisms involved during the treatment and decomposition are not well understood and highly complex, this is also the case for the NP nucleation and growth; stating that an oxygen-based plasma may be more efficient is not well established and, from Figure 6.3, it seems that the decomposition of the precursor is the slowest for the Ar:O₂ plasma. This needs to be confirmed by a systematic study. Moreover, uncertainties on the derived parameters are relatively important regardless of plasma chemistry; no notable difference emerges taking into account this fact.

6.3 Morphology of the synthesized nanoparticles

The morphology of the synthesized NPs were checked thanks to TEM/STEM images analysis. Each acquisition was performed on samples obtained after the complete decomposition of the precursor which was monitored by OES and XRD measurement as discussed above. Figure 6.7 presents the STEM micrographs for the three plasma chemistries. The particle size distributions were derived from these images by processing with the software ImageJ. The NPs are homogeneously dispersed on the carbon matrix for each plasma conditions as seen in Figure 6.7; modification of the transmitted power and plasma chemistry being responsible for the different particle size distributions observed. From image analysis, it was found that the size distribution is unimodal regardless of the plasma condition. The Ar:O₂ and Ar:N₂ plasma treatments at 200 W both result in the lowest average particle size, which are $\sim 4 \pm 0.5$ and $\sim 2 \pm 0.5$ nm respectively (Figure 6.7(a)-(b)). On the other hand, the average particle size increases with the transmitted power for the Ar:NH₃ treatments, going from 3 ± 0.5 nm at 90 W (Figure 6.7(c)) up to $5-6 \pm 1$ nm at 200 W (Figure 6.7(d)). Finally, the average NP sizes (including the Ni₃N crystal domains) estimated by XRD are systematically overestimated in comparison with the measurements performed on the TEM/STEM images; this is often reported in the literature [224] and, in our case, could be due to the presence of several crystalline aggregates.

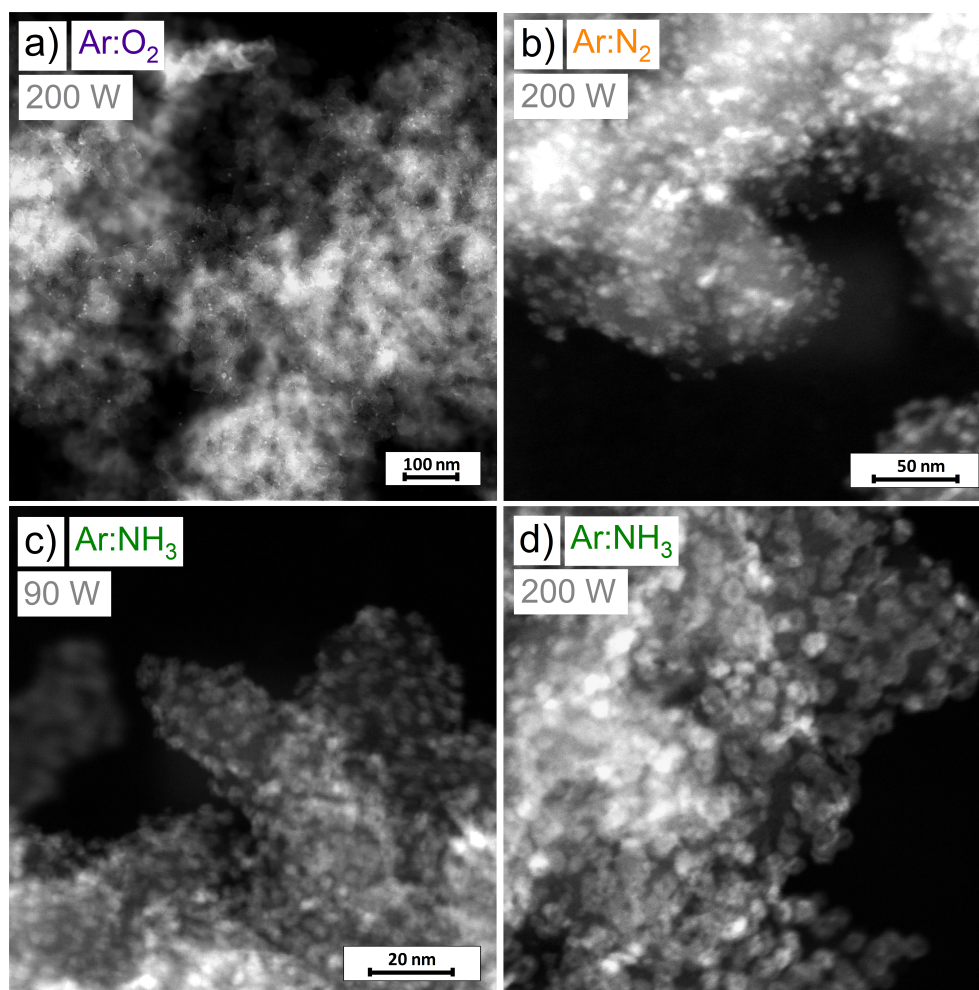


Figure 6.7: High-angle annular dark field (HAADF) STEM micrographs of the Ni/xerogel NPs, seen as bright spots in the different images. Images of the a) Ar:O₂ and b) Ar:N₂ plasma treatments at 200 W are shown while the Ar:NH₃ plasma treatments at c) 90 W and d) 200 W are presented. The focus in image d) highlights a brighter shell (where contrast was exacerbated on purpose for a better visualization) specific to the ammonia plasma treatments.

6.4 Analysis of the Ni/C nanocatalysts chemical composition and state

A systematic analysis of the overall chemical composition was performed for each plasma condition explored by XPS. The spot size was fixed at 250 μm for every analysis; survey and high-resolution (C 1s, N 1s, O 1s and Ni 2p) spectra were acquired with a pass energy of 200 and 30 eV, respectively. The signal-to-

noise ratios of each element analyzed were controlled by varying the scan number in order to have similar values between the samples. In other words, the number of scans was higher for weak signals coming from the elements in presence. The same calibration as presented in chapter 5 was applied and the main C 1s peak (C-C/C-H bonds) was systematically fixed at 284.8 eV. The quantification of the atomic percentage for O, Ni and N was realized by analyzing their corresponding HR-XPS spectra (O 1s, Ni 2p and N 1s) together with the C 1s spectra, results are shown in Figure 6.8. The amount of oxygen present in the samples is the highest for the Ar:O₂ plasma (~35-39 at.%) in comparison with the nitrogen-containing treatments (~23 at.% for Ar:N₂ and ~28 at.% for Ar:NH₃) as it was expected (Figure 6.8(a)). The oxygen for these last two plasma chemistries comes more likely from the OM precursor; more specifically, it could be explained by plasma surface interaction and deposit formation of organic fragments, released by the OM decomposition, at the surface of the carbon support. The next section will discuss the carbon functionalization which could confirm the hypothesis of deposited organic fragments onto the surface of the different samples.

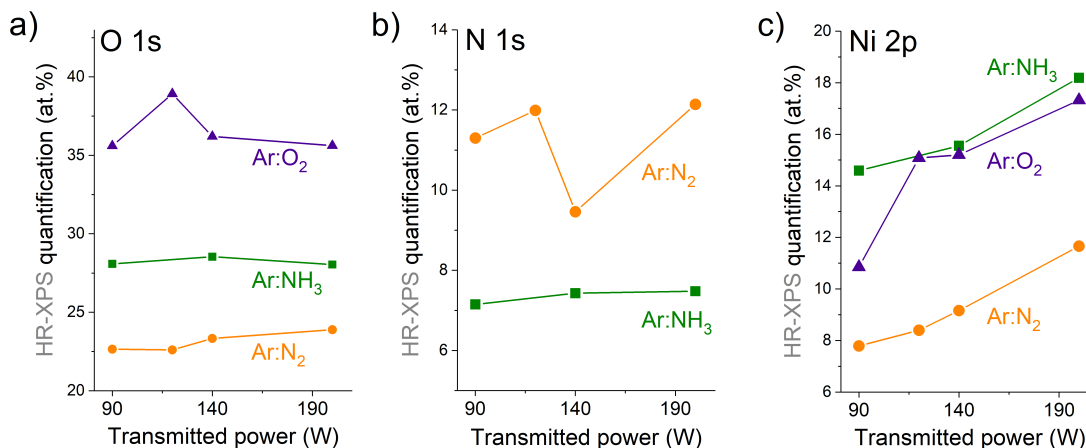


Figure 6.8: Atomic percentage quantification derived from the analysis of HR-XPS spectra for a) oxygen, b) nitrogen and c) nickel as a function of the transmitted power.

Regarding the nitrogen content (Figure 6.8(b)), it is clear that Ar:N₂ plasma treatments allow a higher incorporation of N atoms (~11 at.%) compared to the Ar:NH₃ treatments (~7 at.%). At this point, it is important to clearly mention the hypothesis taken while analyzing the treated samples by XPS. It was assumed, for the quantification, that the surface is homogeneous over the first nanometers of the materials. For heterogeneous surfaces, peak BE positions and calculated atomic percentages are affected by the presence of nanoscale domains due to their various sizes and morphologies. The nitrogen functionalization will be discussed in details further in the present section.

Finally, the elemental and chemical compositions of the Ni NPs were studied thanks to the Ni $2p_{3/2}$ spectra. The smallest amount of Ni is found for the Ar:N₂ plasma treatment (~ 8 up to 12 at.%) while it reaches up to 18 at.% for the Ar:O₂ and Ar:NH₃ discharges. This is explained by the difference in the NP size distribution seen on STEM images (Figure 6.7); a higher amount of Ni is measured when the size distributions are larger (around 1–3 nm for Ar:N₂ and more than 4 nm for both Ar:O₂ and Ar:NH₃). Indeed, the quantification being affected by the presence of nanoscale domains for heterogeneous surfaces [174, 175], which is the case here, larger domains at the surface result in a higher Ni content derived from the XPS spectra.

The Ni chemical states were then analyzed thanks to the Ni $2p_{3/2}$ high-resolution (HR) XPS spectra, Figure 6.9(a) shows these spectra for plasma treatments at 90 and 200 W. Besides the relative complexity in analyzing the Ni 2p spectra, three oxidation states were fitted at 852.4 eV, 854.6 eV and 855.8 eV BEs (Figure 6.9(b)) and are ascribed to metallic (Ni⁰), divalent (Ni²⁺) and trivalent (Ni³⁺) nickel, respectively [225, 226]. Their corresponding shake-up satellite peaks are also present at higher BEs (see Appendix E) [225, 226]. HR-XPS spectra shown in Figure 6.9(a) indicate that Ar:NH₃ plasmas allow the formation of nickel in its less oxidized state with a metallic fraction (Ni⁰) from 13 up to 23% of the total Ni $2p_{3/2}$ peak area for discharges between 90 to 200 W. The comparison of the different HR-XPS spectra for the ammonia-based treatments indicates that the chemical composition does not vary significantly with the plasma power. Only the size distributions are affected by varying the transmitted power, increasing when the latter increases, as seen on the insert in Figure 6.4. The formation of Ni₃N NPs, their size distributions and morphologies were already discussed thanks to the analysis of XRD diffractograms and TEM/STEM images, as seen in Figure 6.4 and 6.7. For the Ar:N₂ treatments, analysis of the Ni $2p_{3/2}$ spectra indicates that the Ni oxidation state shows no metallic component at lower plasma power (<140 W) and clearly appears at 200 W (Figure 6.9(a)), for which the contribution accounts for $\sim 20\%$ of the total Ni $2p_{3/2}$ peak area (Figure 6.9(c)). Therefore, such a plasma chemistry allows the formation of metallic NPs when degrading the OM precursor at relative high plasma power but, as seen in Figure 6.4(a), weak peaks in their diffractograms indicate mainly amorphous materials. A possible explanation comes from the effect of Ar⁺ species present in the plasma which causes a preferential sputtering of the oxygen atoms in the oxidized Ni NPs [227]. Lastly, HR-XPS spectra show fully oxidized nickel for all Ar:O₂ treatments. However, the ratio between trivalent and divalent nickel (Ni⁺³/Ni⁺²), calculated from the fitting of the spectra, decreases when the applied power is increased (ratio of 6.2 at 90 W dropping to 3.8 at 200 W). Thus, it is expected that an increased amount Ar⁺ species formed at higher transmitted power are also involved in reducing the oxidized NPs.

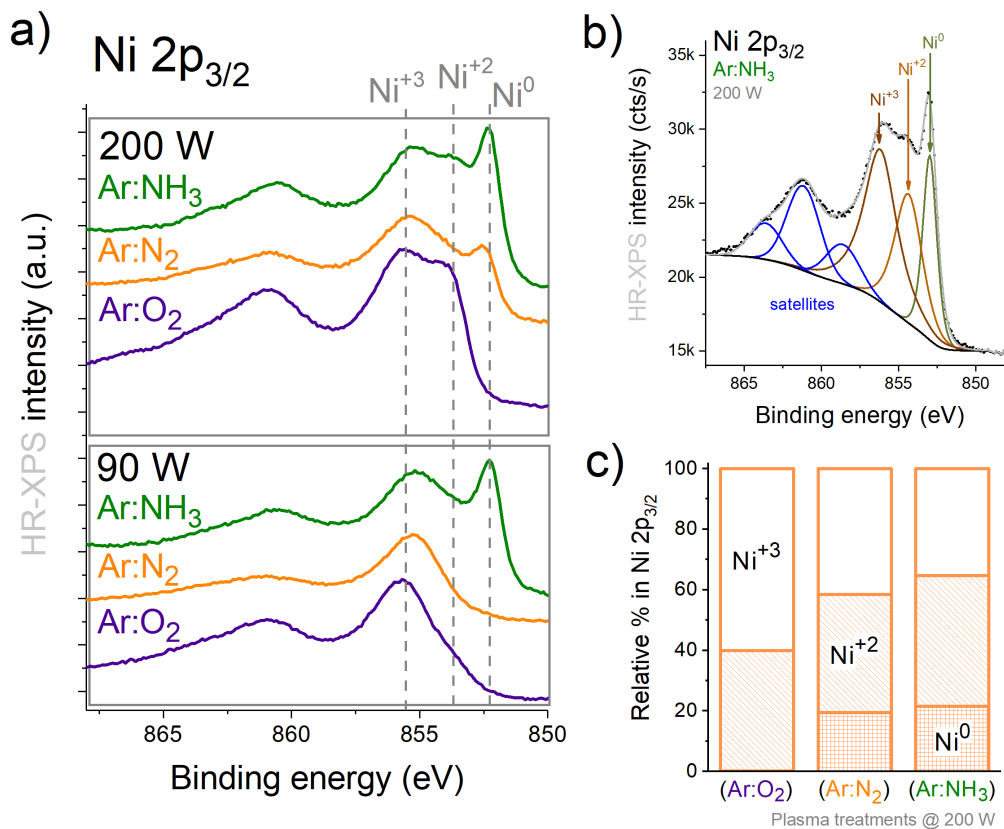


Figure 6.9: a) HR-XPS Ni 2p_{3/2} spectra at 90 and 200 W for the three plasma chemistries. b) Peak fitting of the HR-XPS Ni 2p_{3/2} spectrum for an Ar:NH₃ treatment at 200 W allowing the quantification of the chemical oxidation state of the Ni NPs. c) Nickel oxidation states derived from the fitting of the HR-XPS spectra for the different plasma chemistries at a 200 W transmitted power.

6.5 Functionalization of the carbon support

The carbon support functionalization was investigated thanks to the analysis of the HR-XPS spectra of carbon C 1s and nitrogen N 1s. A systematic fitting of the different spectra was performed to identify the functional groups added to the support and to quantify their amount. The first study is focused on the carbon functionalization and is shown in Figure 6.10. The HR-XPS C 1s spectra of the carbon xerogel, the Ni precursor and the untreated powder mixture are shown in Figure 6.10(a–c) and the functional groups ascribed to the fitted peaks are in agreement with the chemical composition of the OM precursor molecule. However, for the untreated powder mixture, an unexpected additional component at 290.2 eV appears and is attributed to carbonates. A proposed explanation for such a contribution is a partial alteration of the precursor molecule due to the mechanical mixing of the reactants.

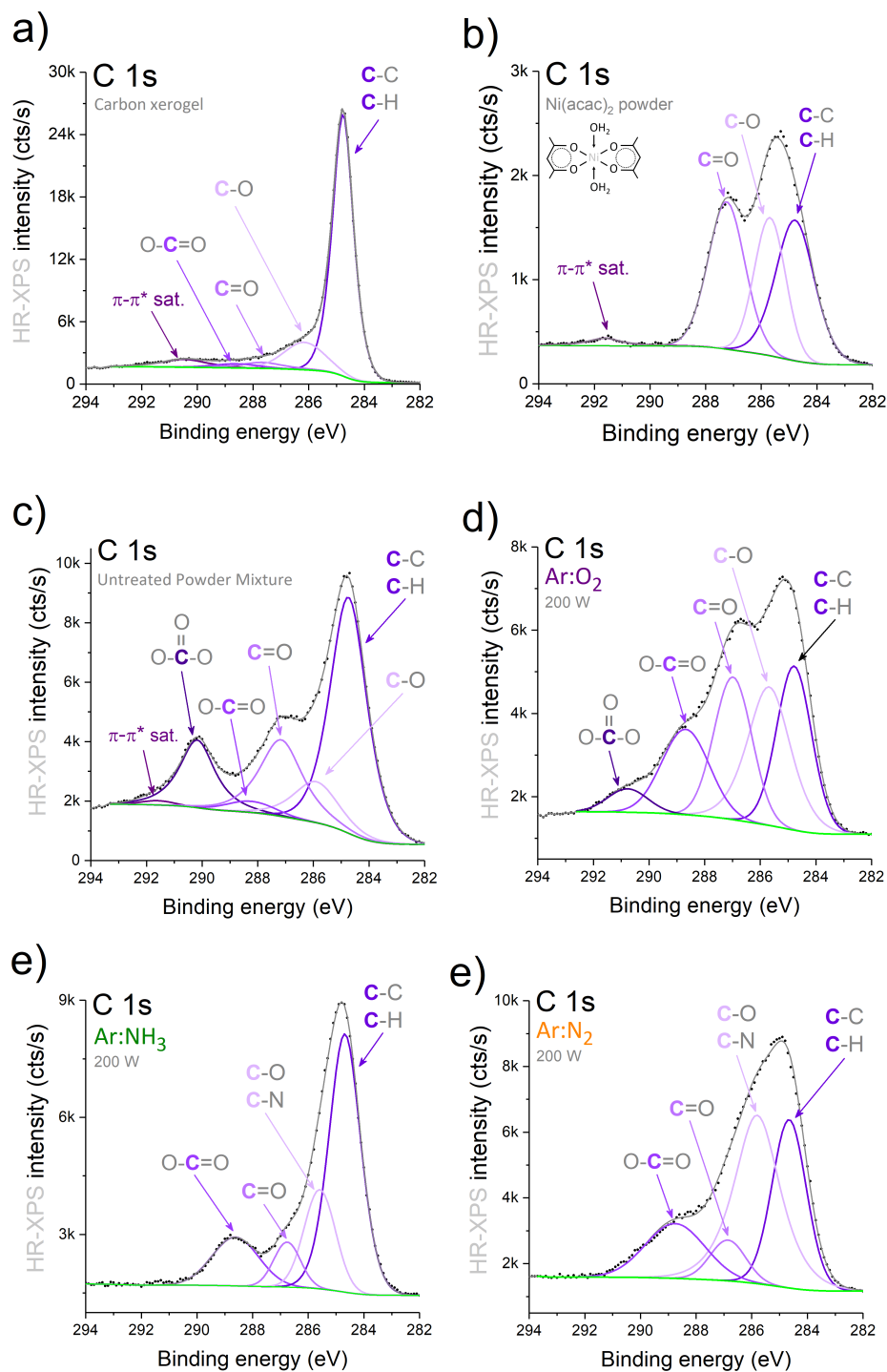


Figure 6.10: High-resolution C 1s spectrum of a) the untreated powder mixture, b) the modified surface after an Ar:O₂ plasma, c) the modified surface after an Ar:NH₃ plasma and d) the modified surface after an Ar:N₂ plasma.

The functionalization for an Ar:O₂ plasma treatment at 200 W (Figure 6.10(b)) is the highest compared to the nitrogen-based plasmas and with a contribution over 70% of the total C 1s peak area attributed to C-O, C=O and O-C=O groups. In the case of nitrogen-based plasmas, 45% of the total C 1s peak area comes from the contribution of functional groups (C-O, C-N, C=O and O-C=O) and results in the lowest functionalization for the Ar:NH₃ treatment (Figure 6.10(c)) while, for the Ar:N₂ plasma, the functionalization reaches around 60% of the total C 1s peak area with a dominant C-O/C-N contribution. The global carbon functionalization is summarized in Figure 6.12(a). An important point must be underlined about the origin of the functional groups seen in the HR-XPS spectra; most likely three contributions could explain the results found for the different plasma treatments : (i) oxygen or nitrogen atoms are able to be incorporated onto the surface of the carbon support by replacing carbon atoms, (ii) functional groups could be grafted from the interaction of free radicals produced in the plasma discharge and the surface, and (iii) deposition of organic fragments, coming from the OM precursor degradation, which leads to the formation of a polymer-like coating onto the carbon surface. Moreover, the analysis of C 1s spectra are relatively difficult, for nitrogen-based treatments, due to the impossibility to separate the contributions of C-O and C-N bonds. Indeed, the BEs of both functional groups are extremely close and cannot be distinguished from each other.

A close look at the HR-XPS N 1s spectra allows to determine the amount of nitrogen and the chemical groups added to the carbon support (Figure 6.11 and Figure 6.12). The quantification of nitrogen for plasmas at 200 W indicates that the highest content is found for the Ar:N₂ treatments with ~12 at.% of N atoms at the surface, while it reaches ~7 at.% for the Ar:NH₃ plasma. Going further, three components ascribed to nitrogen groups can be fitted at 398.5, 400.0, and 401.0 eV BEs which corresponds to pyridinic, pyrrolic and graphitic-N groups, respectively [213]. Additionally, a peak at 397.5 eV was also fitted and is assigned to Ni₃N [228]. The Ar:NH₃ discharge at 200 W (Figure 6.11(a)) exhibits a main contribution from pyridinic-N groups (~65% of the total N 1s peak area) while, for the Ar:N₂ treatment, it reaches up to 50% (Figure 6.12(b)). However, the contributions from pyrrolic-N and graphitic-N groups are higher for the Ar:N₂ gas mixture which represent ~30% and ~8% of the total N 1s peak area, respectively. This is summarized in Figure 6.12(b). The difference between the two nitrogen-based chemistries could be particularly interesting for applications in which the functionalization has to be controlled and requires to avoid some types of functional groups; especially, in catalysis, researches have shown the enhancement effect of the N-function types on the catalytic activity [108, 110, 229].

Therefore, the XPS analysis clearly indicates that the functionalization of the carbon support as well as the NP oxidation states depend on the plasma chemistry. Depending on the application and the need for avoiding specific functional groups,

it has been shown that the functionalization can be controlled through a relatively simple change of the gas mixture employed during the synthesis.

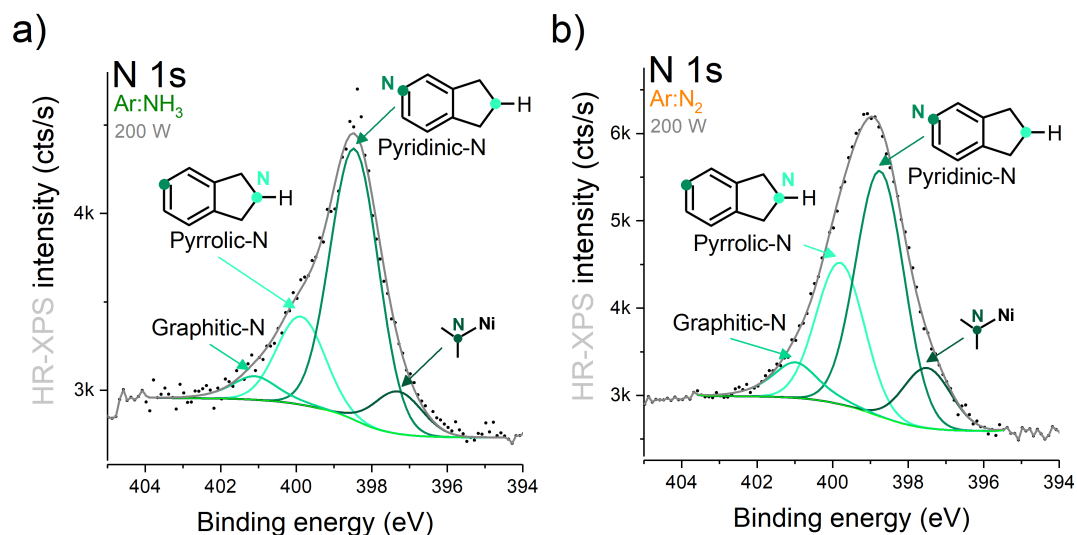


Figure 6.11: HR-XPS N 1s spectra of a 200 W plasma treatment for an a) Ar:NH₃ and b) an Ar:N₂ gas mixture.

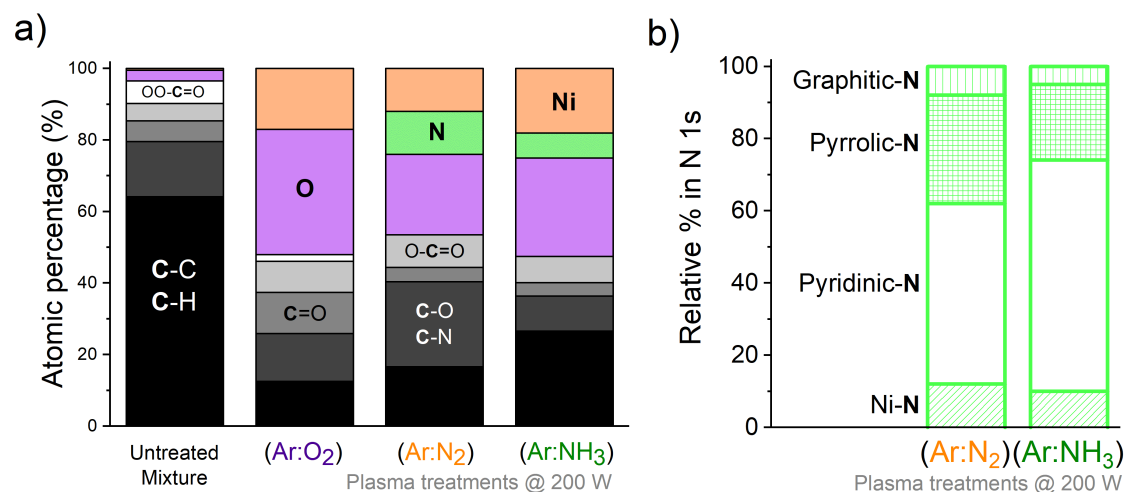


Figure 6.12: a) Global chemical composition of the treated samples (200 W) for the different plasma chemistries. b) Relative percentage of the nitrogen-groups derived from the analysis of the N 1s spectra for the two explored N-containing gas mixtures explored (200 W).

6.6 Conclusions and perspectives

The present chapter discussed on the synthesis of Ni/C nanocatalysts with the help of an original plasma-based methodology allowing to decompose the Ni(acac)₂ precursor and form Ni NPs on carbon xerogel. This study aimed to get new insights into the processes involved during the plasma treatment by exploring an oxidizing (Ar:O₂), a reductive (Ar:NH₃) and an inert (Ar:N₂) plasma chemistry. The plasma power was varied from 90 to 200 W for each gas mixture and systematic studies were performed including the precursor decomposition kinetics, morphology of the NPs and their chemical composition, and the carbon xerogel functionalization.

First, it was shown that, by analogy with an Arrhenius law, an "activation power" (*i.e.* power needed to start the OM decomposition) could be derived for each plasma chemistry. Despite the relative high activation power for the Ar:NH₃ discharge, results tend to show a more effective decomposition at higher plasma power (200 W). This is attributed to an increased amount of reducing hydrogen atoms in the plasma, coming from the dissociation of ammonia, leading to new precursor degradation ways. For the Ar:N₂ plasmas, the activation power is intermediate in comparison with the two other gas mixtures. However, the activation powers for the different plasma chemistries seem to be close to each other considering the error bars and further investigations on that point have to be performed.

The analysis of TEM/STEM images indicate that the NP size distributions depend on the treatment conditions, *i.e.* the transmitted power and plasma chemistry. The lowest sizes were found for the inert Ar:N₂ treatment with size distributions around 1–3 nm. On the other hand, for Ar:O₂ and Ar:NH₃, the size distributions are similar with a range between 3 and 6 nm for the explored conditions. However, for all the investigated treatments, TEM images clearly show homogeneously dispersed NPs.

Finally, results derived from the XRD measurements and XPS analysis show the formation of partially metallic and Ni₃N NPs for Ar:NH₃ plasmas. The formation of Ni₃N could be particularly interesting for catalysis applications as already reported in the literature [223]. The inert Ar:N₂ treatments result in completely oxidized NPs at low plasma power while a metallic contribution appears at higher power; this was attributed to the formation of an increased fraction of reducing Ar⁺ species in the plasma helping the precursor degradation and the reduction of the oxidized NPs. Moreover, every plasma treatment allows the functionalization of the carbon support. As it was expected, Ar:O₂ plasmas result in the highest incorporation of functional groups including carbonyl and carboxyl functions. For the Ar:NH₃ plasmas, it was shown that the functionalization is mainly due to pyri-

dinic and pyrrole-type groups but result in the lowest nitrogen incorporation in comparison with the Ar:N₂ treatments. In addition, a pretreatment of the carbon support could be performed in a plasma discharge by using a specific gas mixture. This can lead to the incorporation of desired functional groups and, afterwards, synthesize the NPs by adding the metal precursor and treat the reactants with a plasma suitable for degrading the precursor while maintaining, at least to some extent, the functionalization of the carbon support. The incorporation of functional groups into the support has several positive effects as discussed in section 1.5.

In summary, the low-pressure plasma discharge methodology demonstrated its ability to synthesize nickel nanoparticles anchored on carbon xerogel and allowing to control both the NPs' chemical composition and carbon functionalization by only varying the plasma treatment and gas mixture. Therefore, the relatively easy and fast synthesis of nickel NPs by low-pressure plasma validates the methodology for several applications among which catalysis.

Chapter 7

Defective Pt-Ni/graphene composites fabricated by low-pressure oxygen plasma treatment

This chapter describes results that have been the object of the following publication [230] :

M. da Silva Pires, E. Haye, A. Zubiaur, N. Job, J.-J. Pireaux, L. Houssiau, & Y. Busby, Defective Pt-Ni/graphene nanomaterials by simultaneous or sequential treatments of organometallic precursors by low-pressure oxygen plasma, *Plasma Processes and Polymers*, 16(5):1800203, 2019.

7.1 Introduction

Recently, strategies have been developed to lower the platinum-group metal content in the nanoparticles (NPs) used for electrochemical reactions, especially in polymer electrolyte membrane fuel cells (PEMFCs). However, alternatives do not always exhibit high enough catalytic activities and improvements are needed. As discussed in section 1.3.4, several promising ways to achieve those goals are based on the use of a second metal ($M = \text{Co}, \text{Fe}, \text{Ni}, \text{Mn}, \text{etc.}$), including but not limited to Pt-M alloys, Pt-M core-shell NPs, hollow Pt-M NPs or defective Pt-M NPs [59, 67, 69, 162]. This last possibility regroups small aggregates, the presence of grain boundaries induced by multiple domains orientations and bulk defects. At the same time, improving the catalytic activity could be achieved by modifying the high surface area carbon support by creating structural defects at its surface; these play a major role as they act as anchoring sites for the nucleation of the growing NPs.

In the present chapter, bimetallic Pt-Ni/C were fabricated by the decomposition of two organometallic (OM) precursors, *i.e.* Pt(II) acetylacetonate and Ni(II) acetylacetonate (see Table 3.1), with the help of low pressure RF plasma discharges. The advantages of such a process have already been presented as these treatments allow a control over the morphology and chemistry of the synthesized NPs by simply varying different parameters. The first part of this chapter (section 7.2) is dedicated to the experimental setup for the synthesis of Pt-Ni/GNP composites. Two strategies have been explored for the NPs processing in order to get new insights into the degradation and the growth mechanisms. A simultaneous (one-step) or sequential (two-step) treatment was applied to decompose the OM precursors and will be explained in section 7.2.1.

The OM precursors decomposition was checked by XRD measurements (section 7.3); both precursors employed in this study exhibit peaks in the diffractogram due to their crystalline structure, which disappear after their decomposition in the plasma discharge. Furthermore, the NPs formation was investigated by XRD and the average sizes of the crystalline domains were calculated as well thanks to the Debye-Scherrer formula (Equation 4.5). In section 7.3.1, the morphology of the synthesized Pt-Ni/GNP composites was then investigated by TEM/STEM at an acceleration voltage of 200 kV. Images acquired were analyzed to determine the NP size distributions by using the image software ImageJ. Elemental analysis of the synthesized NPs were performed thanks to the EDX maps allowing to correlate the plasma conditions with the nucleation mechanism. In section 7.4, the chemical composition and carbon functionalization were derived from the XPS analysis; high-resolution C 1s, O 1s, Ni 2p, and Pt 4f spectra were acquired at a fixed pass energy of 30 eV. The number of scans was set between 8 and 32 to get signal-to-noise ratios which were similar between the different analyses. Finally, the electrochemical properties were investigated in a three-electrode cell at room temperature, the procedure setup for the catalytic activity measurements and results are discussed in section 7.5.

The contribution of the author of this thesis to the present work includes (1) the synthesis of the Pt-Ni/C composites by low-pressure plasma discharges, (2) the acquisition of the XPS spectra, TEM images and XRD diffractograms, (3) the processing of the collected data, and (4) the preparation of the manuscript for publication. The Physico-Chemical Characterization (PC²) platform of the University of Namur is acknowledged for the XRD and ICP-OES measurements; SERMA Technologies (Grenoble) is acknowledged for the TEM/STEM images with EDX maps acquisitions; the Synthesis, Irradiation and Analysis of Materials (SIAM) platform of the University of Namur is acknowledged for the XPS measurements; and the Department of Chemical Engineering - Nanomaterials, Catalysis, Electrochemistry (NCE) at the University of Liège is acknowledged for the electrochemical characterizations.

7.2 Experimental section

7.2.1 Experimental section

Bimetallic composites were fabricated on a carbon matrix made of GNPs (Strem Chemicals); their physical characteristics are a lateral size of $\sim 5 \mu\text{m}$, a thickness of $\sim 6 \text{ nm}$ and a surface area of $\sim 150 \text{ m}^2\text{g}^{-1}$. The procedure described in section 3.3 was used in both simultaneous and sequential processes and a sketch of the later is shown in Figure 7.1.

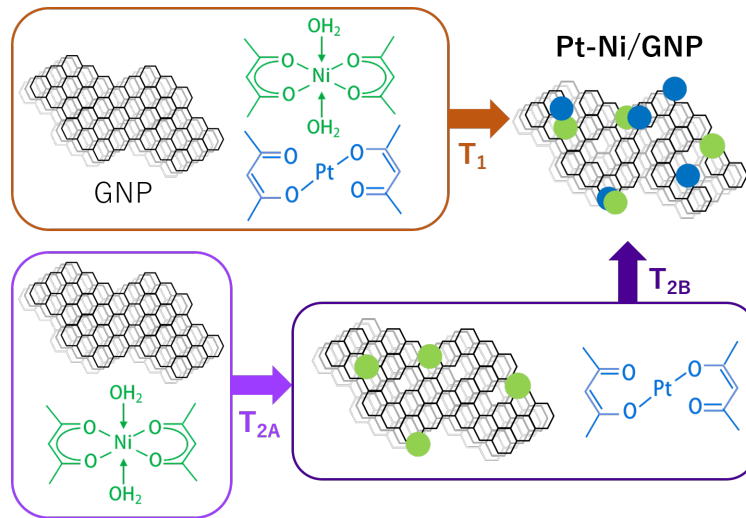


Figure 7.1: Sketch of the simultaneous (T_1) and sequential (T_{2A} and T_{2B}) treatments employed for the fabrication of the Pt-Ni/GNP nanocomposites.

The simultaneous treatment (denoted as T_1) consisted in mixing both OM precursors with the carbon support and uniformly disperse the reactants in a glass Petri box. The sample was then placed in the plasma reactor which was pumped down to reach a vacuum of $\sim 10^{-2}$ mbar. Afterwards, a turbomolecular pump was used for at least 10 minutes to remove as much as possible residual molecules that could interact with the sample during the treatment and cause contamination. An oxygen flux, fixed at 5 sccm, was injected in the reactor and the oxygen plasma treatment without stirring (to avoid the aggregation of Ni atoms on the magnet due to the ferromagnetic behavior of Ni) was then applied to the mixture. The primary pump was employed during the treatment and the pressure in the chamber about $\sim 10^{-1}$ mbar. For the sequential process (denoted as T_2), the carbon matrix was first mixed with the Ni precursor and treated following the same procedure as described above (T_{2A}). Thereafter, the sample was removed from the chamber, the Pt precursor added and followed by a second plasma treatment to degrade the Pt OM leading to the nucleation of Pt NPs (T_{2B}).

A low-energy pulsed plasma has been employed in T_1 and T_{2B} during 40 minutes characterized by a power of 80 W, a duty cycle of 50% and a frequency of 10 Hz. Immediately after, a high-energy continuous plasma treatment was used during 8 minutes at 100 W followed by 5 minutes at 150 W. The choice of these conditions was based on previous treatments, too energetic plasma discharges led to coalescence of the metal NPs while lower energies do not permit the degradation of the OM precursors. In the case of T_{2A} , the same low-energetic plasma treatment as describe for T_1 and T_{2B} was applied to allow the nucleation of Ni seeds onto the carbon matrix.

7.2.2 Reducing effect of the oxygen plasma

The use of an oxygen plasma instead of N_2 or Ar, which are considered as less reactive gases, was motivated by its ability to decompose the OM precursors and reduce the metallic content to a zerovalent state. High-resolution (HR) XPS spectra of the Pt 4f doublet shows such a reducing effect of an O_2 plasma for the T_2 treatment as illustrated in Figure 7.2. The main doublet components centered at 71.1 (Pt 4f_{7/2}) and 74.1 (Pt 4f_{5/2}) eV binding energies are attributed to metallic Pt, as already reported in section 5.2.3, while doublet peaks at 72.8 (Pt 4f_{7/2}) and 76.2 (Pt 4f_{5/2}) eV binding energies are ascribed to Pt hydroxide [209].

The mechanisms involved during these treatments are still not yet well understood due to the difficulty of obtaining information on electrons or other reactive species present in the low-pressure plasmas. Nevertheless, Wang et al. [101] advanced a possible process at the origin of the reducing effect mechanism in a plasma discharge; highly energetic electrons produced during the plasma treatment could act as reducing agents by interacting with the metal NPs and forming an electric shell on the latter. This results in electrostatic repulsion between the NPs which could also lead to their restrained sizes. Zou *et al.* [165] evidenced the same reduction effect on noble-metal-based NPs with the help of an O_2 plasma. However, based in Figure 7.2, electrons could not be solely responsible for such a reducing effect due to differences between gases employed for the treatment. More specifically, O_2 plasma led to the mainly metallic Pt content compared to N_2 and Ar treatments. Another or complementary mechanism is proposed here to explain the formation of Pt^0 particles : the creation of reducing species in the oxygen plasma, such as ionized hydrogen atoms or reactive molecular species, released by the decomposition of the OM precursors. Further experiments should be conducted to confirm or not both mechanisms presented above.

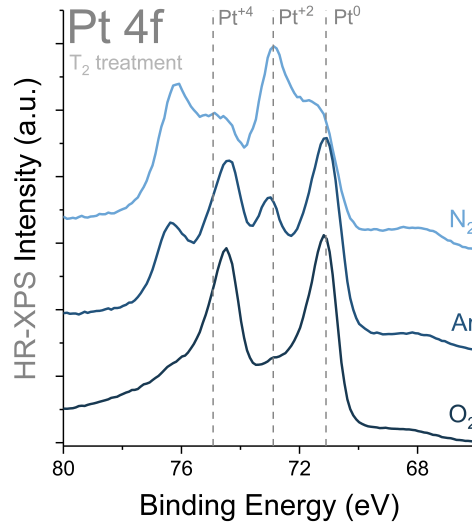


Figure 7.2: HR-XPS Pt 4f spectra resulting of an O₂, Ar and N₂ plasma treatments respectively following the conditions presented for T₂. The reducing effect in the case of an O₂ discharge is clearly evidenced.

7.3 Decomposition of the precursors and nanoparticle formation

The precursor decomposition and the formation of crystalline particles were analyzed by XRD for both employed strategies. Figure 7.3 shows the diffractograms obtained for the Pt and Ni acetylacetonate, for the simultaneous (T₁) treatment and the two steps (T_{2A} and T_{2B}) of the sequential treatment. In order to allow a comparison between the different plasma-treated signals, a normalization was performed considering the intensity of the graphene (111) peak. For the two organometallic precursors, the signal presents a main contribution between 5 and 30°. These peaks almost completely disappear after the most energetic plasma treatment for both simultaneous and sequential treatments. However, precursor traces are more visible for T_{2B} in comparison with T₁ which could indicate that the sequential treatment is not powerful enough to completely degrade the precursors. Two peaks located at 27 and 54.9° are attributed to the graphene sheets [231], while peaks at 39.9, 46.3 and 67.5° are attributed to face-centered cubic Pt crystalline NPs [207].

For both treatment strategies, peaks attributed to Pt show a comparable FWHM leading to similar domain average size around 5.2 ± 1.3 and 4.0 ± 1.0 nm for T₁ and

T_{2B} , respectively. Interestingly, no signal characteristic of the presence of crystalline Ni^0 , NiO or $Ni(OH)_2$ domains is present which may be due to amorphous or too small crystal domains; the formation of crystalline NiO domains could only happen at higher plasma power as discussed in section 6.2. However, as mentioned in section 5.3.3, the main reason to limit the transmitted plasma power with such a carbon matrix is to avoid the presence of too many defects at its surface which could have a negative impact on the physico-chemical properties and thus being not useful in catalysis for example [212].

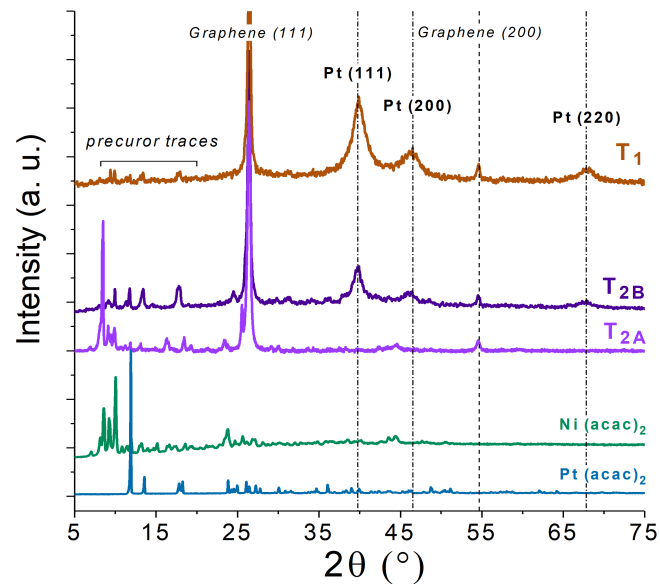


Figure 7.3: Diffractograms of the metallic precursors (blue and green lines), the sequential treatment (T_{2A} and T_{2B} , purple lines) and the simultaneous treatment (T_1 , rust-colored line). The graphene and platinum peaks are clearly indicated with the corresponding Miller indexes as well as the precursor traces.

7.3.1 Morphology of the Pt-Ni/graphene nanocomposites

As mentioned above, the morphology of the fabricated nanocomposites was investigated by TEM/STEM images analysis. In the case of the simultaneous (T_1) treatment, HR-TEM images clearly show a complex morphology in which some of the formed NPs exhibit fringes due to the electron diffraction with the crystallographic planes (Figure 7.4(a)). The NP size distribution derived from the TEM images is comprised between 3 up to 6-7 nm with an average size of 4.7 ± 0.9 nm (Figure 7.5). In Figure 7.4(b), the high-angle annular dark field (HAADF) STEM image confirms the complex morphology found previously and shows the presence of nanostructured domains with a size up to 10 nm. Moreover, the gray-

scale contrast in the HAADF STEM image highly depends on the atomic number of the present elements. Therefore, the T_1 treatment leads to interconnected domains, *i.e.* areas constituted of Pt particles surrounded by Ni and which are not PtNi alloys (even if it is possible to form them under the explored conditions, see Appendix F for the Ni-Pt phase diagram), with various compositions and with a rather high variability over the surface as it can be seen in Figure 7.4(b). Furthermore, the EDX maps confirm that Ni and Pt tend to form both nanostructured and interconnected domains.

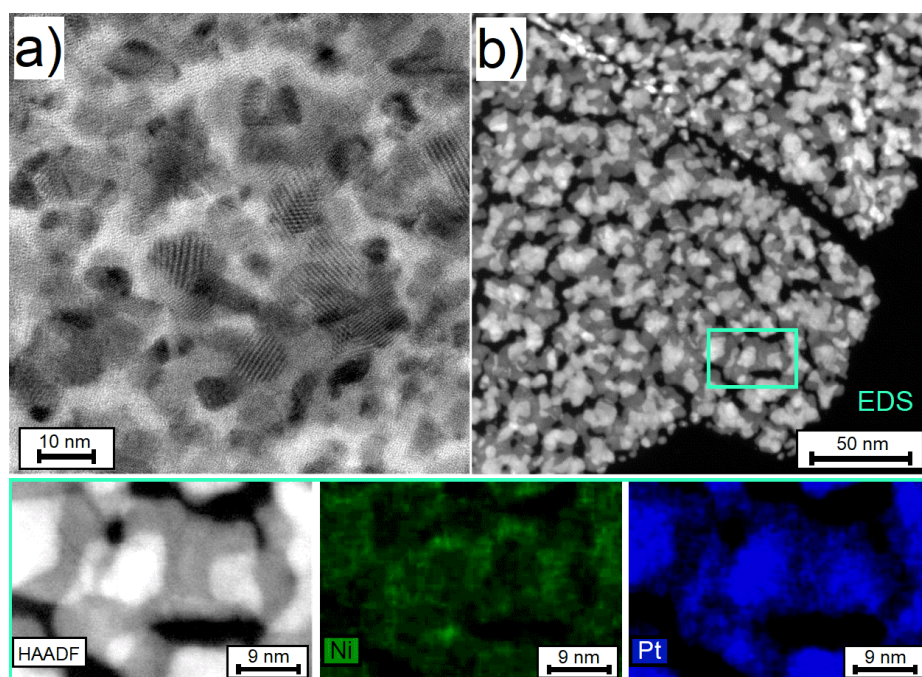


Figure 7.4: (a) High-resolution TEM image of the Pt-Ni/GNP composites obtained after the simultaneous plasma treatment (T_1). (b) STEM image together with the EDX maps acquired on a specific region (shown on the STEM image) highlighting the Pt and Ni species distribution on the surface.

The effect of the T_{2A} plasma treatment on the formation of Ni particles was first investigated. The plasma conditions presented in section 7.2.1 were applied to a mixture comprising both GNPs and the Ni precursor. The plasma treatment clearly induces the formation of Ni seeds on the surface of the GNPs. This can be seen when comparing the pristine and the treated mixture (Figure 7.6(a) and (b)). It is believed that the creation of structural defects (which consists in low coordinated carbon atoms) occurred and help in the formation of NPs by acting as nucleation sites when an OM precursor is added and then treated under the plasma discharge. Thus, the first step of the proposed nucleation mechanism consists in the formation of preferential nucleation sites in which Ni seeds are able to grow.

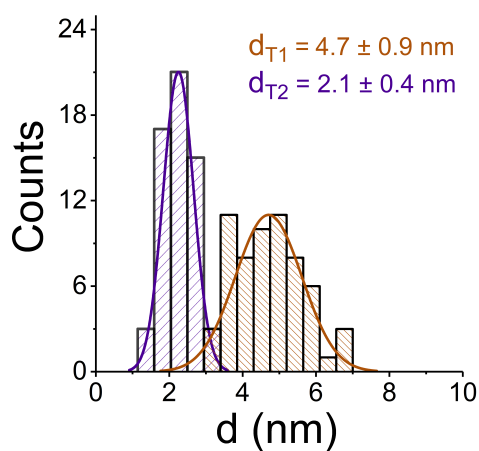


Figure 7.5: Size distribution for the simultaneous (T_1 , rust-colored line) and sequential (T_2 , purple line) plasma treatments derived from the TEM/STEM images.

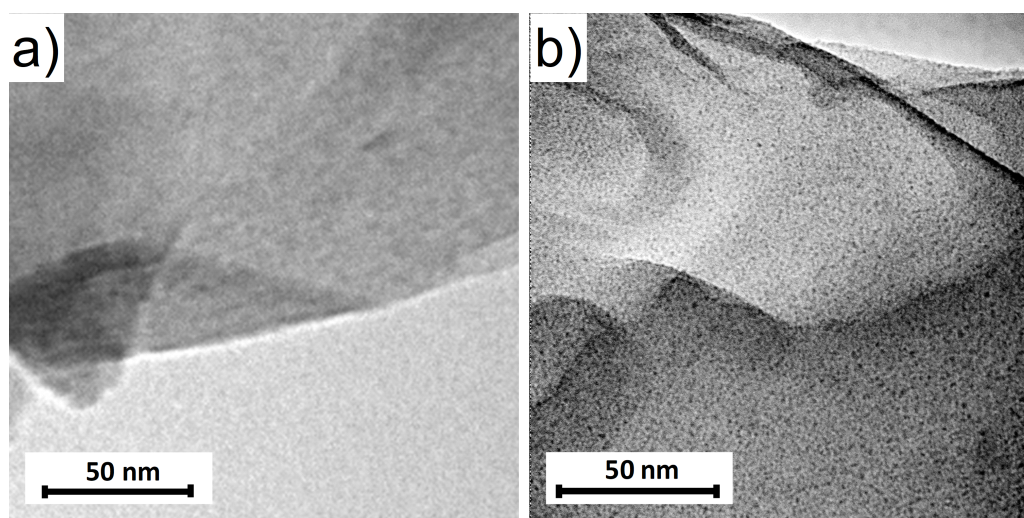


Figure 7.6: Bright field TEM images of (a) the pristine GNPs employed as a support for the NPs and (b) sub-nanometer Ni seeds formed on the carbon support surface after the T_{2A} plasma treatment of the GNP mixed the Ni precursor.

Regarding the global T_2 treatment of the Ni precursor and then the Pt one, it is interesting to note a completely different morphology for the synthesized NPs in comparison with the T_1 plasma treatment. From the different areas analyzed, NPs with a size comprised between 1 and 3 nm, with an average size of 2.1 ± 0.4 nm (Figure 7.5), are homogeneously dispersed at the surface of the graphene sheets with no particle coalescence (Figure 7.7). Thus, as mentioned above, the Ni NPs

formed during the T_{2A} treatment seemed to act as preferential nucleation sites for the growth of Ni particles. Then, the formation of Pt particles occurred during the T_{2B} treatment. Moreover, the morphology analysis indicates that the T_{2B} plasma treatment is the main step responsible for the growth of the Pt nanoparticles.

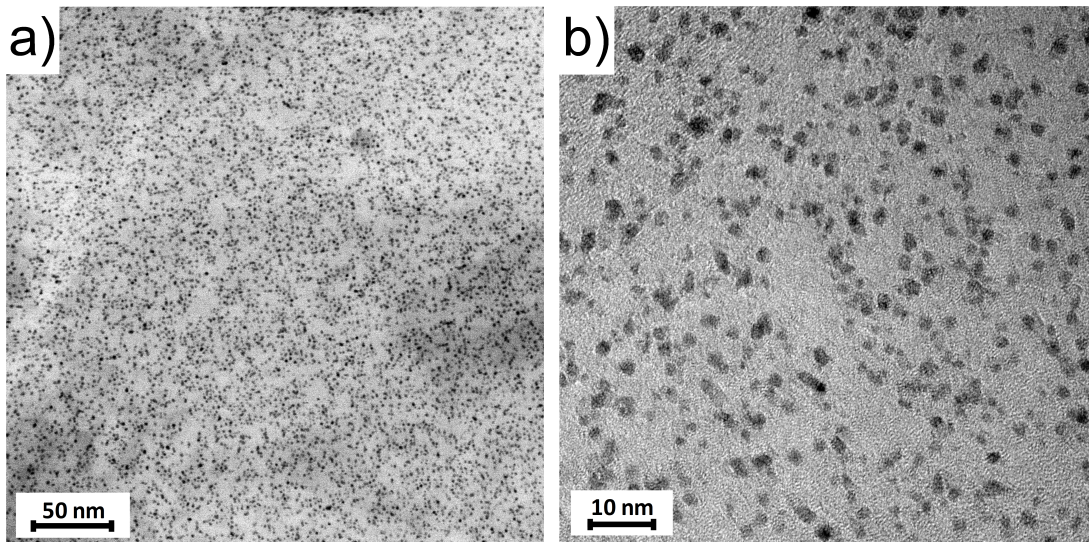


Figure 7.7: (a) Low magnification and (b) high magnification bright field TEM images of the Pt-Ni/GNP composites obtained after the sequential plasma treatment (T_2). Well-separated 1-3 nm Pt-Ni nanocomposites are clearly homogeneously dispersed at the surface of the graphene sheets.

Finally, a comparison of the morphologies obtained after the two strategies (T_1 and T_2) employed for the synthesis of Pt-Ni/GNP nanocomposites, as seen in Figure 7.8, suggests different nucleation and growth mechanisms. For the simultaneous T_1 treatment, the plasma is assumed to create defects, which consists in carbon vacancies, at the surface of the graphene sheets or the adjunction of oxygen functional groups; these act as anchoring sites where the Ni and Pt particles are able to nucleate simultaneously [164, 232]. On the other hand, the mechanism involved in the sequential T_2 treatment is hypothetically explained by the binding of molecular fragments from the Pt precursor, activated by the plasma, on the previously formed Ni particles. Thus, it results in the formation of Pt-Ni aggregates. This is in agreement with the analysis of XRD diffractograms (Figure 7.3) which indicates the presence of precursor residuals. Moreover, the plasma treatment could partially decompose the precursor into amorphous molecular fragments which do not appear in the diffractograms. The presence of these molecular fragments could be highlighted from the XPS analysis (section 7.4).

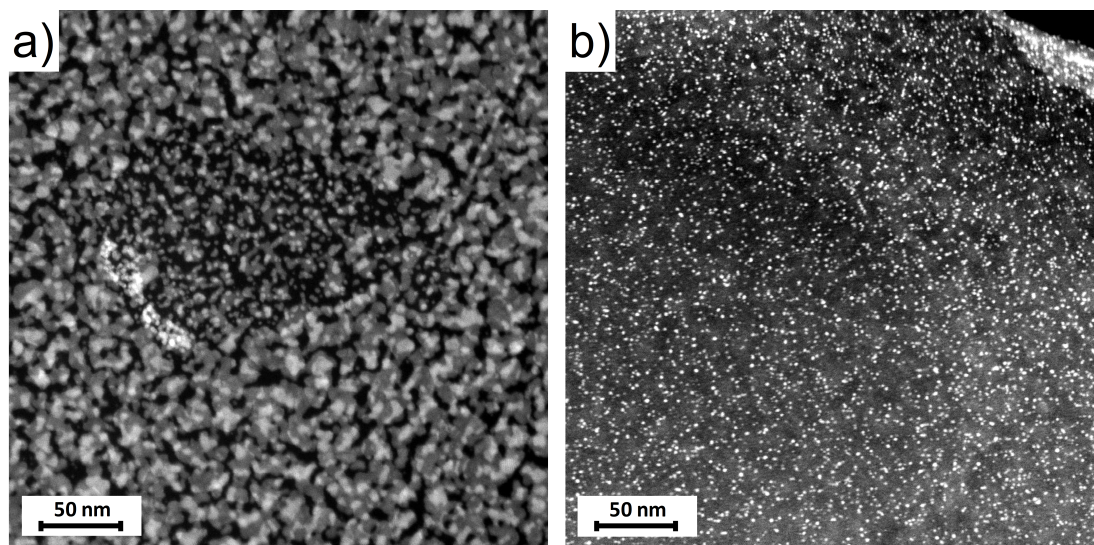


Figure 7.8: High angle annular dark field STEM image of the synthesized Pt-Ni/GNP nanocomposites after (a) the one-step (T_1) plasma treatment and (b) the two-step (T_2) plasma treatment of the two OM precursors. The brighter spots correspond to elements with a high element number and are due to the metal atoms, while the darker areas correspond to carbon.

7.4 Chemical analysis of the Pt-Ni/graphene composites

The chemical compositions of the two plasma treatment conditions T_1 and T_2 were studied by XPS, the elemental quantification was performed from the survey spectra (see Appendix G) while the chemical environment of the synthesized NPs was investigated from the HR-XPS C 1s, O 1s, Pt 4f and Ni 2p core level spectra (Figure 7.9). In both cases, the atomic percentages of oxygen are similar, with 17 at.% for T_1 and 16 at.% for T_2 . The same observation is reported for the Ni content (6.0 and 4.0 at.% for T_1 and T_2 , respectively). The main difference is found for the Pt content, the T_1 treatment exhibiting an atomic percentage almost three times higher than the T_2 treatment (12.5 and 4.5 at.%, respectively).

The analysis of the C 1s spectra in Figure 7.9(a) does not indicate that the plasma conditions have a strong influence on the carbon functionalization; both spectra exhibit a main component at 284.8 eV corresponding to the C-C and C-H bonds which represent $\sim 73\%$ of the C 1s total peak area. Three other components attributed to C-O (286.1 eV, $\sim 17\%$), C=O (287.9 eV, $\sim 5\%$) and O-C=O (289.9 eV, $\sim 5\%$) are also clearly visible. The carbon functionalization is believed to come from organic fragments present in the plasma depositing after the organometallic precursors decomposition, non-degraded residuals (characteristic XRD peaks still

visible in Figure 7.3) and from the interaction between the O₂ plasma and the graphene sheets.

Interestingly, a comparison of the HR-XPS O 1s core level spectra (Figure 7.9(b)) for the simultaneous and sequential treatments shows an evident difference : three components can be fitted at 528.5, 531.0 and 532.6 eV which are ascribed to metal oxides, hydroxides and organic oxygen groups, respectively. The contribution of metal oxides to the total peak area reaches up to $\sim 10\%$ for the T₁ treatment while it only represents $\sim 5\%$ for the T₂ treatment.

Regarding the Pt 4f doublet spectra in Figure 7.9(c), the main components at 70.8 (Pt 4f_{7/2}) and 74.1 (Pt 4f_{5/2}) eV binding energies are ascribed to metallic Pt; the asymmetric shape of this component was previously fitted on a reference Pt electrode. Additional Pt 4f_{7/2} components at 72.3, 73.8 and 74.9 eV binding energies were fitted; according to the literature, these are ascribed to Pt hydroxides, or possibly OM precursor residuals (see the HR-XPS Pt 4f spectra of the OM precursor in Figure 5.5), and to Pt oxides [209]. Thus, the mechanisms leading to the formation of Pt-O-C or Pt-O-Ni bonds on the carbon matrix or on the surface of Ni particles is believed to occur due to the presence of Pt hydroxides. For the sequential T₂ treatment, a peak clearly appears at ~ 68.0 eV binding energy which is attributed to the Ni 3p doublet. As mentioned previously, it is noteworthy that the quantification analysis indicates a three times higher content of Pt after the simultaneous treatment in comparison with the sequential one. The proposed explanations of such a difference are a more complete Pt precursor decomposition after T₁ and/or the completely different morphology of the Pt particles. Indeed, the first 3 nm of the sample surface are responsible for over 90% of the XPS signal intensity due to the limited escape depth of the photoelectrons. Therefore, the metal atomic percentages deviate from the expected mass ratio values in the case of heterogeneous surfaces like metal particles of few nanometers on carbon, as mentioned in section 4.1. Figure 7.8 illustrates the completely different morphologies resulting of the two strategies explored. The surface covered by Pt domains seems higher for T₁ when compared with T₂. It results in a higher quantification in Pt content for the simultaneous treatment, which is in agreement with the XPS analysis.

The analysis of the Ni 2p doublet is rather complex due to the difficulty to distinguish the different components present in the spectrum. However, by simply observing the shake-up satellites at 860.6 and 879.5 eV and their line-shapes (Figure 7.9(d)), the presence of Ni hydroxides is unambiguous. Indeed, based on the work of Biesinger *et al.* [226] and Grosvenor *et al.* [233] (see Appendix E), the characteristic signature of Ni hydroxides appears clearly in the HR-XPS Ni 2p spectra. The simultaneous treatment exhibits a non-negligible contribution from Ni⁰ (Ni 2p_{3/2} at 852.5 eV) which accounts for less than 5% of the Ni 2p_{3/2} peak

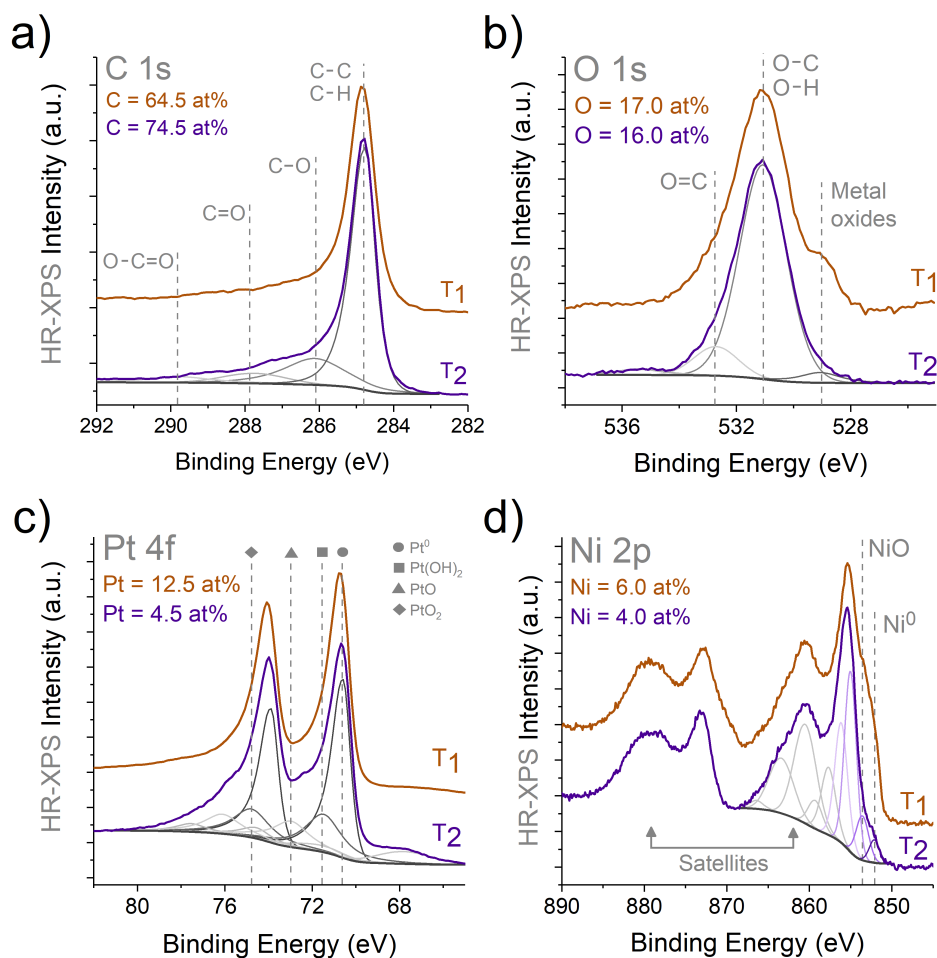


Figure 7.9: HR-XPS core level spectra of the a) C 1s, b) O 1s, c) Pt 4f and d) Ni 2p elements after the simultaneous (T₁, rust-colored line) and the sequential (T₂, purple line) treatments.

area while, for the sequential treatment, it only represents a weak contribution. For both treatments, the presence of NiO at ~ 853.5 eV binding energy (Ni 2p_{3/2}) is also found and accounts for less than 10% of the Ni 2p_{3/2} peak area. The shoulder peak attributed to metal oxides in the O 1s spectrum of the T₁ treatment is therefore believed to come from the NiO state oxygen atoms, the oxygen affinity of Ni being higher in comparison with Pt. Moreover, from the Pt 4f spectrum (rust-colored line in Figure 7.9(c)), only weak oxide components are derived. Finally, for the T₁ process, regardless of the complexity in fitting the Ni 2p spectrum, the amount of metal hydroxides represents ~ 2.0 at.% of the surface composition (which was estimated from the O 1s spectrum) and the Pt(OH)₂ content derived from the Pt 4f spectrum was estimated at ~ 1.0 at.%. Thus, the amount of Ni and Pt hydroxide are similar. For the T₂ treatment, no significant formation of

Ni-O or Pt-O bonds is noticed. From the O 1s spectrum, the quantification of metal hydroxides represents ~ 3.0 at.% of the surface composition which is mainly attributed to Ni hydroxide (~ 2.5 at.%), the Pt(OH)₂ content reaches only ~ 0.5 at.%.

Thus, results found by analyzing the XPS spectra indicate that T₁ allows to form more metallic nanocomposites in comparison with T₂. Indeed, T₁ was also able to form more Ni⁰ than T₂. Moreover, the three times higher Pt content after the simultaneous treatment could be explained by a high coverage of Pt domains at the surface of the GNPs. For the sequential T₂ treatment, the present of a higher Pt oxidation state is believed to come from a partial decomposition of the OM precursor (which is confirmed by the diffractograms, Figure 7.3). Therefore, a slightly higher energetic plasma treatment could lead to the formation of an increased amount of metallic Pt.

7.5 Catalytic activity of the Pt-Ni/graphene composites

The last section concerns the electrochemical properties of the Pt-Ni/GNP composites. The sample preparation and the electrochemical characterizations were performed by Mr. A. Zubiaur (ULg) following the procedure described in appendix H and section 7.5.1.

7.5.1 Procedure setup for the electrochemical characterizations

The electroactive surface area of the NPs was measured by the CO stripping experiment [72, 200, 201]. The procedure was initiated by the application of a steady potential of 0.1 V vs. RHE (reference hydrogen electrode) to the working electrode, while gaseous CO was bubbled in the electrolyte solution for 6 minutes. After an Ar purge of 39 minutes which removes the CO dissolved in the electrolyte, the CO chemisorbed at the surface of the particles was electrooxidized into CO₂ by increasing the electrode potential from 0.05 to 1.23 V vs. RHE at 0.02 V s⁻¹. The electroactive surface area was calculated from the CO oxidation peak current, assuming that the electrooxidation of a full monolayer of CO_{ads} requires 4.2 C m_{Pt}⁻² [234].

The activity of the catalysts for the ORR was measured on a Rotating Disk Electrode (RDE) setup. After saturation of the electrolyte by oxygen bubbling during 15 minutes, the electrode potential was (i) set at 0.4 V vs. RHE, (ii) then increased at 0.001 V s⁻¹ to 1.05 V vs. RHE, and (iii) decreased back to 0.4 V vs. RHE at the same scan rate while measuring the reduction current. This

measurement was repeated at two different rotation speeds of the electrode (1600 and 2500 rpm). For each rotation speed of the electrode, the kinetic current was calculated by correcting the measured current for the effect of the external mass transfer limitations in the solution using the Koutecky-Levich equation [194] :

$$\frac{1}{i_k} = \frac{1}{i} - \frac{1}{i_{l,c}} \quad (7.1)$$

where i_k is the kinetic current, *i.e.* the current without any mass transfer limitations, i is the experimental current, and $i_{l,c}$ is the cathodic limit current which depends on the rotation speed of the electrode. These two kinetic current values (one for each rotation speed) were then averaged in order to obtain the kinetic current of the catalysts. The values of this averaged kinetic current were divided by the electroactive surface of the catalysts in order to obtain the specific activity of the catalysts ($\text{A m}_{\text{Pt}}^{-2}$).

In order to compare the activity of the catalysts, the Tafel plots, *i.e.* the potential curves expressed as a function of the logarithm of the specific activity, were drawn. In addition to the specific activity (SA), the mass activity (MA) was also calculated by dividing the averaged kinetic current by the Pt mass present on the electrode. The mass of Pt on the electrode was set taking into account the previous measurements performed by ICP-OES (as explained in section 4.4) allowing to determine the amount of Pt present in the sample and, thus, expected on the electrode. The electrochemical results were compared to a reference commercial catalyst (Pt/C Tanaka 37 wt.%) measured in the same conditions.

7.5.2 Electrochemical characterizations of the Pt-Ni/C composites

The electrochemical properties of the T₁ and T₂ Pt-Ni/GNP composites were investigated by CO stripping and ORR activity measurements (with the corresponding Tafel curves). These properties are compared to those of a commercial Pt/C reference catalyst in Figure 7.10, showing the average results obtained with two different working electrodes prepared from the same catalyst ink. At this point, it is important to note that carbon black is employed as a catalyst support for the reference sample. Therefore, results from the comparison between the catalysts synthesized following the plasma approach and the Pt/C reference should be considered with caution.

The CO stripping voltammograms are normalized to the Pt surface area measured on the electrode because of the substantially different Pt loading and electroactive Pt surface (Figure 7.10(a)). The voltammograms show a broad peak at about 0.70 V vs. RHE which is not observed in the reference Pt/C catalyst and is attributed to defective crystallites. This feature is associated to low-coordinated

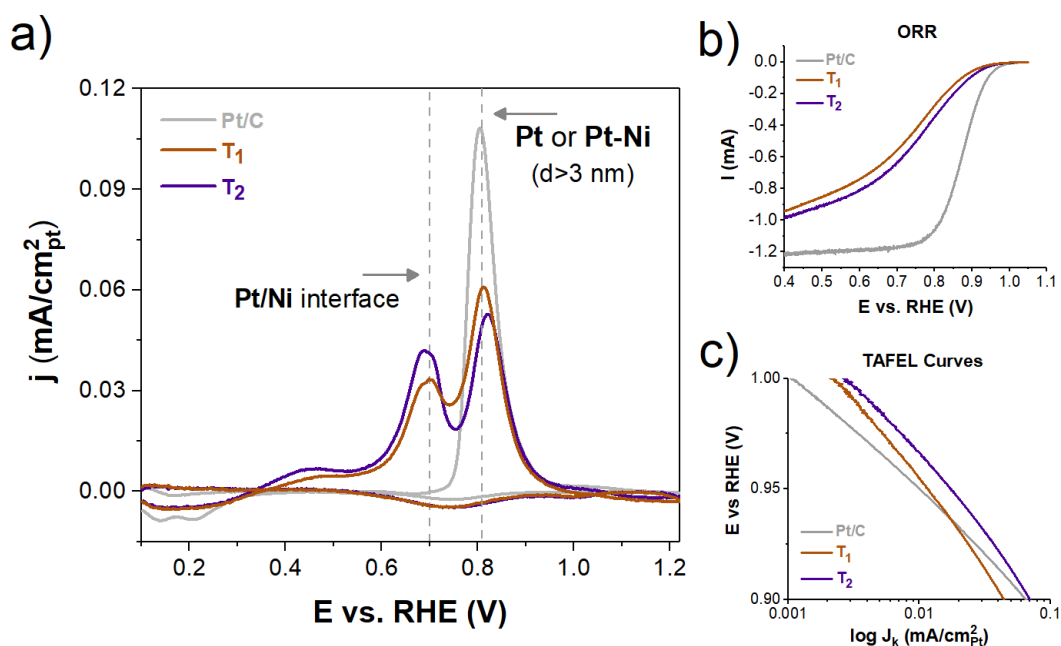


Figure 7.10: Electrochemical characterizations of the simultaneous (T_1) and sequential (T_2) Pt-Ni/GNP catalysts and the reference Pt/C catalyst. a) CO stripping voltammograms, b) ORR voltammograms and c) the derived Tafel plot.

Pt atoms at the grain boundaries between Ni and Pt or at the interconnection area between the small NP aggregates observed in STEM images (Figure 7.8). The other peak around 0.82 V vs. RHE is ascribed to Pt particles with a size of around 3 nm or higher, or possibly to PtNi alloys [69]. The electroactive surface area values obtained for T_1 , T_2 and the Pt/C reference catalysts are 21, 18 and 109 m² g_{Pt}⁻¹. The low values obtained for the electroactive surface area for the plasma treatments could be explained by a stacking of the graphene flakes on the electrode that prevent a full contact between the Pt particles and the electrolyte.

The ORR voltammograms acquired at 2500 rpm rotating speed are shown in Figure 7.10(b). The associated Tafel plots are visually compared in Figure 7.10(c); from the slope of the Tafel plots, we see that, for the T_1 and T_2 composites, we have a similar decay rate of 76 and 70 mV/dec which is higher than what is observed in the commercial catalyst (55 mV/dec). Taking into account the metal loading, the MA values at 0.95 V vs. RHE obtained for T_1 , T_2 composites and the Pt/C reference measured in the same conditions are 2.3, 3.3 and 10.9 A g_{Pt}⁻¹. Interestingly, the SA values at 0.95 V vs. RHE obtained for T_1 , T_2 and the Pt/C reference catalysts are 0.011, 0.019 and 0.010 A m_{Pt}⁻², respectively. The sequential treatment results thus in the highest SA value. This may be due to

two phenomena: (i) the presence of PtNi alloys at the surface of the NPs and (ii) the higher density of structural defects, as shown by the higher intensity of the CO oxidation peak situated at 0.70 V vs. RHE. Indeed, it is well known that the presence of PtNi alloy and of a high density of structural defects at the surface of the NPs improves the SA for the ORR [69, 72, 201, 234, 235]. However, from the XRD diffractogram (Figure 7.3), it was shown that most probably no PtNi alloy was formed after the plasma treatments. Therefore, the higher density of structural defects should be responsible for the higher SA of the T₂ treatment.

In summary, the plasma treated catalysts exhibit low electroactive surface area in comparison with the Pt/C reference. However, the values obtained for T₁ and T₂ are most probably underestimated due to graphene stacking on the electrode. Interestingly, from the ORR voltammograms, the T₂ treatment leads to the highest SA. Further analysis is thus required to get new insights into the electroactive surface and the stability of the plasma treated Pt-Ni/GNP nanocomposites. Therefore, it could confirm if these are promising for applications in catalysis.

7.6 Conclusions and perspectives

The present chapter showed the successful synthesis of bimetallic Pt-Ni/GNP nanocomposites through the decomposition of organometallic precursors in low-pressure RF-ICP plasma discharges. The original approach was based on a simultaneous (T₁) or a sequential (T₂) strategy in which oxygen plasmas were able to decompose the metal precursors and then form anchored Pt and Ni particles on the graphene sheets. The nucleation mechanisms and the morphology of the fabricated nanocomposites were investigated and related to the different plasma conditions. For the T₁ treatment, it has been shown that a simultaneous formation of defective Pt- and Ni-based particles on the carbon matrix occurred leading to a complex morphology. The chemical analysis together with the morphological investigations indicate the presence of interconnected Pt⁰, Ni⁰, Ni(OH)₂ and NiO domains characterized by a lateral size going from few nanometers up to 10 nm. For the T₂ treatment, homogeneously dispersed Ni particles anchored on the carbon support were previously formed which were believed to act as seeds for the nucleation and growth of defective Pt- and Ni-based particle aggregates with a size diameter about 2-3 nm. A sketch of the proposed mechanism is shown in Figure 7.11. Furthermore, the metal particles formed on the graphene sheets seem to be stabilize thanks to the formation of oxygen bonds during the plasma treatment as it was indicated by the XPS analysis.

The main limitation in the present study comes from the difficulty to provide an accurate elemental quantification due to the highly different morphologies. Indeed, the T₁ treatment leads to a complex morphology with interconnected domains, while T₂ allows to form homogeneously dispersed NPs at the surface of

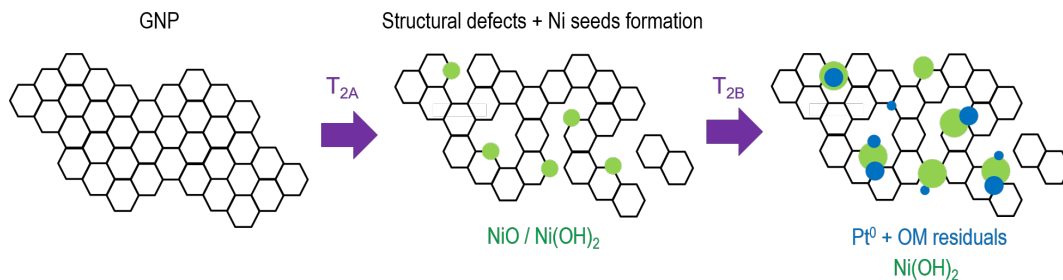


Figure 7.11: Sketch of the proposed NP nucleation and growth mechanism for the sequential (T_2) plasma treatment.

the carbon support. To quantitatively compare the results between the T_1 and T_2 treatments, it would be necessary to model the XPS quantification taking into account the particle morphology derived from the TEM/STEM analysis and a dedicated study should be performed in the future.

The electrochemical characterizations of the Pt-Ni/GNP composites obtained after both T_1 and T_2 plasma conditions were performed and compared to a reference Pt/C catalyst. The Pt-Ni/GNP composite obtained after the sequential treatment exhibits a slightly higher catalytic activity than the sample fabricated after the simultaneous treatment. This could be explained by the formation of a more important number of structural defects during T_2 . However, the values of the electroactive surface area found for the plasma treated samples are lower compared to the reference catalyst. It is expected that these values are underestimated and is probably due to the lack of contact between the Pt particles and the electrolyte. An alternative ink preparation could be investigated to prevent this effect and allow to completely access the surface of the particles on the surface of the graphene sheets.

In summary, it was shown that the low-pressure RF plasma treatment of metal precursors employed in this study is suitable for synthesizing defective bimetallic nanocomposites on graphene sheets. This method could be extended to other supports with a controlled morphology and surface chemical composition of the fabricated NPs. Moreover, this methodology is flexible, fast and requires a low-energy consumption. This opens up a new way for the synthesis of materials with broad applications in various domains such as catalysis and energy materials.

Chapter 8

Nitrogen-doping of carbon xerogels by low-pressure plasma discharges

8.1 Introduction

The present chapter is dedicated to the study of the nitrogen-doping (N-doping) of carbon xerogels. These nanomaterials consist in interconnected amorphous carbon particles with an almost spherical shape. Therefore, they present a specific structure and pore texture which can be controlled during the synthesis [95, 236]. This makes carbon xerogels highly promising as carbon supports for a wide range of applications among which catalysis, supercapacitors, etc. [237]. Nevertheless, tuning the properties of these materials is needed to improve their characteristics; it has been shown that N-doping allows an enhancement of the ORR catalytic activity, a better stability of the supported particles and affects the growth mechanisms [105, 112, 119], as already discussed in section 1.5.

Conventional methods employed to incorporate nitrogen atoms into the carbon support are numerous (Figure 1.12). However, as also discussed in section 1.5, most of the methodologies involve toxic solvents, relatively long treatment times and high temperatures [112]. For these reasons, a growing interest has been paid to N-doping by dry plasma-related treatments. Plasma-based methods are versatile, fast, simple, cost effective and more environment friendly because they are solvent-free [119, 120]. Lin *et al.* [238] worked on the N-doping of graphene sheets by using NH_3 plasma and demonstrated that this method allows to highly control the amount of dopant incorporated. The original approach developed in this work consists in performing the incorporation of nitrogen functional groups into a carbon xerogel by using a NH_3 or N_2 low-pressure plasma discharge. Before giving the results found for the global XPS quantification and the chemical environment of the functionalized CXGs, a study of the E-to-H transition was first achieved to determine the threshold power between the capacitive (E) and inductive (H) plasma modes at different pressures. As discussed in section 2.3.4, Vesel *et al.* [141]

showed that electron and neutral species densities depend on the coupling mode. Thus, it is expected that the amount of nitrogen incorporated and the carbon functionalization could differ between the E and H modes. The same setup as described in section 3.2 was employed. A turbomolecular pump was used to reach vacuum down to 10^{-6} – 10^{-7} mbar. For both NH_3 and N_2 plasma chemistries, the gas flux injected was fixed at 10 sccm. The modification and control of the pressure in the vacuum chamber was achieved by partially closing a valve leading to the turbomolecular pump. The plasma discharge was finally ignited and OES was then used to characterize the E-to-H transition by monitoring specific emission line intensities present in the spectra.

Afterwards, a carbon xerogel supplied by the group of Prof. N. Job from the University of Liège and characterized by an average pore size of 50 nm and a specific surface area of $\sim 650 \text{ m}^2 \text{ g}^{-1}$, was employed to achieve N-doping. For each plasma parameter investigated, 50 mg of the carbon matrix was homogeneously dispersed in a glass petri box. A magnet was placed in the powder allowing to perform plasma treatments under stirring conditions. Therefore, it ensured to obtain homogeneously treated carbon matrices. The different parameters explored for the N-doping will be discussed in sections 8.3 and 8.4. A systematic study of the chemical environment and the carbon functionalization was then performed by XPS measurements.

8.2 E-to-H transition for NH_3 and N_2 plasma discharges

The first point developed in this chapter concerns the E-to-H transition in NH_3 and N_2 plasma discharges at two different pressures : 7.10^{-3} and 133.10^{-3} mbar, respectively. The transmitted plasma power was varied between 20 and 200 W with a step of 10 W. An OES spectrum was recorded for each transmitted power, while the integration time was adapted to avoid saturation of the spectrometer. A background spectrum was also acquired when the integration time was adapted and, afterwards, individual OES spectrum subtracted by its corresponding background. This allows comparison between all the recorded data. The wavelength calibration was performed following the same procedure as described in section 6.2. Figure 8.1 shows the results obtained for the NH_3 and N_2 plasma chemistries at four different powers (20, 90, 150 and 200 W). The NH 0–0 and the N_2 second positive bands¹ appear in the range 290–410 nm and are overlapping, while

¹A *positive system* refers to a spectrum which is detected in an area located at the cathode side in an electric discharge using direct current. On the other hand, a *negative system* refers to a spectrum which is detected in an area located at the anode side. The N_2 first positive band corresponds to transition between the $\text{B}^3\Pi_g$ and $\text{A}^3\Sigma_u^+$ energy levels, while, for the N_2 second positive band, it corresponds to the transition between $\text{C}^3\Pi_u$ the $\text{B}^3\Pi_g$ and levels. See ref. [239] for more information.

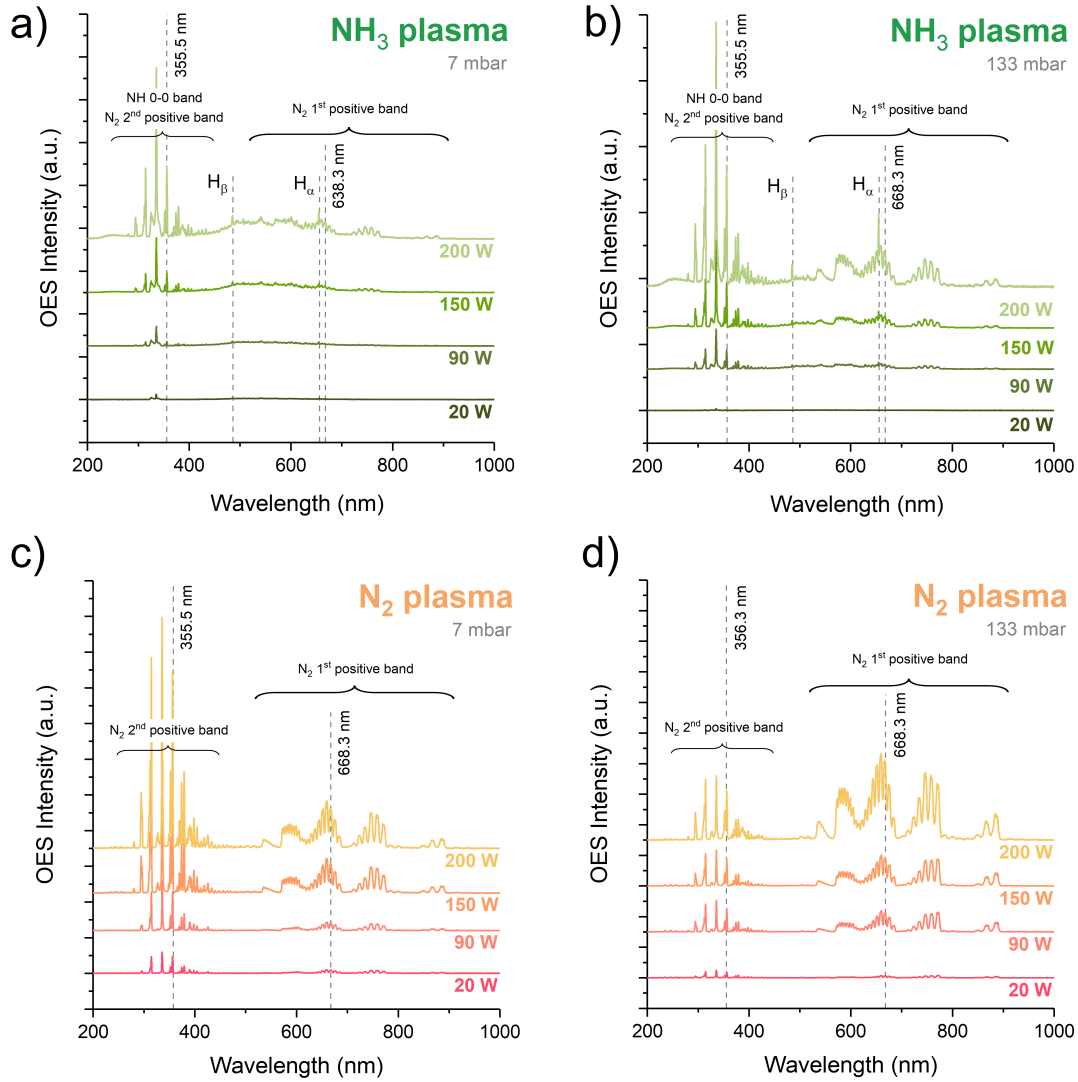


Figure 8.1: OES spectra at pressures of $7 \cdot 10^{-3}$ (a,c) and $133 \cdot 10^{-3}$ (b,d) mbar for the NH₃ and N₂ plasma discharges, respectively.

the N₂ first positive lines are present in the range 500–900 nm [240]. For the NH₃ plasmas, emission lines at 486.7 and 656.3 nm are attributed to H_β and H_α Balmer lines, respectively [221, 222]. Interestingly, in the NH₃ plasmas, species produced at both pressures and 20 W plasma power are similar. They are mainly due to molecular radiations. However, the NH 0–0 band and/or N₂ second positive lines are the most intense independently of the transmitted power, while the contribution of N₂ first positive lines clearly appear at higher power and pressure (Figure 8.1(a,b)). The hydrogen emission lines only clearly appear at both high pressure and power. For the N₂ plasma discharges, the N₂ first positive band

is visible already at both low pressure and power (Figure 8.1(c)). Surprisingly, these emission lines are dominant at plasma power above 90 W for a pressure of 133.10^{-3} mbar (Figure 8.1(d)). On the other hand, the N_2 second positive band constitutes the most intense contribution in the different spectra at 7.10^{-3} mbar, while it does not increase roughly at 133.10^{-3} mbar. Therefore, such a difference between the plasma chemistries and the explored pressures could lead in a different functionalization of the carbon matrix due to the different species released in the plasma.

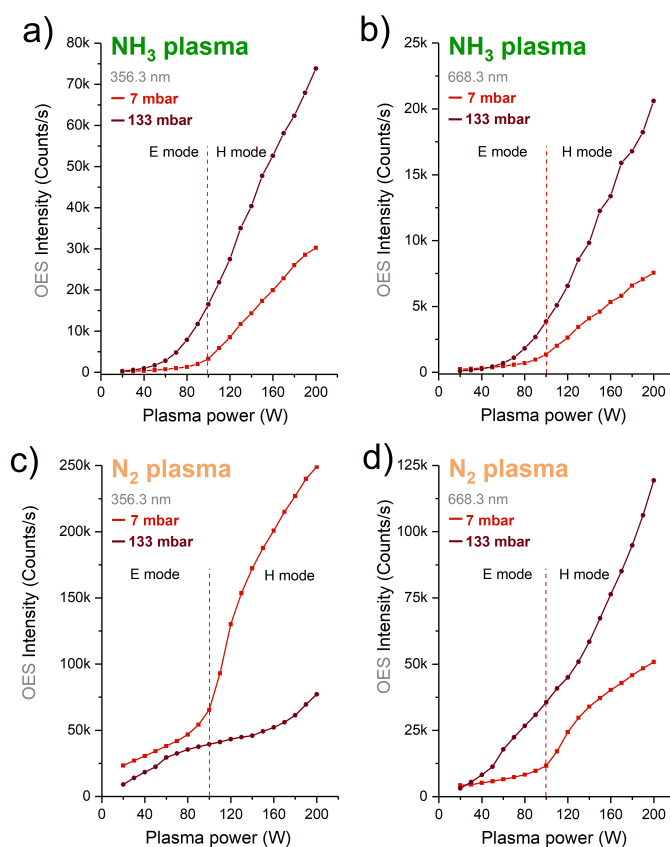


Figure 8.2: Evolution of the OES intensities for the NH_3 and N_2 plasma discharges as a function of the transmitted power. The evolution of the emission lines at 356.3 (b,d) and 668.3 (a,c) nm, respectively, are shown for both plasma chemistries.

Regarding the E-to-H transition, the intensity of two emission lines were recorded as a function of the plasma power, as seen in Figure 8.2. These two lines were chosen in order to derive at least twice the threshold powers for the NH_3 and N_2 gas discharges. More specifically, the intensity variation of the lines at 356.3 and 668.3 nm, both related to a N system, were monitored in order to avoid as much

as possible the overlapping between the NH 0–0 and N₂ second positive bands as well as the overlapping between the H_α and the N₂ first positive band. As discussed in section 2.3.4, the E-to-H transition corresponds to an abrupt change in electron density and light emission at a specific threshold power.

For the NH₃ discharges, the transition between the E and H modes shows a dependence over the pressure, as expected (Figure 8.2(a,b)). Typically, the threshold powers are located at ~ 100 W for 7.10^{-3} mbar and ~ 80 W for 133.10^{-3} mbar. Moreover, the transition is steeper for 7.10^{-3} mbar and less marked at higher pressure. For the N₂ gas mixture, the same observation as for the NH₃ cause can be stated; the E-to-H transition is clearly visible at 7.10^{-3} mbar with a threshold power of ~ 100 W. Interestingly, at 133.10^{-3} mbar, no transition is unambiguously present which makes it harder to describe. Nevertheless, it seems that a slight increase of the OES intensity occurred at ~ 50 W. This value could be in agreement with the lower one found in the case of the NH₃ plasmas. Finally, the N₂ second positive system is particularly intense at low pressure for the N₂ plasma in comparison with the NH₃ gas mixture. Therefore, as already mentioned above, these difference in species released within the plasma region could affect the nitrogen-based functional groups incorporated to the carbon xerogel. The chemical analysis of the treated samples by XPS could confirm, or not, an effect depending of such an observation.

8.3 Elemental and chemical analysis of NH₃ treated carbon xerogels

The experiments on carbon xerogel were first and foremost performed by applying an NH₃ plasma during treatment times comprised between 100 and 1200 s for three transmitted plasma powers (20, 90 and 200 W). According to the results derived from the OES analysis, the threshold power of the E-to-H transition is located close to 90 W at the two pressures explored. Thus, this value was chosen in order to have an intermediate step between the capacitive E and inductive H modes. A systematic XPS analysis was then realized to get insights on the overall chemical composition. The spot size of the X-ray beam was fixed at 300 μm ; survey and HR-XPS (C 1s, N 1s and O 1s) spectra were acquired with a pass energy of 200 and 30 eV, respectively. As already discussed in section 6.4, the number of scans was adapted in order to get as much as possible similar signal-to-noise ratios for every element present in the sample. Specifically, the number of scans for the C 1s, N 1s and O 1s core level spectra was of 8, 32 and 16, respectively. The main contribution of the C 1s peak was also systematically fixed at 284.8 eV BE (C-C/C-H bonds).

The global chemical composition of the samples was controlled by analyzing the HR-XPS C 1s, N 1s and O 1s core level spectra. Figures 8.3 and 8.4 show these spectra for the untreated xerogel and samples treated with a NH_3 plasma during 1200 s at the three explored plasma powers. The HR-XPS C 1s spectra are highly similar with a main contribution at 284.8 eV corresponding to the C-C/C-H bonds (Figures 8.3(b) and 8.4(a,b)). Moreover, a peak centered at 290.1 eV was attributed to π - π^* satellite. The two last contributions at 285.9 and 287.3 eV were ascribed to C-O/C-N and C=O functional groups. As already explained in section 5.3.3, it is nearly impossible to distinguish the C-O and C-N peaks due to an overlapping of these bonds in the spectrum. The HR-XPS O 1s spectra are shown in Figures 8.3(d) and 8.4(e,f). Four components were fitted at 531.2, 532.1, 532.9 and 534.0 eV and are attributed to oxide (C-O-C), hydroxides (C-OH), carbonyls (R-C=O) and carboxylic acid (O-C=O) functional groups, respectively [241, 242].

The analysis of the N 1s spectra indicates a chemical environment constituted of three components fitted and centered at 398.4, 399.6 and 400.9 eV BE; these are attributed to pyridinic-, pyrrolic- and graphitic-N functional groups (Figure 8.4(c,d)). Considering the pressures and plasma powers explored, the formation of pyridinic- and pyrrolic-N groups are sensibly the same with a contribution of ~ 50 and $\sim 40\%$ of the total peak area, respectively, regardless the treatment conditions. Surprisingly, the different reactive species released in the plasma, which were depending on the various conditions investigated as seen with the OES experiments (Figure 8.1(a,b)), seem to have a low impact on the functionalization of the carbon support.

The evolution of the N 1s content as a function of the treatment time for three transmitted powers and for the two pressures was then derived (Figure 8.5). At 7.10^{-3} mbar, the amount of nitrogen incorporated to the carbon support drastically increases after 100 s of treatment, while it seems that a slower increase rate occurs for longer treatment time (Figure 8.5(a)). Moreover, low-energetic plasma (20 W) allows to achieve N-doping with a nitrogen content up to ~ 2.5 at.% after 1200 s. Interestingly, no significant difference can be noticed between the 90 and 200 W treatments; the amount of nitrogen follows a similar evolution with a maximum content of ~ 4.5 at.%. Therefore, these results indicate that increasing the plasma power does not allow to significantly increase the incorporation of nitrogen into the carbon xerogel. A proposed explanation for such a phenomenon could be a content saturation of the reactive species or gas molecules present in the plasma which are able to interact with the surface. Thus, it limits the doping rate of the carbon matrix. At 133.10^{-3} mbar, as seen in Figure 8.5(b), the incorporation of N atoms increases as well. However, the amount of nitrogen reaches up to ~ 2.0 at.% and is similar for the transmitted plasma powers explored. Moreover, the evolution of the N content is clearly influenced by the transmitted

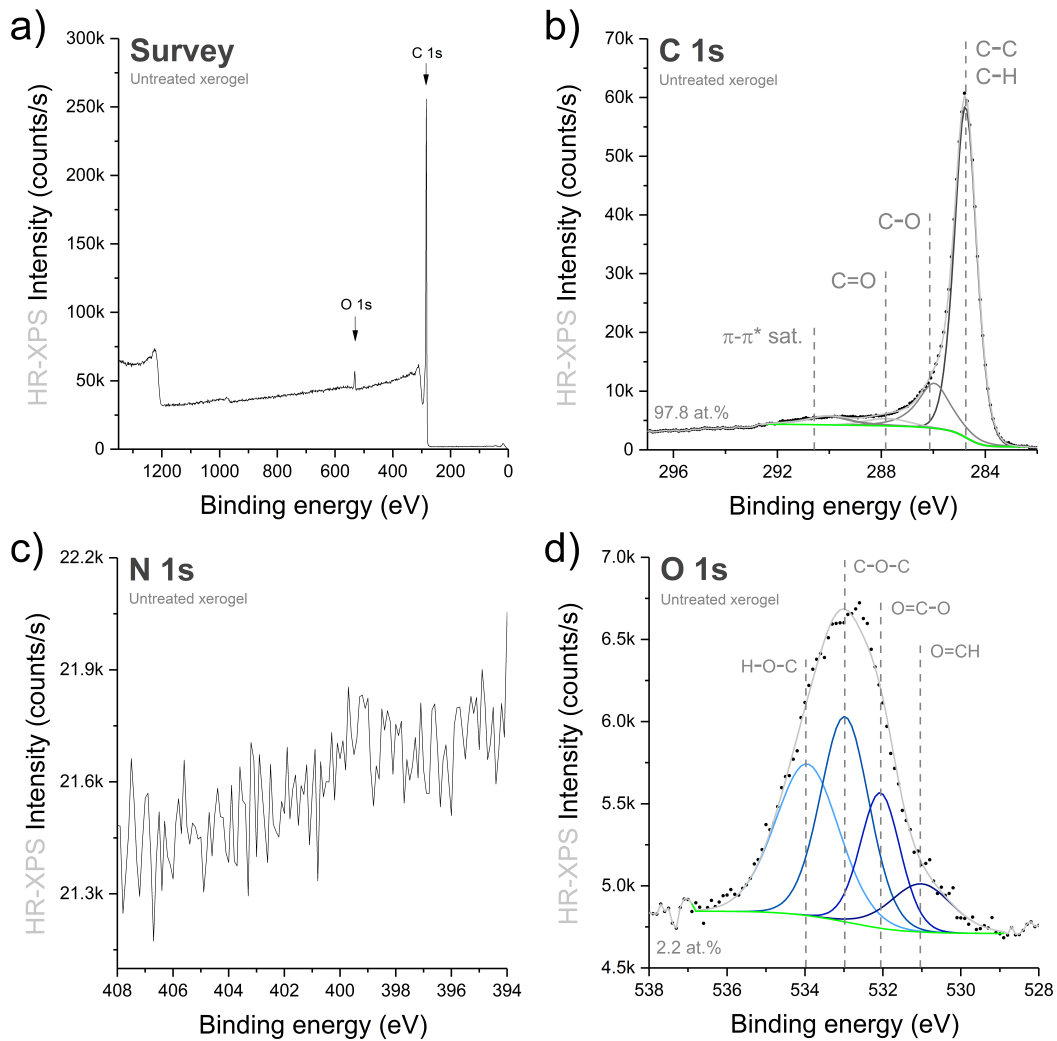


Figure 8.3: a) Survey and HR-XPS b) C 1s, c) N 1s and d) O 1s spectra of the untreated carbon xerogel.

power, it seems to follow a regular increase for the low-energetic plasma (20 W), while it is more chaotic for the high-energetic ones (90 and 200 W). It is well-known that the thickness of the plasma sheath depends on the pressure [243]. At higher pressure, the plasma sheath is more thick and reactive species lose partially their energy due to collisions in that region. Therefore, efficiency of the N-doping is decreased which results in a less important N incorporation. Such an effect should be investigated with various carbon support in order to determine the impact of the support morphology on the functionalization. In summary, results indicate that the plasma power and pressure in the plasma reactor only affect the amount of nitrogen incorporated into the carbon support and have a rather low impact on the chemical environment.

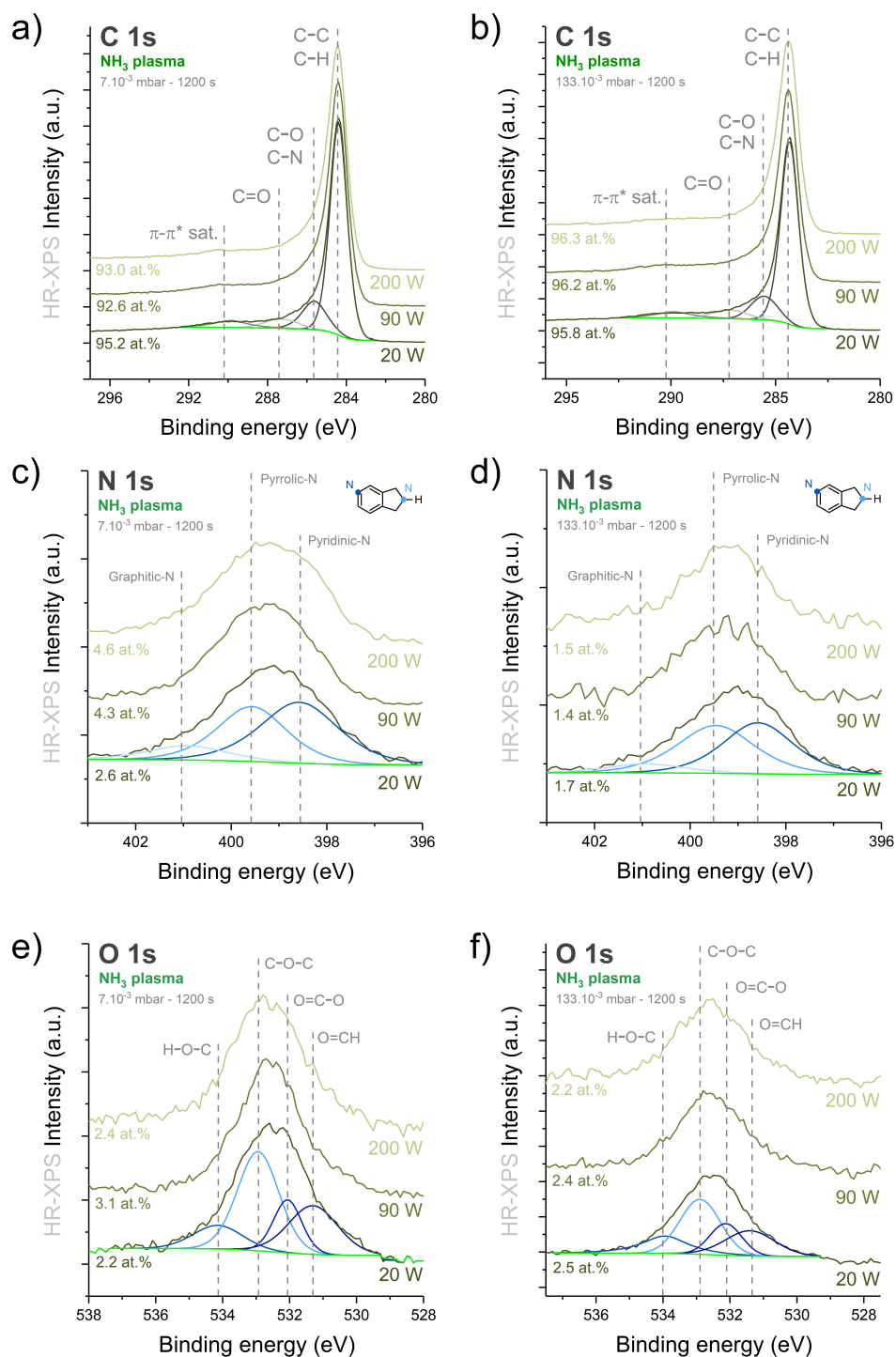


Figure 8.4: HR-XPS C 1s, N 1s and O 1s core level spectra at 7.10⁻³ (a,c,e) and 133.10⁻³ mbar (b,d,f) for the NH₃ plasma discharge at 90 W transmitted power.

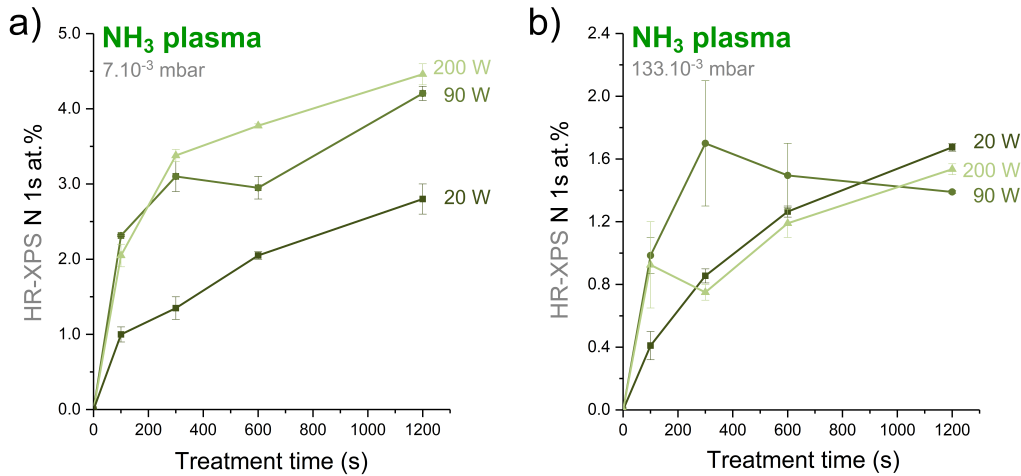


Figure 8.5: Evolution of the N 1s content for the NH₃ discharges (20, 90 and 200 W) as a function of the treatment time at a) 7.10^{-3} and b) 133.10^{-3} mbar.

Finally, the analysis of the O 1s spectra tends to show that the oxygen functional groups already present in carbon xerogel are not modified after the plasma treatments. Figure 8.3(d) shows the HR-XPS O 1s spectrum of the untreated xerogel. Two components were fitted at 531.1 and 532.8 eV BEs and are attributed to O=C and O-C/O-H bonds, respectively. The elemental quantification unambiguously shows that the amount of oxygen is rather constant with a value comprised between 2.2 and 2.5 at.% (Figure 8.4(e,f)). This confirms the hypothesis of no surface modification of the oxygen-based functions already incorporated into the carbon matrix.

8.4 Elemental and chemical analysis of a N₂ treated carbon xerogel

Further investigations on the N-doping of carbon xerogel was achieved with a N₂ plasma treatment. The conditions were chosen with respect to the results obtained for the NH₃ experiments. The pressure was fixed at 7.10^{-3} mbar, the transmitted power at 90 W and the treatment time at 1200 s. Figure 8.6 shows the XPS spectra resulting from these treatment conditions. As discussed in section 8.3, the same analysis was performed on the HR-XPS C 1s, N 1s and O 1s core level spectra. The elemental quantification derived from the C 1s, N 1s and O 1s spectra indicates that the N₂ treatment leads to similar amount of nitrogen incorporated (3.2 at.%), while the oxygen content seems to stay roughly constant (2.8 at.%). Moreover, the carbon functionalization as well as the oxygen groups, as seen in Figure 8.6(b,c), do not significantly change in comparison with the NH₃ treated samples.

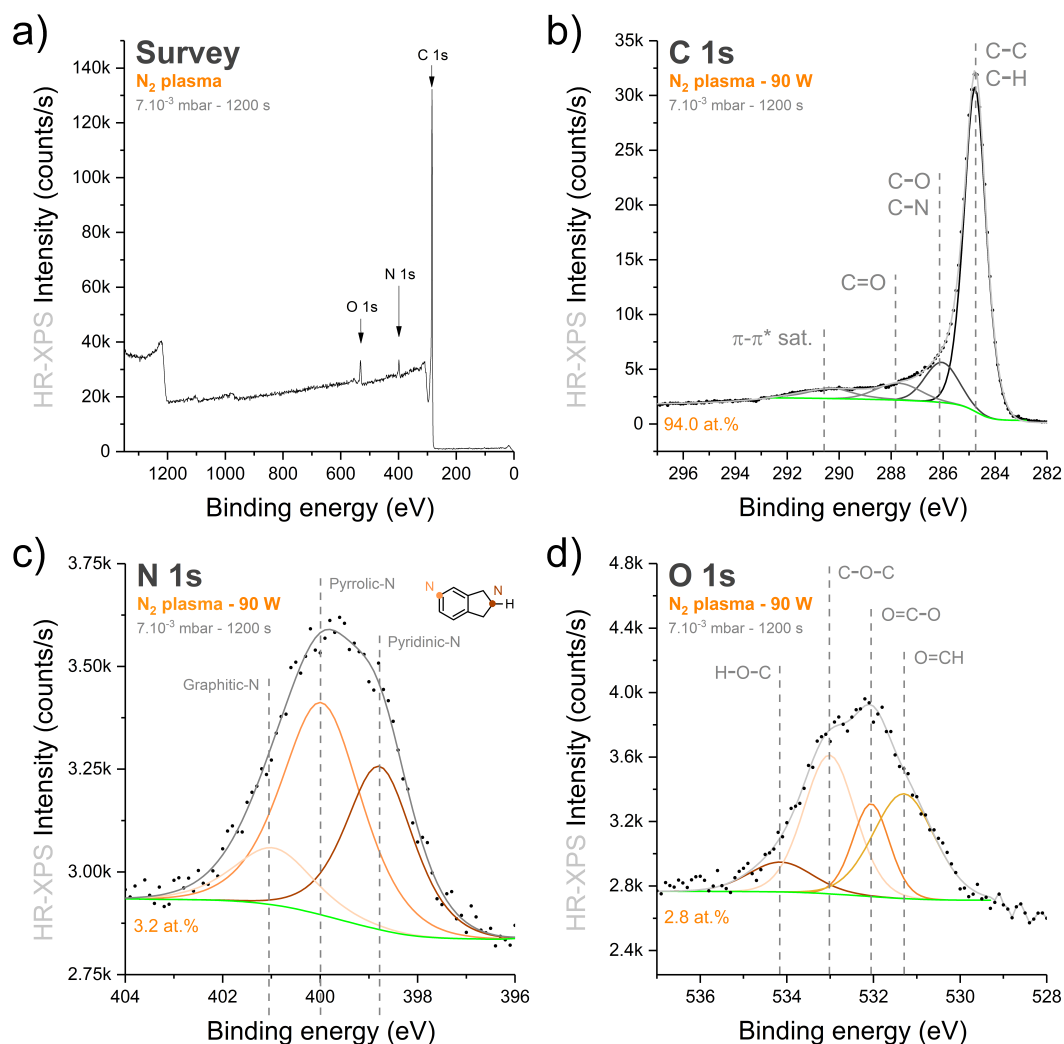


Figure 8.6: a) Survey spectrum and HR-XPS b) C 1s, c) N 1s and d) O 1s core level spectra at 7.10^{-3} mbar for the N_2 plasma discharge at 90 W transmitted power.

The N-functionalization is shown in Figure 8.6(c); the pyrrolic-N functional group ($\sim 50\%$ of the total N 1s peak area) is dominant in comparison with the pyridinic-N one ($\sim 35\%$). Few studies demonstrated the key role played by pyridine-type groups in the enhancement of the catalytic activity in ORR [244,245]. Therefore, N_2 plasma could be promising as an efficient way to add the desired functional groups into the carbon support. However, results found with these plasma conditions do not allow to state a strong difference between the N_2 and NH_3 plasma discharges in terms of functional groups incorporated. A more complete study should be achieved to determine the effect of the various parameters explored with the NH_3 plasma chemistry on the N-doping.

8.5 Impact of the plasma treatment on the pore texture

The impact of the plasma treatment on the pore texture was investigated by using the N₂ adsorption/desorption method as described in section 4.6. The analyses were performed with an ASAP 2020 analyzer (Micromeritics, USA) on the untreated and treated CXG in a NH₃ or N₂ plasma discharge under a pressure of 7.10⁻³ mbar and for two treatment times (600 and 1200 s). Prior to any measurement, the samples were put under vacuum and heated at 90 °C during 1h followed by 6h at 200 °C in order to outgas them. The surface area, the average pore size (APS) and pore volume were then derived in each case. Table 8.1 summarizes the results obtained. \mathbf{a}_{BET} are the surface areas calculated by using the BET theory in the 0.005 - 0.05 relative pressure range, \mathbf{V}_p are the total pore volumes calculated from the volume of nitrogen adsorbed at a relative pressure P/P₀ of 0.985, $\mathbf{a}_{\mu m}$ and $\mathbf{V}_{\mu m}$ are the micropore areas and volumes, respectively, derived from the Harkins-Jura t-plot model applied to the adsorption branch of the isotherms, \mathbf{a}_t are the external surface areas calculated as the differences between \mathbf{a}_{BET} and $\mathbf{a}_{\mu m}$, respectively, while the $\mathbf{V}_{meso/macro}$ correspond to the mesoporous/macroporous volumes calculated as the differences between \mathbf{V}_p and $\mathbf{V}_{\mu m}$, respectively. Finally, the APS were calculated by using the BJH theory applied to the adsorption branches (maximum peak).

Sample name	Surface area (m ² g ⁻¹)			APS (nm)	Pore volume (cm ³ g ⁻¹)		
	\mathbf{a}_{BET}	\mathbf{a}_t	$\mathbf{a}_{\mu m}$		\mathbf{V}_p	$\mathbf{V}_{\mu m}$	$\mathbf{V}_{meso/macro}$
Untreated CXG	630	181	449	50	1.0	0.17	0.83
CXG_NH ₃ _10	610	181	429	50	1.0	0.17	0.83
CXG_NH ₃ _20	613	183	430	45	0.93	0.17	0.76
CXG_N ₂ _10	625	191	434	60	1.0	0.17	0.83
CXG_N ₂ _10	627	190	437	50	0.98	0.17	0.81

Table 8.1: Textural parameters derived from the N₂ adsorption/desorption analysis of the untreated and plasma treated samples.

Interestingly, it seems that the different plasma treatments of the CXG do not significantly modify the pore texture; the comparison of the characteristics derived from the N₂ adsorption/desorption shows similar surface area, APS and pore volume for all the analyzed samples. Therefore, the plasma methodology allows to achieve N-doping while the pore texture is not modified. This could be particularly useful for applications requiring the incorporation of nitrogen atoms with no or limited impact on the carbon support.

8.6 Conclusions and perspectives

In this chapter, the N-doping of a carbon xerogel was achieved by using nitrogen-based low-pressure plasma discharges. The E-to-H transition in NH_3 and N_2 plasmas was investigated at various transmitted powers and at two different pressures. The OES analysis indicated threshold powers of 100 and 80 W for the NH_3 gas mixture at $6.7 \cdot 10^{-3}$ and $133 \cdot 10^{-3}$ mbar, respectively. For the N_2 discharges, the threshold power of the $133 \cdot 10^{-3}$ mbar experiment was not be clearly visible. Nevertheless, a slight increase of the intensity was noticed around 50 W. On the other hand, at $7 \cdot 10^{-3}$ mbar, the change of coupling mode seemed to occur at ~ 100 W.

Furthermore, the kind of reactive species released in the plasmas was also checked by OES. For the NH_3 gas mixture, the N_2 first positive band does not exhibit an important contribution at low plasma powers, regardless the pressure in the vacuum chamber, while a clear signature was seen at higher power and even more at higher pressure. For the N_2 gas mixture, the N_2 second positive band was the most intense at $7 \cdot 10^{-3}$ mbar, while the N_2 first positive band was dominant at $133 \cdot 10^{-3}$ mbar. In general, the N_2 first positive band is more active for the N_2 plasmas compared to the NH_3 discharges.

The elemental analysis and quantification of the NH_3 treated samples showed that, at $7 \cdot 10^{-3}$ mbar, a transmitted plasma power higher than the threshold power does not lead to a significant increase of the incorporation of N atoms. The N-content reaches up to ~ 4.5 at.% at 200 W. Surprisingly, at $133 \cdot 10^{-3}$ mbar, the amount of nitrogen incorporated does not exceed ~ 1.5 at.% and is similar at the different powers explored. A proposed explanation for such a phenomenon is the release of too many reactive species or the presence of too many gas molecules at higher power which limits the interaction of the active species with the carbon xerogel. Therefore, an intermediate transmitted power is sufficient to perform an efficient N-doping. Regarding the type of functions added to the xerogel, it is interesting to note there was almost no dependence on the plasma power or pressure. Pyridine- and pyrrole-type functions are grafted with a relative same proportion. Results found for the N_2 plasma treated sample only seems to show a slightly more important proportion of pyrrole-type functions compared to the amount of pyridine-type functions. However, no conclusion can be stated at this point and further experiments should be conducted to confirm the trend observed. Indeed, the key-role played by pyridinic-N groups on the enhancement of the ORR has been demonstrated. Thus, N_2 plasmas could be promising to treat materials useful for such an application.

Finally, N_2 adsorption-desorption experiments allowed to determine the effect of the treatment time and plasma chemistry on the porous texture. Interestingly,

it seems that there is no or limited modification of the texture, regardless the treatment parameters, which could be useful in applications requiring the incorporation of N atoms while avoiding the degradation of the pore texture. Thus, the study presented in this work validates the low-pressure plasma discharge treatments as a suitable, easy and fast method to graft N-functions at the surface of CXGs.

General conclusion and perspectives

The leading theme of the present thesis was characterizations of nanomaterials fabricated or modified by low-pressure RF-ICP discharges. The main motivation was based on potential applications in various fields among which catalysis, and more specifically, greener ways to produce energy. To this end, this work focused on a type of fuel cells promising as an alternative to non-renewable sources of energy, the so-called PEMFCs. Before developing the core business of this study, chapter 1 was dedicated to the understanding of the PEMFC working principle and presented the different parts playing a key role in such a kind of device. A special attention was paid on the catalytic layers in PEMFCs; NPs supported on a carbon matrix employed to faster the chemical reaction in these devices are most of the time made of expensive and critical raw materials, such as platinum. Therefore, it is required to develop alternatives to reduce the use of these critical resources or replace them, such as bimetallic or non-noble metal catalysts. Thus, it allows to lower the cost and negative environmental impact of this part. Recent developments were presented for both HOR and ORR occurring in the fuel cell. Moreover, a discussion on different carbon matrices promising as support for the synthesized NPs were presented. Indeed, the most common supports employed, carbon blacks, do not present the best characteristics (*i.e.* high catalytic activity, durability, resistance to corrosion, etc.) and improving the properties of the support is also essential to allow this technology to be widely commercialized in the near future. Finally, this beneficial effect of N-doping and conventional methodologies used to achieve it were briefly depicted. The incorporation of N atoms in the carbon support was demonstrated to improve the ORR catalytic activity, to affect the stability of the NPs supported on the carbon as well as their growth mechanism.

The original approach of this study consisted to use low-pressure plasmas discharges to fabricate NPs from the decomposition of an OM precursor. In chapter 2, basics on plasma physics and details about the RF-ICP discharges employed to treat the nanomaterials were given. Furthermore, the E-to-H transition was also discussed; such a phenomenon was believed to affect the functionalization of the carbon support and was investigated in chapter 8. Afterwards, chapter 4 dealt with the techniques used to characterize the nanomaterials regarding their chemical, structural, morphological and electrochemical properties. The conventional

methods used to fabricate nanomaterials were then considered in chapter 3 and the methodology employed in the present thesis detailed with the experimental setup.

The core of this work was then discussed in chapters 5, 6, 7 and 8. Based on the patent of Pireaux *et al.* [163] and the work of Laurent-Brocq *et al.* [164], it was shown that RF-ICP treatments were suitable to synthesize nanomaterials on various carbon support from the degradation of an OM precursor. In chapter 5, new insights on the nucleation and growth mechanisms of Pt/C were investigated. Plasma treatments of three different precursors, each mixed with a carbon xerogel, were performed to form supported Pt/C NPs. The second part of this chapter focused on the formation of Pt NPs supported on graphene sheets. The nucleation mechanism proposed by Laurent-Brocq *et al.* [164] was in agreement with the results found in both cases. Moreover, a comparison between the "one-pot" and the new "2-step" methodologies showed that too energetic plasma treatments lead to frequent agglomeration of the NPs, while a combination of low- and high-energy plasma discharges (*i.e.* pulsed or continuous plasmas and short or long treatment time) allows to better control the morphology of the fabricated NPs.

As previously mentioned, the use of non-noble metal is promising to reduce the cost of the catalyst layer. For this reason, chapter 6 aimed to extend the use of low-pressure RF-ICP treatments to a Ni precursor and form NPs anchored on a carbon xerogel. It was shown that controlling the carbon functionalization, NPs oxidation state and morphology were easily achieved by simply modifying the plasma treatments conditions (gas mixture, transmitted power, etc.). Furthermore, nitrogen-based plasmas were investigated and led to the incorporation of N atoms into the xerogel. The control over the functional groups grafted onto the surface of the carbon support, by simply modifying the plasma chemistry, could be interesting in various applications. Indeed, research demonstrated the beneficial effect of pyridine-type groups on the ORR catalytic activity.

Afterwards, in chapter 7, both Pt and Ni precursors were degraded in order to form bimetallic Pt-Ni NPs anchored on graphene sheets. The use of a second metal allowed to fabricate defective Pt-Ni nanocomposites. This is promising to lower the content in critical raw materials employed in catalysts for applications such as PEMFCs. Two strategies were set up to perform the synthesis of the bimetallic particles : simultaneous and sequential oxygen plasma treatments of the OM precursors. For the simultaneous treatment, the precursors decomposition resulted in a rather complex morphology with Pt and Ni forming interconnected domains, while, for the sequential treatment, well defined and homogeneously dispersed NPs were formed at the surface of the support. Thus, different nucleation and NP growth mechanisms are expected. The simultaneous treatment is believed to create structural defects at the surface of the support which act as anchoring

site for the formation Ni and Pt NP that nucleate at the same time. In the case of the sequential treatment, it is believed that, first, structural defects are induced and sub-nanometer Ni seeds grow in these preferential anchoring sites. The second step then allows Pt to nucleate on the previously fabricated Ni NPs which is consistent with the morphology observed. However, the electrochemical measurements indicated a rather low catalytic activity for both nanocatalysts synthesized and further improvements should be performed to increase the attractiveness of such a material for catalysis applications.

Finally, in chapter 8, special attention was given to the N-doping of a carbon xerogel by using the low-pressure NH_3 or N_2 plasma treatments. The E-to-H transition was determined for both gas mixtures and related to the species in the plasma by using OES. It was shown that the threshold power was roughly the same at low pressure for the NH_3 and N_2 plasmas. However, the OES analysis indicated completely different reactive species produced in the discharges, as expected. These different conditions were believed to affect the carbon functionalization. Surprisingly, the global chemical composition and N-content derived from the HR-XPS N 1s core level spectra showed that the incorporation of N atoms, for the NH_3 gas mixture, does not increase significantly while increasing the transmitted plasma power above the threshold value. Moreover, increasing the treatment time by a factor of two does not allow to increase significantly the N-content, reaching up to ~ 4.5 at.% after 1200 s at 200 W. Furthermore, the N-doping seems to be more efficient at low pressure; a proposed explanation for such a phenomenon is the presence of too many species in the plasma sheath at higher pressure leading to more collisions in that region. It results in a net loss of energy preventing the interaction of reactive species with the carbon support. For the N_2 treatment, the incorporation of N atoms is sensibly lower compared with the NH_3 plasma under the same treatment conditions and reached ~ 3.2 at.%. Regarding the carbon functionalization, it seemed that almost no difference could be noticed between the two strategies employed. The pyrrolic- and pyridine-N functional groups contribution to the HR-XPS N 1s signal is almost equivalent. It was found, only for the N_2 treatment, a slightly higher contribution of the pyrrole-type. However, this result should be confirmed with further studies. In the near future, it would be interesting to perform several experiments in order to determine the optimized conditions to graft N functional groups on the surface of the carbon matrix and confirm the trends observed in this work. Indeed, few studies demonstrated the effects of pyrrole- and pyridine-N defects in different catalytic reactions. Therefore, by simply varying the plasma treatment conditions, it could be possible to incorporate the desired functional groups when looking for a specific N functionalization related to the investigated application.

Regarding the results obtained in the present thesis, answers has been replied to three key questions :

- (1) This thesis confirms the proposed explanation given by Laurent-brocq *et al.* [164]; the NP nucleation mechanism consists in (i) the creation of structural defects acting as germination site for the growth of NPs and the grafting of functional groups at the surface of the support, (ii) the decomposition of the metallic precursor by chemical and thermal processes followed by seeds formation anchoring at the previously formed defects, and (iii) the growth of the NPs.
- (2) It has been shown that the methodology employed for the NP synthesis allows to control the morphology, the oxidation state and the homogeneity at the surface of the fabricated NPs by simply varying the plasma treatment parameters such as the transmitted power, the treatment time, the gas chemistry, the pressure, etc. This is particularly interesting for various applications requiring materials with specific characteristics.
- (3) The "one-pot" strategy was not efficient to fabricate homogeneously dispersed NPs with an important control on the chemical environment. The original "2-step" approach developed in this work allowed to have a better control on these characteristics.

In the near future, further developments should be conducted to improve the nucleation of NPs anchored on the carbon support and, especially, homogeneously dispersed while avoiding agglomeration. A dedicated study on the "2-step" strategy with other transition metals could be performed. It would also be interesting to explore alternative materials such as iron particles anchored on N-doped carbon support (Fe-N-C) and synthesized by low pressure plasma. Indeed, research performed in the past few years [77, 246, 247] indicate that they are promising for applications in PEMFCs. Moreover, it has been shown that the plasma methodology allows to easily incorporate N atoms in the carbon matrix. Therefore, studies should be conducted to decompose a precursor containing iron and form NPs on a N-doped carbon support.

As a final word, the present thesis demonstrated that the original approach based on low-pressure RF-ICP methodology is a versatile, efficient, flexible, fast, eco-friendly and low-energy consumption tool to fabricate NP supported on carbon supports or to perform N-doping. Thus, materials investigated and resulting from the plasma treatments could be useful in numerous applications.

Appendix A

Bright field TEM images of the Pt/CXG nanomaterials

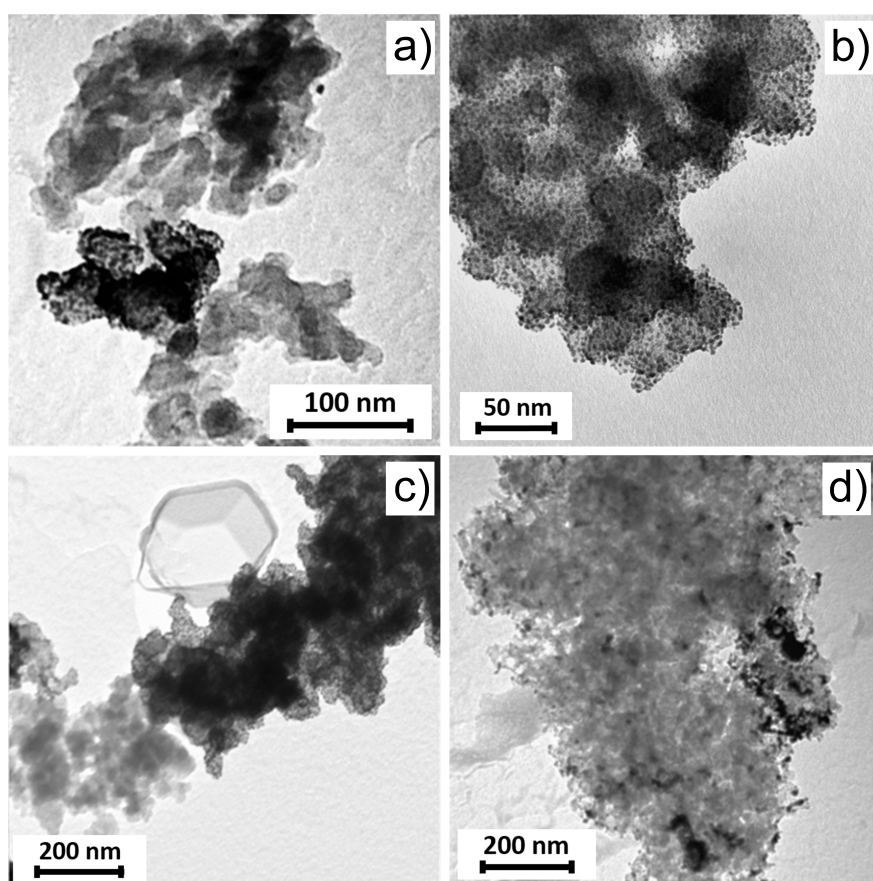


Figure A.1: Bright field TEM images of the a) OM1-1, b) OM1-2, c) OM2-4 and d) AM2 samples. The non-uniform distributions of the nanoparticles at the surface is clearly visible in most cases as well as agglomeration.

Appendix B

High-resolution C 1s and O 1s XPS spectra of Pt/CXG nanomaterials

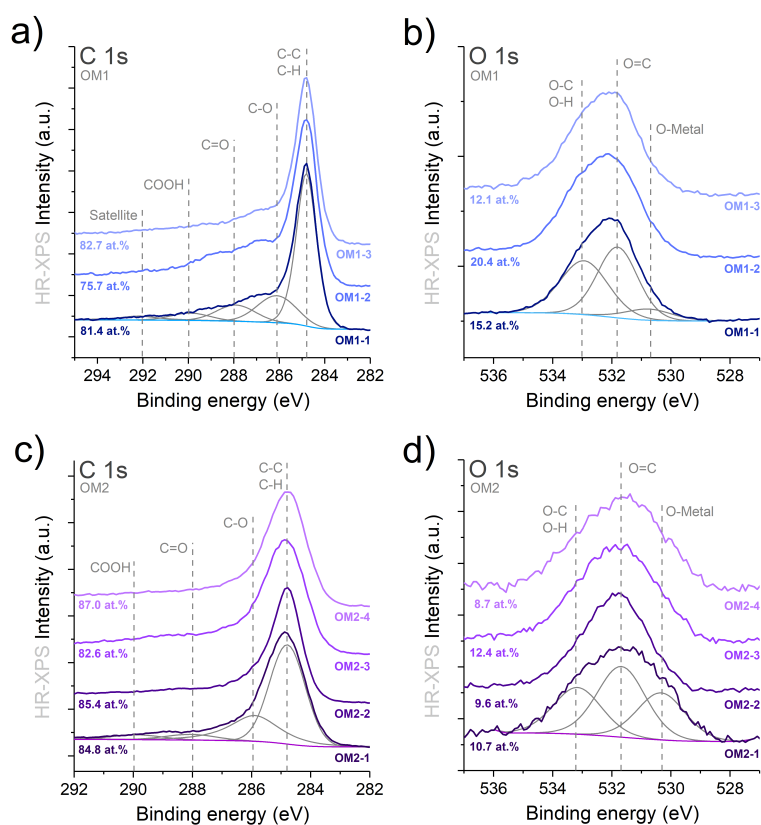


Figure B.1: High-resolution XPS spectra of the C 1s and O 1s elements for the organometallic Pt(acac)₂ (OM1, (a,b)) and Pt(cod)(Me)₂ (OM2, (c,d)) precursors. The different chemical environments were fitted for all spectra and are shown for the O₂ plasma treatments.

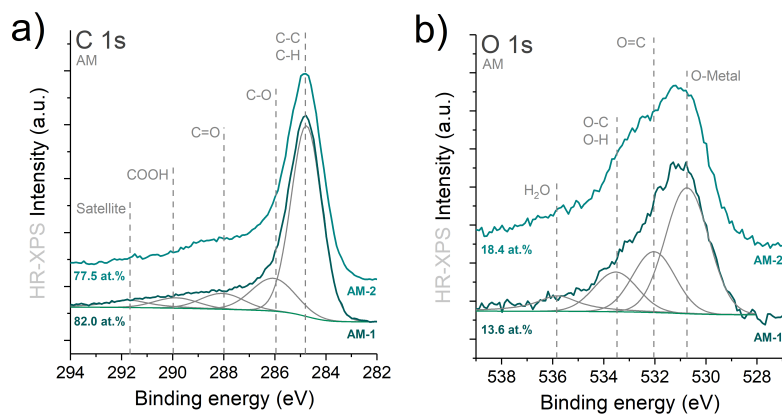


Figure B.2: High-resolution XPS spectra of the C 1s and O 1s elements for the inorganic platonic acid precursor (AM, (e,f)). The different chemical environments were fitted for all spectra and are shown for the O₂ plasma treatment.

Appendix C

Asymmetrical shape fitting in XPS

Peak fitting in XPS consists to sum a series of functions, which depends on numerous parameters, in order to represent as much as possible the experimental signal. In the literature, the most basic peak shapes are a combination of Gaussian and Lorentzian functions [177]. The use of these two functions comes from the photoemission process and various other factors such as instrumental factor and phonon broadening. However, it was demonstrated that asymmetrical line shapes are required when fitting pure metallic contributions such as Pt [248]. The most common way to add an asymmetric peak relies on including tail information which allows to reproduce the characteristic tail found for metals. The following equation gives the tail function T used in the Avantage software [177] :

$$T = TM.CT + (1 - TM).e^{-D_x.ET} \quad (C.1)$$

where TM is the tail mixing ratio (which is comprised between 0, for a pure exponential tail, and 1, for a constant tail), CT is a constant tail, D_x is the separation from the peak centre in channels and ET is exponential tail. Considering the symmetric Gaussian-Lorentzian function, denoted as GL , the final peak function F taking into account the asymmetry is given by the following equation

$$F = H.(GL + (1 - GL).T) \quad (C.2)$$

where H is the peak height.

Appendix D

XRD diffractogram of Pt/GNP nanomaterials

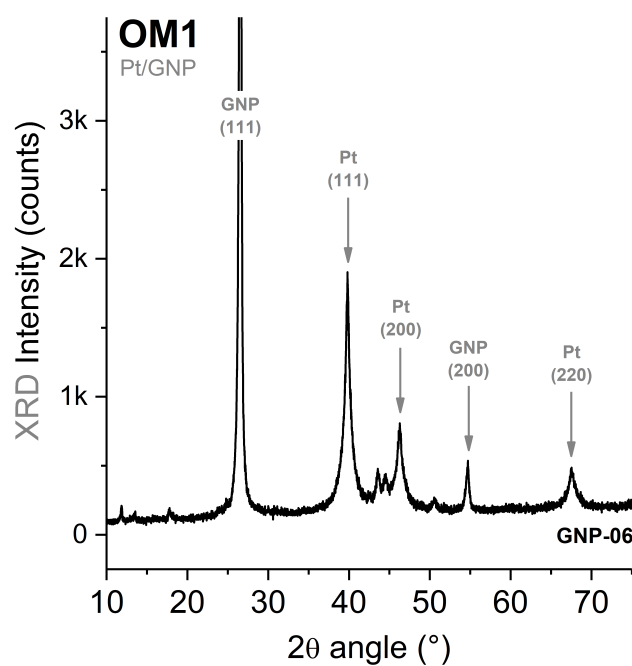


Figure D.1: XRD diffractogram of the GNP-06 sample. The analysis of the peaks positions indicate the presence of cubic face centered Pt crystallites with an average size derived from the Debye-Scherrer formula (Equation 4.5) of 9.7 ± 1.4 nm. No precursor trace was visible after the plasma conditions explored in the present case.

Appendix E

High-resolution Ni 2p XPS spectra of metal nickel and oxides

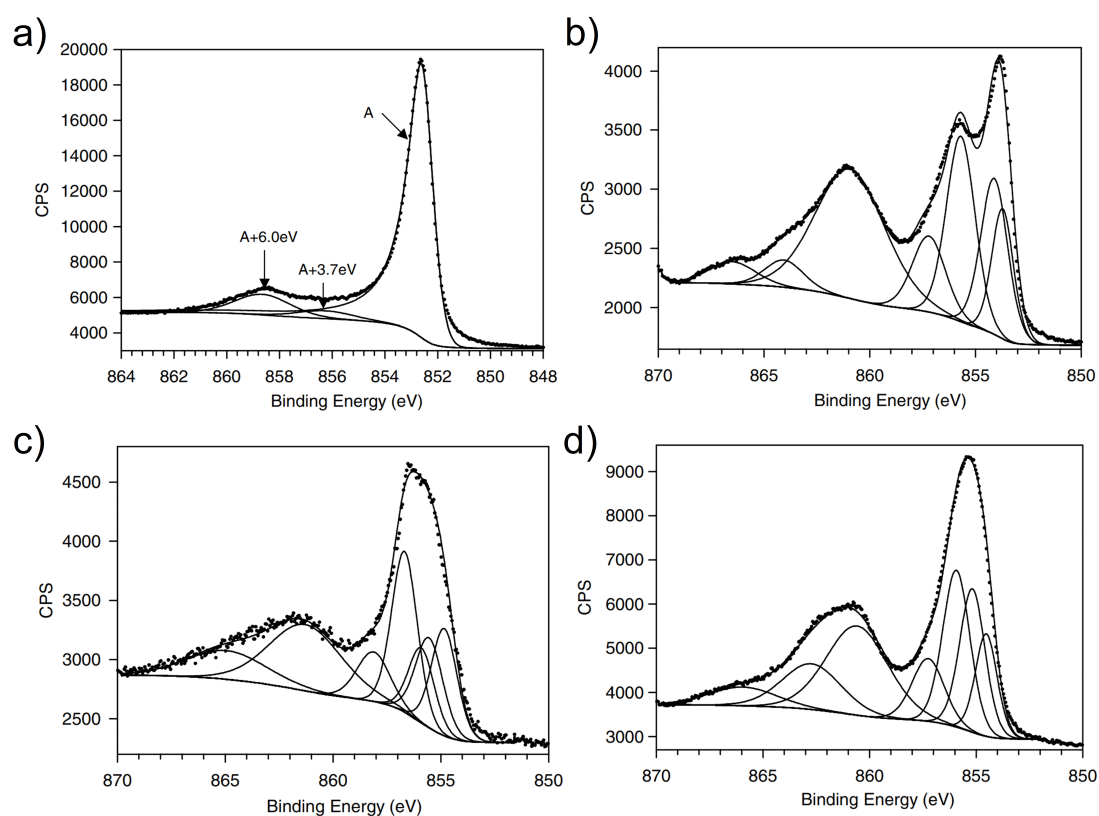


Figure E.1: High-resolution Ni 2p XPS spectra of a) metallic Ni, b) NiO, c) γ -NiOOH and d) Ni(OH)₂ (Taken from [233]).

Appendix F

Ni-Pt phase diagram

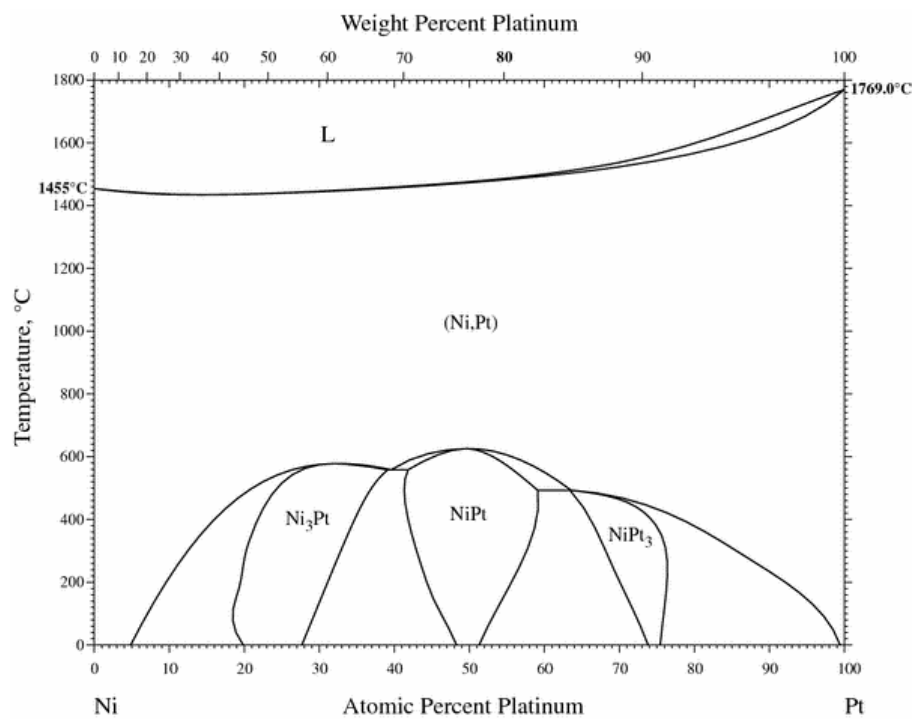


Figure F.1: Ni-Pt phase diagram (Taken from [249]).

Appendix G

XPS survey spectra of Pt-Ni/graphene nanomaterials

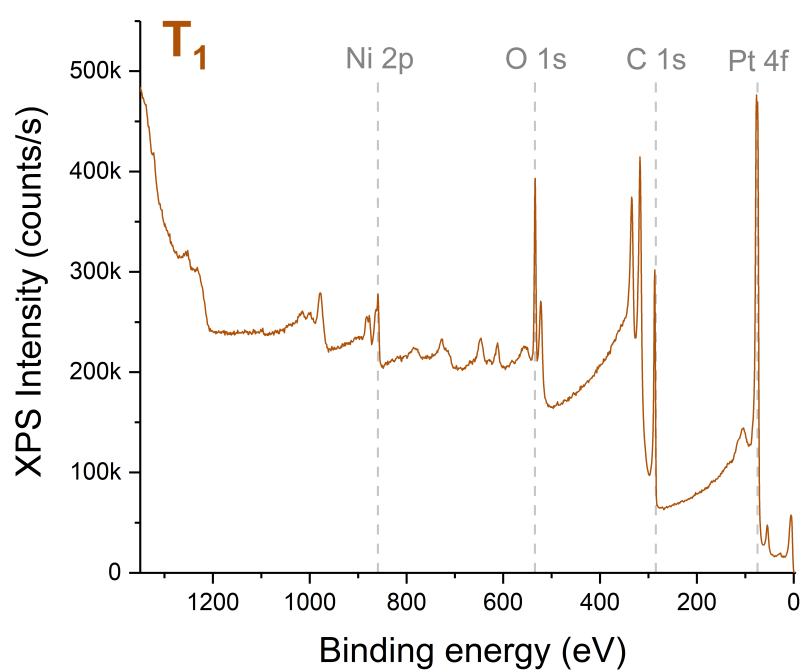


Figure G.1: XPS survey spectra of the simultaneous (T_1) treatment.

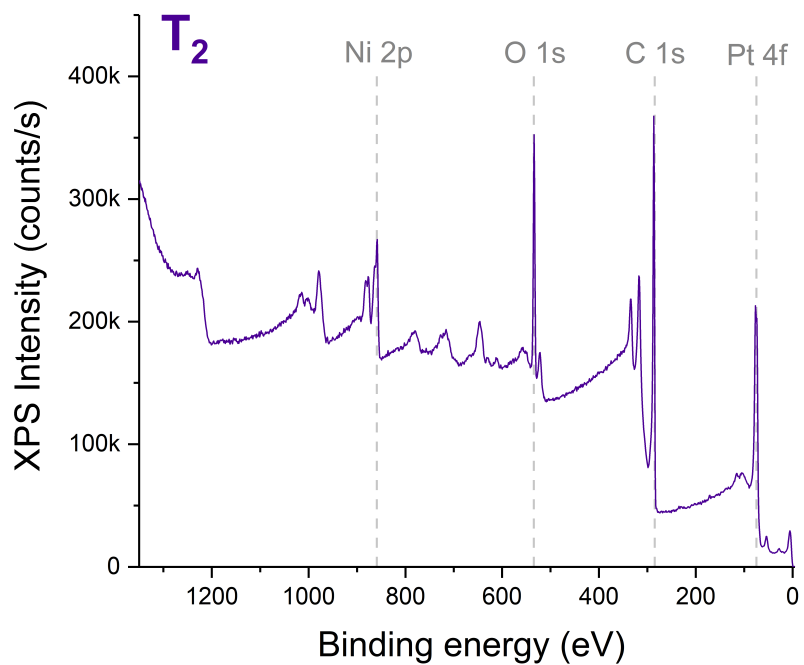


Figure G.2: XPS survey spectra of the sequential (T_2) treatment.

Appendix H

Electrochemical characterizations : sample preparation

Every glassware employed for the analysis was cleaned by immersion in a $\text{H}_2\text{SO}_4:\text{H}_2\text{O}_2$ solution overnight, thoroughly rinsed with ultrapure water (with a resistivity of $18 \text{ M}\Omega\cdot\text{cm}$), and, once immersed in ultrapure water, brought to a boil. The electrolytic solutions were prepared from ultrapure water and perchloric acid (HClO_4 , 70%, Suprapur, Merck). The electrochemical properties were measured with an Autolab PGSTAT204 in a three-electrode cell at room temperature. The reference electrode used during the electrochemical characterization was a commercial reversible hydrogen electrode (RHE, Hydroflex, Gaskatel GmbH) connected to the cell by a Luggin capillary filled by the electrolytic solution (HClO_4 , 0.1 M). The counter-electrode was a platinum gauze soldered on a platinum wire. The working electrode was the catalytic layer deposited on the glassy carbon disk, as explained in the next paragraph.

To measure the electrochemical properties of the catalysts, inks were prepared first. The ink composition was chosen to obtain a Pt loading on the electrode of $40 \text{ g}_{\text{Pt}} \text{ cm}^{-2}$. The right amount of catalyst was crushed in a mortar, then mixed with ultrapure water, 5 wt.% Nafion solution, and isopropanol. The Nafion over carbon mass ratio was equal to 0.295, the water/isopropanol volume ratio was equal to 2.5 and the total volume of ink was equal to 5 mL. In order to blend it homogeneously, the mixture was then processed in an ultrasonic bath for 15 minutes. Once the ink was homogeneous, 10 L of ink were deposited on a glassy carbon (GC) disk put in rotation and gently dried with a heat gun during 15 minutes to evaporate the solvents and stick the catalyst on the GC disk. The catalytic layer deposited on the GC disk composes the working electrode for all electrochemical measurements.

For the electrochemical measurements, the electrode was immersed in a 0.1 M HClO_4 aqueous solution (*i.e.* electrolyte), which should enable full wetting of

the metal particles by the electrolyte [250]. To ensure that all the pores were fully filled, a drop of electrolyte was first deposited onto the catalytic layer, in such a way that all the layer was covered. Then, the electrode was put under vacuum in order to outgas the layer by bubbling air through the drop. Once no air bubbles were visible, the electrode and the drop were put back under atmospheric pressure so that the drop filled the empty porosity of the layer, which ensured the full wetting of the catalyst. With this wetting procedure, the electrochemical measurements were usually steady and reproducible. Applied to other carbons (*i.e.* carbon xerogels), this procedure ensures that the platinum particle utilization factor is close to 100%. Indeed, previous works [250–252] performed on similar systems showed good consistency between the electroactive surface area measured after using this wetting procedure and the surface calculated from TEM micrographs.

Prior to any measurement, the electrolyte was deaerated by Ar bubbling. Then, the working electrode, *i.e.* the catalytic layer deposited on the glassy carbon disk, was immersed in the electrolyte at a fixed potential of 0.4 V vs. RHE. Fifty voltammetry cycles were then performed between 0.05 V vs. RHE and 1.23 V vs. RHE at 0.5 V s⁻¹. Afterwards, three additional cycles were recorded at 0.02 V s⁻¹ with the same voltage boundaries.

Bibliography

- [1] R. B. Jackson, C. Le Quéré, R. M. Andrew, J. G. Canadell, J. I. Korsbakken, Z. Liu, G. P. Peters, and B. Zheng. Global energy growth is outpacing decarbonization. *Environmental Research Letters*, 13(12):120401, 2018.
- [2] G. O'Brien, P. O'Keefe, J. Rose, and B. Wisner. Climate change and disaster management: Climate Change and Disaster Management. *Disasters*, 30(1):64–80, 2006.
- [3] R. Kothari, V.V. Tyagi, and A. Pathak. Waste-to-energy: A way from renewable energy sources to sustainable development. *Renewable and Sustainable Energy Reviews*, 14(9):3164–3170, 2010.
- [4] B. S. *Renewable energy*. Energy science and engineering. Academic Press, London ; New York, 1979.
- [5] G. W. Crabtree and M. S. Dresselhaus. The Hydrogen Fuel Alternative. *MRS Bulletin*, 33(4):421–428, 2008.
- [6] L. Carrette, K. A. Friedrich, and U. Stimming. Fuel Cells: Principles, Types, Fuels, and Applications. *ChemPhysChem*, 1(4):162–193, 2000.
- [7] W. R. Grove. LVI. On a new voltaic combination. *The London, Edinburgh, and Dublin Philosophical Magazine and Journal of Science*, 13(84):430–431, 1838.
- [8] F. T. Bacon. Fuel cells, past, present and future. *Electrochimica Acta*, 14(7):569–585, 1969.
- [9] M. Warshay and P. R. Prokopius. The fuel cell in space: yesterday, today and tomorrow. *Journal of Power Sources*, 29(1-2):193–200, 1990.
- [10] L. Duclos, M. Lupsea, G. Mandil, L. Svecova, P.-X. Thivel, and V. Laforest. Environmental assessment of proton exchange membrane fuel cell platinum catalyst recycling. *Journal of Cleaner Production*, 142:2618–2628, 2017.
- [11] Platinum 2013 - PMM.

- [12] F. Zereini and C. L. S. Wiseman. *Platinum Metals in the Environment*. Springer, 2014.
- [13] I. K. Kalavrouziotis and P. H. Koukoulakis. The Environmental Impact of the Platinum Group Elements (Pt, Pd, Rh) Emitted by the Automobile Catalyst Converters. *Water, Air, and Soil Pollution*, 196(1-4):393–402, 2009.
- [14] Z. E. Gagnon, C. Newkirk, and S. Hicks. Impact of Platinum Group Metals on the Environment: A Toxicological, Genotoxic and Analytical Chemistry Study. *Journal of Environmental Science and Health, Part A*, 41(3):397–414, 2006.
- [15] P. Boscolo, L. Di Giampaolo, M. Reale, M. L. Castellani, A. Ritavolpe, M. Carmignani, J. Ponti, R. Paganelli, E. Sabbioni, P. Conti, and M. Di Gioacchino. Different effects of platinum, palladium, and rhodium salts on lymphocyte proliferation and cytokine release. *Annals of Clinical and Laboratory Science*, 34(3):299–306, 2004.
- [16] C. Botre, M. Tosi, F. Mazzei, B. Bocca, F. Petrucci, and A. Alimonti. Automotive catalytic converters and environmental pollution: role of the platinum group elements in the redox reactions and free radicals production. *International Journal of Environment and Health*, 1(1):142, 2007.
- [17] J. Zhang, editor. *PEM fuel cell electrocatalysts and catalyst layers: fundamentals and applications*. Springer, London, 2008.
- [18] L. Piccolo, A. Piednoir, and J.-C. Bertolini. Absorption and oxidation of hydrogen at Pd and PdAu (111) surfaces. *Surface Science*, 600(18):4211–4215, 2006.
- [19] S. Völkening, K. Bedürftig, K. Jacobi, J. Wintterlin, and G. Ertl. Dual-Path Mechanism for Catalytic Oxidation of Hydrogen on Platinum Surfaces. *Physical Review Letters*, 83(13):2672–2675, 1999.
- [20] G. Pauer and A. Winkler. Water formation on Pd(111) by reaction of oxygen with atomic and molecular hydrogen. *The Journal of Chemical Physics*, 120(8):3864–3870, 2004.
- [21] J. Benziger, J. Nehlsen, D. Blackwell, T. Brennan, and J. Itescu. Water flow in the gas diffusion layer of PEM fuel cells. *Journal of Membrane Science*, 261(1-2):98–106, 2005.
- [22] J. P. Owejan, J. E. Owejan, W. Gu, T. A. Trabold, T. W. Tighe, and M. F. Mathias. Water Transport Mechanisms in PEMFC Gas Diffusion Layers. *Journal of The Electrochemical Society*, 157(10):B1456, 2010.

- [23] C. Spiegel. Flow-field design. <https://www.fuelcellstore.com/blog-section/flow-field-design>, last accessed on April 08, 2020.
- [24] C. Spiegel. Pressure distribution in bipolar plate flow channels. <https://www.fuelcellstore.com/blog-section/pressure-distribution-in-bipolar-plate-flow-channels>, last accessed on April 08, 2020.
- [25] A. Hermann, T. Chaudhuri, and P. Spagnol. Bipolar plates for PEM fuel cells: A review. *International Journal of Hydrogen Energy*, 30(12):1297–1302, 2005.
- [26] D. S. Su and G. Sun. Nonprecious-Metal Catalysts for Low-Cost Fuel Cells. *Angewandte Chemie International Edition*, 50(49):11570–11572, 2011.
- [27] N. Guerrero Moreno, M. Cisneros Molina, D. Gervasio, and J. F. Pérez Robles. Approaches to polymer electrolyte membrane fuel cells (PEMFCs) and their cost. *Renewable and Sustainable Energy Reviews*, 52:897–906, 2015.
- [28] E. Middelmann. Improved PEM fuel cell electrodes by controlled self-assembly. *Fuel Cells Bulletin*, 2002(11):9–12, 2002.
- [29] B. E. Conway and G. Jerkiewicz. Relation of energies and coverages of underpotential and overpotential deposited H at Pt and other metals to the volcano curve for cathodic H₂ evolution kinetics. *Electrochimica Acta*, 45(25):4075–4083, 2000.
- [30] O. Antoine, Y. Bultel, R. Durand, and P. Ozil. Electrocatalysis, diffusion and ohmic drop in PEMFC: Particle size and spatial discrete distribution effects. *Electrochimica Acta*, 43(24):3681–3691, 1998.
- [31] F. Maillard, S. Pronkin, and E. R. Savinova. Size Effects in Electrocatalysis of Fuel Cell Reactions on Supported Metal Nanoparticles. In *Fuel Cell Catalysis*, pages 507–566. John Wiley & Sons, Ltd, 2008.
- [32] T. Schmidt, Z. Jusys, H. Gasteiger, R. Behm, U. Endruschat, and H. Boenemann. On the CO tolerance of novel colloidal PdAu/carbon electrocatalysts. *Journal of Electroanalytical Chemistry*, 501(1-2):132–140, 2001.
- [33] P. Ruvinsky, S. Pronkin, V. Zaikovskii, P. Bernhardt, and E. Savinova. On the enhanced electrocatalytic activity of Pd overlayers on carbon-supported gold particles in hydrogen electrooxidation. *Physical Chemistry Chemical Physics*, page 14, 2008.
- [34] S. N. Pronkin, A. Bonnefont, P. S. Ruvinskiy, and E. R. Savinova. Hydrogen oxidation kinetics on model Pd/C electrodes: Electrochemical impedance spectroscopy and rotating disk electrode study. *Electrochimica Acta*, 55(9):3312–3323, 2010.

- [35] M. S. Rau, P. M. Quaino, M. R. Gennero de Chialvo, and A. C. Chialvo. Hydrogen oxidation reaction: Evidences of different electrocatalytic activity between α and β Pd-H. *Electrochemistry Communications*, 10(2):208–212, 2008.
- [36] K. Kwon, S. Jin, K. H. Lee, D. J. You, and C. Pak. Performance enhancement of Pd-based hydrogen oxidation catalysts using tungsten oxide. *Catalysis Today*, 232:175–178, 2014.
- [37] R. B. Levy and M. Boudart. Platinum-Like Behavior of Tungsten Carbide in Surface Catalysis. *Science*, 181(4099):547–549, 1973.
- [38] C. J. Barnett, G. T. Burstein, A. R. J. Kucernak, and K. R. Williams. Electrocatalytic activity of some carburised nickel, tungsten and molybdenum compounds. *Electrochimica Acta*, 42(15):2381–2388, 1997.
- [39] E. C. Weigert, A. L. Stottlemeyer, M. B. Zellner, and J. G. Chen. Tungsten Monocarbide as Potential Replacement of Platinum for Methanol Electrooxidation. *The Journal of Physical Chemistry C*, 111(40):14617–14620, 2007.
- [40] B. Li, J. Qiao, D. Yang, J. Zheng, J. Ma, J. Zhang, and H. Wang. Synthesis of a highly active carbon-supported Ir α V/C catalyst for the hydrogen oxidation reaction in PEMFC. *Electrochimica Acta*, 54(24):5614–5620, 2009.
- [41] M. Gattrell and B. MacDougall. Reaction mechanisms of the O₂ reduction/evolution reaction. In W. Vielstich, A. Lamm, H. A. Gasteiger, and H. Yokokawa, editors, *Handbook of Fuel Cells*. John Wiley & Sons, Ltd, Chichester, UK, 2010.
- [42] K. C. Neyerlin, H. A. Gasteiger, C. K. Mittelstaedt, J. Jorne, and W. Gu. Effect of Relative Humidity on Oxygen Reduction Kinetics in a PEMFC. *Journal of The Electrochemical Society*, 152(6):A1073, 2005.
- [43] C. Song, Y. Tang, J. L. Zhang, J. Zhang, H. Wang, J. Shen, S. McDermid, J. Li, and P. Kozak. PEM fuel cell reaction kinetics in the temperature range of 23–120°C. *Electrochimica Acta*, 52(7):2552–2561, 2007.
- [44] J. K. Norskov, J. Rossmeisl, A. Logadottir, L. Lindqvist, J. R. Kitchin, T. Bligaard, and H. Jónsson. Origin of the Overpotential for Oxygen Reduction at a Fuel-Cell Cathode. *The Journal of Physical Chemistry B*, 108(46):17886–17892, 2004.
- [45] D. E. Curtin, R. D. Lousenberg, T. J. Henry, P. C. Tangeman, and M. E. Tisack. Advanced materials for improved PEMFC performance and life. *Journal of Power Sources*, 131(1-2):41–48, 2004.
- [46] C. Chen and Thomas F. Fuller. Modeling of H₂O₂ formation in PEMFCs. *Electrochimica Acta*, 54(16):3984–3995, 2009.

- [47] O. Antoine and R. Durand. RRDE study of oxygen reduction on Pt nanoparticles inside Nafion: H₂O₂ production in PEMFC cathode conditions. *Journal of Applied Electrochemistry*, 30(7):839–844, 2000.
- [48] W. Smeltzer and D. Young. Oxidation properties of transition metals. *Progress in Solid State Chemistry*, 10:17–54, 1975.
- [49] M. Turner, V. Golovko, O. Vaughan, P. Abdulkin, A. Berenguer-Murcia, M. Tikhov, B. Johnson, and R. Lambert. Selective oxidation with dioxygen by gold nanoparticle catalysts derived from 55-atom clusters. *Nature*, 454(7207):981–983, 2008.
- [50] A. Hashmi, Stephen K., and Graham J. Hutchings. Gold Catalysis. *Angewandte Chemie International Edition*, 45(47):7896–7936, 2006.
- [51] M. Haruta. Size- and support-dependency in the catalysis of gold. *Catalysis Today*, 36(1):153–166, 1997.
- [52] M. Shao, A. Peles, and K. Shoemaker. Electrocatalysis on Platinum Nanoparticles: Particle Size Effect on Oxygen Reduction Reaction Activity. *Nano Letters*, 11(9):3714–3719, 2011.
- [53] S. Mukerjee. Particle size and structural effects in platinum electrocatalysis. *Journal of Applied Electrochemistry*, 20(4):537–548, 1990.
- [54] F. J. Perez-Alonso, D. N. McCarthy, A. Nierhoff, P. Hernandez-Fernandez, C. Strebler, I. E. L. Stephens, J. H. Nielsen, and I. Chorkendorff. The Effect of Size on the Oxygen Electroreduction Activity of Mass-Selected Platinum Nanoparticles. *Angewandte Chemie International Edition*, 51(19):4641–4643, 2012.
- [55] J. Greeley, I. E. L. Stephens, A. S. Bondarenko, T. P. Johansson, H. A. Hansen, T. F. Jaramillo, J. Rossmeisl, I. Chorkendorff, and J. K. Norskov. Alloys of platinum and early transition metals as oxygen reduction electrocatalysts. *Nature Chemistry*, 1(7):552–556, 2009.
- [56] S. Mukerjee and S. Srinivasan. Enhanced electrocatalysis of oxygen reduction on platinum alloys in proton exchange membrane fuel cells. *Journal of Electroanalytical Chemistry*, 357(1):201–224, 1993.
- [57] C. Venkateswara Rao and B. Viswanathan. ORR Activity and Direct Ethanol Fuel Cell Performance of Carbon-Supported Pt-M (M = Fe, Co, and Cr) Alloys Prepared by Polyol Reduction Method. *The Journal of Physical Chemistry C*, 113(43):18907–18913, 2009. Publisher: American Chemical Society.
- [58] A. Wieckowski. *Fuel Cell Catalysis: A Surface Science Approach*. John Wiley & Sons, 2009.

- [59] K. Zhang, Q. Yue, Gu. Chen, Y. Zhai, L. Wang, H. Wang, J. Zhao, J. Liu, J. Jia, and H. Li. Effects of Acid Treatment of Pt@Ni Alloy Nanoparticles@Graphene on the Kinetics of the Oxygen Reduction Reaction in Acidic and Alkaline Solutions. *The Journal of Physical Chemistry C*, 115(2):379–389, 2011.
- [60] U. A. Paulus, A. Wokaun, G. G. Scherer, T. J. Schmidt, V. Stamenkovic, V. Radmilovic, N. M. Markovic, and P. N. Ross. Oxygen Reduction on Carbon-Supported Pt-Ni and Pt-Co Alloy Catalysts. *The Journal of Physical Chemistry B*, 106(16):4181–4191, 2002.
- [61] V. R. Stamenkovic, B. Fowler, B. S. Mun, G. Wang, P. N. Ross, C. A. Lucas, and N. M. Markovic. Improved Oxygen Reduction Activity on Pt₃Ni(111) via Increased Surface Site Availability. *Science*, 315(5811):493–497, 2007.
- [62] W. Li, Z. Chen, L. Xu, and Y. Yan. A solution-phase synthesis method to highly active Pt-Co/C electrocatalysts for proton exchange membrane fuel cell. *Journal of Power Sources*, 195(9):2534–2540, 2010.
- [63] C. Wang, N. M. Markovic, and V. R. Stamenkovic. Advanced Platinum Alloy Electrocatalysts for the Oxygen Reduction Reaction. *ACS Catalysis*, 2(5):891–898, 2012. Publisher: American Chemical Society.
- [64] B. Hammer and J.K. Norskov. Electronic factors determining the reactivity of metal surfaces. *Surface Science*, 343(3):211–220, 1995.
- [65] B. Hammer and J.K. Norskov. Theoretical surface science and catalysis—calculations and concepts. In *Advances in Catalysis*, volume 45, pages 71–129. Elsevier, 2000.
- [66] S. De, J. Zhang, R. Luque, and N. Yan. Ni-based bimetallic heterogeneous catalysts for energy and environmental applications. *Energy & Environmental Science*, 9(11):3314–3347, 2016.
- [67] L. Dubau, J. Nelayah, S. Moldovan, O. Ersen, P. Bordet, J. Drnec, T. Asset, R. Chattot, and F. Maillard. Defects do Catalysis: CO Monolayer Oxidation and Oxygen Reduction Reaction on Hollow PtNi/C Nanoparticles. *ACS Catalysis*, 6(7):4673–4684, 2016.
- [68] T. Asset, N. Job, Y. Busby, A. Crisci, V. Martin, V. Stergiopoulos, C. Bonnaud, A. Serov, P. Atanassov, R. Chattot, L. Dubau, and F. Maillard. Porous Hollow PtNi/C Electrocatalysts: Carbon Support Considerations To Meet Performance and Stability Requirements. *ACS Catalysis*, 8(2):893–903, 2018.
- [69] L. Dubau, T. Asset, R. Chattot, C. Bonnaud, V. Vanpeene, J. Nelayah, and F. Maillard. Tuning the Performance and the Stability of Porous Hollow

- PtNi/C Nanostructures for the Oxygen Reduction Reaction. *ACS Catalysis*, 5(9):5333–5341, 2015.
- [70] A. Kuzume, E. Herrero, and J. M. Feliu. Oxygen reduction on stepped platinum surfaces in acidic media. *Journal of Electroanalytical Chemistry*, 599(2):333–343, 2007.
- [71] O. V. Cherstiouk, P. A. Simonov, V. I. Zaikovskii, and E.R. Savinova. CO monolayer oxidation at Pt nanoparticles supported on glassy carbon electrodes. *Journal of Electroanalytical Chemistry*, 554-555:241–251, 2003.
- [72] F. Maillard, S. Schreier, M. Hanzlik, E. R. Savinova, S. Weinkauff, and U. Stimming. Influence of particle agglomeration on the catalytic activity of carbon-supported Pt nanoparticles in CO monolayer oxidation. *Phys. Chem. Chem. Phys.*, 7(2):385–393, 2005.
- [73] J. Li and F. Jaouen. Structure and activity of metal-centered coordination sites in pyrolyzed metal-nitrogen-carbon catalysts for the electrochemical reduction of O₂. *Current Opinion in Electrochemistry*, 9:198–206, 2018.
- [74] G. Faubert, R. Côté, D. Guay, J.P. Dodelet, G. Dénès, and P. Bertrandc. Iron catalysts prepared by high-temperature pyrolysis of tetraphenylporphyrins adsorbed on carbon black for oxygen reduction in polymer electrolyte fuel cells. *Electrochimica Acta*, 43(3-4):341–353, 1998.
- [75] S. L. Gojkovic, S. Gupta, and R. F. Savinell. Heat-treated iron(III) tetramethoxyphenyl porphyrin chloride supported on high-area carbon as an electrocatalyst for oxygen reduction Part II. Kinetics of oxygen reduction. *Journal of Electroanalytical Chemistry*, page 10, 1999.
- [76] Y. Chen, Z. Liang, F. Yang, Y. Liu, and S. Chen. Ni@Pt Core-Shell Nanoparticles as Oxygen Reduction Electrocatalysts: Effect of Pt Shell Coverage. *The Journal of Physical Chemistry C*, 115(49):24073–24079, 2011.
- [77] M. Lei, P.G. Li, L.H. Li, and W.H. Tang. A highly ordered Fe@N/C nanoarray as a non-precious oxygen-reduction catalyst for proton exchange membrane fuel cells. *Journal of Power Sources*, 196(7):3548–3552, 2011.
- [78] E. Proietti, F. Jaouen, M. Lefèvre, N. Larouche, J. Tian, J. Herranz, and J.-P. Dodelet. Iron-based cathode catalyst with enhanced power density in polymer electrolyte membrane fuel cells. *Nature Communications*, 2(1), 2011.
- [79] J. Kibsgaard, Y. Gorlin, Z. Chen, and T. F. Jaramillo. Meso-Structured Platinum Thin Films: Active and Stable Electrocatalysts for the Oxygen Reduction Reaction. *Journal of the American Chemical Society*, 134(18):7758–7765, 2012.

- [80] B. Lim, M. Jiang, P. H. C. Camargo, E. C. Cho, J. Tao, X. Lu, Y. Zhu, and Y. Xia. Pd-Pt Bimetallic Nanodendrites with High Activity for Oxygen Reduction. *Science*, 324(5932):1302–1305, 2009.
- [81] D. van der Vliet, C. Wang, D. Tripkovic, D. Strmcnik, X. Zhang, M. Debe, R. Atanasoski, N. Markovic, and V. Stamenkovic. Mesostructured thin films as electrocatalysts with tunable composition and surface morphology. *Nature Materials*, 11(12):1051–1058, 2012.
- [82] F. Maillard, W. O. Silva, L. Castanheira, L. Dubau, and F. H. B. Lima. Carbon Corrosion in Proton-Exchange Membrane Fuel Cells: Spectrometric Evidence for Pt-Catalysed Decarboxylation at Anode-Relevant Potentials. *ChemPhysChem*, 20(22):3106–3111, 2019.
- [83] K. H. Kangasniemi, D. A. Condit, and T. D. Jarvi. Characterization of Vulcan Electrochemically Oxidized under Simulated PEM Fuel Cell Conditions. *Journal of The Electrochemical Society*, 151(4):E125, 2004.
- [84] N. Macauley, D. D. Papadias, J. Fairweather, D. Spornjak, D. Langlois, R. Ahluwalia, K. L. More, R. Mukundan, and R. L. Borup. Carbon Corrosion in PEM Fuel Cells and the Development of Accelerated Stress Tests. *Journal of The Electrochemical Society*, 165(6):F3148–F3160, 2018.
- [85] S. Maass, F. Finsterwalder, G. Frank, R. Hartmann, and C. Merten. Carbon support oxidation in PEM fuel cell cathodes. *Journal of Power Sources*, 176(2):444–451, 2008.
- [86] E. Auer, A. Freund, J. Pietsch, and T. Tacke. Carbons as supports for industrial precious metal catalysts. *Applied Catalysis A: General*, 173(2):259–271, 1998.
- [87] Y. Shao, G. Yin, and Y. Gao. Understanding and approaches for the durability issues of Pt-based catalysts for PEM fuel cell. *Journal of Power Sources*, 171(2):558–566, 2007.
- [88] F. Coloma, A. Sepulvedaescibano, and F. Rodriguezreinoso. Heat-Treated Carbon-Blacks as Supports for Platinum Catalysts. *Journal of Catalysis*, 154(2):299–305, 1995.
- [89] D. A. Stevens, M. T. Hicks, G. M. Haugen, and J. R. Dahn. Ex Situ and In Situ Stability Studies of PEMFC Catalysts. *Journal of The Electrochemical Society*, 152(12):A2309, 2005.
- [90] F. Maillard, P. A. Simonov, and E. R. Savinova. Carbon Materials as Supports for Fuel Cell Electrocatalysts. In *Carbon Materials for Catalysis*, pages 429–480. John Wiley & Sons, Ltd, 2008.

- [91] K. Kinoshita. *Carbon: Electrochemical and Physicochemical Properties*. Wiley, 1988.
- [92] Y. Shao, S. Zhang, C. Wang, Z. Nie, J. Liu, Y. Wang, and Y. Lin. Highly durable graphene nanoplatelets supported Pt nanocatalysts for oxygen reduction. *Journal of Power Sources*, 195(15):4600–4605, 2010.
- [93] R. W. Pekala. Organic aerogels from the polycondensation of resorcinol with formaldehyde. *Journal of Materials Science*, 24(9):3221–3227, 1989.
- [94] N. Job, R. Pirard, J. Marien, and J.-P. Pirard. Porous carbon xerogels with texture tailored by pH control during sol-gel process. *Carbon*, 42(3):619–628, 2004.
- [95] N. Job, A. Théry, R. Pirard, J. Marien, L. Kocon, J.-N. Rouzaud, F. Béguin, and J.-P. Pirard. Carbon aerogels, cryogels and xerogels: Influence of the drying method on the textural properties of porous carbon materials. *Carbon*, 43(12):2481–2494, 2005.
- [96] A. K. Geim and K. S. Novoselov. The rise of graphene. In *Nanoscience and Technology*, pages 11–19. Co-Published with Macmillan Publishers Ltd, UK, 2009.
- [97] M. J. McAllister, J.-L. Li, D. H. Adamson, H. C. Schniepp, A. A. Abdala, J. Liu, M. Herrera-Alonso, D. L. Milius, R. Car, R. K. Prud’homme, and I. A. Aksay. Single Sheet Functionalized Graphene by Oxidation and Thermal Expansion of Graphite. *Chemistry of Materials*, 19(18):4396–4404, 2007.
- [98] B. P. Vinayan, R. I. Jafri, R. Nagar, N. Rajalakshmi, K. Sethupathi, and S. Ramaprabhu. Catalytic activity of platinum-cobalt alloy nanoparticles decorated functionalized multiwalled carbon nanotubes for oxygen reduction reaction in PEMFC. *International Journal of Hydrogen Energy*, 37(1):412–421, 2012.
- [99] R. W. Pekala and C.T. Alviso. Carbon Aerogels and Xerogels. *MRS Proceedings*, 270, 1992.
- [100] I. A. Vasyukova, A. A. Gusev, and A. Y. Ubogov, A. Y. Godymchuk. Study of MWNTS Influence upon Liver Histological and Histochemical Parameters in Laboratory Mice: Preliminary Results. *Advanced Materials Research*, 1085:376–383, 2015.
- [101] Y. Wang, J. Yu, W. Dai, Y. Song, D. Wang, L. Zeng, and N. Jiang. Enhanced thermal and electrical properties of epoxy composites reinforced with graphene nanoplatelets. *Polymer Composites*, 36(3):556–565, 2015.

- [102] J. H. Chen, W. Z. Li, D. Z. Wang, S. X. Yang, J. G. Wen, and Z. F. Ren. Electrochemical characterization of carbon nanotubes as electrode in electrochemical double-layer capacitors. *Carbon*, 40(8):1193–1197, 2002.
- [103] J. Landon, X. Gao, B. Kulengowski, J. K. Neathery, and K. Liu. Impact of Pore Size Characteristics on the Electrosorption Capacity of Carbon Xerogel Electrodes for Capacitive Deionization. *Journal of The Electrochemical Society*, 159(11):A1861–A1866, 2012.
- [104] Y. Zhou, R. Pasquarelli, T. Holme, J. Berry, D. Ginley, and R. O’Hayre. Improving PEM fuel cell catalyst activity and durability using nitrogen-doped carbon supports: observations from model Pt/HOPG systems. *Journal of Materials Chemistry*, 19(42):7830, 2009.
- [105] Y. Zhou, K. Neyerlin, T. S. Olson, S. Pylypenko, J. Bult, H. N. Dinh, T. Gennett, Z. Shao, and R. O’Hayre. Enhancement of Pt and Pt-alloy fuel cell catalyst activity and durability via nitrogen-modified carbon supports. *Energy & Environmental Science*, 3(10):1437, 2010.
- [106] R. Wang, H. Wang, T. Zhou, J. Key, Y. Ma, Z. Zhang, Q. Wang, and S. Ji. The enhanced electrocatalytic activity of okara-derived N-doped mesoporous carbon for oxygen reduction reaction. *Journal of Power Sources*, 274:741–747, 2015.
- [107] P. Matter, E. Wang, and U. Ozkan. Preparation of nanostructured nitrogen-containing carbon catalysts for the oxygen reduction reaction from SiO₂- and MgO-supported metal particles. *Journal of Catalysis*, 243(2):395–403, 2006.
- [108] P. Matter, L. Zhang, and U. Ozkan. The role of nanostructure in nitrogen-containing carbon catalysts for the oxygen reduction reaction. *Journal of Catalysis*, 239(1):83–96, 2006.
- [109] V. V. Strelko and V. S. Kuts’. The effect of nitrogen in the carbon matrix on the donor-acceptor and catalytic activity of activated carbons in electron transfer reactions. *Theoretical and Experimental Chemistry*, 35(6):315–318, 1999.
- [110] V. Strelko, V. Kuts, and P. Thrower. On the mechanism of possible influence of heteroatoms of nitrogen, boron and phosphorus in a carbon matrix on the catalytic activity of carbons in electron transfer reactions. *Carbon*, 38(10):1499–1503, 2000.
- [111] S. Maldonado and K. J. Stevenson. Influence of Nitrogen Doping on Oxygen Reduction Electrocatalysis at Carbon Nanofiber Electrodes. *The Journal of Physical Chemistry B*, 109(10):4707–4716, 2005.

- [112] E. Antolini. Formation, microstructural characteristics and stability of carbon supported platinum catalysts for low temperature fuel cells. *Journal of Materials Science*, 38(14):2995–3005, 2003.
- [113] B. H. Morrow and A. Striolo. Platinum nanoparticles on carbonaceous materials: the effect of support geometry on nanoparticle mobility, morphology, and melting. *Nanotechnology*, 19(19):195711, 2008.
- [114] Y. Xiao, G. Yu, J. Yuan, J. Wang, and Z. Chen. Fabrication of Pd-Ni alloy nanowire arrays on HOPG surface by electrodeposition. *Electrochimica Acta*, 51(20):4218–4227, 2006.
- [115] C. E. Cross, J. C. Hemminger, and R. M. Penner. Physical Vapor Deposition of One-Dimensional Nanoparticle Arrays on Graphite: Seeding the Electrodeposition of Gold Nanowires. *Langmuir*, 23(20):10372–10379, 2007.
- [116] T. Holme, Y. Zhou, R. Pasquarelli, and R. O’Hayre. First principles study of doped carbon supports for enhanced platinum catalysts. *Physical Chemistry Chemical Physics*, 12(32):9461–9468, 2010.
- [117] N. A. Kumar, H. Nolan, N. McEvoy, E. Rezvani, R. L. Doyle, M. E. G. Lyons, and G. S. Duesberg. Plasma-assisted simultaneous reduction and nitrogen doping of graphene oxide nanosheets. *Journal of Materials Chemistry A*, 1(14):4431, 2013.
- [118] H. Tao, C. Yan, A. W. Robertson, Y. Gao, J. Ding, Y. Zhang, T. Ma, and Z. Sun. N-Doping of graphene oxide at low temperature for the oxygen reduction reaction. *Chemical Communications*, 53(5):873–876, 2017. Publisher: The Royal Society of Chemistry.
- [119] Y. Wang, F. Yu, M. Zhu, C. Ma, D. Zhao, C. Wang, A. Zhou, B. Dai, J. Ji, and X. Guo. N-Doping of plasma exfoliated graphene oxide *via* dielectric barrier discharge plasma treatment for the oxygen reduction reaction. *Journal of Materials Chemistry A*, 6(5):2011–2017, 2018.
- [120] I. Bertóti, M. Mohai, and K. László. Surface modification of graphene and graphite by nitrogen plasma: Determination of chemical state alterations and assignments by quantitative X-ray photoelectron spectroscopy. *Carbon*, 84:185–196, 2015.
- [121] C. Bittencourt, A. Felten, B. Douhard, J.-F. Colomer, G. Van Tendeloo, W. Drube, J. Ghijsen, and J.-J. Pireaux. Metallic nanoparticles on plasma treated carbon nanotubes: Nano2hybrids. *Surface Science*, 601(13):2800–2804, 2007.
- [122] P. Chabert and N. Braithwaite. *Physics of Radio-Frequency Plasmas*. Cambridge University Press, 2011.

- [123] I. Langmuir. The adsorption of gases on plane surfaces of glass, mica and platinum. *Journal of the American Chemical Society*, 40(9):1361–1403, 1918.
- [124] L. Tonks. The Birth of Plasma. *American Journal of Physics*, 35(9):857–858, 1967.
- [125] R. O. Dendy. *Plasma Dynamics*. Clarendon Press, 1990.
- [126] D. Hastings and H. Garrett. *Spacecraft-Environment Interactions*. Cambridge University Press, 2004.
- [127] J. Meichsner, M. Schmidt, R. Schneider, and H.-E. Wagner. *Nonthermal Plasma Chemistry and Physics*. CRC Press, 2012.
- [128] K. Wiesemann. A Short Introduction to Plasma Physics. *arXiv:1404.0509 [physics]*, 2014.
- [129] M. A. Lieberman and A. J. Lichtenberg. *Principles of Plasma Discharges and Materials Processing: Lieberman/Plasma 2e*. John Wiley & Sons, Inc., Hoboken, NJ, USA, 2005.
- [130] B. P. Pandey and S. V. Vladimirov. A simple formula for the wall potential in the plasma sheath. *Europhysics Letters*, 94(5):55002, 2011.
- [131] A. Felten. *Electronic and structural properties of plasma functionalized and metal decorated carbon nanotubes*. Phd thesis, University of Namur, 2007.
- [132] A. Fridman and L. A. Kennedy. *Plasma Physics and Engineering*. CRC Press, 2004.
- [133] A. Bogaerts, E. Neyts, R. Gijbels, and J. van der Mullen. Gas discharge plasmas and their applications. *Spectrochimica Acta Part B: Atomic Spectroscopy*, 57(4):609–658, 2002.
- [134] F. Denes. Macromolecular plasma-chemistry: an emerging field of polymer science. *Progress in Polymer Science*, 29(8):815–885, 2004.
- [135] W. Hittorf. Ueber die Electricitätsleitung der Gase. *Annalen der Physik*, 257(1):90–139, 1884.
- [136] Y. W. Lee, H. L. Lee, and T. H. Chung. E-H mode transition in low-pressure inductively coupled nitrogen-argon and oxygen-argon plasmas. *Journal of Applied Physics*, 109(11):113302, 2011.
- [137] J. T. Gudmundsson and M. A. Lieberman. Magnetic induction and plasma impedance in a cylindrical inductive discharge. *Plasma Sources Science and Technology*, 6(4):540–550, 1997.

- [138] M. M. Turner and M. A. Lieberman. Hysteresis and the E-to-H transition in radiofrequency inductive discharges. *Plasma Sources Science and Technology*, 8(2):313–324, 1999.
- [139] I. M. El-Fayoumi, I. R. Jones, and M. M. Turner. Hysteresis in the E- to H-mode transition in a planar coil, inductively coupled rf argon discharge. *Journal of Physics D: Applied Physics*, 31(21):3082–3094, 1998. Publisher: IOP Publishing.
- [140] U. Kortshagen, N. D. Gibson, and J. E. Lawler. On the E - H mode transition in RF inductive discharges. *Journal of Physics D: Applied Physics*, 29(5):1224–1236, 1996.
- [141] A. Vesel, R. Zaplotnik, G. Primc, X. Liu, K. Xu, K. C. Chen, C. Wei, and M. Mozetic. Functionalization of Polyurethane/Urea Copolymers with Amide Groups by Polymer Treatment with Ammonia Plasma. *Plasma Chemistry and Plasma Processing*, 36(3):835–848, 2016.
- [142] S. Bashir and J. Liu. Overviews of Synthesis of Nanomaterials. In *Advanced Nanomaterials and their Applications in Renewable Energy*, pages 51–115. Elsevier, 2015.
- [143] J. Speder, L. Altmann, M. Roefzaad, M. Bäumer, J. J. K. Kirkensgaard, K. Mortensen, and M. Arenz. Pt based PEMFC catalysts prepared from colloidal particle suspensions â a toolbox for model studies. *Physical Chemistry Chemical Physics*, 15(10):3602, 2013.
- [144] M. Watanabe, M. Uchida, and S. Motoo. Preparation of highly dispersed Pt + Ru alloy clusters and the activity for the electrooxidation of methanol. *Journal of Electroanalytical Chemistry and Interfacial Electrochemistry*, 229(1):395–406, 1987.
- [145] P. Gélin and M. Primet. Complete oxidation of methane at low temperature over noble metal based catalysts: a review. *Applied Catalysis B: Environmental*, 39(1):1–37, 2002.
- [146] H. Liu, C. Song, L. Zhang, J. Zhang, H. Wang, and D. P. Wilkinson. A review of anode catalysis in the direct methanol fuel cell. *Journal of Power Sources*, 155(2):95–110, 2006.
- [147] F. Rahmani, M. Haghghi, Y. Vafaeian, and P. Estifae. Hydrogen production via CO₂ reforming of methane over ZrO₂-Doped Ni/ZSM-5 nanostructured catalyst prepared by ultrasound assisted sequential impregnation method. *Journal of Power Sources*, 272:816–827, 2014.
- [148] X. Zhou, Q. Chen, Y. Tao, and H. Weng. Influence of Ultrasound Impregnation on the Performance of Co/Zr/SiO₂ catalyst during Fischer-Tropsch Synthesis. *Chinese Journal of Catalysis*, 32(6-8):1156–1165, 2011.

- [149] B. L. Cushing, V. L. Kolesnichenko, and C. J. O'Connor. Recent Advances in the Liquid-Phase Syntheses of Inorganic Nanoparticles. *Chemical Reviews*, 104(9):3893–3946, 2004.
- [150] A. Caillard, P. Brault, J. Mathias, C. Charles, R. W. Boswell, and T. Sauvage. Deposition and diffusion of platinum nanoparticles in porous carbon assisted by plasma sputtering. *Surface and Coatings Technology*, 200(1):391–394, 2005.
- [151] A. Caillard, S. Cuynet, T. Lecas, P. Andreazza, M. Mikikian, A.-L. Thomann, and P. Brault. PdPt catalyst synthesized using a gas aggregation source and magnetron sputtering for fuel cell electrodes. *Journal of Physics D: Applied Physics*, 48(47):475302, 2015.
- [152] O. K. Alexeeva and V. N. Fateev. Application of the magnetron sputtering for nanostructured electrocatalysts synthesis. *International Journal of Hydrogen Energy*, 41(5):3373–3386, 2016.
- [153] S. Hussain, H. Erikson, N. Kongi, M. Merisalu, P. Ritslaid, V. Sammelselg, and K. Tammeveski. Heat-treatment effects on the ORR activity of Pt nanoparticles deposited on multi-walled carbon nanotubes using magnetron sputtering technique. *International Journal of Hydrogen Energy*, 42(9):5958–5970, 2017.
- [154] L. Dreesen, J.-F. Colomer, H. Limage, A. Giguère, and S. Lucas. Synthesis of titanium dioxide nanoparticles by reactive DC magnetron sputtering. *Thin Solid Films*, 518(1):112–115, 2009.
- [155] N. Nuntawong, M. Horprathum, P. Eiamchai, K. Wong-ek, V. Patthanasettakul, and P. Chindaudom. Surface-enhanced Raman scattering substrate of silver nanoparticles depositing on AAO template fabricated by magnetron sputtering. *Vacuum*, 84(12):1415–1418, 2010.
- [156] D.-Q. Yang and E. Sacher. Strongly Enhanced Interaction between Evaporated Pt Nanoparticles and Functionalized Multiwalled Carbon Nanotubes via Plasma Surface Modifications: Effects of Physical and Chemical Defects. *The Journal of Physical Chemistry C*, 112(11):4075–4082, 2008.
- [157] J.-C. Charlier, L. Arnaud, I. V. Avilov, M. Delgado, F. Demoisson, E. H. Espinosa, C. P. Ewels, A. Felten, J. Guillot, R. Ionescu, R. Leghrib, E. Llobet, A. Mansour, H.-N. Migeon, J.-J. Pireaux, F. Reniers, I. Suarez-Martinez, G. E. Watson, and Z. Zanolli. Carbon nanotubes randomly decorated with gold clusters: from nano² hybrid atomic structures to gas sensing prototypes. *Nanotechnology*, 20(37):375501, 2009.
- [158] D. Merche, T. Dufour, J. Baneton, G. Caldarella, V. Debaille, N. Job, and F. Reniers. Fuel Cell Electrodes From Organometallic Platinum Precursors:

- An Easy Atmospheric Plasma Approach. *Plasma Processes and Polymers*, 13(1):91–104, 2016.
- [159] P. Brault, S. Roualdès, A. Caillard, A.-L. Thomann, J. Mathias, J. Durand, C. Coutanceau, J.-M. Léger, C. Charles, and R. Boswell. Solid polymer fuel cell synthesis by low pressure plasmas: a short review. *The European Physical Journal Applied Physics*, 34(2):151–156, 2006.
- [160] C.-L. Sun, L.-C. Chen, M.-C. Su, L.-S. Hong, O. Chyan, C.-Y. Hsu, K.-H. Chen, T.-F. Chang, and L. Chang. Ultrafine Platinum Nanoparticles Uniformly Dispersed on Arrayed CN_x Nanotubes with High Electrochemical Activity. *Chemistry of Materials*, 17(14):3749–3753, 2005.
- [161] L. Xie, P. Brault, C. Coutanceau, J.-M. Bauchire, A. Caillard, S. Baranton, J. Berndt, and E. C. Neyts. Efficient amorphous platinum catalyst cluster growth on porous carbon: A combined molecular dynamics and experimental study. *Applied Catalysis B: Environmental*, 162:21–26, 2015.
- [162] P. Brault. Review of low pressure plasma processing of proton exchange membrane fuel cell electrocatalysts. *Plasma Processes and Polymers*, 13:10–18, 2016.
- [163] J.-J. Pireaux, F. Reniers, J. Guillot, M. Gulas, N. Claessens, A. Batan, and A. Mansour. Method for Depositing Nanoparticles on Substrates, 2012.
- [164] M. Laurent-Brocq, , N. Job, D. Eskenazi, and J.-J. Pireaux. Pt/C catalyst for PEM fuel cells: Control of Pt nanoparticles characteristics through a novel plasma deposition method. *Applied Catalysis B: Environmental*, 147:453–463, 2014.
- [165] J.-J. Zou, Y. Zhang, and C.-J. Liu. Reduction of Supported Noble-Metal Ions Using Glow Discharge Plasma. *Langmuir*, 22(26):11388–11394, 2006.
- [166] X. Gillon. *Chemistry and physics of plasma polymerization probed by mass spectrometry*. Phd thesis, Université de Namur, 2014.
- [167] E. Haye, Y. Busby, M. da Silva Pires, F. Bocchese, N. Job, L. Houssiau, and J.-J. Pireaux. Low-Pressure Plasma Synthesis of Ni/C Nanocatalysts from Solid Precursors: Influence of the Plasma Chemistry on the Morphology and Chemical State. *ACS Applied Nano Materials*, 1(1):265–273, 2018.
- [168] S. Flanagan, E. Hall, W. Bowie, J. W. Fuhs, R. Logan, F. Maniei, and A. Hunt. A design-of-experiments approach to modeling activity coefficients in solvent mixtures: a case study using platinum(ii) acetylacetonate in mixtures of acetone, cyclohexanol, 1,2,3,4-tetrahydronaphthalene and propylene carbonate. *Green Chemistry*, 7(5):333, 2005.

- [169] S. E. Bozbag, N. S. Yasar, L. C. Zhang, M. Aindow, and C. Erkey. Adsorption of Pt(cod)me₂ onto organic aerogels from supercritical solutions for the synthesis of supported platinum nanoparticles. *The Journal of Supercritical Fluids*, 56(1):105–113, 2011.
- [170] D. L. Perry. *Handbook of Inorganic Compounds*. CRC Press, 2016.
- [171] J. G. Jenkin, R. C. G. Leckey, and J. Liesegang. The development of x-ray photoelectron spectroscopy: 1900–1960. *Journal of Electron Spectroscopy and Related Phenomena*, 12(1):1–35, 1977.
- [172] S. Oswald. X-Ray Photoelectron Spectroscopy in Analysis of Surfaces Update based on the original article by Steffen Oswald, Encyclopedia of Analytical Chemistry, 2000, John Wiley & Sons, Ltd. In *Encyclopedia of Analytical Chemistry*. American Cancer Society, 2013.
- [173] A. W. Drummond. *XPS: Instrumentation and Performance*. SurfaceSpectra Limited, 2003.
- [174] H. P. C. E. Kuipers, H. C. E. Van Leuven, and W. M. Visser. The characterization of heterogeneous catalysts by XPS based on geometrical probability 1: Monometallic catalysts. *Surface and Interface Analysis*, 8(6):235–242, 1986.
- [175] J. E. Fulghum and R. W. Linton. Quantitation of coverages on rough surfaces by XPS: An overview. *Surface and Interface Analysis*, 13(4):186–192, 1988.
- [176] M. P. Seah and W. A. Dench. Quantitative electron spectroscopy of surfaces: A standard data base for electron inelastic mean free paths in solids. *Surface and Interface Analysis*, 1(1):2–11, 1979.
- [177] D. Briggs and M. P. Seah. *Practical Surface Analysis, Auger and X-ray Photoelectron Spectroscopy*. Wiley, 1996.
- [178] W. Friedrich, P. Knipping, and M. Laue. Interferenzerscheinungen bei Röntgenstrahlen. *Annalen der Physik*, 346(10):971–988, 1913.
- [179] William Henry Bragg and William Lawrence Bragg. The reflection of X-rays by crystals. *Proceedings of the Royal Society of London. Series A, Containing Papers of a Mathematical and Physical Character*, 88(605):428–438, July 1913. Publisher: Royal Society.
- [180] A. L. Patterson. The Scherrer Formula for X-Ray Particle Size Determination. *Physical Review*, 56(10):978–982, November 1939. Publisher: American Physical Society.

- [181] L. de Broglie. Recherches sur la théorie des Quanta. *Annales de Physique*, 10(3):22–128, 1925.
- [182] C. Davisson and L. H. Germer. Diffraction of Electrons by a Crystal of Nickel. *Physical Review*, 30(6):705–740, 1927.
- [183] G. P. Thomson and A. Reid. Diffraction of Cathode Rays by a Thin Film. *Nature*, 119(3007):890–890, 1927.
- [184] M. Knoll and E. Ruska. Das Elektronenmikroskop. *Zeitschrift für Physik*, 78(5):318–339, 1932.
- [185] P. Champness. *An Introduction to Electron Diffraction in the Transmission Electron Microscope*. BIOS Scientific Publishers, October 2001.
- [186] D. B. Williams and C. B. Carter. *Transmission electron microscopy: a textbook for materials science*. Springer, New York, 2nd ed edition, 2008.
- [187] Stephen J. Pennycook and Peter D. Nellist, editors. *Scanning Transmission Electron Microscopy: Imaging and Analysis*. Springer-Verlag, 2011.
- [188] S. J. Pennycook and D. E. Jesson. High-resolution Z-contrast imaging of crystals. *Ultramicroscopy*, 37(1):14–38, 1991.
- [189] Sina Ebnesajjad. Chapter 4 - Surface and Material Characterization Techniques. In Sina Ebnesajjad, editor, *Surface Treatment of Materials for Adhesive Bonding (Second Edition)*, pages 39–75. William Andrew Publishing, 2014.
- [190] J. W. Coburn and M. Chen. Optical emission spectroscopy of reactive plasmas: A method for correlating emission intensities to reactive particle density. *Journal of Applied Physics*, 51(6):3134–3136, 1980.
- [191] K. Behringer. Diagnostics and modelling of ECRH microwave discharges. *Plasma Physics and Controlled Fusion*, 33(9):997–1028, 1991.
- [192] M. V. Malyshev and V. M. Donnelly. Trace rare gases optical emission spectroscopy: Nonintrusive method for measuring electron temperatures in low-pressure, low-temperature plasmas. *Physical Review E*, 60(5):6016–6029, 1999. Publisher: American Physical Society.
- [193] J. B. Boffard, C. C. Lin, and C. A. DeJosephJr. Application of excitation cross sections to optical plasma diagnostics. *Journal of Physics D: Applied Physics*, 37(12):R143–R161, 2004.
- [194] A. J. Bard and L. R. Faulkner. *Electrochemical Methods: Fundamentals and Applications*. Wiley, 1980.

- [195] K. Mayrhofer. *Oxygen Reduction and Carbon Monoxide Oxidation on Pt - from Model to Real Systems for Fuel Cell Electrocatalysis*. Phd thesis, Vienna University of Technology, 2006.
- [196] O. Yamazaki, Y. Oomori, H. Shintaku, and T. Tabata. Study on Degradation of the Pt-Ru Anode of PEFC for Residential Application (2): Analyses of the MEAs Degraded in the Anode Performance. *ECS Transactions*, 11(1):287, 2007. Publisher: IOP Publishing.
- [197] S. Zhang, X.-Z. Yuan, J. N. C. Hin, H. Wang, K. A. Friedrich, and M. Schulze. A review of platinum-based catalyst layer degradation in proton exchange membrane fuel cells. *Journal of Power Sources*, 194(2):588–600, 2009.
- [198] M. Sun, Y. Lv, Y. Song, H. Wu, G. Wang, H. Zhang, M. Chen, Q. Fu, and X. Bao. CO-tolerant PtRu@h-BN/C core-shell electrocatalysts for proton exchange membrane fuel cells. *Applied Surface Science*, 450:244–250, August 2018.
- [199] M. González-Hernández, E. Antolini, and J. Perez. CO tolerance and stability of PtRu and PtRuMo electrocatalysts supported on N-doped graphene nanoplatelets for polymer electrolyte membrane fuel cells. *International Journal of Hydrogen Energy*, 45(8):5276–5284, February 2020.
- [200] F. Maillard, M. Eikerling, O. V. Cherstiouk, S. Schreier, E. Savinova, and U. Stimming. Size effects on reactivity of Pt nanoparticles in CO monolayer oxidation: The role of surface mobility. *Faraday Discussions*, 125:357, 2004.
- [201] F. Maillard, E. R. Savinova, and U. Stimming. CO monolayer oxidation on Pt nanoparticles: Further insights into the particle size effects. *Journal of Electroanalytical Chemistry*, 599(2):221–232, 2007.
- [202] S. Brunauer, P. H. Emmett, and E. Teller. Adsorption of Gases in Multimolecular Layers. *Journal of the American Chemical Society*, 60(2):309–319, 1938.
- [203] Micromeritics Instrument Corporation. Gas adsorption theory. https://www.micromeritics.com/Repository/Files/Gas_Adsorption_Theory_poster.pdf, last accessed on April 08, 2020.
- [204] Y. Nishi and M. Inagaki. Gas Adsorption/Desorption Isotherm for Pore Structure Characterization. In *Materials Science and Engineering of Carbon*, pages 227–247. Elsevier, 2016.
- [205] E. P. Barrett, L. G. Joyner, and P. P. Halenda. The Determination of Pore Volume and Area Distributions in Porous Substances. I. Computations from Nitrogen Isotherms. *Journal of the American Chemical Society*, 73(1):373–380, 1951.

- [206] P. Klobes. *Porosity and Specific Surface Area Measurements for Solid Materials*. U.S. Department of Commerce, Technology Administration, National Institute of Standards and Technology, 2006.
- [207] E. Antolini and F. Cardellini. Formation of carbon supported PtRu alloys: an XRD analysis. *Journal of Alloys and Compounds*, 315(1-2):118–122, 2001.
- [208] X. Tang, N. Reckinger, O. Poncelet, P. Louette, F. Ureña, H. Idrissi, S. Turner, D. Cabosart, J.-F. Colomer, J.-P. Raskin, B. Hackens, and L. A. Francis. Damage evaluation in graphene underlying atomic layer deposition dielectrics. *Scientific Reports*, 5(1):13523, 2015.
- [209] G. Zhang, D. Yang, and E. Sacher. X-ray Photoelectron Spectroscopic Analysis of Pt Nanoparticles on Highly Oriented Pyrolytic Graphite, Using Symmetric Component Line Shapes. *The Journal of Physical Chemistry C*, 111(2):565–570, 2007.
- [210] J. R. Croy, S. Mostafa, H. Heinrich, and B. R. Cuenya. Size-selected Pt Nanoparticles Synthesized via Micelle Encapsulation: Effect of Pretreatment and Oxidation State on the Activity for Methanol Decomposition and Oxidation. *Catalysis Letters*, 131(1-2):21–32, 2009.
- [211] G. K. Wertheim and L. R. Walker. Many-body effects in transition metals: role of the density of states. *Journal of Physics F: Metal Physics*, 6(12):2297–2306, 1976.
- [212] N. Gorjizadeh, A. Farajian, and Y. Kawazoe. The effects of defects on the conductance of graphene nanoribbons. *Nanotechnology*, 20(1):015201, 2009.
- [213] H. Wang, T. Maiyalagan, and X. Wang. Review on Recent Progress in Nitrogen-Doped Graphene: Synthesis, Characterization, and Its Potential Applications. *ACS Catalysis*, 2(5):781–794, 2012.
- [214] J. P. S. Sousa, M. F. R. Pereira, and J. L. Figueiredo. Catalytic oxidation of NO to NO₂ on N-doped activated carbons. *Catalysis Today*, 176(1):383–387, 2011.
- [215] S. Rauf and M. J. Kushner. Argon metastable densities in radio frequency Ar, Ar/O₂ and Ar/CF₄ electrical discharges. *Journal of Applied Physics*, 82(6):2805–2813, 1997.
- [216] N. Job, J. Marie, S. Lambert, S. Berthon-Fabry, and P. Achard. Carbon xerogels as catalyst supports for PEM fuel cell cathode. *Energy Conversion and Management*, 49(9):2461–2470, 2008.

- [217] Z. Kregar, M. Biscan, S. Milosevic, and A. Vesel. Monitoring Oxygen Plasma Treatment of Polypropylene With Optical Emission Spectroscopy. *IEEE Transactions on Plasma Science*, 39(5):1239–1246, 2011.
- [218] Z. Machala, M. Janda, K. Hensel, I. Jedlovský, L. Leštinská, V. Foltin, V. Martišovits, and M. Morvová. Emission spectroscopy of atmospheric pressure plasmas for bio-medical and environmental applications. *Journal of Molecular Spectroscopy*, 243(2):194–201, 2007.
- [219] C.-C. Hsu and Y.-J. Yang. The Increase of the Jet Size of an Atmospheric-Pressure Plasma Jet by Ambient Air Control. *IEEE Transactions on Plasma Science*, 38(3):496–499, 2010.
- [220] S. S. Harilal, R. C. Issac, C. V. Bindhu, V. P. N. Nampoori, and C. P. G. Vallabhan. Optical emission studies of species in laser-produced plasma from carbon. *Journal of Physics D: Applied Physics*, 30(12):1703–1709, 1997.
- [221] P. Saikia, B. K. Saikia, and H. Bhuyan. Study on the effect of hydrogen addition on the variation of plasma parameters of argon-oxygen magnetron glow discharge for synthesis of TiO₂ films. *AIP Advances*, 6(4):045206, 2016. Publisher: American Institute of Physics.
- [222] Z. Bo, Y. Yang, J. Chen, K. Yu, J. Yan, and K. Cen. Plasma-enhanced chemical vapor deposition synthesis of vertically oriented graphene nanosheets. *Nanoscale*, 5(12):5180–5204, 2013. Publisher: The Royal Society of Chemistry.
- [223] M. Shalom, D. Ressnig, X. Yang, G. Clavel, T. P. Fellingner, and M. Antonietti. Nickel nitride as an efficient electrocatalyst for water splitting. *Journal of Materials Chemistry A*, 3(15):8171–8177, 2015.
- [224] J. Mürbe, A. Rechtenbach, and J. Töpfer. Synthesis and physical characterization of magnetite nanoparticles for biomedical applications. *Materials Chemistry and Physics*, 110(2-3):426–433, 2008.
- [225] B. P. Payne, A. P. Grosvenor, M. C. Biesinger, B. A. Kobe, and N. S. McIntyre. Structure and growth of oxides on polycrystalline nickel surfaces. *Surface and Interface Analysis*, 39(7):582–592, 2007.
- [226] M. C. Biesinger, B. P. Payne, A. P. Grosvenor, L. W. M. Lau, A. R. Gerson, and R. St. C. Smart. Resolving surface chemical states in XPS analysis of first row transition metals, oxides and hydroxides: Cr, Mn, Fe, Co and Ni. *Applied Surface Science*, 257(7):2717–2730, 2011.
- [227] R. Steinberger, J. Walter, T. Greunz, J. Duchoslav, M. Arndt, S. Molodtsov, D.C. Meyer, and D. Stifter. XPS study of the effects of long-term Ar⁺ ion and Ar cluster sputtering on the chemical degradation of hydrozincite and iron oxide. *Corrosion Science*, 99:66–75, 2015.

- [228] B. Zhang, C. Xiao, S. Xie, J. Liang, X. Chen, and Y. Tang. Iron-Nickel Nitride Nanostructures in Situ Grown on Surface-Redox-Etching Nickel Foam: Efficient and Ultrasustainable Electrocatalysts for Overall Water Splitting. *Chemistry of Materials*, 28(19):6934–6941, 2016.
- [229] H.-P. Boehm. Catalytic Properties of Nitrogen-Containing Carbons. In *Carbon Materials for Catalysis*, pages 219–265. John Wiley & Sons, Ltd, 2008.
- [230] M. da Silva Pires, E. Haye, A. Zubiaur, N. Job, J.-J. Pireaux, L. Houssiau, and Y. Busby. Defective Pt-Ni/graphene nanomaterials by simultaneous or sequential treatments of organometallic precursors by low-pressure oxygen plasma. *Plasma Processes and Polymers*, 16(5):1800203, 2019.
- [231] R. J. Seresht, M. Jahanshahi, A. M. Rashidi, and A. A. Ghoreyshi. Synthesis and characterization of thermally-reduced graphene. *Iran.J.Energy Environ.*, 4(1):53–59, 2013. Cited By :33.
- [232] D.-H. Lim and J. Wilcox. DFT-Based Study on Oxygen Adsorption on Defective Graphene-Supported Pt Nanoparticles. *The Journal of Physical Chemistry C*, 115(46):22742–22747, 2011.
- [233] A. P. Grosvenor, M. C. Biesinger, R. St. C. Smart, and N. S. McIntyre. New interpretations of XPS spectra of nickel metal and oxides. *Surface Science*, 600(9):1771–1779, 2006.
- [234] S. Trasatti and O. A. Petrii. Real surface area measurements in electrochemistry. *Journal of Electroanalytical Chemistry*, 327(1):353–376, 1992.
- [235] R. Chattot, T. Asset, P. Bordet, J. Drnec, L. Dubau, and F. Maillard. Beyond Strain and Ligand Effects: Microstrain-Induced Enhancement of the Oxygen Reduction Reaction Kinetics on Various PtNi/C Nanostructures. *ACS Catalysis*, 7(1):398–408, 2017.
- [236] T. Horikawa, J. Hayashi, and K. Muroyama. Controllability of pore characteristics of resorcinol-formaldehyde carbon aerogel. *Carbon*, 42(8):1625–1633, 2004.
- [237] H. Jin, H. Zhang, H. Zhong, and J. Zhang. Nitrogen-doped carbon xerogel: A novel carbon-based electrocatalyst for oxygen reduction reaction in proton exchange membrane (PEM) fuel cells. *Energy & Environmental Science*, 4(9):3389–3394, 2011. Publisher: The Royal Society of Chemistry.
- [238] Y.-C. Lin, C.-Y. Lin, and P.-W. Chiu. Controllable graphene N-doping with ammonia plasma. *Applied Physics Letters*, 96(13):133110, 2010. Publisher: American Institute of Physics.

- [239] M. Moisan, D. Kéroack, and L. Stafford. *Physique atomique et spectroscopie optique*. EDP Sciences, 2017.
- [240] S. J. Kang and V. M. Donnelly. Optical absorption and emission spectroscopy studies of ammonia-containing plasmas. *Plasma Sources Science and Technology*, 16(2):265–272, 2007. Publisher: IOP Publishing.
- [241] B. Yu, X. Wang, X. Qian, W. Xing, H. Yang, L. Ma, Y. Lin, S. Jiang, L. Song, Y. Hu, and S. Lo. Functionalized graphene oxide/phosphoramidate oligomer hybrids flame retardant prepared via in situ polymerization for improving the fire safety of polypropylene. *RSC Advances*, 4(60):31782–31794, 2014.
- [242] D. Liu, L. Li, and T. You. Superior catalytic performances of platinum nanoparticles loaded nitrogen-doped graphene toward methanol oxidation and hydrogen evolution reaction. *Journal of Colloid and Interface Science*, 487:330–335, 2017.
- [243] N. Mutsukura, K. Kobayashi, and Y. Machi. Plasma sheath thickness in radio-frequency discharges. *Journal of Applied Physics*, 68(6):2657–2660, 1990. Publisher: American Institute of Physics.
- [244] S. Hou, X. Cai, H. Wu, X. Yu, M. Peng, K. Yan, and D. Zou. Nitrogen-doped graphene for dye-sensitized solar cells and the role of nitrogen states in triiodide reduction. *Energy & Environmental Science*, 6(11):3356–3362, 2013. Publisher: The Royal Society of Chemistry.
- [245] J. Chen, X. Wang, X. Cui, G. Yang, and W. Zheng. Amorphous carbon enriched with pyridinic nitrogen as an efficient metal-free electrocatalyst for oxygen reduction reaction. *Chemical Communications*, 50(5):557–559, 2013. Publisher: The Royal Society of Chemistry.
- [246] S. Ratso, N. R. Sahraie, M. T. Sougrati, Ma. Käärrik, M. Kook, R. Saar, P. Paiste, Q. Jia, J. Leis, S. Mukerjee, F. Jaouen, and K. Tammeveski. Synthesis of highly-active Fe-N-C catalysts for PEMFC with carbide-derived carbons. *Journal of Materials Chemistry A*, 6(30):14663–14674, 2018. Publisher: The Royal Society of Chemistry.
- [247] L. Wang, X. Wan, S. Liu, L. Xu, and J. Shui. Fe-N-C catalysts for PEMFC: Progress towards the commercial application under DOE reference. *Journal of Energy Chemistry*, 39:77–87, 2019.
- [248] S. Doniach and M. Sunjic. Many-electron singularity in X-ray photoemission and X-ray line spectra from metals. *Journal of Physics C: Solid State Physics*, 3(2):285–291, 1970. Publisher: IOP Publishing.

-
- [249] H. Okamoto. Ni-Pt (Nickel-Platinum). *Journal of Phase Equilibria and Diffusion*, 31(3):322–322, 2010.
- [250] M. Chatenet, L. Dubau, N. Job, and F. Maillard. The (electro)catalyst|membrane interface in the Proton Exchange Membrane Fuel Cell: Similarities and differences with non-electrochemical Catalytic Membrane Reactors. *Catalysis Today*, 156(3):76–86, October 2010.
- [251] N. Job, S. Lambert, M. Chatenet, C. J. Gommès, F. Maillard, S. Berthon-Fabry, J. R. Regalbuto, and J.-P. Pirard. Preparation of highly loaded Pt/carbon xerogel catalysts for Proton Exchange Membrane fuel cells by the Strong Electrostatic Adsorption method. *Catalysis Today*, 150(1):119–127, 2010.
- [252] A. Zubiaur, M. Chatenet, F. Maillard, S. D. Lambert, J.-P. Pirard, and N. Job. Using the Multiple SEA Method to Synthesize Pt/Carbon Xerogel Electrocatalysts for PEMFC Applications. *Fuel Cells*, 14(3):343–349, 2014.

